

Layer-fMRI acquisition and analysis

Daniel Craig Marsh MSci

Thesis presented to
The University of Nottingham
for the degree of
Doctor of Philosophy
October 2023

Abstract

Functional Magnetic Resonance Imaging (fMRI) is a widely adopted imaging modality used to study human brain function. The advancements in MR hardware and acquisition have enabled researchers to investigate brain function at sub-millimetre resolution, detecting brain activation at depths across the cortex. Layer-fMRI at ultra-high field (UHF, defined as $B_0 \geq 7$ T) has the potential to answer many neuroscience questions that were previously untenable due to low spatial resolution or a low signal-to-noise ratio (SNR). In addition, the combination of layer-fMRI with electroencephalography (EEG) provides a tool to investigate neuronal oscillation across cortical depths.

This thesis develops methods for the analysis of layer-dependent simultaneous EEG-fMRI data acquired at 7 T using a gradient echo (GE) Blood Oxygenation Level Dependent (BOLD) sequence during an eyes open, eyes closed task to assess the origins of human alpha oscillations. An optimal pipeline is developed for the combination of EEG and fMRI data with structural MRI data in order to calculate layer-specific alpha activation profiles. These methods will be an important building block for the growth of layer-dependent EEG-fMRI as an imaging tool, with only one previous 3 T study to date known to have acquired such data [1]. A key limitation of the methods was found to be the draining vein effect present in GE-BOLD data, with multiple methods considered to correct for it.

To improve understanding of alpha oscillations, the bespoke analysis pipeline was applied to layer-dependent EEG-fMRI data acquired on 10 subjects at 7 T during an eyes open, eyes closed task. The results showed significant negative correlation between EEG alpha power and the BOLD response in the visual cortex. The cortical layer profiles of negative alpha-BOLD correlations exhibited a dip in the middle cortical depths and peaked in the deeper and superficial depths, suggesting that during an eyes open/closed paradigm alpha is predominantly generated during top-down processing through corticocortical mechanism.

This is then followed by a study using the non-BOLD fMRI contrast of vascular space occupancy (VASO) for layer-fMRI measures. High spatial resolution VASO has greater spatial specificity and does not suffer from the impacts of the draining vein effect making it a good option for layer-fMRI. However, VASO has inherently lower signal than GE-BOLD and is often SNR limited. In this thesis, a denoising method of NOise Reduction with DIstribution Correction (NORDIC) Principal Component Analysis (PCA) was assessed for its application to high resolution 3D-EPI BOLD data before being applied to an optimised 1 mm isotropic VASO sequence for layer-specific measures during a finger-tapping task. The results from ten subjects show a VASO layer profile that peaks in the middle cortical depths. A double peak was expected from the literature however this disparity was most likely due to acquiring at a spatial resolution that was too coarse. When compared, the VASO and ‘deveined’ GE-BOLD layer profiles showed a similar shape for cortical depths 1 – 4 which then diverged in depths 5 and 6, highlighting the need for further work to validate corrections of the draining vein effect.

Finally, NORDIC denoising was applied to T_1 mapping data for structural layer measures. It was found that there was a small improvement in the T_1 fit, represented by an increase in the wellness of the fit value, R^2 . Additionally, there was a tightening in the peaks for both the grey matter (GM) and white matter (WM) T_1 values, shown by decreases in the full width at half maximum (FWHM). WM showed greater improvements than GM for both the R^2 and FWHM.

Contents

Abstract	i
Contents	iii
Acknowledgments	vi
Abbreviations	viii
1 Introduction	1
1.1 Thesis Outline	3
2 Magnetic Resonance Imaging	5
2.1 NMR	5
2.2 Image Acquisition	17
2.3 MR Hardware	21
2.4 Imaging Techniques	27
2.5 Conclusion	32
3 Neurophysiology Theory: Origins of EEG and fMRI signals	33
3.1 Introduction	33
3.2 Origin of the EEG signal	35
3.3 Brain Structure and Cortical Layers	40
3.4 Origin of the fMRI signal	48
3.5 fMRI Analysis	53
3.6 Conclusion	57

4	Analysis pipeline to assess layer-specific alpha signals using EEG-fMRI	58
4.1	Introduction	61
4.2	Acquisition of 7 T EEG-fMRI data	64
4.3	Analysis Pipeline Overview	72
4.4	Functional Analysis Pipeline	75
4.5	Interrogating the fMRI timecourse	91
4.6	Defining Cortical Layers and Columns	92
4.7	Calculating layer profiles	103
4.8	Discussion	118
5	Assessing the origins of alpha oscillations	124
5.1	Introduction	127
5.2	Assessing EEG data quality	129
5.3	EEG alpha HRF Convolution	132
5.4	Subject-specific Retinotopy	133
5.5	EEG-fMRI fixed effects General Linear Model (GLM)	137
5.6	Defining layers and columns from structural scans	143
5.7	Layer Profiles	147
5.8	Discussion	151
6	Denoising for the improved study of VASO and BOLD layer fMRI	156
6.1	Introduction	159
6.2	Implementation of NORDIC denoising	165
6.3	Implementation of 1 mm VASO for layer fMRI	185
6.4	High resolution VASO for layer dependent measures in the motor cortex	201
6.5	NORDIC implementation for T_1 mapping structural measures	217
6.6	Conclusion	224

7 Conclusion	226
7.1 Key Findings	226
7.2 Future Directions	230
References	232
A Denoising β-weights	261
A.1 Determining the Noise Threshold of the β -weights	261
B Vein masks	271
B.1 Masking the veins from the fMRI data	271
B.2 Effect of veins on layer profiles	272
C Timecourse analysis	277
C.1 Comparison of the EEG alpha power and fMRI BOLD response	277

Acknowledgements

I would like to take this opportunity to thank all those who have helped me throughout the course of my PhD. First and foremost I would like to express my utmost gratitude to my supervisors Professor Susan Francis and Doctor Karen Mullinger. Thank you for your expert guidance and support through the incredible challenges of completing a PhD during a pandemic. I've thoroughly enjoyed working with you both and couldn't have asked for better supervisors.

I would also like to thank Michael for all your help with mrTools, debugging code on the old boy Mac and all our video game chats. Thanks to Tobi for all the tea breaks and the Bob Marley sing alongs. Thanks also goes to my fellow PhD students in the Barn for making the office an enjoyable place to live whilst writing up. Thank you to the wider SPMIC community for being so friendly and helpful, whether that be tapping your fingers for me in the scanner or bouncing ideas off each other in the tea room.

Credit also goes to all those who helped me on my quest to visit every pub in Nottingham. Thank you to the Real Ale Society committee for providing me with the opportunity to try some of the best beer around. A special thank you goes to my fellow Plough pub quiz team members. Max for all the corridor chats and checking in at my desk every now and then to make sure I've not lost the plot. Harry for all the years living together, drinking beer, watching sport and surviving lockdown. Alex for always being available for a quick pint and a long chat. I reckon we've done alright.

Thank you to my family for all your love and support throughout my many, many years in education. I am so grateful that you have always encouraged me to do things I love, I wouldn't have made it this far without you all.

Finally, thank you Sarah for sticking by my side through all of this, I'm not sure I'd have made it without your support. Thank you for fuelling me with your delicious cooking for late night writing and agreeing to join me on endless trips to random pubs, our adventures always gave me something to look forward to.

Abbreviations

aCBV	Arterial Cerebral Blood Volume
ADHD	Attention Deficit Hyperactivity Disorder
AFNI	Analysis of Functional NeuroImages
ALFF	Amplitude of Low Frequency Fluctuations
ANTs	Advanced Normalisation Tools
ASL	Arterial Spin Labelling
BBB	Blood Brain Barrier
BET	Brain Extraction Tool
BOLD	Blood Oxygen Level Dependent
BW	Bandwidth
CBF	Cerebral Blood Flow
CBV	Cerebral Blood Volume
CBV_v	Venous Cerebral Blood Volume
CMRO₂	Cerebral Metabolic Rate of Oxygen
CNR	Contrast to Noise Ratio
CPMG	Carr-Purcell-Meiboom-Gill
CSD	Current Source Density
CSF	Cerebrospinal Fluid
DIANA	Direct Imaging of Neuronal Activity
DW	Diffusion Weighted
ECG	Electrocardiograph
ECoG	Electrocorticography
EEG	Electroencephalography
EPI	Echo Planar Imaging
EPSP	Excitatory Post Synaptic Potential

FA	Flip Angle
FAST	FMRIB's Automated Segmentation Tool
FEAT	fMRI Expert Analysis Tool
FFT	Fast Fourier Transform
FID	Free Induction Decay
FLASH	Fast Low Angle Shot
FLIRT	FMRIB's Linear Image Registration Tool
fMRI	Functional Magnetic Resonance Imaging
FNIRT	FMRIB's Non-linear Image Registration Tool
FOV	Field Of View
FSL	fMRIB Software Library
FUGUE	fMRIB's Utility for Geometrically Unwarping EPIs
FWHM	Full Width Half Maximum
GA	Gradient Artefacts
GE	Gradient Echo
GLM	General Linear Model
GM	Grey Matter
HRF	Haemodynamic Response Function
HS	Halfscan
ICA	Independent Component Analysis
icEEG	Intracranial EEG
IB	Image Based
IPSP	Inhibitory Post Synaptic Potential
ISMRM	International Society of Magnetic Resonance in Medicine
LCMV	Linear Constraint Minimum Variance
LFP	Local Field Potential
LGN	Lateral Geniculate Nucleus
MA	Motion Artefacts
MCFLIRT	Motion Correction using FMRIB's Linear Image Registration Tool
MEG	Magnetoencephelography
mGluR1	Metabotropic Glutamate Receptor 1
MB	Multiband

MNI	Montreal National Institute
MPRAGE	Magnetisation Prepared Rapid Gradient Echo
MP2RAGE	Magnetisation Prepared 2 Rapid Gradient Echo
MRI	Magnetic Resonance Imaging
NaN	Not a Number
NMR	Nuclear Magnetic Resonance
NORDIC	NOise Reduction with DIstribution Correction
OHBM	Organisation for Human Brain Mapping
PA	Pulse Artefacts
PCA	Principal Component Analysis
PPU	Peripheral Pulse Unit
pRF	Population Receptive Field
PSD	Pulse Sequence Diagram
PSF	Point Spread Function
PSP	Post Synaptic Potential
PSIR	Phase Sensitive Inversion Recovery
PVE	Partial Volume Estimation
RF	Radio Frequency
ROI	Region Of Interest
RETROICOR	Retrospective Correction of Physiological Motion Effects in the Image Domain
rsBOLD	Resting State BOLD
SCP	Scan Control Parameter
SE	Spin Echo
SEM	Standard Error on the Mean
SENSE	Sensitivity Encoding
SMS	Simultaneous Multislice
SNR	Signal to Noise Ratio
SPM	Statistical Parametric Mapping toolbox
TE	Echo Time
TI	Inversion Time
TR	Repetition Time
tSNR	Temporal Signal to Noise Ratio

UHF	Ultra-High Field
VASO	Vascular Space Occupancy
VCG	Vectorcardiograph
VE	Virtual Electrode
VFA	Variable Flip Angle
WM	White Matter

Chapter 1

Introduction

Functional Magnetic Resonance Imaging (fMRI) is a valuable tool widely used by neuroscientists and clinicians around the world. After its discovery in 1990 [2], the Blood Oxygen Level Dependent (BOLD) contrast soon became the most popular imaging modality to study the function of the human brain. BOLD fMRI is a non-invasive, non-ionising imaging technique that has been used to investigate the function and neurophysiology of the healthy brain, as well as understand and diagnose neurovascular disorders, neurodegenerative diseases and mental illness.

Following years of development in MR hardware, acquisition and analysis, it is now possible to image brain function with incredible detail. This has been facilitated by the development of Ultra-High Field (UHF) MRI scanners. The vast majority of scanners worldwide are ≤ 3 T, but since 2005 there has been a rapid growth in the number of UHF MRI scanners, defined as scanners with magnetic field strengths ≥ 7 T, and there are currently ~ 100 worldwide [3]. The increased magnetic field strength provides increased signal-to-noise ratio and greater BOLD contrast enabling functional imaging with greater spatial resolution. The ability to measure brain activity at sub-millimetre resolutions gives rise to the field of layer-fMRI – the investigation of neuronal activity across cortical layers. The cortex has a thickness of 2–4 mm and so at typical fMRI

resolutions of ~ 2 mm isotropic it was previously impossible to differentiate signals from different locations across cortical depths. Layer-fMRI provides a key tool to understand the processing of information in the brain and its hierarchical organisation [4].

Advances in acquisition have brought about non-BOLD contrasts that are sensitive to Cerebral Blood Flow (CBF) or Cerebral Blood Volume (CBV). These additional techniques are more spatially specific measures of neuronal activity than gradient echo BOLD (GE-BOLD) and so can help to provide a more accurate picture of cortical activation in layer-fMRI. However, these techniques have a lower Contrast to Noise Ratio (CNR) than BOLD and need longer acquisition times or to be acquired at UHF to achieve the required spatial resolution.

In addition to developments in UHF hardware, there has been substantial work on combining different neuroimaging modalities in order to capitalise on the unique benefits of each modality. The most widely adopted of these is EEG-fMRI which combines the high temporal resolution of EEG with the high spatial resolution of fMRI. EEG is used extensively in the diagnosis [5, 6], treatment [7] and monitoring [6, 8] of epilepsy. EEG measures the electrical oscillations generated in the brain by 1000s of synchronously firing neurons. The oscillations are separated into five frequency bands: delta, theta, alpha, beta and gamma (see Section 3.2.4). EEG-fMRI allows the study of the relationship between the BOLD response and these electrophysiological frequency bands. One of the most extensively researched frequency bands is the alpha frequency – the first to be detected in the human brain [9]. Despite this, its generating mechanisms are still widely debated. This thesis utilises high resolution simultaneous layer EEG-fMRI data acquired at 7 T to assess the origins of human alpha oscillations through the development and implementation of a bespoke pipeline for the combination of EEG and layer-fMRI data.

In addition, this thesis studies improvements to the Signal to Noise Ratio (SNR) of BOLD fMRI experiments by the removal of thermal noise. The

increase in SNR due to the denoising approach enables the optimisation of a VASO-BOLD layer-fMRI acquisition which is used to investigate layer-specific activation during a motor task. The VASO layer activation profile is compared with a corrected BOLD layer profile to assess a model for correcting the draining vein effect.

1.1 Thesis Outline

Chapter 2 outlines the theory of Nuclear Magnetic Resonance (NMR) and its use to form an image using Magnetic Resonance Imaging (MRI). A detailed description is given for the origins of the signal, image formation, image contrasts and imaging acceleration methods. Details of the 7 T system used to collect all the data in this thesis are also given, along with an overview of the sequences used throughout this thesis.

Chapter 3 provides details on the neuronal origin of the EEG signal, cortical layer cytoarchitecture, top-down and bottom-up processing and previous work that has investigated the origin of alpha oscillations. Following this is an explanation of the origin of the BOLD fMRI signal with additional information on the combination of EEG and fMRI. The chapter concludes with a description of the typical preprocessing and analysis pipelines for fMRI data.

Chapter 4 is the first experimental chapter and covers the development of a bespoke pipeline for the analysis of layer-dependent simultaneous EEG-fMRI data. Including the formation of regressors from the EEG data, precise alignment of the MRI functional and structural data, the definition of subject specific ROIs, and the generation and corrections of layer profiles by correcting GE-BOLD measures using LayNii.

Chapter 5 applies this optimal pipeline to EEG-fMRI layer data collected in 10 healthy subjects to assess the origins of human alpha oscillations.

Chapter 6 first explores the testing and application of the NOise Reduction with DIstribution Correction (NORDIC) PCA denoising method. This is

followed by the implementation of VASO for layer-specific measures and the development and optimisation of a 1 mm isotropic VASO sequence. This sequence is used on healthy subjects to assess layer-specific activation in the motor cortex with a comparison of VASO layer measures with corrected GE-BOLD layer measures. Chapter 6 concludes with the assessment of applying NORDIC to T_1 mapping structural measures.

Chapter 7 concludes the thesis, providing a summary of the key findings from each chapter and outlining directions for future research.

Chapter 2

Magnetic Resonance Imaging

2.1 NMR

2.1.1 Nuclear Spin

Nuclear Magnetic Resonance (NMR) is a phenomenon that arises from the interaction between the nucleus of an atom and an external magnetic field (B_0). All nuclei have the intrinsic properties of mass (m), charge (q) and spin (I). In the nucleus the spin of neutrons and protons combine to give the total spin angular momentum, which is a quantum mechanical property that takes half-integer or integer values. If a nucleus contains an even number of both neutrons and protons, $I = 0$, and the nucleus is NMR inactive, for example ^{12}C . NMR is only exhibited in nuclei when $I \neq 0$. If there are an odd number of both neutrons and protons the nucleus will have integer I , for example deuterium ^2H . If there is an odd number of neutrons or protons, the nucleus will have half-integer I , the most common half-integer nucleus is proton ^1H (Table 2.1).

Isotope	Spin	γ (MHzT ⁻¹)	Natural abundance %
¹ H	1/2	42.58	99.985
² H	1	6.54	0.015
¹³ C	1/2	10.71	1.11
²³ Na	3/2	11.27	100
³¹ P	1/2	17.25	100

Table 2.1: Common NMR active isotopes, their nuclear spin, gyromagnetic ratio and natural abundance.

A nucleus with non-zero spin can be described as a rotating sphere with a charge, which gives rise to a current and subsequently a magnetic moment $\boldsymbol{\mu}$,

$$\boldsymbol{\mu} = \gamma \boldsymbol{J} \quad (2.1)$$

where γ is the gyromagnetic ratio of the nucleus and \boldsymbol{J} is the spin angular momentum vector. γ is a constant that is dependent on the mass and charge of each nucleus. ¹H is the most commonly imaged nucleus in MRI due to its high concentration in the body (~60%) and its high gyromagnetic ratio of $\gamma = 42.58$ MHzT⁻¹ compared to other nuclei see Table 2.1. The remaining chapter and all work in this thesis uses ¹H MRI, the nucleus of which contains a single proton and therefore has an intrinsic nuclear spin of 1/2.

When placed into an external magnetic field, B_0 , aligned along the z -axis, there are two possible orientations for the magnetic moment of a ¹H nucleus due to a phenomenon known as Zeeman splitting (Figure 2.2). These orientations are the ‘spin up’ and ‘spin down’ state, with the ‘spin up’ orientation corresponding to the magnetic moment aligned parallel to the magnetic field and the ‘spin down’ state corresponding to the magnetic moment aligning anti-parallel to the magnetic field (Figure 2.1).

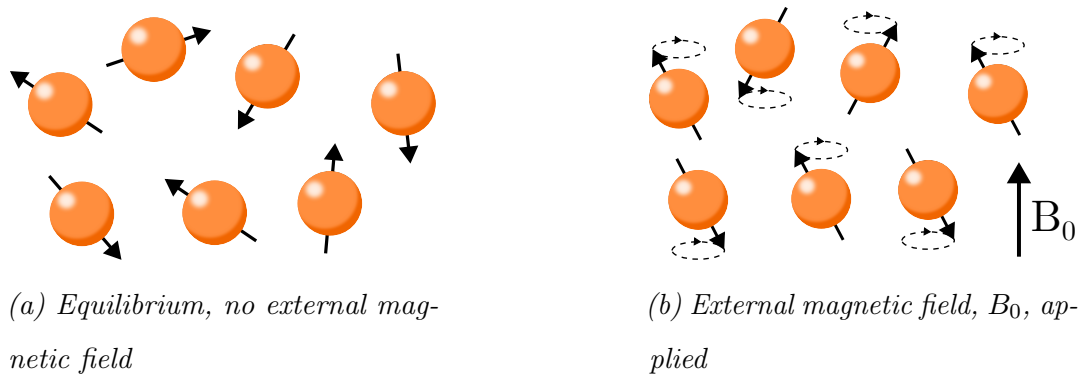


Figure 2.1: a) At equilibrium the spins are distributed randomly. b) Following the application of an external magnetic field B_0 , the spins align parallel or anti-parallel to the field with a resultant net magnetisation aligned with B_0 and the spins precess at the Larmor frequency, ω_0 .

The z component of these magnetic moment orientations is given by

$$\mu_z = m_I \hbar \gamma \quad (2.2)$$

where m_I are the possible spin quantum numbers of the ^1H nucleus, $\pm 1/2$, and \hbar is the reduced Planck's constant, $h/2\pi$. This results in two potential energy states for the 'spin down' state and the 'spin up' states of

$$E_{\downarrow} = +\frac{1}{2} \hbar \gamma B_0, \quad (2.3)$$

$$E_{\uparrow} = -\frac{1}{2} \hbar \gamma B_0. \quad (2.4)$$

The energy difference between these two spin states is given by,

$$\Delta E = \hbar \gamma B_0 = \hbar \omega_0 \quad (2.5)$$

where ω_0 is the Larmor frequency given by

$$\omega_0 = \gamma B_0 \quad (2.6)$$

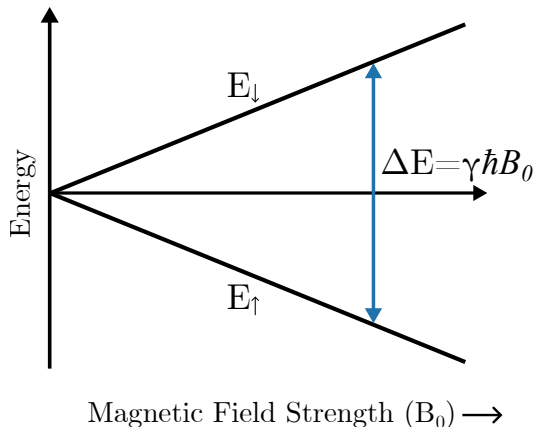


Figure 2.2: The energy difference, ΔE , due to Zeeman splitting, between the ‘spin down’ (E_{\downarrow}) and ‘spin up’ (E_{\uparrow}) state as a function of magnetic field strength, B_0 .

2.1.2 Net Magnetisation

For an ensemble of spins in a magnetic field, B_0 , there is an imbalance in the number of spins occupying the E_{\downarrow} or E_{\uparrow} energy states, with the parallel ‘spin up’ state (E_{\uparrow}) aligned with the magnetic field being slightly more energetically favourable. The distribution of the spins between spin states can be described using Boltzmann statistics,

$$\frac{n_{\uparrow}}{n_{\downarrow}} = \exp\left(\frac{-\Delta E}{k_B T}\right) \quad (2.7)$$

where n_{\uparrow} is the number of spins in the lower energy ‘spin up’ state (E_{\uparrow}), n_{\downarrow} is the number of spins in the higher energy ‘spin down’ state (E_{\downarrow}), k_B is the Boltzmann constant and T is the absolute temperature of the ensemble of spins. The imbalance in spin energy state populations results in a net magnetisation for the ensemble, M_0 which is given by

$$M_0 = \frac{N(\hbar\gamma)^2 B_0}{4k_B T}. \quad (2.8)$$

where N is the number of spins per unit volume. To increase the signal detected with NMR, M_0 can be increased by probing a nuclei with a higher γ , increasing

B_0 or lowering temperature T . For human scanning, it is most viable to increase the magnetic field strength, B_0 .

2.1.3 Precession

A magnetic moment, $\boldsymbol{\mu}$ placed into an external magnetic field, \mathbf{B} , experiences a torque, $\boldsymbol{\tau}$, that acts to align $\boldsymbol{\mu}$ with the direction of the external magnetic field, resulting in a rotation. Torque is defined as the rate of change of angular momentum, resulting in the relation

$$\boldsymbol{\tau} = \frac{d\mathbf{J}}{dt} = \boldsymbol{\mu} \times \mathbf{B} \quad (2.9)$$

substituting for Equation 2.1 gives

$$\frac{d\boldsymbol{\mu}}{dt} = \gamma \boldsymbol{\mu} \times \mathbf{B} \quad (2.10)$$

This equation describes the precessional motion of a single magnetic moment $\boldsymbol{\mu}$ in a magnetic field \mathbf{B} at the Larmor frequency, ω_0 . The Larmor frequency for a proton in a 7 T magnetic field is 298 MHz.

2.1.4 RF Excitation

An NMR signal can be detected by perturbing the precessing net magnetisation vector away from its alignment with the external magnetic field, B_0 . This is achieved by applying a second time varying magnetic field, B_1 , that oscillates with a frequency near to the Larmor frequency of the sample, and is orthogonal to B_0 . The B_1 field typically oscillates at a frequency in the Radio Frequency (RF) range, and is therefore referred to as an RF excitation or RF pulse. The application of B_1 brings the spins into phase and ‘tips’ the net magnetisation vector M_0 into the transverse plane. The extent to which the net magnetisation is tipped, known as the Flip Angle (FA) α , depends on the duration, τ and amplitude B_1 of the RF pulse ($\alpha = \gamma B_1 \tau$). As the magnetisation relaxes back to align with B_0 , it precesses about B_0 at the Larmor frequency. The precession

of the relaxing magnetisation is detectable via the induction of an electromotive force (emf) in a pickup coil, this is the NMR signal.

To simplify the picture of precessing magnetisation and oscillating B_1 fields, the rotating frame is often used as the coordinate system in which to consider the evolution of the spins following RF excitation. The rotating frame is a reference frame that rotates at the Larmor frequency about the z -axis that is aligned with B_0 . Figure 2.3 shows the evolution of the magnetisation vector, \mathbf{M} , following a 90° RF pulse in a) the stationary laboratory frame and b) in the rotating frame. In the laboratory frame the magnetisation vector \mathbf{M} is tipped into the transverse plane to yield transverse magnetisation, M_{xy} , and then rotates around B_0 at the same time as it returns to equilibrium. In the rotating frame matched to the Larmor frequency, \mathbf{M} no longer precesses around B_0 and B_1 is also stationary along the x' -axis.

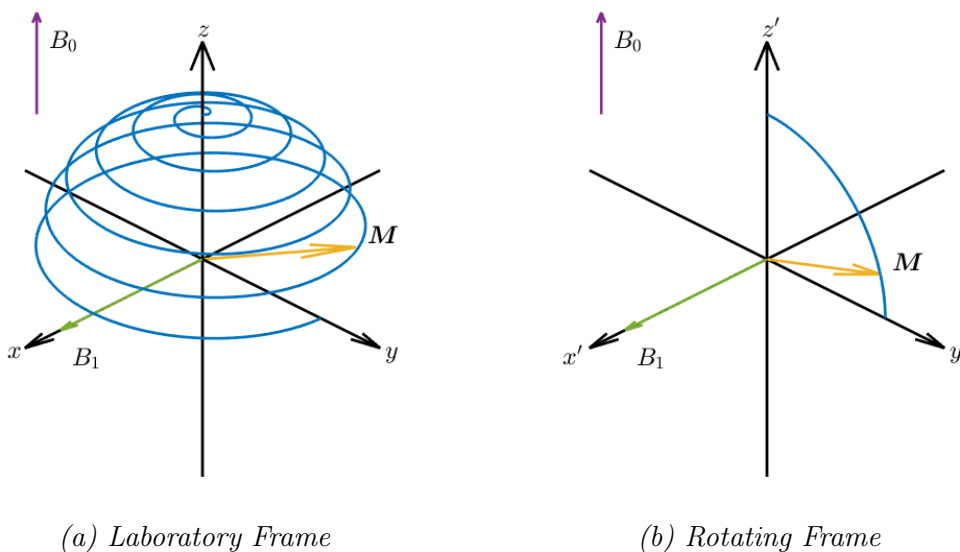


Figure 2.3: Magnetisation evolution following a 90° RF excitation pulse in the a) laboratory and b) rotating reference frames. In the a) laboratory frame \mathbf{M} precesses about B_0 whilst recovering to equilibrium, whereas in the b) rotating frame \mathbf{M} solely rotates around the x' axis.

2.1.5 Relaxation

After an RF excitation pulse has concluded, the net magnetisation vector begins to relax back into its equilibrium state via two independent processes known as the longitudinal relaxation and the transverse relaxation. Longitudinal relaxation is the process by which the longitudinal magnetisation, M_z returns to its equilibrium alignment with B_0 signifying the restoration of the equilibrium spin populations. Transverse relaxation is the dephasing process to return the transverse magnetisation, M_{xy} back to zero. These processes are governed by their own independent time constants T_1 and T_2 respectively, which are dependent on the properties of the local environment and give rise to the different contrasts for tissues in the body. Longitudinal and transverse magnetisation are described by the Bloch equation

$$\frac{d\mathbf{M}}{dt} = \gamma(\mathbf{M} \times \mathbf{B}) - \frac{(M_z - M_0)\mathbf{k}}{T_1} - \frac{M_x\mathbf{i} + M_y\mathbf{j}}{T_2} \quad (2.11)$$

where T_1 is the longitudinal relaxation time, and T_2 is the transverse relaxation time. The first term refers to precession inside the magnetic field, the second longitudinal relaxation and the third transverse relaxation.

2.1.5.1 Longitudinal Relaxation T_1

When an RF pulse is applied to a spin ensemble, energy is transferred into the system altering the longitudinal magnetisation M_z . After the RF pulse, this energy is transferred from the spin ensemble into the surroundings as the spins return to the equilibrium population difference M_0 . The efficiency of this energy transfer is dependent on the timescale on which the molecules move via Brownian motion. This molecular motion has an associated time constant, known as the correlation time τ , that can be related to the frequency of the local magnetic field variation (Figure 2.4). The closer this frequency of field variations is to the Larmor frequency, the more efficient the energy transfer, and the shorter the longitudinal T_1 relaxation time. When molecules are able

to move freely, such as in water, the correlation time is short, therefore the frequency of local field variation is far from the Larmor frequency resulting in a long T_1 . When molecular movement is slow or more restricted, in tissue for example, this leads to a correlation time with a frequency similar to the Larmor frequency, consequently shortening T_1 .

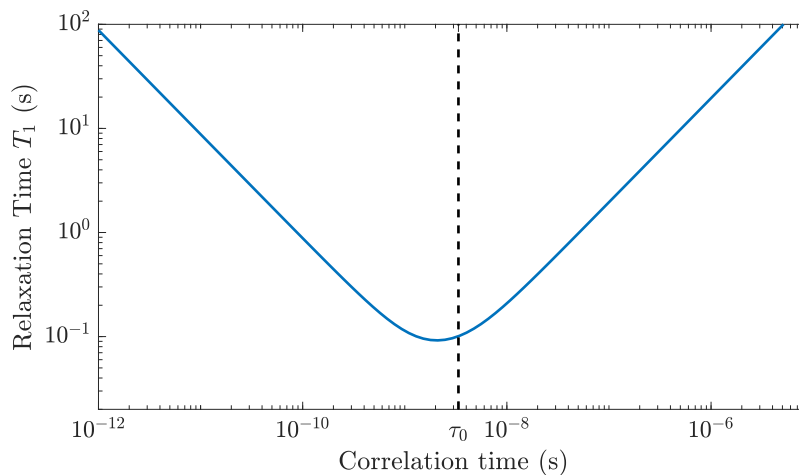


Figure 2.4: T_1 dependence on the molecular correlation τ at a field strength of $7 T$. τ_0 is the correlation time corresponding to the Larmor frequency ω_0 .

The recovery of longitudinal magnetisation over time, $M_z(t)$, is described by the following solution to the Bloch equation

$$M_z(t) = M_0 \left(1 - \exp\left(-\frac{t}{T_1}\right) \right) + M_z(0) \exp\left(-\frac{t}{T_1}\right) \quad (2.12)$$

where M_0 is the equilibrium longitudinal magnetisation and $M_z(0)$ is the longitudinal magnetisation at time $t = 0$.

An inversion recovery sequence is often used to measure T_1 or acquire T_1 -weighted (T_1w) images. In this sequence a 180° inversion pulse is applied to invert $M_z(t)$ from equilibrium M_0 to $-M_0$, $M_z(t)$ then recovers back to equilibrium as governed by Equation 2.12 which is given by

$$M_z(t) = M_0 \left(1 - 2 \exp\left(-\frac{t}{T_1}\right) \right), \quad (2.13)$$

The magnetisation $M_z(t)$ is measured at a given time along the inversion recovery curve, known as the Inversion Time (TI), by applying a 90° RF excitation to produce a Free Induction Decay (FID) with an initial magnetisation $M_{xy}(0)$ equal to the longitudinal magnetisation at that time. This process is then repeated to collect data at multiple TI values to fit T_1 , typically a long repetition time (TR) is left between each repeated measure. Alternatively the incomplete recovery can be accounted for in the fit, as performed in the T_1 mapping used in Chapter 6 [10]. Figure 2.5 shows an inversion recovery sequence, with the magnetisation shown for the three tissue types in the brain, Grey Matter (GM), White Matter (WM) and Cerebrospinal Fluid (CSF) which have different longitudinal relaxation times. These differences in T_1 can be used to optimise the contrast in MR images, for example obtaining high contrast between GM and WM. At 7 T the T_1 of WM has been measured to be ~ 1130 ms [11, 12], ~ 1940 ms for GM [12], ~ 4425 ms for CSF [11] and 2450 ms for arterial blood [13]. For each tissue type there is a given TI at which $M_z(t) = 0$, this is known as the null point, and this difference in T_1 between GM and blood is a key characteristic used in the Vascular Space Occupancy (VASO) sequence used in Chapter 6.

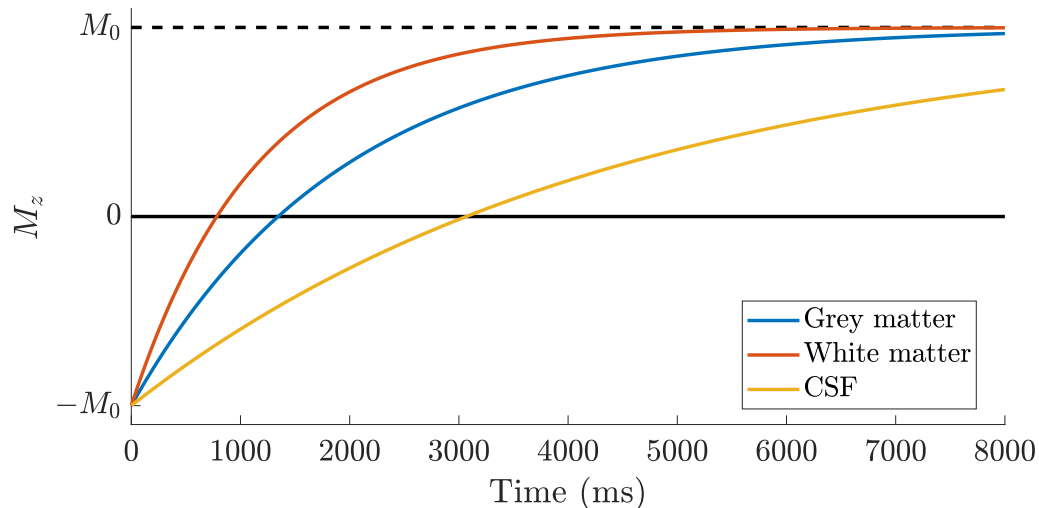


Figure 2.5: The recovery of longitudinal magnetisation M_z following an inversion pulse. $M_z(t)$ is shown for white matter with a simulated T_1 of 1130 ms (orange), grey matter with a simulated T_1 of 1940 ms (blue) and CSF with a simulated T_1 of 4425 ms (yellow).

2.1.5.2 Transverse Relaxation (T_2 & T_2^*)

After the spins are brought into phase coherence by an 90° excitation pulse they immediately begin to dephase via two interactions. Firstly, spin-spin (T_2) relaxation arises from dipole-dipole interactions whereby neighbouring spins induce time varying local magnetic field inhomogeneities resulting in varying precession frequencies across the spin population, and therefore dephasing. Spin-spin dephasing is irreversible, once the M_{xy} magnetisation is lost it cannot be restored. The second mechanism of transverse relaxation is from the dephasing of spins due to static field inhomogeneities and has a time constant T_2' . The loss of magnetisation due to static field inhomogeneities can be restored as it is possible to rephase the spins. The time constants for the intrinsic dephasing T_2 , and the static field inhomogeneity dephasing, T_2' , are combined to give a time constant, T_2^* , that describes the overall time scale for the transverse magnetisation M_{xy} to decay

$$\frac{1}{T_2^*} = \frac{1}{T_2} + \frac{1}{T_2'} \quad (2.14)$$

The recovery of the transverse magnetisation, M_{xy} , is described by the solution to the transverse component of the Bloch equation

$$M_{xy}(t) = M_{xy}(0) \exp\left(-\frac{t}{T_2}\right), \quad (2.15)$$

where $M_{xy}(0)$ is the transverse magnetisation at $t = 0$, and T_2 is the intrinsic T_2 . In this equation T_2 can also be replaced by T_2^* dependent on the pulse sequence used, as described next.

Figure 2.6a illustrates the effect of T_2 and T_2' relaxation on M_{xy} following a 90° RF excitation. The effects of T_2' can be reversed with the addition of a 180° refocusing pulse to form what is known as a Spin Echo (SE). Initially phase coherence is induced by the 90° RF pulse, following this the spins begin to dephase due to T_2^* effects and M_{xy} decays to zero. Due to static field inhomogeneities (T_2'), some spins will precess at higher Larmor frequencies and accrue a larger positive phase difference, and some will precess at lower Larmor frequencies, accruing a larger negative phase difference in the rotating frame of reference (Figure 2.6). If a 180° RF pulse is applied at a time equal to half the Echo Time (TE), the T_2' phase shifts are reversed. The previously higher frequency spins now have a negative phase difference and vice versa. This results in the spins with the higher Larmor frequency ‘catching up’ with the lower frequency spins and refocusing to form an echo at time $t = \text{TE}$. A SE sequence can be used to measure T_2 by repeating the sequence at a range of echo times TE. When repeating acquisitions, the time between each inversion pulse is termed the Repetition Time (TR). Alternatively multiple 180° RF pulses can be applied in a Carr-Purcell-Meiboom-Gill (CPMG) sequence to generate a train of echos that have a peak amplitude weighted by T_2 .

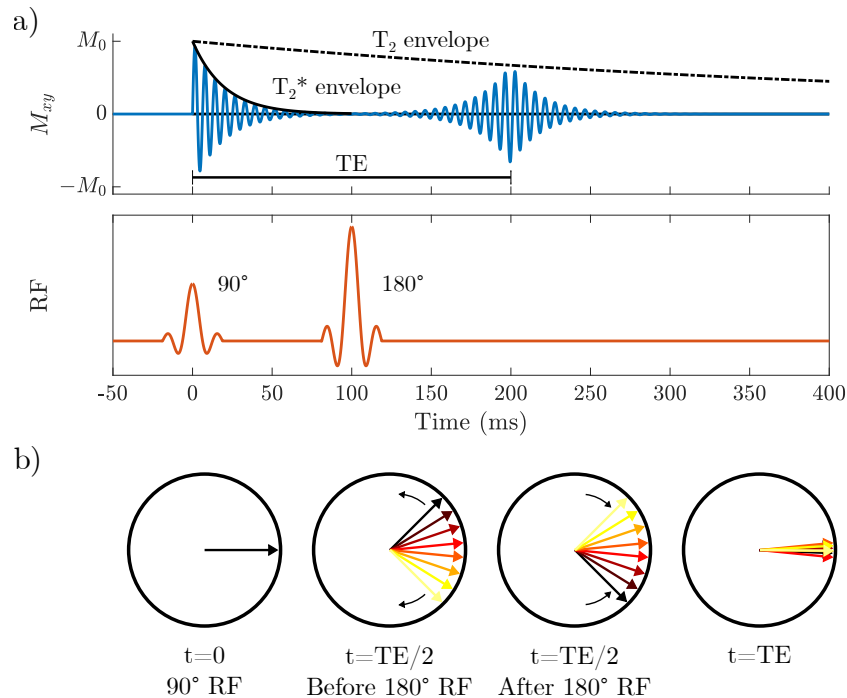


Figure 2.6: a) SE sequence showing the application of a 90° RF pulse followed by a 180° at $t = TE/2$ to generate an echo at $t = TE$. b) The evolution of a spin population during a SE sequence. Phase coherence at $t = 0$, followed by T_2^* dephasing, refocusing after the 180° RF pulse at $TE/2$, with an echo forming at time $t = TE$.

Another option to form an echo is the Gradient Echo (GE) sequence, which is a T_2^* weighted sequence. This is the sequence used throughout this thesis for all fMRI and VASO readouts in Chapters 4, 5 and 6. The gradient coils in an MRI scanner allow for a spatially linear variation in the magnetic field across the sample and are explained further in Section 2.2.2. A 90° RF excitation pulse is applied to tip the magnetisation vector into the transverse plane, at which point a gradient field is applied. Spins in high field areas dephase quickly and spins in low field areas dephase slowly. After a time $TE/2$, the polarity of the gradient field is flipped, leading to the spins refocusing and a gradient echo (GE) being formed at time $t = TE$. Figure 2.7 shows the evolution of M_{xy} , the RF excitation and gradient waveform during a GE sequence. Typically at 7 T the T_2^* of grey matter is ~ 30 ms, compared to a T_2^* of ~ 40 ms at

3 T (however this will vary across brain regions and also change with spatial resolution). As described in Chapter 3, for fMRI the optimal echo time of a GE sequence should be equal to the T_2^* of the tissue.

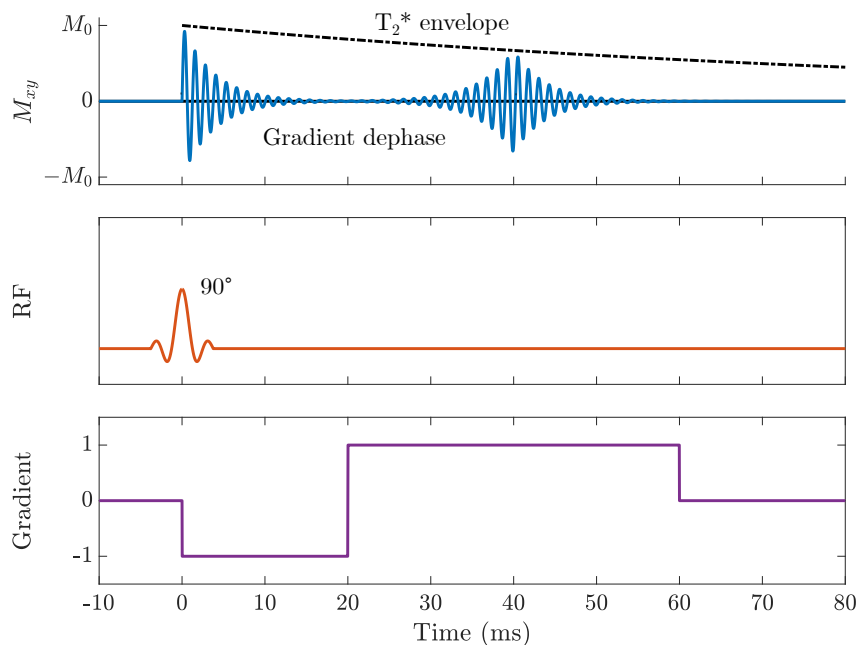


Figure 2.7: A GE sequence with a TE of 40 ms for tissue with a T_2^* of ~ 40 ms.

2.2 Image Acquisition

So far it has been shown how NMR can be used to measure the magnetisation from a sample and how the intrinsic properties of T_1 and T_2 can be determined. This section will build on this to describe how these measures can be spatially localised to acquire an image of a sample with Magnetic Resonance Imaging (MRI), as described by Lauterbur [14] and Mansfield [15] in 1973. Key milestones in the development of MRI include the mathematical framework of k -space [15], slice localisation [16], and finally the implementation of Fourier imaging [17]. These advances led to the acquisition of MR images of the body on realistic time scales. Fast MR acquisition took another leap forward when Mansfield developed Echo Planar Imaging (EPI) [18], enabling images of the human body

to be acquired in less than 100 ms [19]. This was crucial for the development of functional MRI (fMRI) of the brain, the focus of this thesis.

2.2.1 Gradient fields

The magnetisation detected using NMR can be spatially encoded using the relationship between the Larmor frequency and the magnetic field B_0 (Equation 2.6). If a spatially varying magnetic field is applied, the Larmor frequency of the magnetisation will be spatially specific.

This is achieved by applying an additional gradient field \mathbf{G} in addition to B_0 . This can be in any orthogonal direction (x,y,z) using a Maxwell pair or saddle coils (see Section 2.3) described by:

$$\mathbf{G} = G_x \mathbf{i} + G_y \mathbf{j} + G_z \mathbf{k}. \quad (2.16)$$

The B_0 field is typically oriented along the z -axis. The equation for the Larmor frequency of magnetisation in a spatially varying magnetic field is therefore

$$\omega_0(\mathbf{r}) = \gamma(B_0 + \mathbf{G} \cdot \mathbf{r}) \quad (2.17)$$

2.2.2 Slice select

Slice selection is the localisation of the NMR signal to a specific cross section of a volume along a specific axis. Slice selection can be achieved by applying an RF excitation pulse with a specific range of frequencies (bandwidth) to a sample that has a linear gradient field applied along one axis, in this example the z -axis. The slice thickness, Δz , can be decreased by narrowing the bandwidth, $\Delta\omega$, of the RF pulse, or by increasing the gradient amplitude, G_z .

$$\Delta z = \frac{\Delta\omega}{\gamma G_z} \quad (2.18)$$

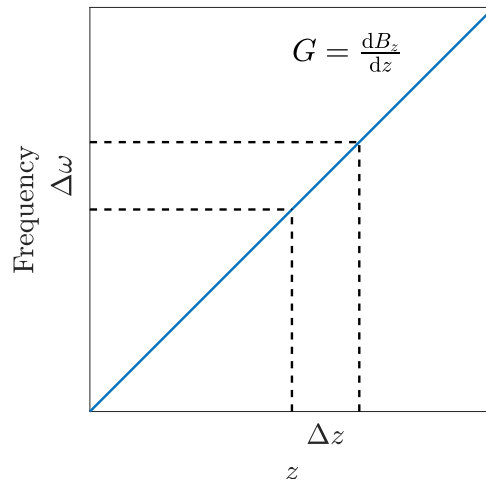


Figure 2.8: A slice of thickness of Δz is excited by applying an RF pulse of bandwidth $\Delta\omega$ together with a gradient field G_z .

To excite a slice, a thin rectangular slab, the required RF pulse shape in frequency space can be calculated by Fourier transforming the required slice profile shape, this results in a sinc RF pulse shape. To achieve a perfect rectangle, the sinc pulse would need to be infinitely wide. However, as there is a limited time to apply RF pulses when acquiring an image, a truncated sinc is used resulting in a slice profile that is not a perfect rectangle.

2.2.3 Phase Encode

After localising the signal to a slice within a volume, phase encoding is used to spatially localise in the y direction. Following slice selection, a linear gradient, G_y , is applied for a short time, this results in each spin in the slice precessing at different Larmor frequencies depending on their position along the y -axis of the slice. After G_y is turned off, the spins return to the Larmor frequency and will have accrued a phase shift that is dependent on their position along the y -axis.

2.2.4 Frequency Encode

Finally, the signal can be localised along the x direction using frequency encoding. This is achieved in a similar way to slice selection and phase encoding by applying a linear gradient, G_x . G_x is applied during the sampling of the signal, also known as the readout, and by doing so each frequency of the signal will correspond to a position along the x -axis. By Fourier transforming the acquired signal from the slice, each frequency will correspond to a spin along the x -axis with a phase corresponding to its position along the y -axis.

2.2.5 k -space

k -space is a useful mathematical tool for interpreting MRI pulse sequences and the frequencies detected in the NMR signal. It provides a way to visualise the effects of phase encoding and frequency encoding when sampling the MR data. MR data are acquired by the scanner in k -space and are then Fourier transformed to form an image. Each point in k -space corresponds to a specific frequency and its magnitude corresponds to the level of its contribution to the image. When acquiring an image, the application of phase and frequency encoding gradients can be thought of as moving through k -space, sampling the point as you go. The centre of k -space corresponds to the low spatial frequencies and low resolution aspects of an image, and the outer parts of k -space correspond to the high spatial frequencies and high resolution aspects of the image.

At the start of the acquisition in a pulse sequence, the sampling of k -space starts at the origin. When a gradient is applied, the sampling moves outwards depending on the polarity and magnitude of the applied gradients and the time they are applied for. The resulting position in k -space is given by,

$$k_x = \gamma G_x t_x \tag{2.19}$$

$$k_y = \gamma G_y t_y \quad (2.20)$$

where G_x and G_y are the gradients in the frequency and phase encode directions respectively and t_x and t_y are the corresponding times the gradients are applied for.

After raw data sampled in k -space has been acquired following a pulse sequence, the data is Fourier transformed. A 2D Fourier transform produces a complex image with magnitude and phase data (shown in Figure 2.9).

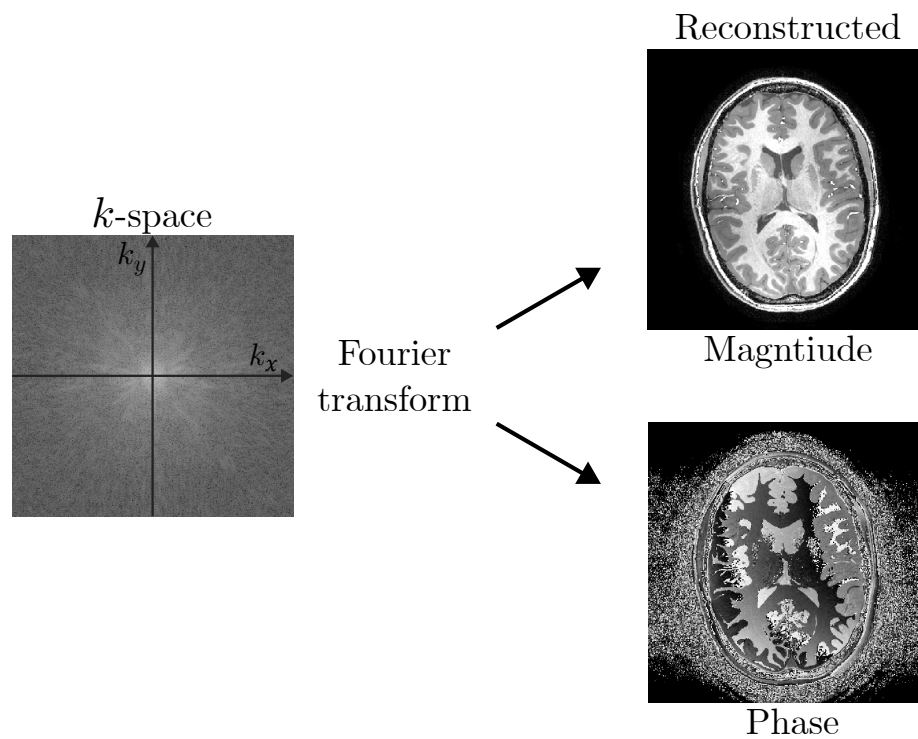


Figure 2.9: a) Raw data sampled in k -space and b) The magnitude and phase data images following a 2D Fourier transform.

2.3 MR Hardware

A typical MRI scanner consists of four main hardware components: the static magnetic field, B_0 , shim coils, gradient coils, and RF coils, as well as the console. A 7 T Philips Achieva scanner was used to acquire all the data presented in

this thesis, a schematic of the position of the coils in the scanner is shown in Figure 2.10.

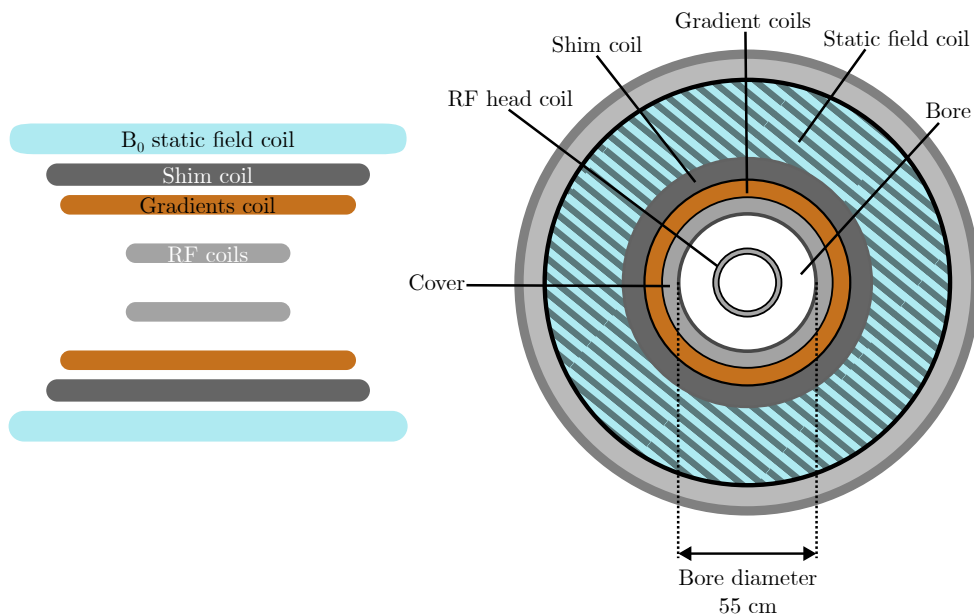


Figure 2.10: Schematic showing 2 cross sections of the Philips Achieva 7 T MRI scanner and its constituent coils.

2.3.1 Static field

The static magnetic field B_0 is oriented horizontally through the bore of the scanner in the z -direction and generated by a superconducting solenoid. The magnetic field generated from a solenoid increases with the number of turns per unit length. To keep the coils of wire at a low enough temperature to maintain superconductivity, the coil is surrounded by a bath of liquid helium. The magnetic field inside the bore of the scanner is $\sim 100,000$ times greater than the Earth's magnetic field, therefore it is important for the safety of others that the scanner is magnetically shielded. The 7 T scanner room in Nottingham is shielded with 230 tonnes of iron to reduce the field to the safe regulatory level of 5 G at a distance of 11 m radially and 16 m axially to the bore of the magnet.

2.3.2 Shim coils

The static field is calibrated to provide a homogeneous magnetic field for a sphere with a diameter of ~ 25 cm in the middle of the bore. However, when a sample is placed into the field, inhomogeneities in the static field arise that are dependent on the size, orientation and properties of the sample. Shim coils provide users with the ability to correct for these distortions and counteract any image distortions that are caused by B_0 field inhomogeneity. Typically shimming gradients can be applied at the start of a scanning session after being calculated from initial calibration scans after the sample is placed in the scanner.

2.3.3 Gradient coils

Gradient coils are used to spatially encode the signals detected from a sample to form an image (see Section 2.2). There are three sets of gradient coils in an MRI scanner, one for each of the orthogonal x , y and z directions. The gradient coils switch rapidly whilst scanning, particularly for echo planar imaging (EPI), requiring large amounts of current, inducing Lorentz forces on the coils themselves and in turn generating a high level of acoustic noise. The rapid gradient switching also leads to heating, which has a knock on effect on gradient performance and the static field, this is known as scanner drift. To combat this, water cooling of the gradients is performed but this can limit the number of high resolution fMRI datasets that can be collected. The gradient coils on the Philips Achieva 7 T system have a maximum gradient strength of 40 mTm^{-1} and a maximum slew rate of $200 \text{ mTm}^{-1}\text{s}^{-1}$.

2.3.4 RF coils

Two RF coils are needed for the acquisition of MR data, one to transmit RF excitation pulses uniformly across the region of interest, and another to receive the much smaller RF signals from the sample. When acquiring fMRI and structural brain images a volume coil or surface coil are used for reception of the

signal as they can be placed close to the brain, increasing the detected signal. For the work in this thesis all data was collected using the NOVA Medical 1TX Head coil as the transmit coil. For the receive coil a 32 channel NOVA head coil was used for Chapter 6 and two 16-channel surface coils were used for Chapter 4 and 5.

Multi-channel high density array surface coils can be positioned closer to the imaging region of interest and therefore provide a much higher sensitivity and Signal to Noise Ratio (SNR) compared to volume coils. The higher SNR allows for high resolution fMRI scans to be acquired without the need to increase the scan duration. In addition, the high density of receive arrays in a surface coil allows an increased parallel acceleration factor (see Section 2.3.5.2 below) in the right-left (R-L) direction of the image acquisition of a 2D or 3D EPI. This reduces the echo train length and in turn: the achievable echo time, TE (which should be matched to the T_2^* of grey matter) and image distortions. These benefits come with the consideration that the geometry of the receive coil results in an inhomogeneous receive profile across the brain.

2.3.5 Accelerated Imaging

Image acquisition time in MRI is always an important factor, whether it is for subject comfort, higher throughput, allowing multiple contrast measures, or improved sampling of functional changes. The development of MR hardware and acquisition strategies is always striving to reduce acquisition time whilst maintaining the SNR of the data. Specifically for functional MRI (fMRI) of the brain, reduced image acquisition time increases the temporal resolution, and therefore the rate at which the haemodynamics relating to brain activity can be sampled. In fMRI the time taken to acquire an entire volume is often referred to as repetition time (TR) but the strict definition of TR is the amount of time between pulse sequences applied to the same slice. For some sequences this can give rise to a TR that is different to the volume acquisition time, therefore TR_{vol} is also reported for some acquisitions.

2.3.5.1 Partial Fourier

One way to reduce acquisition time is to acquire fewer lines of k -space. This can be achieved by using the phase conjugate symmetry of k -space, which could theoretically allow for only half of k -space to be acquired without any loss in resolution. This technique is known as Halfscan (HS) or partial Fourier [20, 21] (see Figure 2.11). The reduction in the amount of k -space does come with a reduction in SNR, as well as impacting the phase of the reconstructed data so care should be taken if phase data is required for further processing.

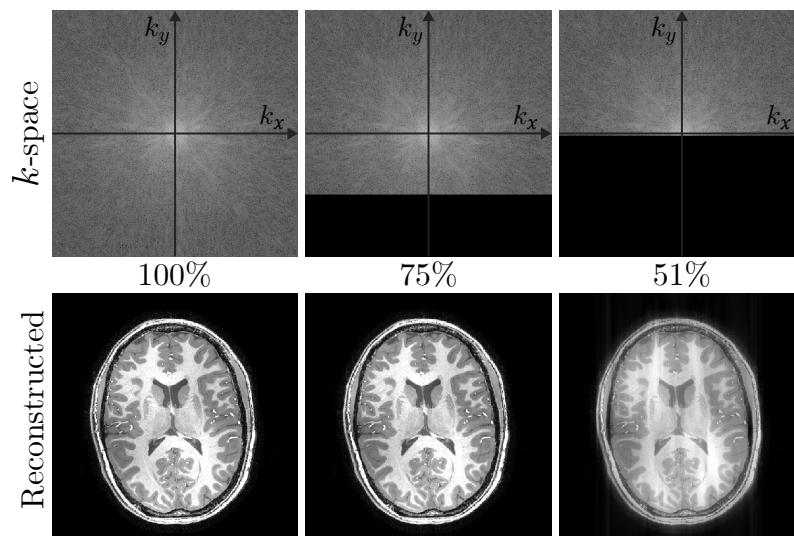


Figure 2.11: Example k -space (top) and reconstructed (bottom) data for 3 levels of halfscan acceleration. Fully sampled k -space (left), 75% halfscan (middle) and 51% halfscan (right).

2.3.5.2 Parallel Imaging

Another common acceleration technique is parallel imaging [22] which uses information provided by the multiple receive coils that are used with current MRI scanners. Each receive coil can detect any given signal but it will be stronger for the receive coils that are closer to the signal's source, leading to a variation in signal strength detected by each individual receive coil. Each receive coil's sensitivity map provides more information about the sample allowing for

more k -space undersampling. When fewer points through k -space are sampled, the Field Of View (FOV) of the image is reduced, resulting in aliasing of the image. Aliased images are acquired simultaneously on each receive coil and the sensitivity maps are used to spatially decode where signals are coming from and reconstruct an unaliased image. For Philips scanners the parallel imaging method is known as Sensitivity Encoding (SENSE) [22, 23]. The total SENSE factor is limited by the number of receive coils and gives rise to a spatially varying amplification of the noise, known as the g -factor [24]. For common fMRI sequences, such as EPI, the decrease in SNR due to SENSE is often outweighed by the increase in signal due to faster acquisition of the signal before it decays due to T_2^* .

2.3.5.3 Simultaneous Multi-Slice

Simultaneous Multislice (SMS) or Multiband (MB) imaging, is another imaging acceleration method. Significant reductions in repetition time TR are achieved by acquiring multiple slices simultaneously following a single RF excitation pulse [25]. The number of simultaneously acquired slices is referred to as the SMS or MB acceleration factor and is typically 2–4. The technique is implemented by combining multiple RF pulses, each with a different frequency offset. Each RF pulse excites a 2D slice in a specific position in the sample. The signals detected at the coils will be an aliased combination of the slices, weighted by the coil sensitivities. Each slice can be unaliased using SENSE reconstruction, based on the sensitivities of the coils along the slice direction. An advantage of this technique is that there is no reduction in SNR due to undersampling of k -space or shortening of the echo train length, however there are losses in SNR and non-uniform spatial noise amplification due to the coil g -factor [26].

2.4 Imaging Techniques

This section outlines the sequences used to acquire functional and structural data for the layer-specific fMRI measures used throughout this thesis.

2.4.1 Echo Planar Imaging (EPI)

To sample all the lines of k -space after a single RF pulse to form a 2D image an echo planar imaging (EPI) sequence can be used [18]. Following a single RF excitation, an entire 2D plane of k -space is traversed by rapidly switching the readout gradient, acquiring an image in <100 ms. By switching the readout gradients rapidly multiple echos are formed, however this can push the limits of the scanner hardware. Due to the acquisition times achievable with EPI, this has become a staple for fMRI research to study the dynamic function of the brain.

Figure 2.12 shows the Pulse Sequence Diagram (PSD) and k -space trajectory for a 2D-EPI sequence. The sequence starts with an RF excitation and slice select gradient to excite the spins in a volumetric 2D slice. Following this a phase encode gradient, G_y and frequency encode gradient, G_x , are applied to move from the centre to the edge of k -space. To transverse through the entire k -space, frequency encode gradients with alternating polarity are applied to move backwards and forwards along k_x with small ‘blips’ between each lobe to move up k_y in k -space.

k -space can be acquired following a single RF excitation, known as single shot, or with multiple RF excitations, known as multishot [27]. The EPI sequence is prone to image distortions due to its low bandwidth in the phase encode direction. Field inhomogeneities cause the mislocation of spins and distort the image along the phase encode direction of the image, these distortions are worse at higher field strengths due to greater field inhomogeneity.

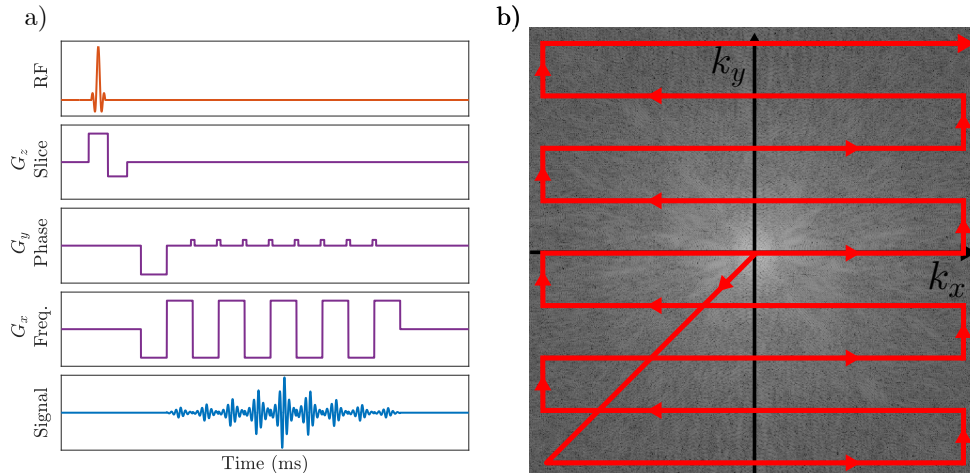


Figure 2.12: a) Pulse sequence diagram and b) k -space trajectory for a 2D-EPI sequence.

2D-EPI is used in Chapter 6 to initially assess the effects of denoising on fMRI data.

2.4.1.1 3D-EPI

For 2D-EPI, a single 2D slice is acquired following each RF excitation, this is repeated for N slices until the desired volume has been acquired in a given volume TR. For this the RF excitation pulse has a flip angle of θ given by the Ernst angle $\cos(\theta) = \exp(-TR/T_1)$. It is important to calculate the correct flip angle for each experiment as if an angle that is above the Ernst angle is used, over flipping occurs and this increases inflow effects in the data [28]. For 3D-EPI, lower flip angle RF pulses are applied to excite a thick slab and gradients are applied along the slice direction, G_z , as an addition phase encoding. The slab is repeatedly excited while the G_z gradients are incremented to cover all the required k_{xy} planes over the range of k_z (see Figure 2.13). 3D-EPI has a higher inherent SNR than 2D-EPI as the whole slab is excited for each acquisition of a k_{xy} plane, all the spins contribute to the acquired signal at each shot leading to increased SNR advantage of $\sqrt{N_{slices}}$ compared to 2D-EPI. Additionally, as there are two phase encode directions, parallel imaging can be applied along

both axis, enabling higher combined image acceleration factors compared to 2D-EPI (see Section 2.3.5.2). For 3D-EPI there is less time for the spins to recover between RF excitations compared to 2D-EPI, therefore lower flip angles are needed for the system to reach a steady state, lowering the overall amplitude of magnetisation. 3D-EPI sequences are used in Chapter 4 and 5 for high resolution fMRI, and Chapter 6 as the readout for the VASO scheme.

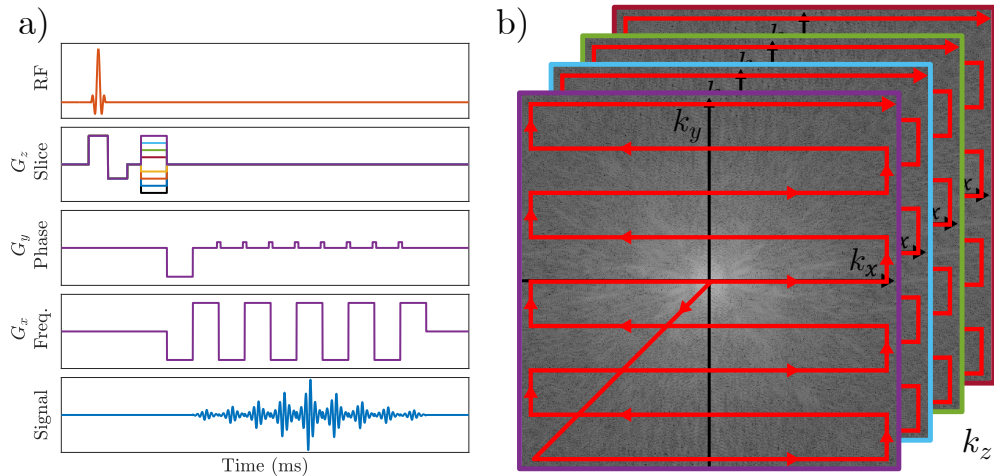


Figure 2.13: a) Pulse sequence diagram and b) k -space trajectory for 3D-EPI sequence.

2.4.2 Magnetisation Prepared Rapid Gradient Echo (MPRAGE)

Whole head anatomical images are often used in an fMRI scan session to plan functional runs and for tissue segmentation and coregistration to standard templates during analysis. T_1 weighted structurals with good GM/WM contrast are frequently used by neuroscientists using a magnetisation prepared rapid gradient echo (MPRAGE) sequence [29]. In an MPRAGE sequence, a 180° inversion is applied followed by a delay to build T_1 weighting. After a time, a rapid gradient echo is acquired to sample the magnetisation and following this the magnetisation is left to recover.

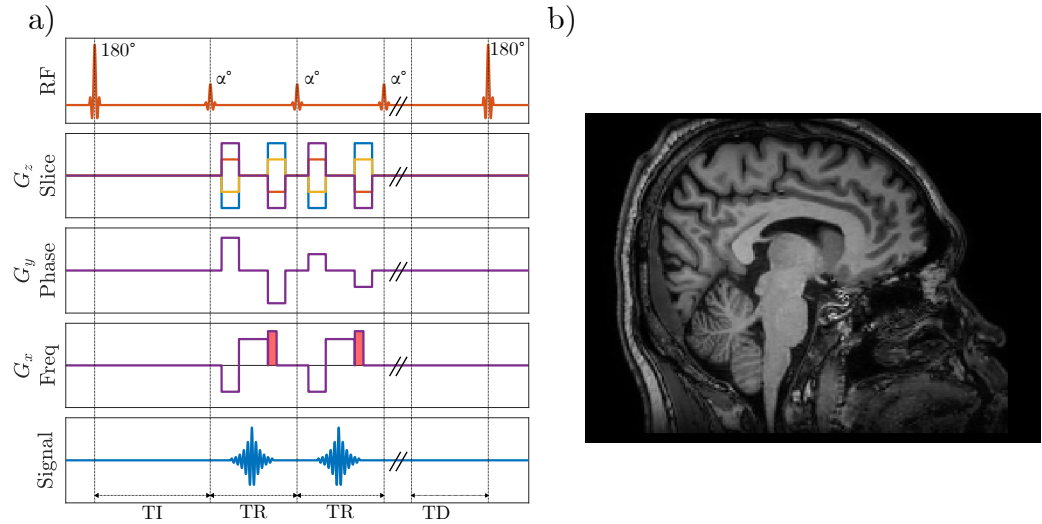


Figure 2.14: a) A schematic of the pulse sequence diagram for the MPRAGE sequence. Shaded red areas indicate spoiler gradients. b) An example of a sagittal slice of an example MPRAGE image.

2.4.3 Phase Sensitive Inversion Recovery (PSIR)

A PSIR sequence is similar to an MPRAGE sequence in that it is T_1 weighted inversion recovery sequence. However a PSIR has a second rapid gradient echo readout, therefore two images are acquired at different points along the inversion recovery with different contrasts. The pulse sequence diagram is shown below in Figure 2.15. Phase correction is used to retrieve the sign of the magnetisation for the first image from the second image. The second image is acquired after the nullpoints of GM, WM and CSF and is used to bias field correct the magnitude of the first image. The timing of the acquisitions results in an image with optimal contrast to noise ratio (CNR) between the WM and GM. The PSIR is the structural scan that was predominantly used throughout Chapters 4, 5 and 6 of this thesis.

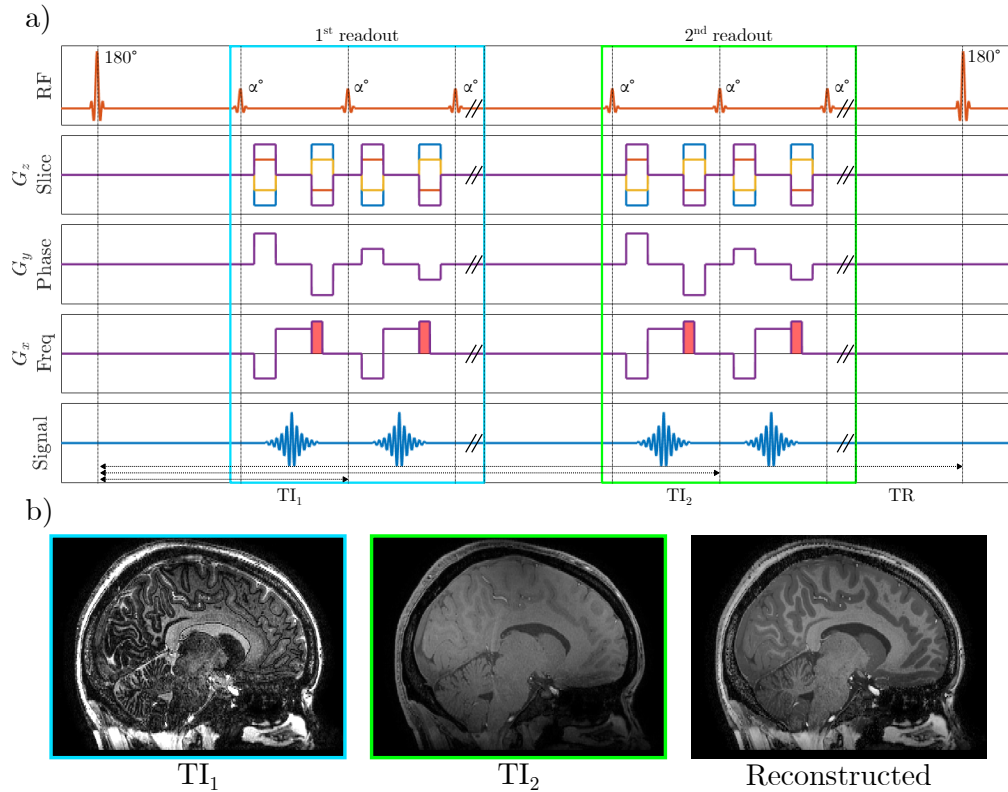


Figure 2.15: a) A schematic of the pulse sequence diagram (PSD) for the PSIR sequence and b) an example of a sagittal slice of the acquisitions at T_{I_1} and T_{I_2} , and the field-bias corrected PSIR image, optimised for contrast at the GM/WM boundary.

2.4.4 Fast Low Angle Shot (FLASH)

The FLASH sequence is a gradient echo sequence that can be T_1 or T_2^* weighted depending on the flip angle, TE and TR used. Using smaller flip angles and a longer TR results in reduced T_1 effects, and lengthening the TE results in T_2^* weighting. FLASH sequences with a long TE are T_2^* weighted and provide good sensitivity for locating veins due to the deoxygenated blood being paramagnetic and therefore have a short T_2^* . This FLASH sequence was used to generate vein masks in Chapter 6.

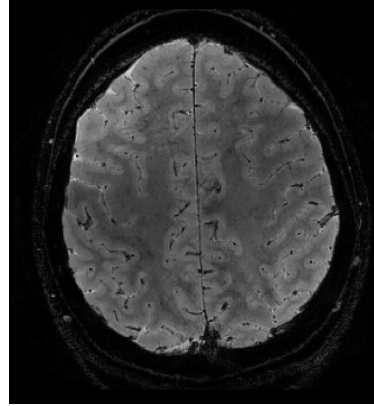


Figure 2.16: An example of an axial slice of a FLASH image, veins are clearly visible in black due to their short T_2^ .*

2.5 Conclusion

This chapter has described the physical origins of the NMR signal and how it can be used to acquire images with tissue specific contrast using MRI. The key sequences that are used in the rest of this thesis have been described. Chapter 3 will describe the physiological origins of signals that can be detected using fMRI in addition to the origins of electroencephalography (EEG) signal.

Chapter 3

Neurophysiology Theory: Origins of EEG and fMRI signals

3.1 Introduction

Understanding the physiology of the human brain has been of great interest in medicine and science for many years. Discoveries have been made using a multitude of techniques, from the study of how individual cells function and interact, to monitoring brain wide networks and sensorimotor interaction. Research in neurophysiology and neuroscience is discovering ways to diagnose and help treat conditions such as epilepsy [6] and schizophrenia [30], and neurodegenerative diseases such as dementia [31]. Early studies of neurophysiology involved intracranial measures on animals or postmortem histological samples from humans. The majority of this work was conducted using electrophysiological measures, with patch clamps [32] and microelectrode [33] Local Field Potentials (LFPs) [34] used for cellular recordings, and electroencephalography [9] (EEG) or magnetoencephalography (MEG) [35] for whole brain recordings.

The invention of EEG provided a non-invasive way to directly measure neuronal activity on a very short timescale. The neuronal signals detected by EEG are split into five frequency bands: delta (0.3 – 4 Hz), theta (4 – 8 Hz),

alpha (8 – 13 Hz), beta (13 – 30 Hz) and gamma (30 – 200 Hz), and the roles of each of these in brain health and function are heavily researched. Due to the mobility and affordability of EEG it is widely adopted clinically, in the diagnosis and treatment of epilepsy [6, 36].

Functional MRI (fMRI) with endogenous contrast was first implemented in the early 1990s [37–39], and since has been the dominant research technique in neuroimaging to study brain function due to being non-invasive and using non-ionising radiation. In fMRI, a series of image volumes are typically acquired in quick succession to measure changes in the MR signal due to the Blood Oxygenation Level Dependent (BOLD) contrast. BOLD contrast is related to the ratio of oxyhaemoglobin and deoxyhaemoglobin in the blood and is therefore an indirect measure of neuronal activity. The temporal resolution of BOLD fMRI is limited by the haemodynamics of the brain, but it has excellent spatial resolution especially when compared to EEG or MEG. The spatial specificity of BOLD fMRI can be limited due to its sensitivity to draining veins so other fMRI image contrasts have been developed to study brain function for example: Arterial Spin Labelling (ASL) which is sensitive to cerebral blood flow (CBF), and Vascular Space Occupancy (VASO) which is sensitive to cerebral blood volume (CBV) and is explored further in Chapter 6.

In this chapter the physiology and origins of the EEG signal are explained, cortical layering is detailed, and the origins of alpha oscillations and their role in top-down and bottom-up processing is discussed. This is followed by an outline of the physiology and origin of the fMRI BOLD signal and how this can be analysed to monitor brain activity.

3.2 Origin of the EEG signal

3.2.1 Neurons

EEG detects the electrical volatages on the surface of the scalp generated by the synchronous firing of thousands of neurons in the brain. Neurons are responsible for the transmission and processing of information in the brain by sending electrical impulses to other neurons. A neuron consists of three main sections: the soma, containing the cell nucleus and its DNA; the dendrites, that branch out from the soma and receive information from other neurons in the form of electrical signals; and the axon, a single long fibre that extends away from the soma and transmits electrical signals to other neurons (see Figure 3.1). The boundary between the soma and the axon is known as the axon hillock and is the final region before the axonal initial segment which triggers the transmission of electrical signals down the axon. Most axons are surrounded by a myelin sheath which provides electrical insulation and increases transmission speed. The ends of the axons (nerve endings) connect to other neurons at synapses, which consist of the presynaptic nerve terminal, the synaptic cleft and the postsynaptic membrane. To transmit an electrical signal to a connecting neuron the presynaptic nerve terminal releases neurotransmitters into the synaptic cleft which bind to the postsynaptic membrane to open ion channels and trigger the onward transmission of electrical stimulation (see Section 3.2.3 for a more detailed explanation). Nerve endings can form synapses with the dendrites, soma, or axon of neighbouring neurons resulting in a highly complex interconnected network by which neurons communicate with each other.

Neurons are highly specialised cells that can vary considerably in size and shape dependent on their location in the body. In the brain there are two main types of neurons, stellate neurons and pyramidal neurons. Stellate neurons are star shaped with the soma in the centre and dendrites propagating outwards in all directions. Pyramidal neurons have dendrites that run parallel to each

other and are often oriented perpendicular to the cortical surface. The structure and orientation of neuronal cells is an important factor that dictates whether they contribute to the EEG signal (see Section 3.3.2). In contrast, the BOLD signal originates from the haemodynamic response to the energy demand of the neuronal cells (see Section 3.4). All cell types contribute to the BOLD signal, and so the neuronal origins of the BOLD and EEG signals are not identical.

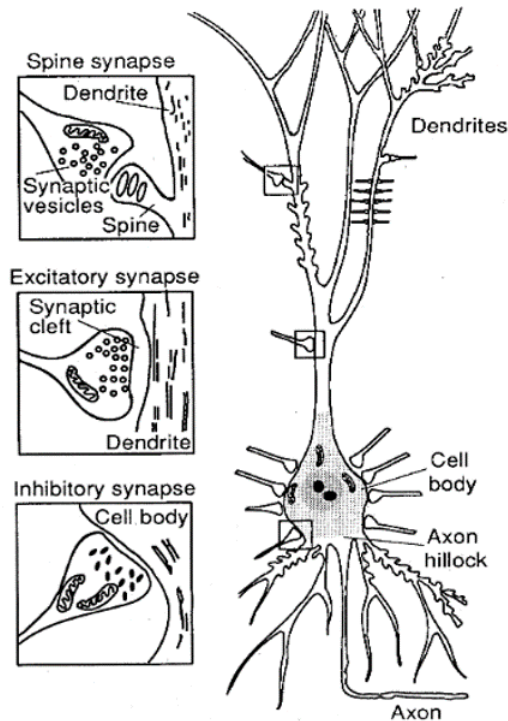


Figure 3.1: Schematic of a pyramidal neuron with dendrites oriented parallel to one another. The soma contains the cell nucleus and connects to the axon via the axon hillock. The transmission of electrical signals between neurons occurs at the synapses. Taken from Hamalainen et al [40]

3.2.2 Action Potentials

The cell membrane of a neuron contains ion pumps that control the flow of potassium (K^+) and sodium (Na^+) ions in and out of the cell. Even during 'rest' a neuron maintains a potential difference, known as the resting potential,

of -70 mV between the inside and outside of the cell due to the difference in ion concentrations in the intracellular and extracellular space. In addition to ion pumps, there are voltage-gated ion channels which are closed whilst the cell is at the resting potential but open when the potential at the axon hillock reaches ~ -40 mV. When a neuron receives a stimulus, some ion channels open and Na^+ ions start to flow into the cell, decreasing the potential difference. If the potential at the axon hillock passes ~ -40 mV an action potential is initiated. More Na^+ ion channels open and Na^+ ions flood into the cell along both an electrical gradient and a chemical gradient. This results in the cell reaching a potential of $\sim +40$ mV and becoming 'depolarised'. The action potential causes neighbouring areas of the membrane to depolarise and leads to the propagation of the action potential along the axon. After depolarisation, K^+ ion pumps begin to move K^+ ions out of the cell against the concentration gradient which returns the potential towards the resting potential, this period is known as repolarisation. During repolarisation, too many K^+ ions leave the cell, resulting in hyperpolarisation where the potential dips below -70 mV before finally returning to the resting potential, this is called the refractory period. The action potential propagates along the axon depolarising and repolarising sections of the cell membrane until it reaches the nerve ending. The local differences in the cell potential caused by depolarisation and repolarisation can be modelled as two anti-parallel current dipoles, forming a quadrupole.

3.2.3 Post Synaptic Potentials

When the action potential reaches the end of the axon at the presynaptic nerve terminal, voltage gated Calcium (Ca^+) ion channels are opened and Ca^+ ions flow into the cell. With the influx of Ca^+ ions, vesicles containing neurotransmitters bind to the cell membrane and release them into the synaptic cleft. The neurotransmitters diffuse across the synaptic cleft and bind to receptors on the post synaptic membrane, triggering the opening of ion channels (Na^+ if excitatory, K^+/Cl^- if inhibitory) into the post synaptic cell and changing

the potential, known as the Post Synaptic Potential (PSP). The influx of ions into the cell induces a current along the direction of the dendrite. Dependent on the type of synapse that was stimulated there are two types of PSP: an Excitatory Post Synaptic Potential (EPSP), where the post synaptic cell is depolarised and the cell voltage increases; and an Inhibitory Post Synaptic Potential (IPSP) where the post synaptic cell is hyperpolarised and the cell voltage decreases, becoming more negative. The more EPSPs that are induced in the post synaptic cell, the more likely it will be for it to reach the -40 mV threshold required to initiate an action potential. Conversely, the more IPSPs that are induced, the further from the threshold the cell potential will be and an action potential will not be initiated. After an action potential has been triggered, K^+ ion pumps begin to move K^+ ions out of the cell against the concentration gradient which returns the potential towards the resting potential. The movement of ions out of the cell creates an extracellular current, known as the volume current, in the opposite direction to the postsynaptic current.

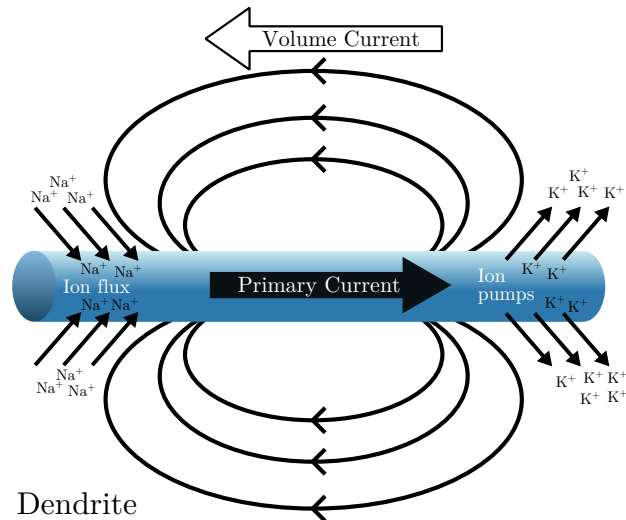


Figure 3.2: Schematic of a current dipole along a dendrite due to the movement of ions in and out of the cell.

3.2.4 EEG signals

Using EEG there are a number of electrical signals which can be measured on the surface of the head including oscillatory activity. It is clear from the sections above that there is more than one electrical signal which is generated during neuronal activity, but not all of these are detected with scalp EEG. The volume current due to the PSP can be modelled as a single current dipole oriented along the dendrites. The field from this postsynaptic current dipole falls off at a rate of $1/r^2$ and the field from the action potential current quadrupole falls off as $1/r^3$. Therefore, at a distance of the scalp, the postsynaptic current is larger than the action potential current. In addition, the action potential current is bi-phasic so multiple action potentials from neighbouring neurons with different timings will lead to cancellations and a reduction in the overall current. The timescales at which PSPs and action potentials operate also differ, with PSPs lasting for tens of milliseconds compared to just 2 ms for action potentials. Therefore, it is believed that the main contributors to EEG signals are dendritic currents from PSPs [41]. Further, due to the symmetrical shape of the dendrites branching from stellate neurons, the resulting currents cancel out at short distances. The currents from pyramidal neurons are detectable at the surface of the scalp as their dendrites run parallel to one another and are typically perpendicular to the cortical surface. As a result, EEG signals are thought to originate from the postsynaptic currents from the dendrites of pyramidal neurons.

EEG signals are typically in the range of 0.5 – 100 μV . The number of synchronously firing neurons required to produce such a signal is on the order of 10^5 . Such large numbers of neurons synchronously firing gives rise to oscillatory variations in the EEG signal. These brain oscillations were first measured in humans in the frequency range of 8 – 13 Hz and were labelled alpha oscillations [9]. Since then, more frequency bands have been defined: delta (1 – 4 Hz), theta (4 – 8 Hz), beta (13 – 30 Hz) and gamma (30 – 200 Hz). Each of these

frequencies behave differently in response to stimuli, with a summary of each provided in Table 3.1.

Precisely how each of these oscillatory signals are generated and their functional role is still debated and an area of active research [42–50]. In this thesis I will be studying the origin of the alpha band signal. One way to elucidate the origins and functional roles of these oscillatory signals is to determine which layers of the grey matter they originate from, as explained further in Section 3.3.

Oscillation	Frequency (Hz)	Amplitude (μ V)	Modulation
Delta	0.3 – 4	100 – 200	concentration, working memory [51]
Theta	4 – 8	50	memory, inhibition [52, 53]
Alpha	8 – 13	50	eyes closed, attention [54, 55]
Beta	13 – 30	< 50	motor tasks [56–58]
Gamma	30+	10 – 20	attention, memory, perception [59–61]

Table 3.1: A summary of the EEG oscillations showing their frequency range, typical amplitude and how they can be modulated.

3.3 Brain Structure and Cortical Layers

The brain can be categorised into three tissue types: the grey matter (GM), largely consisting of dendrites and soma, this is where the majority of communication between neurons occurs; the white matter (WM), consisting of axons, is where the electrical signals travel for communication between neurons in different brain regions; and the cerebral spinal fluid (CSF) which protects the

brain and clears waste products (see Figure 3.3a). The brain is divided into four main anatomically distinguishable regions: the frontal lobe, parietal lobe, temporal lobe and occipital lobe (see Figure 3.3b).

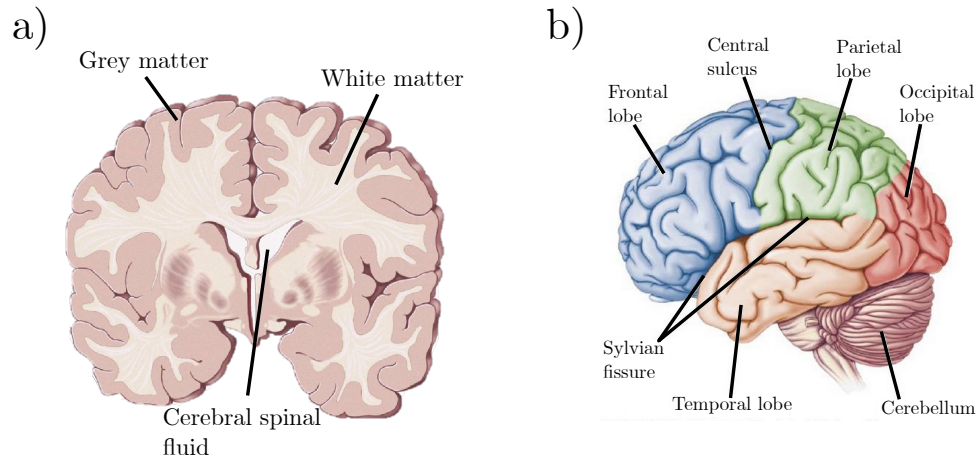


Figure 3.3: a) A coronal cross-section of the brain highlighting the grey matter, white matter and cerebral spinal fluid tissue types. b) A schematic showing the the four lobes of the brain and some other structural landmarks. Adapted from Bear et al. [62]

Each region is commonly further subdivided into Brodmann areas [63] based on the cytoarchitectural organisation of the neurons. Some areas of the brain are responsible for basic functions such as the primary visual cortex processing visual stimuli (as studied in Chapters 4 and 5), the motor cortex processing movement (as studied in Chapter 6), the primary somatosensory cortex processing touch, and the temporal lobe processing hearing. These are referred to as lower order regions and are present in most mammals. Other regions of the brain responsible for cognition such as memory [64], attention [65], speech [66] and decision-making [67] are labelled as higher order regions and tend to only be found in the human brain as the result of millions of years of evolution [68]. How information from stimuli flows between these regions and is combined to form our perception can be categorised into top-down or bottom-up processing (see Section 3.3.1).

The cerebral cortex forms the outer layer of the cerebrum and is a 2 – 4 mm thick layer of grey matter (GM) largely consisting of neuronal cell bodies and dendrites [69]. The cortex has been divided into six layers across the cortical depth from the cortical surface to the WM boundary based on histology (see Figure 3.4). These layers are:

Layer I – Molecular (plexiform) layer: The most superficial layer containing mainly nerve axons and a small number of Cajal-Retzius cells. This layer predominantly consists of axons from deeper layers synapsing with dendrites from other areas of the cortex.

Layer II – Molecular external granular layer: Containing mostly stellate neurons and some small pyramidal neurons. The pyramidal dendrites terminate in other cortical layers, especially the molecular layer, and their axons travel to deeper layers synapsing locally. In addition, some axons are long range and travel through the WM to synapse with other brain regions.

Layer III – External pyramidal layer: Containing predominantly pyramidal cells with dendrites that extend to the molecular layer and also dendrites that extend into the WM and on to the cortex in other regions.

Layer IV – Internal granular layer: Mostly containing stellate neurons and a small percentage of pyramidal neurons, this is the main cortical input layer. The stellate axons synapse locally and the pyramidal axons project to deeper layers and the WM. In the sensory areas of the cortex (such as the primary visual, auditory and sensory cortices) axonal fibres from the thalamus enter layer IV and project horizontally to synapse with the wide distribution of stellate neurons. The higher percentage of myelinated axons running parallel in layer IV results in a thin white strip known as the external band of Baillarger. This is particularly prominent in the primary visual cortex and is known as the Stria of Gennari.

Layer V – External pyramidal layer: Consisting of medium and large pyramidal neurons mostly responsible for the output of information to other cortical regions. This is prominent in the motor cortex, with the pyramidal

axons originating from layer V forming tracts that synapse with other brain regions and subcortical motor centres. Layer V also contains a horizontal myelinated stripe, known as the inner band of Baillarger, formed from the axons of layer IV that synapse locally within the layer.

Layer VI – Multiform cell layer: The deepest layer of the cortex containing mostly fusiform neurons with axons projecting to the thalamus and the opposite hemisphere of the brain.

These histological layers have been shown to have differing responsiveness to external stimuli and roles in cognitive and physiological processes, as is outlined in the next section [70–72].

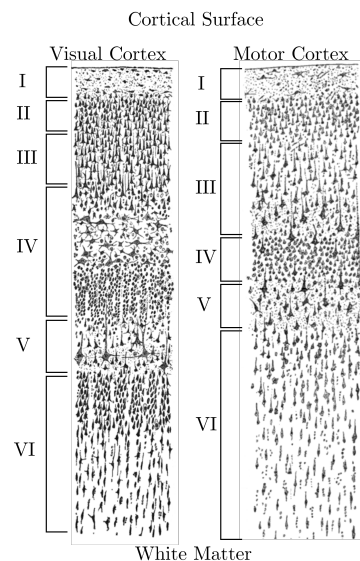


Figure 3.4: A drawing of the cell bodies of neurons in the primary visual (left) and motor (right) cortices by Ramón y Cajal, with the difference in neuron size and shape dictating the the structure of cortical layers I – VI in the human cerebral cortex. [73]

3.3.1 Top down/bottom up processing

Knowing the structure and connectivity of the cortical layers has enabled researchers to form neurophysiological descriptions for how the brain processes

information. Originally posed in psychology, bottom-up and top-down processing are descriptions of how the brain perceives external stimuli [74]. Bottom-up processing starts with sensory information that is converted to an electrical signal that moves on to be interpreted and integrated by the brain to form our experience. In comparison, top-down processing occurs when a sensory input needs more information to be interpreted correctly, for example recognising a face. In top-down processing the sensory information is integrated with prior information in the brain from previous experience and expectations. In relation to the cortical layers, bottom-up connections between brain areas are known to target Layer IV [75], while top-down connections target deeper and superficial layers mainly avoiding Layer IV [1, 4, 76].

Layer-fMRI has the potential to differentiate signals coming into the cortex across GM cortical depths from the WM to pial surface boundaries, and therefore distinguish between bottom-up and top-down responses. These are spatially amalgamated at standard imaging resolutions but at high spatial resolution it is possible to image the activity at different cortical depths using fMRI [77]. It may therefore be possible to separate bottom-up and top-down contributions to neuronal activity by studying cortical layer BOLD fMRI and linking this with electrophysiological signals through simultaneous EEG.

3.3.2 Origins of Alpha Oscillations

Alpha oscillations were the first to be measured in humans [9]. Despite this, their generation and functional mechanisms are poorly understood, with opinions divided between alpha being driven by bottom-up processes, top-down processes, or a combination of both. A key area within the debate is whether alpha oscillations are generated within layer IV of the cortex, regardless of task (and thus bottom-up or top-down processing).

A bottom-up process, in the context of the primary visual cortex (V1), is thought to occur during a simple ‘eyes open’, ‘eyes closed’ stimulus where no higher brain function is required and during which alpha power is significantly

modulated [9, 78]. The hypothesis in this case is that the visual information flows to the thalamus and on to layer IV of V1. In comparison, it is hypothesised that alpha power modulation during a visual attention task is potentially modulated through top-down processing. In this situation the information would flow to the thalamus, then to a higher cortical area (such as the lateral intraparietal area) and finally into layers I, II, III, V or VI in V1 [4] (see Figure 3.5).

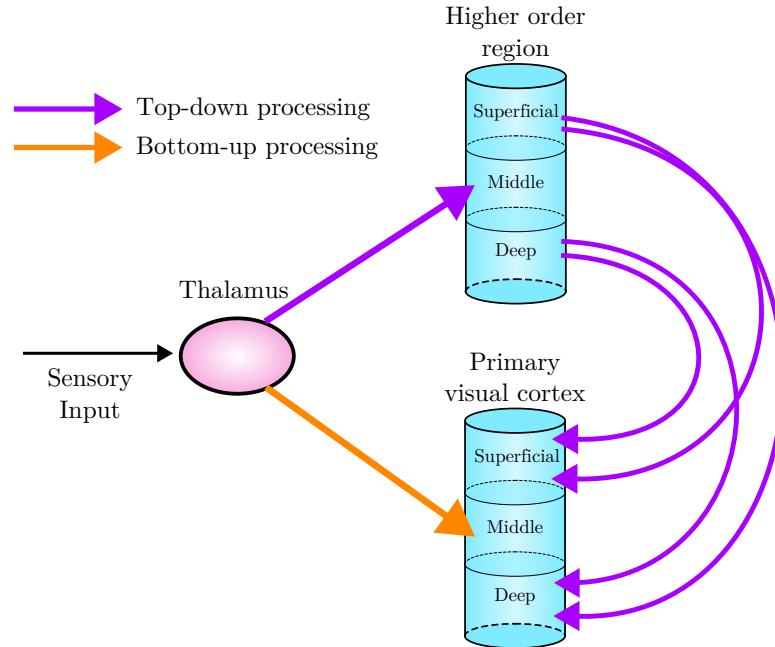


Figure 3.5: Schematic of the flow of information following a sensory input during top-down and bottom-up processing.

It is currently unanswered as to whether such bottom-up and top-down tasks, both of which are accompanied by modulation in alpha oscillations, are the result of different sources of alpha generation or not [45, 46, 70, 79–81]. If different mechanisms of generation do occur, it is predicted that the layers in which we see activity related to the alpha modulations will be different for the two tasks. If the alpha signal originates from a purely fundamental bottom-up process, alpha modulations are hypothesised to always be seen in layer IV. Being able to measure the layer from which the alpha signals are detected can

help define their origin and increase understanding of the function of alpha oscillations.

3.3.2.1 Evidence from animal work

The majority of work investigating the generating mechanisms of alpha oscillations on a laminar level has been conducted on animal models using invasive intracranial measures such as micro-electrodes and local field potentials (LFPs).

Work by Hughes *et al* used micro-electrodes and LFPs to measure EEG data from the Lateral Geniculate Nucleus (LGN) of the thalamus in cats, both *in vitro* and *in vivo* [45]. *In vitro* it was found that activation of Metabotropic Glutamate Receptor 1 (mGluR1) induced synchronised oscillations in the alpha and theta frequencies in the LGN of the thalamus. The *in vivo* recordings with microelectrodes implanted into the LGN showed similar characteristics to the *in vitro* data, suggesting that mGluR1a-induced alpha oscillations are a possible mechanism by which the thalamus promotes EEG alpha activity.

In a review of the work done by Lopes da Silva *et al* it is stated that alpha waves with the same characteristics can be recorded from the visual cortex and the LGN and pulvinar in the thalamus [82]. In addition, it was found that alpha rhythms of the visual cortex are generated by cortical neurons forming an equivalent dipole layer at cortical layers IV/V [83]. It was also found that the coherence of intracortical alpha signals between two regions significantly decreased when the effect of a thalamic site was removed, indicating that thalamic alpha activity influences cortical alpha activity [84]. Finally, despite the removal of the thalamic signal effects it was seen that cortico-cortical coherence remained, suggesting that there is cortico-cortical generation of alpha. Overall this work suggests that there are two generators of alpha, one being thalamo-cortical and the other being cortico-cortical.

in vitro work in rats by Silva *et al* [85] also showed that pyramidal neurons of layer V sustained rhythmic oscillations within the alpha frequency band following triggering with a small current pulse. The rhythmic behaviour was

only observed in layer V suggesting an intrinsic oscillatory mechanism for each neuron in layer V of the cortex.

Work by Buffalo *et al* measured LFPs using microelectrodes implanted into V1, V2 and V4 of the visual cortex at two cortical depths in Rhesus monkeys. Recordings were taken from deep and superficial cortical layers during a visual attention task [46]. The LFPs showed maximum coherence of the alpha band in layer V of the cortex. The synchrony of this alpha activity was reduced by attention, suggesting that alpha synchrony is generated from layer V of the cortex, thus that in this instance top-down mechanisms are generating the alpha signal.

3.3.2.2 Evidence from human work

The acquisition and analysis of layer dependent simultaneous EEG-fMRI in humans has previously only been performed at 3 T by Scheeringa *et al* [1, 86]. In their work they investigated the relationship between EEG alpha, beta and gamma oscillations and the BOLD response across different cortical layers. Interleaved EEG-fMRI data were acquired on 34 subjects during a visual attention task consisting of contracting rings at varying speeds. Functional GE-BOLD data were acquired using 3D-EPI with 0.75 mm isotropic resolution and a volume TR of 3.792 s. The fMRI data were then averaged to form one timecourse per cortical layer within each visual region, these were then input into a General Linear Model (GLM) with EEG regressors.

In the work of Scheeringa *et al* 2016, it was found that during an attention task, gamma-band EEG power correlates positively with the BOLD response in superficial layers, whilst beta-band EEG power is negatively correlated to the BOLD response in deep layers, and alpha-band EEG power is negatively correlated to the BOLD response in both deep and superficial layers. However, this work used a GE-BOLD acquisition which suffers from draining vein effects and can bias EEG-BOLD correlations towards the superficial layers, unlike CBV based acquisitions such as VASO. To account for the draining vein effect, a ratio

of the attention-on effect to the attention-off effect was used when performing the EEG-BOLD layer analysis. These results lay the ground work for the use of layer-fMRI to answer neurophysiological questions and to bridge the gap between human and animal model neuroscience.

More recently the data in Scheeringa *et al* 2016 was reanalysed [86] to assess how EEG power modulations relate to layer-fMRI connectivity between and within brain regions. Continuing on from the analysis in [1], the connectivity of the BOLD fMRI data between two separate layers was assessed and related to EEG power on a group level. It was found that the attention task induced a decrease in beta power that related to an increase in deep-to-deep layer coupling between regions, and increased connectivity of deep/middle-to-superficial layers within brain regions. The attention alpha power decrease predominantly related to reduced connectivity between deep and superficial layers within brain regions. This work suggests that alpha and beta power relate to different top-down neural processes.

3.4 Origin of the fMRI signal

This section describes the origin of the neuronal signals that can be measured using functional MRI (fMRI).

3.4.1 Physiology

Despite being only 2% of the body by weight, the brain has a high energy demand in comparison to other organs, accounting for 20% of the body's total energy expenditure. To maintain regular brain function, neurons require energy from metabolising glucose and oxygen. The brain has a limited capability to store glucose compared to other organs, and so a constant blood supply is required. This is achieved by a complex network of arteries, arterioles and capillaries that transport oxygen rich blood from the heart to the capillary bed where nutrients can cross the Blood Brain Barrier (BBB) into the neurons.

Waste products from the neurons diffuse in the other direction across the BBB back into the capillary bed and travel back towards the heart, with the now deoxygenated blood, through venules and large pial veins on the surface of the cortex.

During neuronal activity, the local demand for glucose and oxygen increases. To meet the demand, the surrounding arterioles and capillaries dilate to increase blood flow. The local increases in cerebral blood flow (CBF), accompanied by changes in cerebral blood volume (CBV), give rise to an increased supply of oxygenated blood. If the supply of oxygenated blood outweighs the demand, this results in a change in the MR signal due to a phenomenon known as the Blood Oxygenation Level Dependent (BOLD) contrast.

3.4.2 BOLD contrast

First demonstrated in 1990, the BOLD contrast is an indirect measure of neuronal activity [2] that can be measured with fMRI. During activation there is a local increase in the Cerebral Metabolic Rate of Oxygen ($CMRO_2$) leading to an increased demand for oxygen. Oxygen is transported in the blood in the form of oxyhaemoglobin in red blood cells, a diamagnetic iron protein complex bound to four O_2 molecules. Once the oxygen dissociates, it is known as deoxyhaemoglobin which is paramagnetic. The paramagnetism of deoxyhaemoglobin causes local magnetic field distortions leading to a variation in the precession frequencies of nearby spins, resulting in dephasing and the shortening of T_2^* around venous blood vessels. To meet the increased demand for oxygen, local arteriole CBF and CBV increase but the increase in these measures is greater than what is required, leading to a higher ratio of oxyhaemoglobin to deoxyhaemoglobin. This local decrease in deoxyhaemoglobin results in an increase in the MR signal, this is known as the BOLD signal.

The T_2^* dephasing effects are increased at higher field strengths, and as a result the BOLD signal increases [87]. As well as increased BOLD signal, the overall SNR increases at higher field strengths. Due to these factors at ultra-high

field (UHF), the higher BOLD fMRI signal can be traded for higher spatial resolution. However, higher field strengths do come with compromises of greater B_1 inhomogeneity, and shorter T_2^* values. The latter shortens the available time that data can be collected before the signal decays and necessitates a shorter echo time (TE). To achieve such short TEs, higher gradient strengths and slew rates are sometimes used, with these reaching 40 mTm^{-1} and $200 \text{ mTm}^{-1}\text{s}^{-1}$, respectively on the 7T Philips Achieva system.

BOLD fMRI is typically acquired with a Gradient Echo EPI (GE-EPI) sequence but a Spin Echo EPI (SE-EPI) sequence can also be used. The design of each of these sequences results in different sensitivities to the BOLD signal. The difference in the BOLD signal between GE and SE EPI arises from the areas surrounding large vessels. The spins surrounding large vessels experience a reasonably constant magnetic field over time and therefore the long range susceptibility dephasing effects from field inhomogeneities (T_2') are refocused by the 180° inversion pulse in the SE sequence but are not refocused in a GE sequence. This results in no contribution to the SE-BOLD signal from the extravascular regions near large vessels, reducing the SE-BOLD sensitivity [88, 89]. The spins in the vicinity of small vessels experience random dephasing effects due to diffusion that cannot be refocused by the SE sequence, resulting in T_2 BOLD contrast. In summary, SE-BOLD is less sensitive to the BOLD contrast than GE-BOLD but has better spatial specificity to the small vessels in the capillary bed, and therefore the area of neuronal activity.

After neuronal activity the BOLD signal varies over time, this is referred to as the BOLD Haemodynamic Response Function (HRF). The BOLD HRF consists of three features: the primary response, the post stimulus undershoot, and the ‘initial dip’ which is included in some models but is still debated [90]. A schematic of these features is shown in Figure 3.6. The primary response is a positive increase in signal from baseline immediately after the stimulus onset, reaching its peak after ~ 6 s, this delayed time to the peak is referred to as the haemodynamic lag. Following the primary response is the post stimulus

undershoot where the signal begins to decrease back towards baseline but undershoots before returning to baseline most likely due to an uncoupling of the return to baseline in blood volume compared to blood flow.

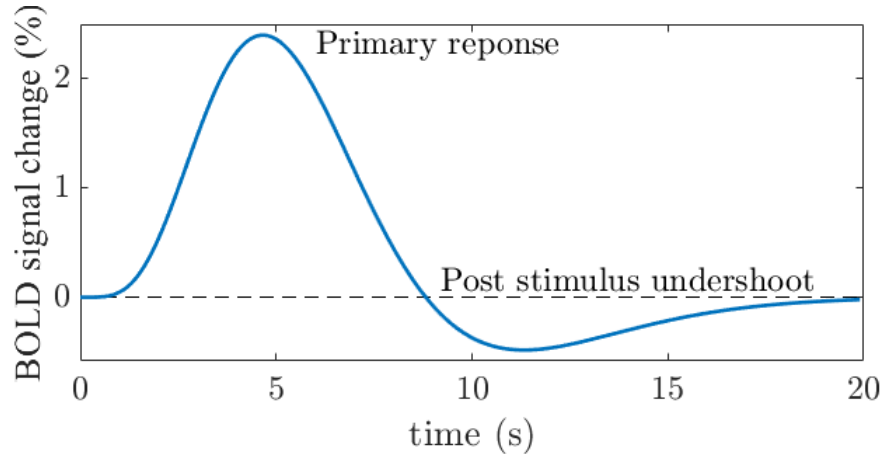


Figure 3.6: The BOLD haemodynamic response function (HRF) following a short stimulus at time 0 s. The primary response which peaks at ~ 6 s, followed by the post stimulus undershoot before returning to baseline. The debated ‘initial deoxy dip’ isn’t shown.

Vascular space occupancy (VASO) is an alternative fMRI contrast whereby changes in the MR signal are induced by changes in the cerebral blood volume. A 180° inversion pulse is applied to invert the grey matter and blood magnetisation, after a period of time the signal is acquired at the null point of the blood magnetisation (described in detail in Section 6.1.1). During neuronal activation, the blood volume increase results in a decrease in the MR signal. VASO is less sensitive than GE-BOLD but is more spatially specific as the CBV response is thought to originate from small vessels, whilst the GE-BOLD signal which originates from venous origin has a suggested spatial accuracy of about 3.5 mm, based on the vascular Point Spread Function (PSF) [91].

3.4.3 Combined EEG-fMRI

Despite Echo Planar Imaging (EPI) acquisitions only requiring 10s of milliseconds per slice, the temporal resolution of fMRI is poor compared to other brain imaging methods such as MEG and EEG. This is because the temporal resolution of fMRI is ultimately limited by the haemodynamic response function as shown in Figure 3.6. Conversely, EEG/MEG detects the electrophysiological activity of synchronously firing neurons and thus is a direct measure of brain activity with temporal resolutions on the order of 1 ms. Combining the high spatial resolution of fMRI with the high temporal resolution of EEG, creates a multimodal technique to probe the haemodynamics of the brain related to specific signatures of neural activity from the EEG, enabling us to investigate the origins of the alpha signal. The combination of EEG and fMRI arose in the mid 1990s, with its development driven by a clinical interest to localise epileptic EEG activity [92]. Since then, further developments of hardware and data analysis [93] have led to multiple approaches to combine EEG and fMRI data. Combined EEG and fMRI data can be collected in an interleaved fashion with EEG collected during temporal gaps in the MRI acquisition (used in Scheeringa *et al*), or in a continuous fashion. In this thesis, continuous EEG-fMRI data is collected. Collecting the EEG data continuously throughout the MRI scan means there are no gaps in the fMRI acquisition for a ‘quiet’ period in which to collect the EEG data. This has two benefits, (1) the signal variation in the EEG signal is collected for the entire fMRI timeseries, and (2) since a pause is not required in the fMRI acquisition (i.e. the fMRI data is not acquired in a sparse-sampling acquisition) the temporal resolution of the acquisition of the fMRI signal is much shorter. For continuous EEG-fMRI one of the biggest concerns is the quality of the EEG data [94, 95]. MRI scanners give rise to multiple artefacts in the EEG data, the most prominent being Pulse Artefacts (PA) [96], Gradient Artefacts (GA) [97] and Motion Artefacts (MA) [98]. Working with EEG-fMRI at UHF is therefore very challenging as the

magnitude and prevalence of PAs and MAs are increased due to the increased magnetic field strength. Additionally, the presence of the EEG electrodes can reduce the MR image quality [95], and if an RF surface coil is used to collect the MR data, then this needs careful planning to ensure the coil is optimally placed over the cortical area of interest.

As EEG and BOLD fMRI are measuring two distinct measures of neuronal activity, it is important to understand how they correspond to each other. EEG detects the electrophysiological signals from 1000s of synchronously firing neurons whereas fMRI BOLD detects changes in blood flow, blood volume and oxygenation. Most commonly features of the EEG timecourse are used as regressors in GLMs (see Section 4.4.3.1). When an oscillatory activity is of interest, often the continuous EEG timecourse is used to form a regressor, averaging all the signal within a TR period and convolving with a HRF.

For effective combination of EEG and fMRI, it is important to understand how these signals predominantly correlate to each other during brain activity. It has been shown that delta power correlates positively with the BOLD response during the resting state [99] and that gamma power correlates positively during a task [100, 101]. Beta power has been shown to correlate positively [102] in the default mode network during rest and negatively [101] during visual stimulus to the BOLD response. Alpha power has been shown to correlate negatively with the BOLD response at rest [101–103] and prefrontal theta power has been shown to correlate negatively [104].

3.5 fMRI Analysis

fMRI data can be acquired during a task or in the resting state. Task fMRI involves the subject being exposed to a stimulus or instructed to perform a task for a given period of time. The data is then analysed using the knowledge of the stimulus characteristics i.e onsets and duration. Stimuli can be presented in defined blocks of ‘ON’ and ‘OFF’, often repeated a number of times during

each fMRI run, or as short events occurring at predefined times throughout the fMRI run. Resting state fMRI is analysed without stimulus information and involves correlating the BOLD fMRI signal between different regions in the brain to define functional connectivity networks [105, 106] or by using another measure of brain activity such as EEG to create a model of expected BOLD response [93, 103, 107, 108].

Following acquisition, multiple analysis steps are required to identify areas of activation in the brain in response to delivery of a stimulus or performing a task. For the work in this thesis this is outlined in Chapter 4.

3.5.1 Analysis of fMRI data

The acquired fMRI data is considered as a 4D matrix with three spatial dimensions x, y, z each with a time-series, t . Statistical tests can be performed on each voxels time-series to determine how it correlates with a predicted timecourse modelled using information about the stimulus timings and the BOLD HRF. Prior to performing such tests, pre-processing steps are required to remove artefacts and noise from the data.

3.5.1.1 Conventional Preprocessing Steps

The following steps are typically used in the pre-processing of fMRI data:

Motion Correction: The spatial registration of sequential volumes of the fMRI data to a specific reference volume to minimise the effect of subject head movement. The reference volume is often the first or middle volume acquired during the fMRI run. This step is especially important for high spatial resolution fMRI studies so that specific localisation of activation can be maintained.

Spatial Smoothing: This reduces the influence of noise on the detection of brain activation. Typically, a smoothing kernel with a Full Width Half Maximum (FWHM) of 1.5 – 2 times the voxel size is used. This step is very common in whole brain fMRI studies at 3 T with lower spatial resolutions (>2

mm isotropic), but is detrimental for fMRI studies using high spatial resolution as it reduces specificity.

Temporal filtering: Typically high pass filtering (> 0.01 Hz) is used to remove slow changes in the baseline from the data due to scanner drift. Scanner drift is predominantly caused by gradient heating, which can often occur during high resolution fMRI acquisitions as the acquisition is often at the limit of the hardware.

Normalisation: Finally, registration is often performed so that subjects can be aligned to a ‘standard’ space template. The Montreal National Institute (MNI) template is a widely adopted common coordinate system used to define regions of the brain. There are multiple atlases that have been defined in this space to give an estimate template of common brain structures, or functional regions. Relevant to this thesis is the Benson atlas which defines areas of the visual cortex [109], and is described in Chapter 4.

3.5.1.2 General Linear Model (GLM)

Once the fMRI data has been pre-processed, statistical analysis can be performed to separate regions of noise from regions of brain activation in the data. A common analysis is to use a general linear model (GLM). For the GLM the data is modelled as a linear combination of multiple models (called regressors) collectively known as the design matrix, X . The contribution of each regressor to the variance of each voxel’s timecourse, Y , is assessed and a weighting, β , is given according to its contribution. The model regressors in the design matrix are generated by predicting the shape of the BOLD signal in response to the stimulus. This is done by convolving a standard HRF with a boxcar function of the stimulus, with the boxcar being 1 when the stimulus is ON and 0 when at REST. The remaining variance unexplained by $X\beta$ is assumed to be noise, e , this results in the matrix equation,

$$Y = X\beta + e \tag{3.1}$$

where Y is the fMRI data, X is the design matrix (or regressors), β is the amplitude weighting (known as β -weights) and e is the noise vector (or residuals). The analysis adjusts the β -weights until the best description of the variance in Y is found, large β -weights correspond to a voxel timecourse that is well explained by the regressor. First-level GLM analysis is used for data from a single subject. Second-level analysis is used to combined results from multiple sessions or subjects.

3.5.2 t/z statistics

To identify areas of statistically significant activity the β -weights can be tested against a null hypothesis using a t -test.

$$t = \frac{\bar{x} - \mu}{\sigma/\sqrt{n}} \quad (3.2)$$

where \bar{x} is the mean of the sample, μ is population mean, σ is the standard deviation of the error and n is the degrees of freedom – usually the number of data points minus the number of regressors. The measured t -statistic is compared with a t -distribution to determine if the t -statistic has arisen by chance if the means are the same. The t -stats are transformed to z -stats using a standard statistical transform and activation maps are usually displayed at a set z threshold that corresponds to a specified p-value.

3.5.3 Noise sources in fMRI data and correction

fMRI data has two main sources of noise, thermal noise and physiological noise. Thermal noise arises from MR hardware and the sample and is the dominant source of noise in high spatial resolution acquisitions of < 1 mm isotropic. fMRI studies using high spatial resolution are often in the thermal noise dominated regime and Temporal Signal to Noise Ratio (tSNR) limited. To overcome such low tSNR, long block stimuli are used and multiple fMRI runs are acquired to reduce noise by averaging over a number of trials. This increases total scan

session time and reduces the time available to acquire other fMRI paradigms or structural measures. Recently Noise Reduction using DIstribution Corrected PCA (NORDIC PCA) denoising has been developed for the removal of thermal noise from fMRI and diffusion MRI data [110, 111] and its application to high spatial resolution BOLD and VASO fMRI data is considered in Chapter 6.

Physiological noise, consists of cardiac noise and respiratory noise and is the dominant noise source in fMRI data with spatial resolutions > 3 mm isotropic. Physiological noise increases with magnetic field strength, but methods can be used to correct for this such as Retrospective Correction of Physiological Motion Effects in the Image Domain (RETROICOR) [112]. RETROICOR can be applied during pre-processing using the cardiac and respiratory data collected from the respiratory bellows and a Peripheral Pulse Unit (PPU) during fMRI scanning. The phase of the cardiac and respiratory data is used to calculate and remove the corresponding noise.

To assess the data quality and noise levels in fMRI data, the image stability over time is measured using a metric known as temporal signal-to-noise ratio (tSNR). tSNR is calculated by dividing the mean signal of each voxel by the standard deviation of the voxels timecourse.

$$\text{tSNR} = \frac{\text{mean signal of timecourse}}{\text{standard deviation of timecourse}}. \quad (3.3)$$

3.6 Conclusion

This chapter has provided an outline of the origins of EEG and fMRI signals, as well as the processing pipelines for fMRI. These methods will be applied in Chapters 4 and 5 in combined EEG-fMRI of layer-specific alpha response, and in Chapter 6 to study BOLD and VASO responses to a motor task.

Chapter 4

Analysis pipeline to assess
layer-specific alpha signals using
EEG-fMRI

Abstract

In this chapter a simultaneous 7 T EEG-fMRI study is described and the optimal pipeline for layer-dependent analysis of this EEG-fMRI data is explored. This is then applied to study the origins of human alpha oscillations in Chapter 5.

7 T EEG-fMRI data with a 3D GE-EPI readout was previously acquired on ten healthy subjects during an eyes open/closed paradigm along with structural MRI and retinotopic mapping fMRI measures. This chapter outlines optimal motion correction and coregistration of the fMRI data, using a single concatenated transformation matrix, followed by B_0 field map distortion correction to maintain spatial resolution of the functional data and align it with the structural data. The EEG alpha power timecourse during the eyes open/closed paradigm is used as a regressor for the fixed effects GLM, with the convolution of the EEG timeseries at 500 Hz with a HRF found to be optimal and temporally downsampling to generate alpha specific BOLD responses. From a separate scan session, retinotopic mapping fMRI data is used to define a Region Of Interest (ROI) for visual regions V1, V2 and V3. The PSIR structural data from the EEG-fMRI and retinotopy scan session are coregistered, and the resulting transforms applied to the V1, V2 and V3 ROIs to move these into the EEG-fMRI space.

The EEG-fMRI PSIR structural data are segmented into tissue type and upsampled to result in GM masks within V1, V2 and V3 ROIs with manual correction used to avoid any large vessels. Equivolume cortical layers are then calculated and 4,000 cortical columns generated across the GM ribbon.

Finally, the optimal parameters for layer-specific BOLD analysis are explored to show the effect of active voxel choice, denoising and deveining. The columns within V1, V2 and V3 are filtered for those containing significant alpha-BOLD correlation and denoised using a threshold equal to 5% of the maximum value in the visual region. The β -weights within the remaining columns are then deveined in LayNii using the spatial

deconvolution leakage model. Methods to study the uncorrected and deconvolved layer profiles are then presented.

This work was presented as an oral presentation at International Society of Magnetic Resonance in Medicine (ISMRM) 2020 ‘Assessing the origin of human alpha oscillations using laminar layer 7 T fMRI-EEG’; a talk at the ISMRM UHF Workshop Lisbon 2022 ‘Laminar layer 7 T fMRI-EEG reveals human alpha oscillations are predominately from superficial and deep layers’; a digital poster at ISMRM 2022 ‘Laminar layer 7 T fMRI-EEG reveals human alpha oscillations are predominately from superficial and deep layers’; and a poster at Organisation for Human Brain Mapping (OHBM) 2022, Glasgow ‘Layer 7 T fMRI-EEG: human alpha oscillations originate from visual cortex superficial and deep layers’.

4.1 Introduction

In recent years advances in the acquisition and analysis of functional Magnetic Resonance Imaging (fMRI) and the push to higher field strengths has made the measurement of cortical depth dependent fMRI signals viable in humans [113–116]. Using fMRI to obtain measures from across the cortical layers in the human brain opens up opportunities to investigate neuroscience questions that were previously only possible using animal models or invasive methods such as electrocorticography (ECoG). Studying functional activation and connectivity of the cortical layers can help to answer questions on the hierarchical organisation of the brain and how it processes information [117–119]. In hierarchical brain systems, such as in humans, neural inputs from one region to another are known to arrive in different cortical layers, dependent on whether this is a top-down or bottom-up process (for a complete description see Section 3.3.1).

To achieve high spatial resolution and sufficient temporal resolution to detect such subtle neurovascular changes in thin cortical layers, the majority of researchers use ultra-high-field (UHF) MR systems with highly optimised, bespoke sequences in order to maximise contrast-to-noise ratio (CNR) and signal-to-noise ratio (SNR). UHF MR scanners (defined to be 7 T and higher) are used in over 80% of layer-fMRI publications, with Siemens being the most common vendor and used in over 80% of layer-fMRI publications [120]. These publications predominantly use gradient echo (GE) EPI BOLD contrast or vascular space occupancy (VASO) measurements collected with 2D-EPI or 3D-EPI readouts, whilst a small number of studies collect spin echo (SE) EPI BOLD contrast and Arterial Cerebral Blood Volume (aCBV) [121–124]. Typically the functional acquisitions are collected with a small field of view (FOV) and a thin stack of slices covering the domain of interest, typically the primary sensorimotor or visual cortex. Layer-specific fMRI paradigms mostly use block stimuli (of up to 30s ON/OFF periods) for strong activation of the sensorimotor or visual cortex, for example by displaying a flashing checkerboard or performing

fingertapping. Multiple runs of the functional data are acquired alongside high resolution structural scans, usually a Magnetisation-Prepared Rapidly Acquired Gradient Echo (MPRAGE) [125], Magnetisation Prepared 2 Rapid Gradient Echo (MP2RAGE) [126] or Phase Sensitive Inversion Recovery (PSIR) scan [127]. Stringent motion correction and distortion correction is required to best align the high spatial resolution (≤ 1 mm) functional and structural data. Functional data has then predominantly been analysed using a general linear model (GLM) followed by cortical layer analysis.

Most layer-specific fMRI studies follow the methods described above but compromise and concessions for the acquisitions and analysis are required (as described in [128]). The key limitations are low sensitivity/specificity, small coverage, asymmetric voxel sizes and the need for manual intervention in the analysis pipeline. Each of these points are discussed below.

Low sensitivity and specificity: There is a drastic reduction in signal-to-noise ratio (SNR) when acquiring data at sub-millimetre voxel sizes for layer-specific fMRI compared to standard fMRI acquisitions. For example, increasing the spatial resolution from 2 mm isotropic to 0.8 mm isotropic results in a 15-fold reduction in volume (from 8 mm³ to 0.512 mm³) and therefore a similar reduction in the signal. The reduced SNR of acquisitions necessitates the use of block-design tasks with longer ‘ON’ and ‘OFF’ periods to study brain activation in primary areas. Sensitivity is highest for GE-EPI BOLD and reduced when acquiring SE-EPI BOLD, VASO or aCBV contrasts as these have inherently lower contrast-to-noise ratio (CNR) than GE-EPI BOLD [129, 130] (see Chapter 3 for a detailed discussion of this point). Therefore, GE-EPI BOLD is often used for high resolution fMRI studies. However, due to its sensitivity to extravasculature T_2^* changes [131], the large draining veins in the cortex blur the fMRI activity towards the pial surface. This signal blurring is a substantial limitation to layer-specific fMRI using GE-BOLD and must be corrected for using post processing methods, which are outlined in Section 4.7 of this chapter.

Small coverage: In order to achieve sufficient spatial resolution but collect fMRI data with a reasonable temporal resolution, acquisitions are often limited to a few slices in a stack covering a single brain region of interest. This poses challenges when the experimenter is setting up and planning the protocol and care must be taken to ensure the brain area(s) of interest are not cropped or missed in the data acquisition. The recent development of multiband (MB) [132], also known as simultaneous multislice (SMS), which acquires data from different slices simultaneously provides acquisitions with greater coverage without changing the total readout time for a volume. However, care must be taken to avoid aliasing between slices [133] using a MB acquisition, particularly for thin slices and a small stack of slices.

Asymmetric voxel sizes: To increase the sensitivity of an fMRI acquisition, asymmetric voxel sizes are often used, typically with sub-millimetre resolution in-plane and lower resolution (~ 1.5 mm) through plane. Brain regions that have stable folding patterns across subjects (e.g. the motor cortex) are more accommodating to this approach. However, careful slice positioning is required to ensure sufficient sampling across the cortical ribbon. For higher order brain regions, which have more complex folding patterns and higher variability between subjects, isotropic resolution is vital to capture the brain activation across the cortical ribbon.

Manual intervention: At high spatial resolution, distortion correction and registration is vital for maximum alignment between functional EPI-based data and structural data. This requires manual checking of registrations and can be improved by manual adjustments of realignment parameters on a subject-by-subject basis. Layer modelling is highly dependent on high quality, accurate definitions of the GM/CSF and GM/WM boundaries. There are software libraries (such as fMRIB Software Library (FSL) [134], Statistical Parametric Mapping toolbox (SPM) [135] and Freesurfer [136]) available to segment structural brain images into GM, WM and CSF tissue types but these need checking and typically need manual editing to achieve the required quality for

layer analysis. Each dataset can require as much as 8 – 12 hours for precise editing of the GM boundaries.

To take full advantage of layer-fMRI to aid understanding of the origin of EEG scalp signals there are a number of methodological challenges yet to be fully addressed. These include: 1) The origin of the alpha signal in terms of the specific location(s) in the visual cortex from which it is originating is unknown, therefore the region of interest (ROI) which is imaged with fMRI must cover the whole of visual areas V1, V2 and V3 whilst minimally compromising spatial and temporal resolution. 2) How to combine the EEG and fMRI data using higher spatial resolution GE-BOLD or VASO acquisitions which have longer repetition times (TR) (of the order of 4 s) than standard spatial resolution EEG-fMRI studies (typically TR of 2 s [137, 138]). 3) How to account for the draining vein effect which alters the specificity of layer-specific fMRI.

This chapter outlines the details of the EEG-fMRI acquisition at 7 T for layer-specific fMRI. The development of an analysis pipeline to overcome the associated challenges of layer-specific EEG-fMRI is then presented with steps primarily illustrated in a single subject. This pipeline is then applied to the full dataset in Chapter 5 to investigate the overarching question of ‘*What is the origin of the EEG Alpha signal?*’. The data acquisition was performed prior to the commencement of my PhD studies, my contribution relates to the development of the analysis pipeline to apply to these datasets. For completeness full details of the data acquisitions are provided in Section 4.2.

4.2 Acquisition of 7 T EEG-fMRI data

This study was conducted with approval from the local ethics committee and complied with the Code of Ethics of the World Medical Association (Declaration of Helsinki). Ten healthy, experienced fMRI subjects (four female) with a mean age 28 ± 5 years, participated in this study. Each subject gave written, informed consent before participation. The protocol involved a core experimental eyes

open/eyes closed paradigm during which simultaneous EEG-fMRI data was collected, alongside this functional and structural data were acquired to define core visual cortex regions (V1, V2 and V3) and define the grey matter for layer analysis.

4.2.1 Experimental Paradigm: Eyes open/closed

A simple ‘eyes open/eyes closed’ core paradigm was chosen to induce bottom-up alpha modulation for during the study of EEG and fMRI responses. Subjects were cued to open or close their eyes by delivery of a short (100 ms) vibrotactile stimulus to their finger applied using a piezoelectric stimulation device (Dancer Designs). A fixation cross was present during the eyes open periods. Blocks consisted of 30 s of eyes open and 30 s of eyes closed, with four blocks per run as shown in Figure 4.1. Four or five runs were acquired per subject (5 subjects had five runs and 5 subjects had four runs).

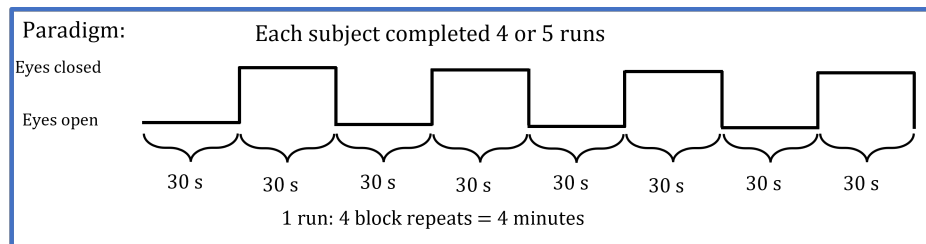


Figure 4.1: Eyes open, eyes closed paradigm used to modulate alpha power.

4.2.2 Session 1: EEG-fMRI and associated structural measures

All MRI data were acquired on a 7 T Phillips Achieva MR scanner (Phillips Medical Systems, Best, Netherlands) using a volume transmit coil (Nova Medical, Wilmington, USA) and two 16 channel high density array surface receive coils (MR Coils, Netherlands). Cardiac and respiratory traces were simultaneously

recorded throughout using the scanner’s physiological monitoring system (vector cardiogram (VCG) and respiratory belt).

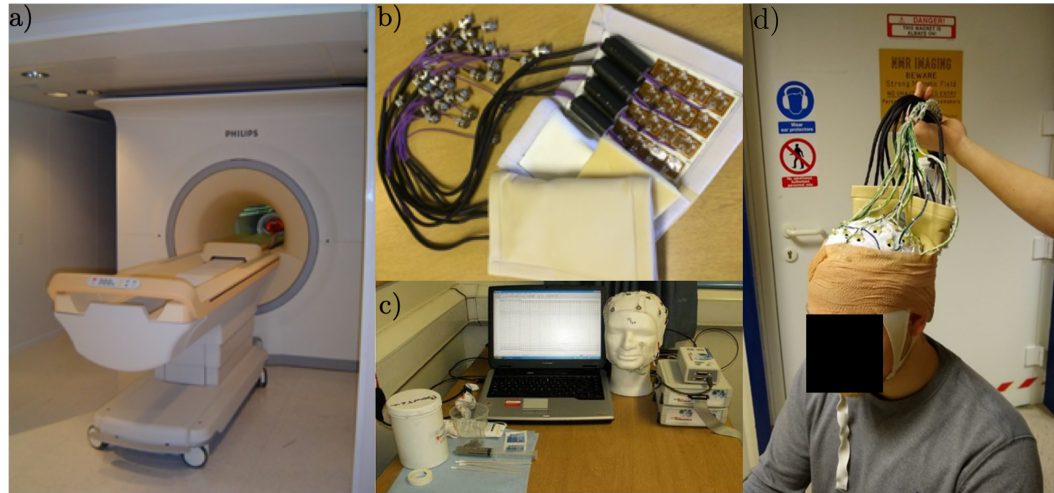


Figure 4.2: The apparatus used to acquire the MRI data. a) 7 T Philips Achieva MR scanner, b) the two 16 channel high density array surface receive coils with one showing the individual 16 receive coils elements, c) MR-compatible EEG cap, BrainAmp MR-plus EEG amplifier and Brain Vision Recorder d) The EEG cap and positioning of the two surface receive coils on a volunteer using Coban Tape prior to scanning.

The surface coils were positioned over the individual subject’s occipital cortex using a previously acquired structural image for each subject and the known relative position of the EEG electrodes to the individuals anatomy. Coban Tape was used to hold the surface coils in position prior to the subject being placed in the scanner. To ensure the correct positioning of the coil, survey scans were initially collected using the linear coil for both transmit and receive to allow a 3-dimensional survey image to be collected. A survey scan was then performed using the the high density array surface receive coils and, if required, the surface coils were moved to ensure optimal sensitivity to V1.

EEG data were recorded using an MR-compatible EEG cap (EasyCap, Herrsching, Germany) with 63 scalp electrodes following the extended interna-

tional 10 – 20 system and an additional channel for recording the electrocardiograph (ECG). The reference electrode was positioned at FCz. A BrainAmp MR-plus EEG amplifier (Brain Products, Munich) and Brain Vision Recorder (Version 1.10) was used for data acquisition.

fMRI data: These were collected using the two 16-channel surface receive coils with a 3D GE-EPI sequence (see Figure 4.3) at 0.8 mm isotropic resolution, $TE/TR = 32/76$ ms, $FA = 28^\circ$, $TR_{\text{volume}} = 3.8$ s, Bandwidth (BW) in EPI frequency = 740.4 Hz, acquired matrix size 88×168 (AP \times RL), SENSE 3.45×1.7 (Phase \times Slice) (reconstructed matrix = 256×256), slices were positioned centred along the calcarine sulcus (Figure 4.3) with 44 slices in an axial orientation and Image Based (IB) shimming. The two 16-channel surface receive coils allowed a high SENSE factor to be used in the RL phase encoding direction. A single scan consisted of 68 volumes, resulting in a scan duration of ~ 4 minutes, a minimum of 4 functional runs were acquired for each subject.

In addition, following the functional runs, multi-TE 3D GE-EPI data were collected at a range of echo times ($TE = 30$ ms, 35 ms, 40 ms and 50 ms) with 6 dynamics collected at each, to allow for a T_2^* map to be calculated. This was collected with the goal of subsequently using this data to define the veins and Stria of Gennari from either the T_2^* map or the associated proton density (M_0 map) fitting the data voxel-wise to $M_0 e^{-t/T_2^*}$ (Equation 2.15).

Prior to the fMRI acquisition, a B_0 field map was acquired with the same geometry as the 3D-EPI data ($TR = 20$ ms, $TE/\Delta TE = 5.92/1$ ms, 4 mm isotropic resolution, 64×64 matrix, 40 slices, $FA = 25^\circ$, SENSE 2) with the same image based (IB) shim volume as used for the fMRI data acquisition to match the field perturbations. This B_0 field map could then be used for distortion correction of the 3D-EPI fMRI datasets.

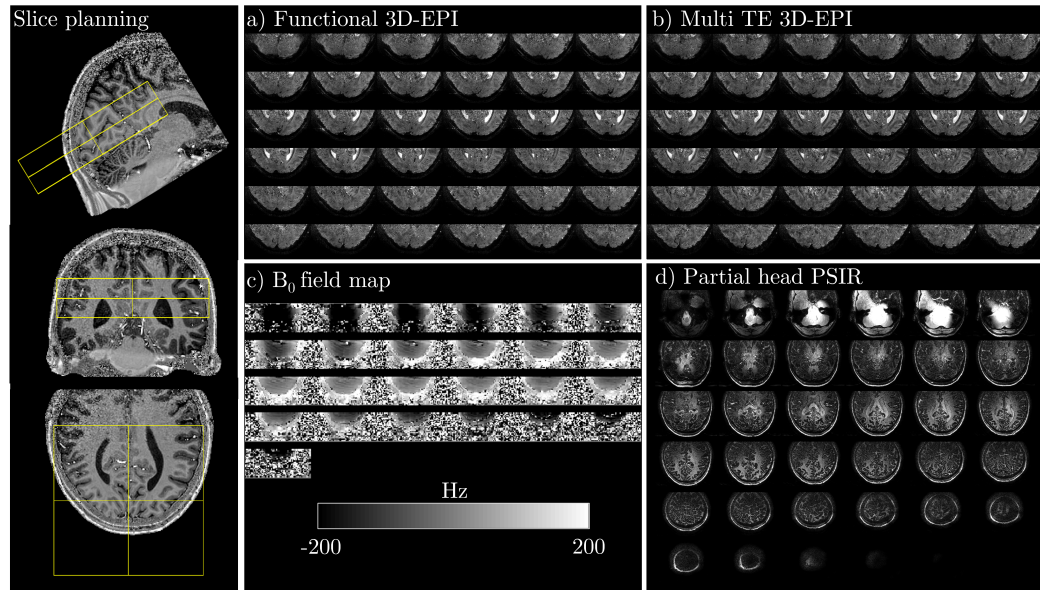


Figure 4.3: A summary of the acquisitions collected using the two 16-channel surface receive coils. Showing a) an example the dynamic of functional 3D GE-EPI data b) an example TE (40 ms) of the Multi TE 3D GE-EPI data c) a B_0 field map in Hz and d) a single phase ($TI = 780$ ms) of the PSIR data.

EEG data: These were recorded using a sampling rate of 5 kHz and hardware filtering to the frequency range of 0.016 – 250 Hz with a roll-off of 30 dB/octave at high frequency. The electrode impedances were kept below 20 k Ω . EEG artefacts from the MRI environment were minimised by isolating the EEG amplifiers from the scanner bed and reducing the MR room noise by switching off the cold head pumps during acquisition [139]. The optimal correction of the gradient artefact was made possible by adapting the 3D GE-EPI sequence to ensure that the TR was equal to a multiple of the EEG sampling period and by synchronising the EEG and MRI scanner clocks [140]. The MRI scanner’s vectorcardiograph (VCG) was used to monitor the cardiac trace to enable the correction of the pulse artefact.

After completion of MRI scanning, the locations of the EEG electrodes on the scalp surface, and the shape of the subject’s head were digitally recorded using a Polhemus isotrack 3D system (Polhemus, Vermont, USA). The 3D digitised

head shape was subsequently fit to each subject’s whole-head anatomical MRI scan (see below) in order to compute the location of each electrode with respect to the individuals brain anatomy.

Anatomical data: These were also collected using the two 16-channel surface receive coils with the same geometry as the 3D GE-EPI fMRI data using a phase-sensitive inversion recovery (PSIR) sequence [141]: 0.7 mm isotropic resolution, 252×250 matrix, 175 slices, $TI = 780/2280$ ms, SENSE factors: 2.2 (right-left, phase encode), 2 (foot-head, slice selection). As with the 3D GE-EPI fMRI acquisition this was a partial head acquisition covering the visual cortex.

4.2.3 Session 2: Retinotopic Mapping

In a second scan session, data was collected on a separate day using a 32-channel whole head receive coil (Nova-Medical) with no EEG cap in place. A whole head PSIR (0.7 mm isotropic) dataset was acquired with matched image parameters to the PSIR dataset acquired in Session 1 (see Figure 4.4). 2D GE-EPI fMRI data were acquired (2D-EPI, $TR = 2$ s, $TE = 25$ ms, 1.5 mm^3 isotropic resolution, 124×121 matrix, 85° FA, SENSE 2.5, receiver bandwidth 1,089 Hz/pixel, phase encode direction: foot-head) for retinotopic mapping. 32 coronal oblique slices were acquired to cover the entire visual stream (V1 to IPS), with IB shimming performed over this target region, and 120 volumes collected per run.

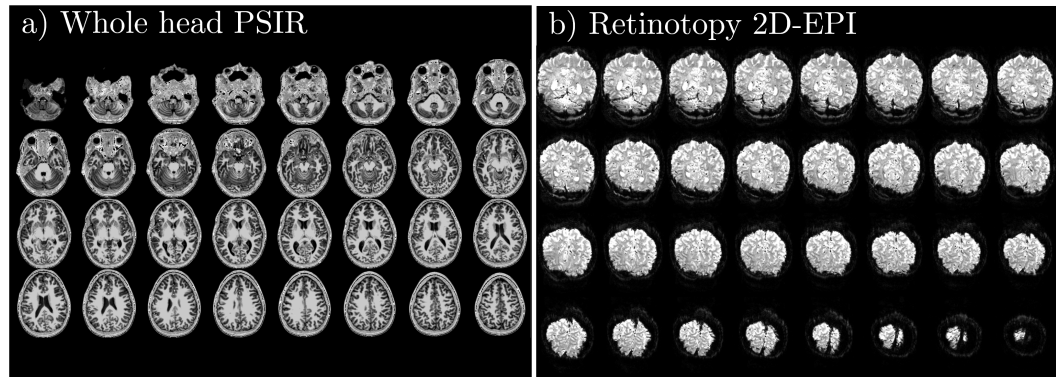


Figure 4.4: The dataset acquired in the second scan session using the 32-channel whole head receive coil (Nova Medical). This comprised a 0.7 mm isotropic whole head PSIR and a functional 2D GE-EPI retinotopy dataset.

Eccentricity and polar angle maps were measured using standard retinotopic mapping procedures comprising an expanding annulus and rotating wedge (see Figure 4.5) to define visual areas (V1, V2, V3) for each subject, as performed in [142].

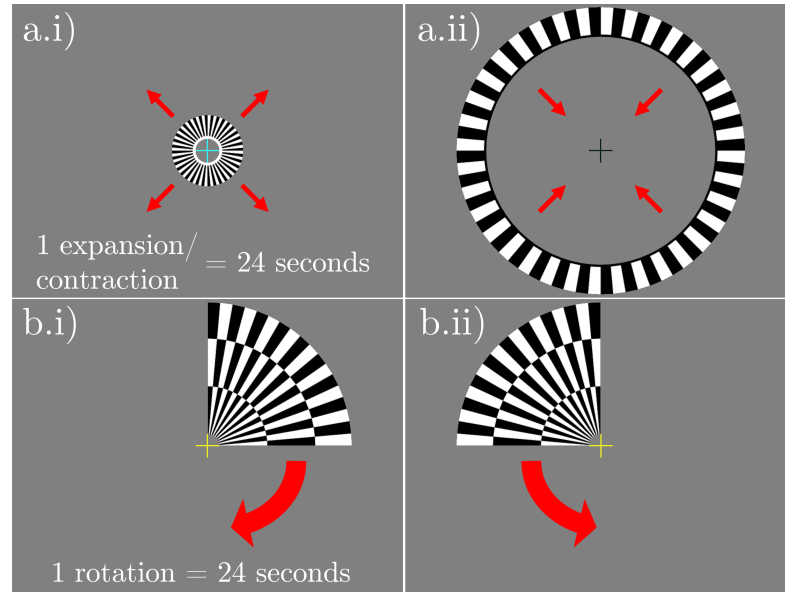


Figure 4.5: Retinotopic mapping paradigm using a) expanding/contracting rings and b) clockwise/anti-clockwise wedges. One complete expansion/contraction/rotation took 24 seconds.

These are standard retinotopic stimuli provided in the `mgl` toolbox [143]. Visual eccentricity was measured using an expanding annulus that started from a fixation point at the fovea and moved out to the periphery. To measure polar angle in the visual cortex, a wedge rotated clockwise. Both the annulus and wedge stimuli were textured with a checkerboard with alternating chromatic contrast. One period of stimulation (i.e., a full expansion from fovea to the periphery or a complete clock-wise rotation of the wedge) took 24 s, with 10 repeats collected per scan. For both annuli and wedges, a second scan was collected with a reverse order (i.e., from expansion to contraction, or clockwise to counter-clockwise) to control for the spatiotemporal haemodynamic response function. For all conditions subjects fixated on a central cross which flickered between red and grey.

4.3 Analysis Pipeline Overview

The use of simultaneous EEG-fMRI data for layer analysis is a very new field, thus the methods for analysing and combining these data have necessitated the development of an optimal analysis pipeline which will be outlined in the following sections. Section 4.4 outlines the functional analysis pipeline of the EEG-fMRI data to the eyes open/closed task and associated retinotopic mapping fMRI data. Section 4.6 outlines the definition of cortical layers and columns, whilst Section 4.7 outlines how layer profiles can be generated including the deveining process for GE-BOLD data. These components are illustrated as a schematic overview in Figure 4.6 to show how the structural and functional components are combined together for layer analysis of alpha modulations. Figure 4.7 provides a detailed flow chart with a detailed description of each of the steps in the analysis pipeline and how they feed into one another. In this chapter, the results of optimising each of the individual analysis steps are shown for a single subject to illustrate the development of the processing pipeline. Results for all subjects who took part in the full study are then provided in Chapter 5.

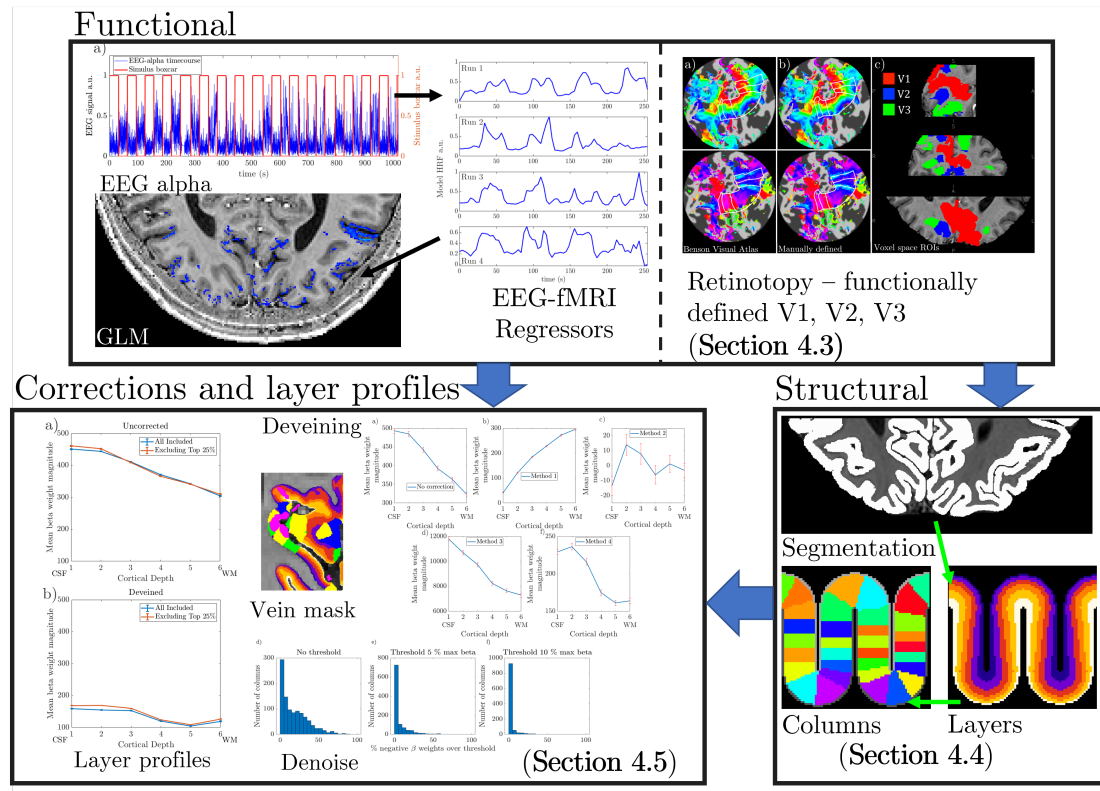


Figure 4.6: A summary of the analysis steps implemented in this chapter for the multiple streams of data. This shows an overview of the combination of the ‘Functional’ simultaneously collected EEG-fMRI data doing an eyes open/closed task and retinotopy fMRI data with the ‘Structural’ data. The functional data then undergoes corrections prior to computing layer profiles.

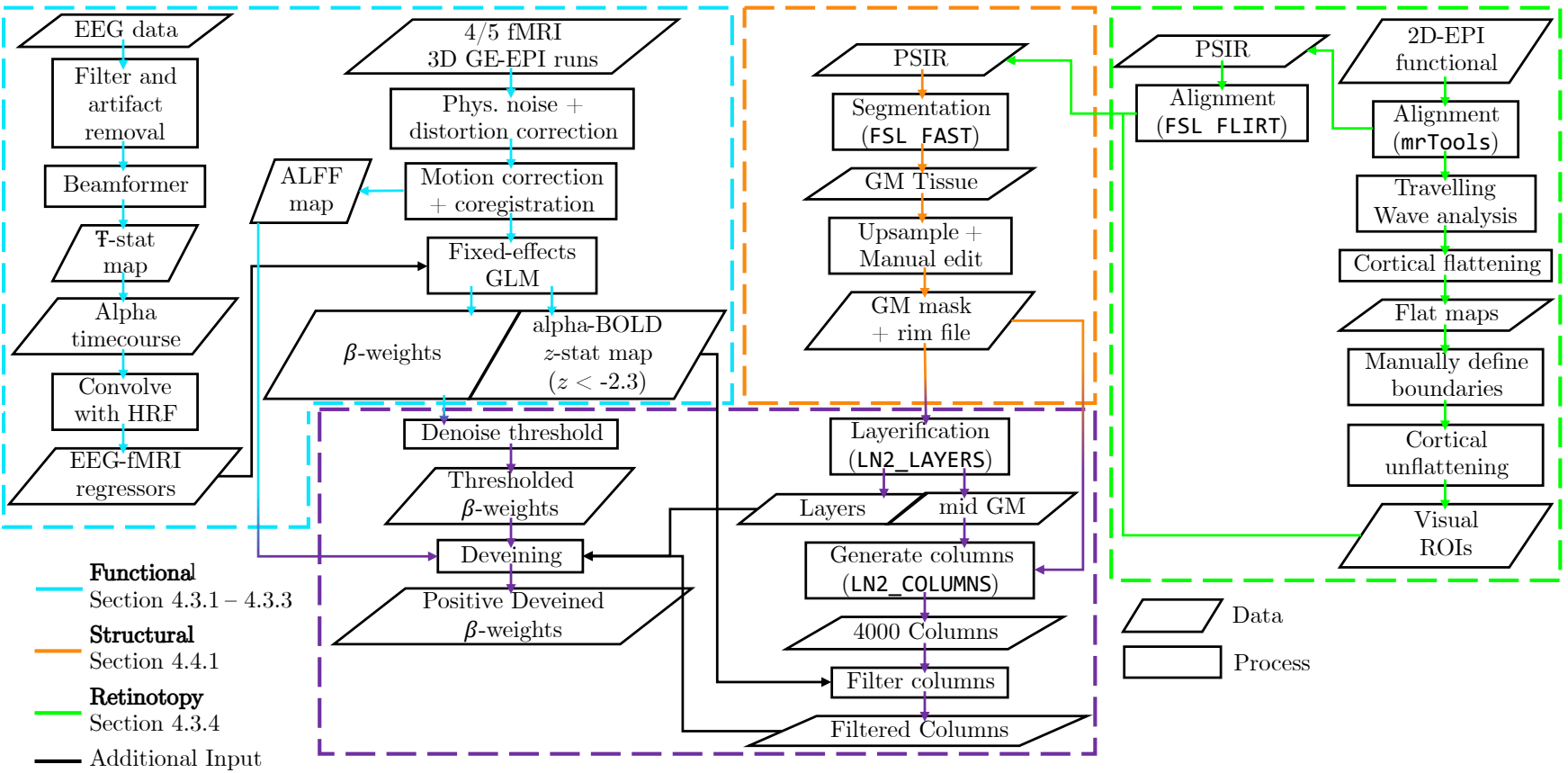


Figure 4.7: Processing pipeline for the analysis of simultaneous layer-dependent EEG-fMRI data.

4.4 Functional Analysis Pipeline

4.4.1 EEG processing

The pre-processing of the raw EEG data was not carried out as part of this PhD, but the ‘cleaned’ EEG data was provided for each subject. In brief, the EEG data was gradient artefact (GA) and pulse artefact (PA) corrected by Dr Rodika Sokoliuk using Brain Vision Analyzer2. Data were then filtered 0.1 – 40 Hz and downsampled to 500 Hz and exported to FieldTrip [144] where all further analysis was performed. Noisy channels were removed and Independent Component Analysis (ICA) was performed on the remaining data, with components corresponding to eye blinks removed. The remaining independent components were back projected to channel space and data were re-referenced to an average of all the non-noisy channels. Data were then filtered into the alpha (8 – 13 Hz) frequency band. Only the alpha frequency band is studied for this simultaneous UHF fMRI-EEG study. This is because the other frequency bands are too noisy to be assessed due to the artefacts introduced in the EEG data due to the UHF MR environment. Higher frequency bands are affected by residual gradient artefacts and the lower bands are affected by pulse and motion artefacts.

Source localisation was performed using a Linear Constraint Minimum Variance (LCMV) beamformer. Pseudo-T-statistic (T-stat) maps showing significant task-related changes between eyes open and eyes closed in oscillatory alpha-power were calculated over the whole head. The location of the maximum change in alpha power between eyes open and eyes closed in the occipital cortex was identified from each subject’s T-stat map (see Figure 4.8) and chosen as the site of the Virtual Electrode (VE). Selecting this peak ensured the maximum signal-to-noise ratio of the alpha-timecourse [145].

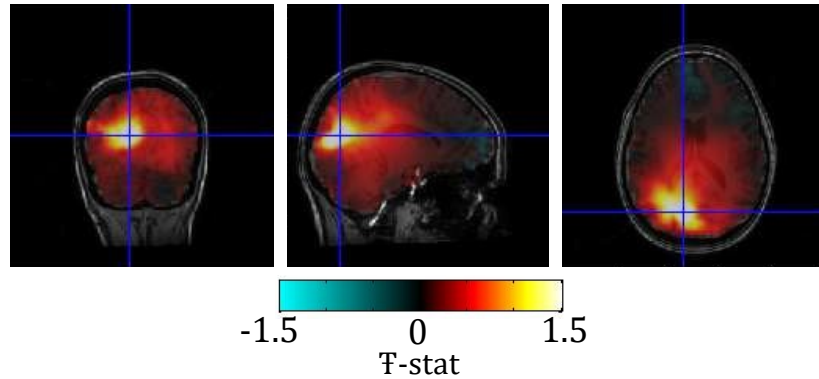


Figure 4.8: Source localisation using an LCMV beamformer for a representative subject (Subject 1) showing maximum change in alpha power between eyes closed and eyes open in the occipital cortex. This was selected as the location for a VE-timecourse of the activity to be extracted for each run.

A VE-timecourse of the alpha activity during the entire experiment was extracted from this location for each run. These VE alpha timecourses were produced for each run and time locked to the beginning of the EPI data acquisition, to be used in the current work. From this point I took the Fast Fourier Transform (FFT) of the EEG timecourse from the peak VE for each run and averaged over runs to assess each subjects alpha power modulation (see Figure 4.9).

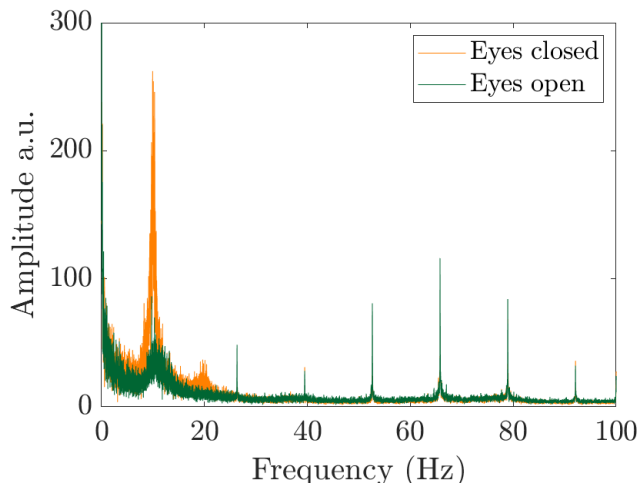


Figure 4.9: FFT of the EEG timecourses extracted from the peak VE for a representative subject (Subject 1). The FFT was determined per run and averaged over runs. Orange shows the measured responses when the eyes were closed and the green overlay shows the eyes open response with diminished alpha power (8 – 13 Hz).

Due to the long volume TR (3.8 s) of the 3D GE-EPI acquisition, the optimal way to produce a model of the EEG fluctuations in the BOLD signal was first investigated. The primary question here was whether to convolve at high temporal resolution and then downsample to the TR of the fMRI data or whether to downsample to the fMRI TR and then convolve with the haemodynamic response function (HRF). To address this the different methods explored were (i) to keep the EEG data at its original sample rate of 500 Hz, or (ii) to downsample to 10 Hz as an intermediate, or (iii) to downsample to the fMRI rate of 0.26 Hz ($1/\text{TR}$), before convolving with a HRF. Figure 4.10 shows the results. It can be seen that downsampling the data prior to convolution leads to a spurious timecourse that is not as well matched to the stimulus timings when compared to a convolution using the 10 Hz and 500 Hz EEG data. The optimal pipeline was found to be when the EEG data were kept at the

original sampling rate of 500 Hz (2 ms) before convolving with the HRF and downsampling to the sampling rate of the fMRI (0.26 Hz = $1/3.8$ s).

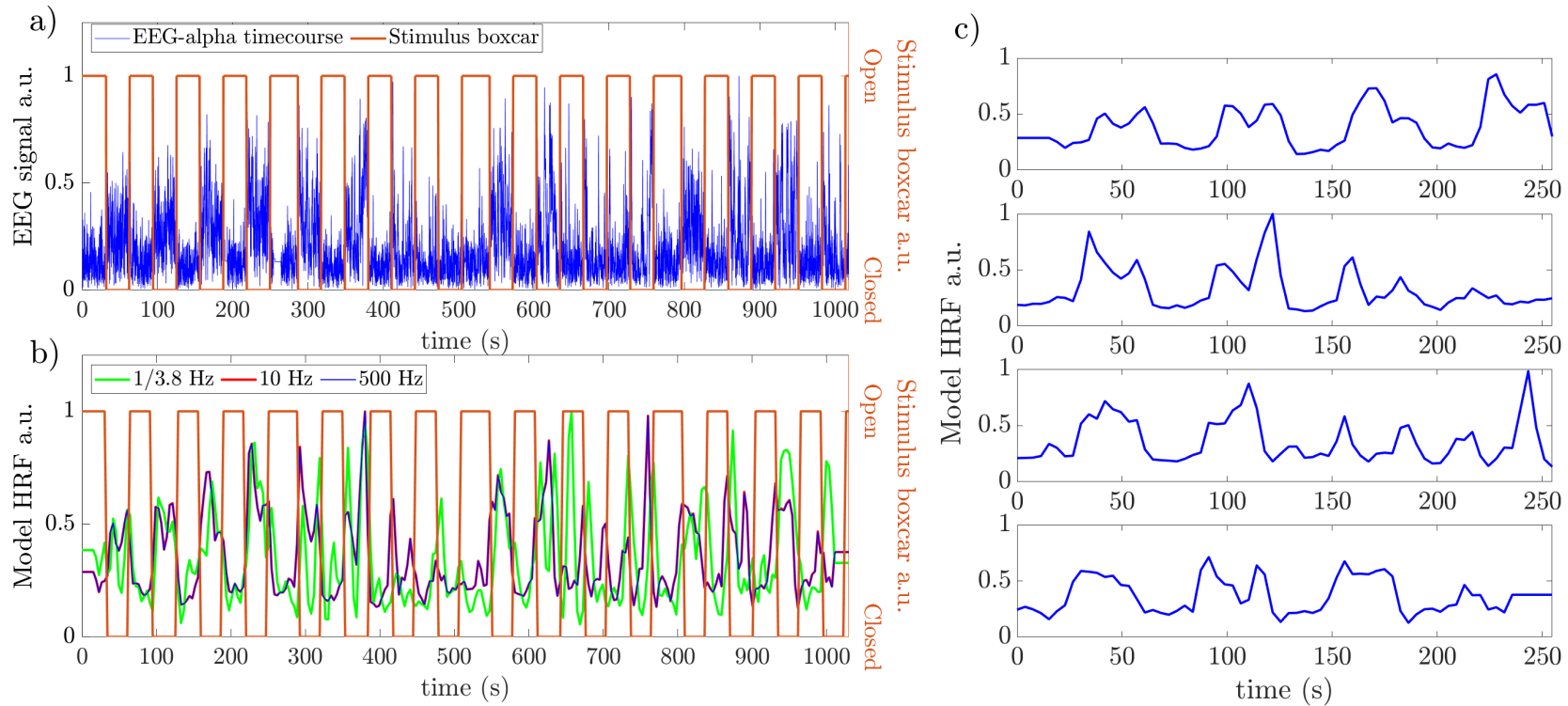


Figure 4.10: Assessment of the optimal method to produce an EEG alpha model for the BOLD GLM. a) EEG alpha power timecourse downsampled to 10 Hz and with all runs concatenated together (blue line). Overlaid in orange are the stimulus timings. b) Comparison of the EEG timecourse at a sampling rate of 500 Hz, 10 Hz or 0.26 Hz after convolution with a HRF and then downsampled to 0.26 Hz ($1/TR$). c) Each run of the ‘eyes open/eyes closed’ task for the model paradigm derived from the pre-processed 500 Hz EEG data convolved with a HRF and then downsampled to the TR of each 3D GE-EPI volume. All data shown for an example subject (Subject 1)

4.4.2 Pre-processing of 3D GE-EPI eyes open/closed data

The 3D-EPI data were first corrected for physiological noise, due to respiratory and cardiac motion, using retrospective image correction (RETROICOR) [112]. Following this, the functional data were corrected for distortions due to B_0 inhomogeneities. Two methods were assessed: 1) non-linear registration correction and 2) B_0 field map based distortion correction.

For the non-linear registration, the 3D GE-EPI data were cropped and the structural PSIR data were cropped and resampled to the 0.8 mm^3 resolution of the 3D GE-EPI data such that they were in matched space (see Figure 4.11). Non-linear registration was performed using FMRIB's Non-linear Image Registration Tool (FNIRT) in FSL [146] registering the 3D GE-EPI data to the second ($\text{TI} = 2280\text{ms}$) image of the PSIR data, with a warp resolution equal to the acquisition resolution (0.8 mm).

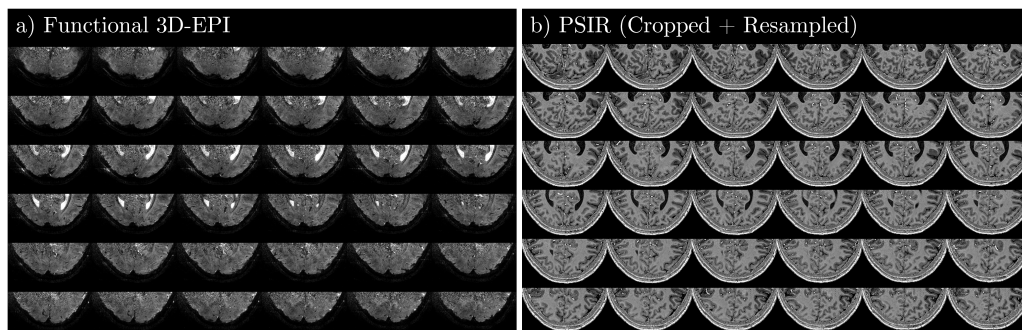


Figure 4.11: The 3D GE-EPI data (a) prior to being B_0 distortion corrected and the PSIR data (b) after being cropped and resampled to match the 3D GE-EPI native space

For distortion correction, the B_0 field maps were resampled and cropped to the same spatial resolution and field of view as the 3D GE-EPI data (see Figure 4.12). These data were then used to perform B_0 distortion correction using fMRIB's Utility for Geometrically Unwarping EPIs (FUGUE) in FSL. The distortion correction shifts the voxels in the image to correct for the frequency

change in the data due to magnetic field inhomogeneities. This processing involved first creating a skull-stripped brain mask of the modulus of the field map and applying this to the phase of the field map, converting the phase map to radians, and applying the field map to correct the EPI mean image using FUGUE. For this data, the water-fat-shift was 61.4 in pixels resulting in an echo spacing of 1.71 ms which is converted to an effective echo spacing taking account of the parallel imaging SENSE factors. The warp field was saved for application to the functional 3D GE-EPI data.

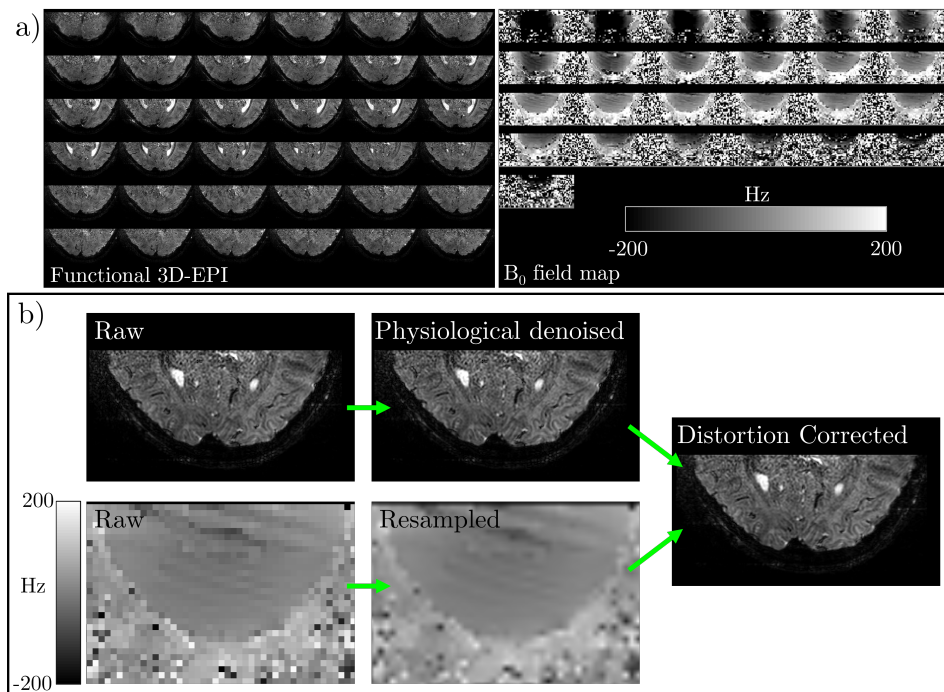


Figure 4.12: a) multiple axial slices of the unprocessed 3D GE-EPI (left panel) and multiple axial slices of the B_0 field map (right panel). b) The pathway from unprocessed 3D GE-EPI image to distortion corrected 3D GE-EPI image shown for a single slice. The top middle panel of b) shows the 3D GE-EPI after physiological noise has been removed using RETROICOR. The bottom panel of b) shows the B_0 map (in Hz) after being resampled and cropped to match the 3D GE-EPI data. The right panel shows the 3D GE-EPI data after distortion correction using FUGUE (FSL).

To assess which method was optimal, the resultant distortion corrected images were overlaid on the PSIR image for visual assessment. In addition, the non-linear FNIRT registration warp field and the B_0 distortion correction warp were each applied to an ‘activation map’ following GLM analysis (Section 4.4.3.1). The overlap of each warped activation map with a GM mask of the PSIR was calculated. It was found that qualitatively visual inspection of the B_0 field map corrected data resulted in a more optimal match. Quantitatively the B_0 distortion corrected activation had 75.5% overlap with a GM mask and the non-linear registration had 71.8% overlap. Therefore B_0 distortion correction was the chosen method.

Next, motion correction of the multiple fMRI 3D GE-EPI runs was performed using linear registration methods. The motion transformation matrices were calculated in FSL (Motion Correction using FMRIB’s Linear Image Registration Tool (MCFLIRT) and FMRIB’s Linear Image Registration Tool (FLIRT)) for within each fMRI run and also between each fMRI run, such that each volume could be aligned to the central dynamic of the entire session. These matrices were then concatenated (FSL, `convert_xfm`) and applied to each of the datasets using spline interpolation which minimised blurring. By applying a single transformation matrix the effects of spatial blurring were minimised as shown in Figure 4.13.

Having now distortion-corrected and aligned the datasets to the same native space whilst maintaining the spatial resolution, next the functional BOLD response was modelled.

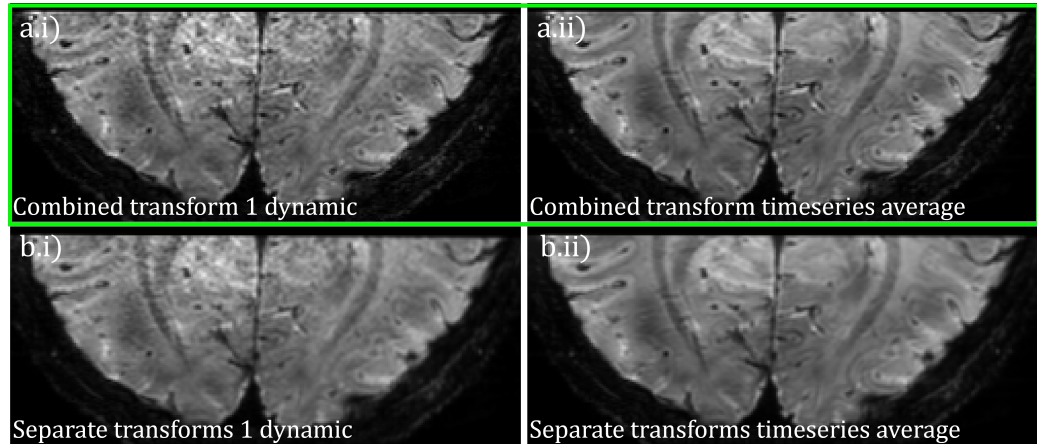


Figure 4.13: Comparison of the methods for the motion correction within and between runs of the functional 3D GE-EPI data. a) Applying within and between motion correction in one step using a combined transformation matrix with spline interpolation shown for a single slice of i) a single dynamic and ii) the average across all runs. b) Applying within and between motion correction separately using multiple transformation matrices with the default tri-linear interpolation shown for a single slice of i) a single dynamic and ii) the average across all runs. Note the increased blurring for b (ii) compared to a (ii).

4.4.3 Defining the EEG/fMRI General Linear Model

A model of the BOLD response was created using the EEG timecourse as described in Section 4.4.1. At the first-level, for each run, the main effect of the EEG alpha response regressor and motion parameters as regressors of no interest were modelled in a GLM (FSL, fMRI Expert Analysis Tool (FEAT)). For each subject the average response was calculated across all runs using a second-level fixed-effects analysis to produce the z -stat map across all runs per subject. Since alpha oscillations are known to correlate negatively with the BOLD response [103], a threshold of $z < -2.3$ was applied to all z -stats and cluster correction ($p < 0.05$) performed. Voxels with large negative z -stats ($z < -2.3$) indicate an area with high alpha-modulation to the task. In preparation for the layer

analysis (see Section 4.6.1), the z -stat maps were then up-sampled to 0.175 mm isotropic resolution using nearest neighbour resampling (FSL).

4.4.3.1 Combining EEG and fMRI

Figure 4.14 shows the results of using the GLM analysis to model the EEG alpha power for Subject 1. Only the negative z -stats are shown with a threshold of $z > -2.3$ since alpha oscillations negatively correlate with the BOLD response. The threshold z -stat maps formed from second level analysis in FEAT across all runs are shown overlaid on to the subjects PSIR image. It can be seen that the areas with high correlation to the alpha BOLD timecourse are localised to the visual cortex and are spatially specific to the grey matter.

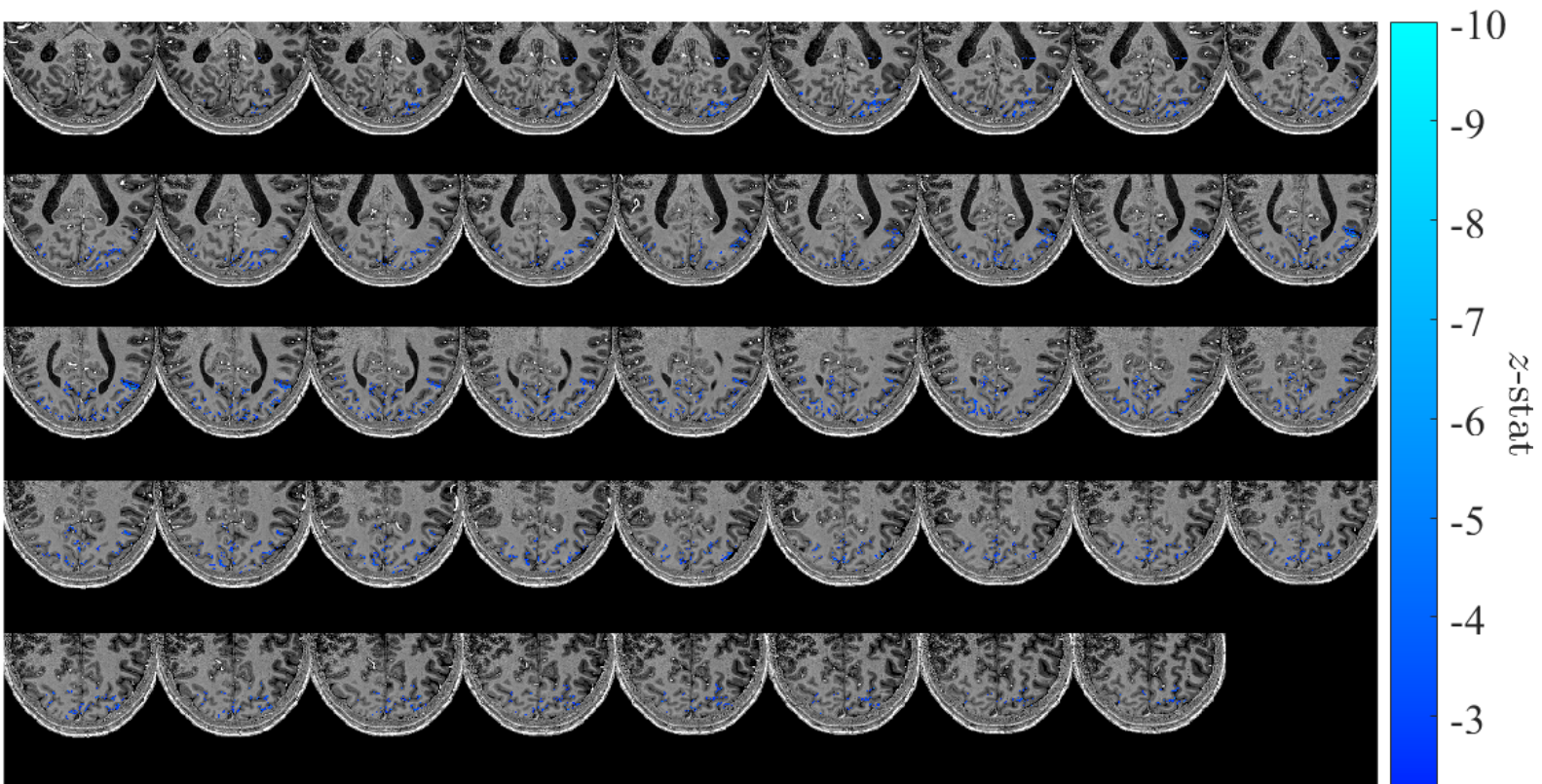


Figure 4.14: Overlay of the GLM of the EEG alpha response convolved with a double gamma HRF. The z -stat map is thresholded at $z < -2.3$ and overlaid on the PSIR image, this is shown for a single subject (Subject 1). The responses can be seen to map onto the grey matter.

4.4.4 Retinotopic Mapping to define visual boundaries

The visual retinotopic mapping dataset [147] acquired in Session 2 (see Figure 4.4) was used to provide functional boundaries of V1, V2, and V3 in the visual cortex necessary to define ROIs for the EEG-fMRI dataset. First, each of the four retinotopic runs were individually motion corrected and then coregistered to the second run (FSL, MCFLIRT & FLIRT). The 0.7 mm isotropic whole head PSIR collected in this scan session was down-sampled to 1 mm³ and input into Freesurfer [136, 148] to calculate the GM, WM and CSF surfaces. The 1 mm³ PSIR and functional retinotopic data were then loaded into mrTools [143] and aligned (using mrAlign) before performing a travelling wave analysis [149] to produce retinotopic phase maps of the cortical surface.

The data from the two retinotopic paradigms: the rotating wedges and the expanding/contracting annuli, were analysed to map visual polar angle and eccentricity, respectively. First, scans from both the clockwise and counter-clockwise condition were shifted by two frames, then the order of the volumes of the scans from the counter-clockwise condition were reversed prior to averaging with the scans from the clockwise condition. This reversal and shift was used to cancel out the effects from the spatiotemporal HRF (See Figure 4.15). Following this averaging, the time series at each point was correlated with a cosine function with a frequency that matched the stimulus delivery. This analysis provides a correlation — which indicates model fit, and a phase angle — which corresponds to the phase of the stimulus presentation and thus visual polar angle. Voxels that survived a correlation threshold of 0.4 were analysed to map their phase.

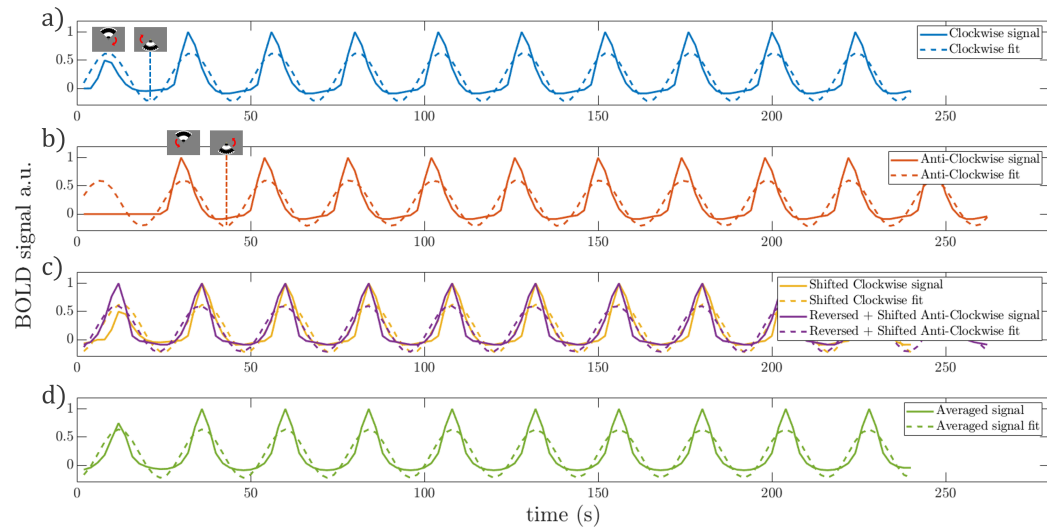


Figure 4.15: Schematic to show the shift and reversal of the retinotopic mapping data to align with the timings of the stimulus and account for the haemodynamic lag. a) The modelled timecourse of the BOLD signal during the clockwise stimulus for a single voxel in the brain with a sinusoidal fit overlaid (dashed). b) The modelled timecourse of the BOLD signal during the anti-clockwise stimulus for the same voxel as in a) with a sinusoidal fit overlaid (dashed). c) The BOLD timecourse from a) (yellow) after being shifted by 2 TRs and b) (purple) after being shifted by 2 TRs and temporally reversed. Overlaid are the sinusoidal fits for both timecourses (dashed). d) Shows the average of the BOLD timecourses from c) with a sinusoidal fit overlaid (dashed). This final timecourse was used to calculate the phase and correlation of the voxel location compared to a cosine function.

The GM and WM surfaces were imported into mrTools. The phase, eccentricity and correlation results from the travelling wave analysis were overlaid onto the surface of the brain. An area of high correlation near the calcarine sulcus is selected (middle panel of Figure 4.16) and a circular area of the cortex surrounding this point is flattened to create a cortical flat patch (right panel of Figure 4.16). The correlation and phase maps from the travelling wave analysis can be overlaid on the cortical flat patch.

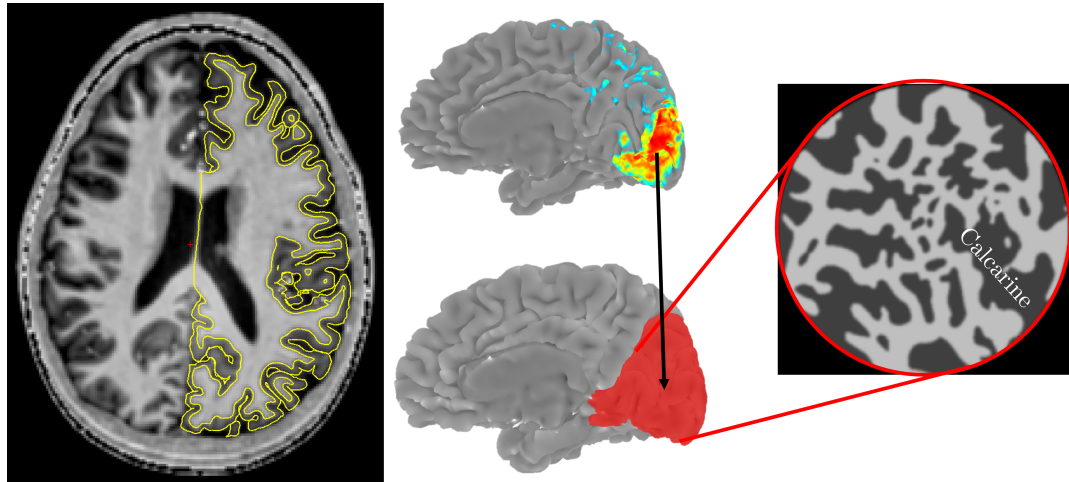


Figure 4.16: Cortical flattening using the GM and WM surfaces from Freesurfer and selecting an area around the calcarine sulcus. A cortical flat patch is created for the definition of ROIs for V1, V2 and V3.

Half of the visual hemifield contained phases that ranged from $[0, \pi]$ whereas the other half ranged from $[\pi, 2\pi]$. Boundaries where the phase reverses denote the border of visual areas [150, 151]. A similar procedure was repeated for the annuli paradigm.

Since the phase reversal is not always clearly defined it was advantageous to be guided by an atlas of where the V1, V2 and V3 boundaries were expected. The Benson atlas [109] is an atlas of the visual areas generated using Bayesian mapping. This was imported into mrTools [143] (Figure 4.17) and used to aid the manual definition of V1, V2 and V3 ROIs for each of the subjects.

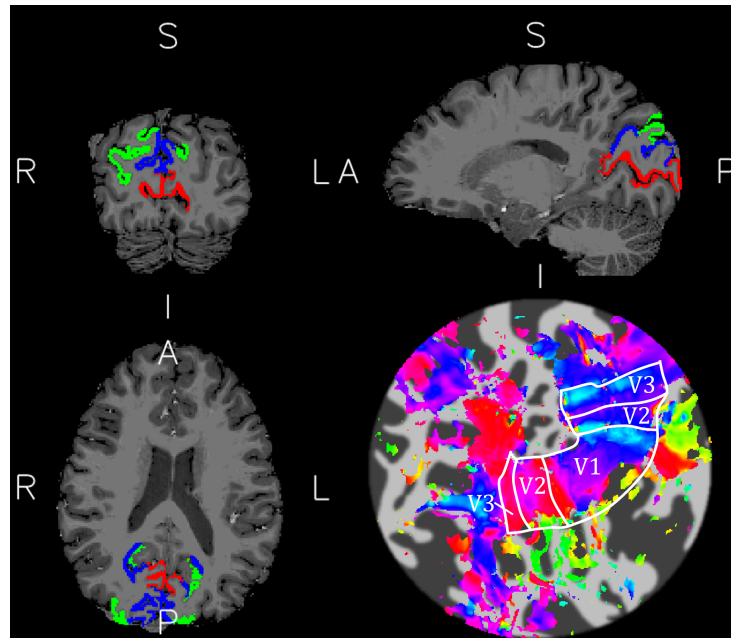


Figure 4.17: The Benson atlas in voxel space (Top left, Top right and Bottom Right) showing V1 (Red), V2 (Blue) and V3 (Green). Retinotopic phase map from Subject 1 overlaid onto a cortical flatpatch with the Benson atlas V1, V2 and V3 ROIs shown overlaid as white ROIs (bottom right).

Comparing the boundaries denoted in Figure 4.17, which shows the Benson boundaries, and Figure 4.18, which shows the manual defined boundaries, there are clear differences between boundaries for this subject due to individual subject anatomical variation. This illustrates the need to use manual individual subject boundaries and use the Benson atlas as a guide only.

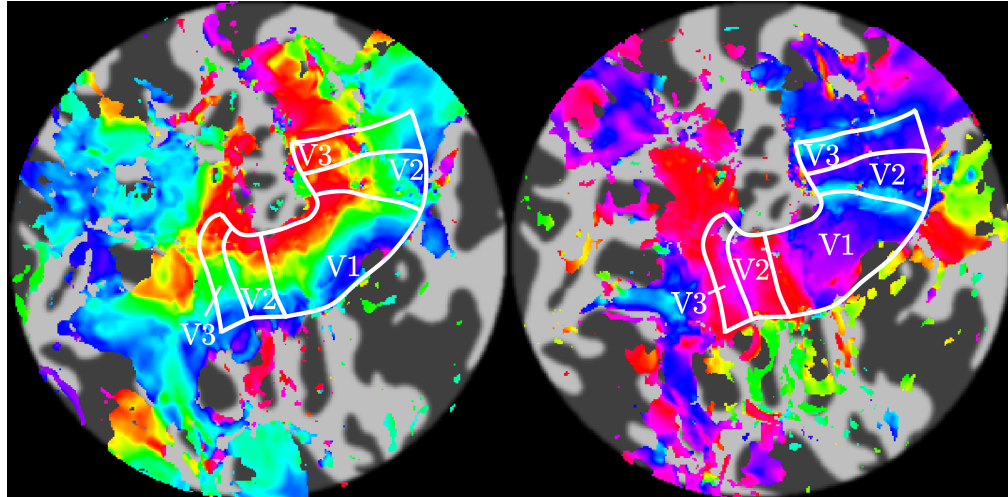


Figure 4.18: Results of retinotopic mapping for a single subject showing the phase flat map (right) from the expanding/contracting rings stimulus, and the phase flat map for rotating wedges stimulus (right). The manually defined V1, V2 and V3 and boundaries are labelled in white.

Once the ROIs had been defined, the 1 mm^3 whole head PSIR from scan session 2 was then registered to the partial head PSIR from the EEG-fMRI scan session 1 (FSL, FLIRT). The transformation matrix from this registration was then applied to the ROIs from the retinotopic mapping, thus moving the maps of V1, V2, and V3 into native EEG-fMRI space. ROIs had a threshold applied to counteract the smoothing due to the registration and were viewed in FSLeyes [146] with manual correction applied to account for overlaps between V1, V2 or V3. The final ROIs of visual areas V1, V2 and V3 were then upsampled to 0.175 mm to allow for layer analysis to be performed on the data.

Figure 4.19 shows the retinotopic mapping definitions of visual areas V1, V2 and V3 for Subject 1.

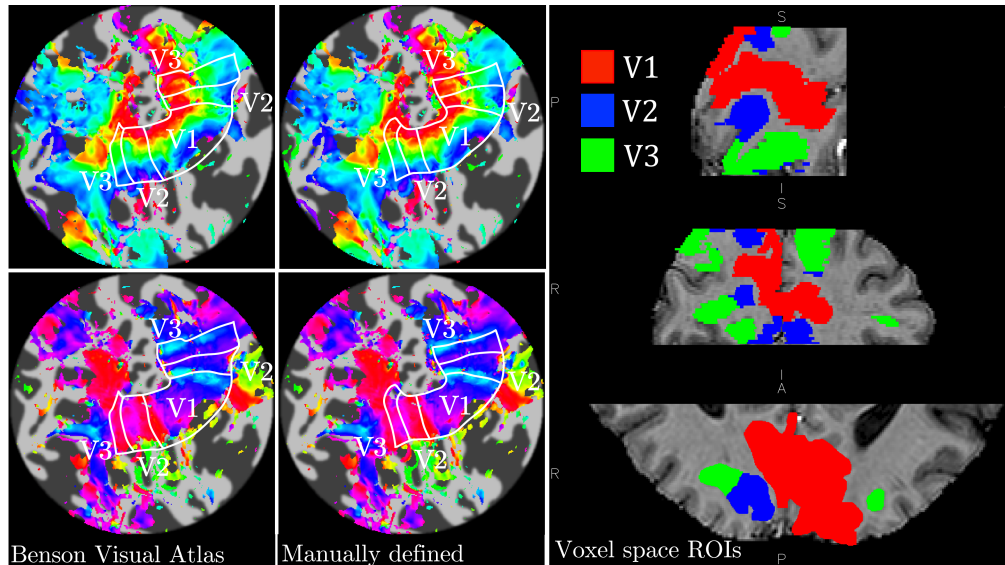


Figure 4.19: a) The Benson atlas V1, V2 and V3 ROIs overlaid on the flat patch for a single subject, b) The subject specific boundary definitions for V1, V2 and V3, informed by the Benson ROIs. The top of a) and b) shows the eccentricity which indicates the extent of the visual region. The bottom images of a) and b) show the polar angle of the visual field, where cycles in phase indicate the boundaries of the visual regions. c) The final V1, V2 and V3 ROIs in voxel space having been transformed to the 0.8 mm isotropic partial head PSIR from the EEG-fMRI session.

4.5 Interrogating the fMRI timecourse

To consider a model free approach to assess alpha-BOLD correlations the mean timecourses from V1, V2 and V3 were calculated. The V1, V2 and V3 ROI masks were used to select the voxels from the fMRI data and the mean calculated in MATLAB.

In addition, the z -stat maps from the second level fixed effects GLM were used to calculate the mean timecourse of all significant negatively ($z < -2.3$) and positively ($z > 2.3$) correlated voxels using the same method. To consider inter trial variability, the EEG alpha power regressors were compared to the

fMRI response for each eyes open/closed period. The EEG regressors along with the mean BOLD response in a region was split into a ~ 65 s time period defined by the eyes open/closed task. The regressor and BOLD ‘responses’ were then ranked from largest to smallest. The largest response was defined as the largest range in the data calculated by taking the difference between the average of the maximum value and its neighbouring values and the minimum value and its neighbouring values. The range of each fMRI response was then plotted against the range of the EEG response in the corresponding period. A line of best fit was determined using a linear regression.

4.6 Defining Cortical Layers and Columns

4.6.1 Cortical Layers

The partial head PSIR data from scan session 1, comprising of magnitude and phase images at two delays ($TI = 780$ ms/ $TI = 2280$ ms), were combined to form a field-bias corrected PSIR image [141] (as shown in Figure 4.20 step 2). Brain extraction tools have generally been optimised for use on whole brain datasets (FSL Brain Extraction Tool (BET), Freesurfer `reconall`), this was not the case for the session 1 PSIR data. To extract the brain from the partial head PSIR the optimal method was to take the magnitude image acquired at $TI = 2280$ ms from the PSIR dataset and skull strip using BET2 in FSL [146]. The resultant image then underwent two erosion iterations using FSL, and was viewed in FSLEyes and any manual correction of the brain mask performed (as shown in Figure 4.20 step 3).

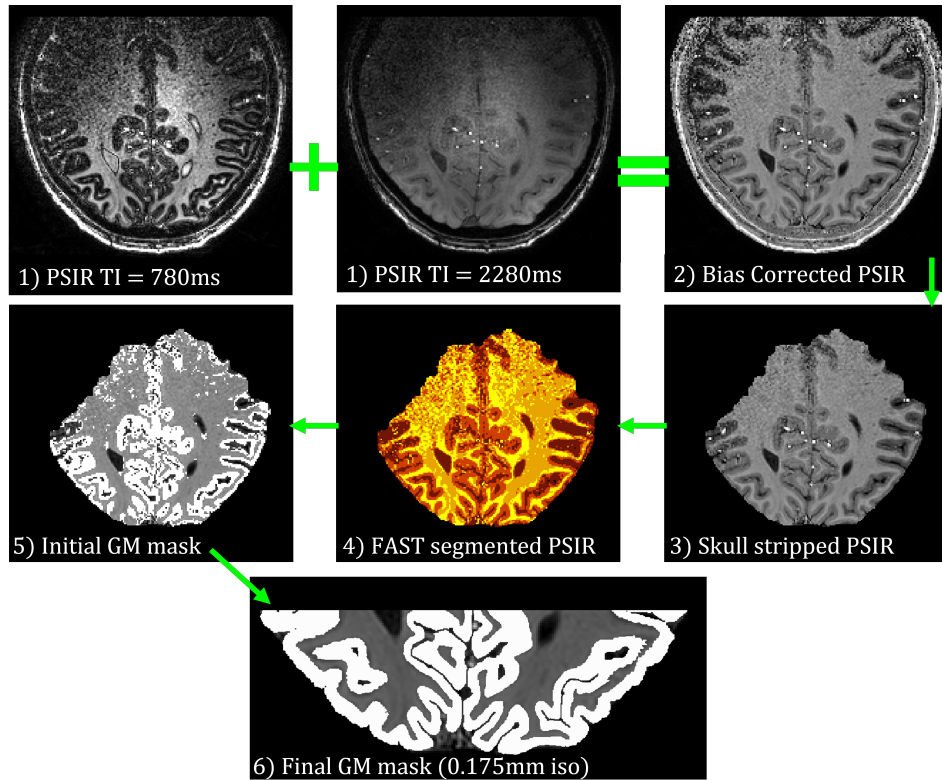


Figure 4.20: Analysis of the partial head PSIR data to create a high resolution GM mask for cortical layer modelling. 2) shows the combination of the 1) PSIR data at $TI = 780$ ms and $TI = 2280$ ms to form the bias field corrected PSIR. The data is then 3) skull stripped, 4) tissue segmented using FSL FAST and 5) the GM mask is upsampled to 0.175 mm in-plane, 0.8 mm through-plane and manually edited to form 6) the final GM mask cropped and upsampled to 0.175 mm isotropic resolution.

This skull stripped partial PSIR image was then segmented into four tissue types (FSL, FMRIB’s Automated Segmentation Tool (FAST) [146]), and a grey matter (GM) binary mask was created from the Partial Volume Estimation (PVE) GM map (as shown in Figure 4.20 steps 4 & 5). The skull stripped partial PSIR image and GM binary mask image were then cropped and resampled to match the field of view (FOV) and resolution of the 3D GE-EPI fMRI data. The GM mask was upsampled to an in-plane resolution of 0.175 mm so that multiple

voxels could be allocated to each layer across the cortex; the slice thickness remained at 0.8 mm to reduce the number of slices to be manually corrected. The slice thickness was later upsampled to 0.175 mm for layer modelling. The GM mask was viewed in FSLEyes and manually corrected within the V1, V2 and V3 ROIs (defined from retinotopic mapping) to create smooth GM boundaries and reallocate any voxels that were mislabelled due to noise/signal drop off of the surface coil (shown in Figure 4.20 step 6). Veins were manually removed from the mask whenever they were visually obvious in the PSIR data (defined to be areas of high intensity). A labelled mask was then created (values of CSF = 1, WM = 2, GM = 3) by visually inspecting the GM mask and filling areas of cerebral spinal fluid (CSF) and white matter (WM). The labelled mask was upsampled to 0.175 mm isotropic resolution and used to define six layers across the cortex (LayNii v2.0.0 [152]). There are other software libraries such as Freesurfer that can be used for layer modelling however these require whole head acquisitions with a continuous GM surface. LayNii is able to generate layers from partial head GM masks.

Two definitions of layers, equidistant and equivolume, were implemented in LayNii. Figure 4.21 shows examples of the original cortical layer model [153] alongside the equidistant and equivolume implementations in LayNii [152]. The equidistant model produces cortical laminae that maintain a constant distance from the WM/GM boundary and the CSF/GM boundary (Figure 4.21b). To improve upon this, the equivolume model produces layers that maintain a constant columnar volume throughout the cortical ribbon (Figure 4.21c) [154]. This results in layers that are thick in areas of high curvature and thin in areas of low curvature, showing better agreement with layers defined using histological samples.

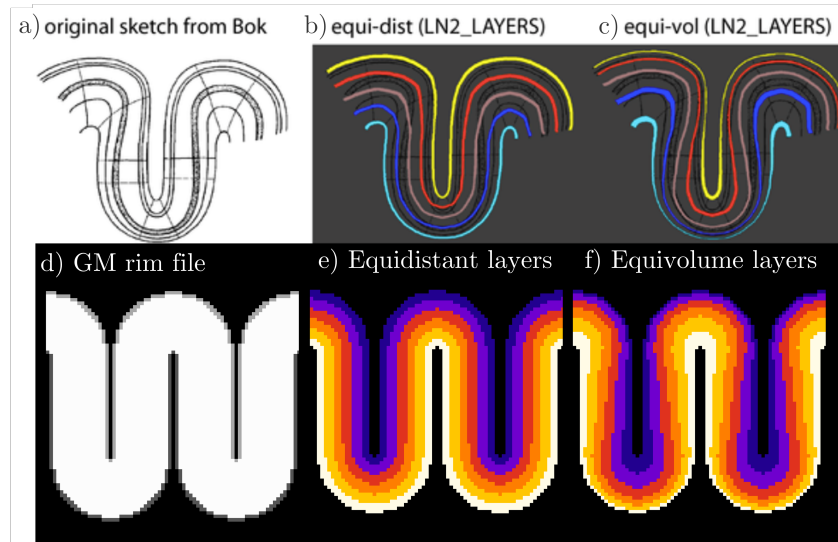


Figure 4.21: Model section of a cortical ribbon, showing a) the original description by Sigfried Thomas [153], and the differences between the b) equidistant and c) equivolume modelling alongside d) the GM rim file used to generate layers in LayNii. From this in LayNii the e) six equidistant layers and f) six equivolume layers generated. Adapted from [155]

4.6.2 Cortical Columns

For the purpose of fMRI layer analysis, cortical columns are defined as small parcellations that lie perpendicular to the cortical surface which are not based on any anatomical structures [156, 157]. These columns will be used in subsequent analysis to correct for the bias of the BOLD signal to the pial surface [75].

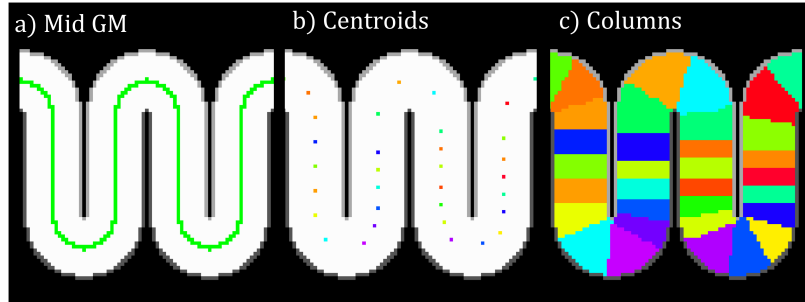


Figure 4.22: A model section of a cortical ribbon, a) The ‘mid GM’ output from LayNii used to seed the centroids for column generation. b) The N centroids in equally spaced locations along the ‘mid GM’ to produce N columns. c) The final columns generated using Voronoi diagramming [158].

The number of cortical columns were calculated based on the assumption that the columns are cylindrical with volume $h\pi r^2$, with height h corresponding to the average cortical depth, estimated to be 2 – 3 mm [69]. The mean column diameter was chosen to be in the range 0.8 – 1 mm, therefore requiring 20,000 columns to be calculated across the GM within the field of view of the 3D GE-EPI functional data collected in the EEG-fMRI scan session. The LayNii layering algorithm outputs the mid-GM voxels, which are used as a seed to calculate cortical columns. The mid-GM voxels are divided into centroids, one for each required column. Each centroid is grown into a full column using Voronoi diagramming [158]. Once the columns were generated they were filtered to contain only those that lay entirely within V1, V2 or V3. These columns were taken forward and refined (see Section 4.6.3) to define the final ROI for each subject. This was the initial number of columns defined, based on the definition of cortical columns originally posed by Mountcastle *et al.* However, it was necessary to optimise this number of columns for analysis later, see Section 4.6.5.

4.6.3 Columnar and Layer Analysis

Columns were filtered so that only those containing significant negative activation ($z < -2.3$) remained. Figure 4.23 shows a schematic to illustrate how columns were chosen to be included or excluded in further analysis. Crucially, in contrast to previous studies, the activation of the whole column, rather than just those voxels which contained $z < -2.3$ [159, 160], were included for further analysis. This was chosen as all layers within a column contribute to the draining vein effect.

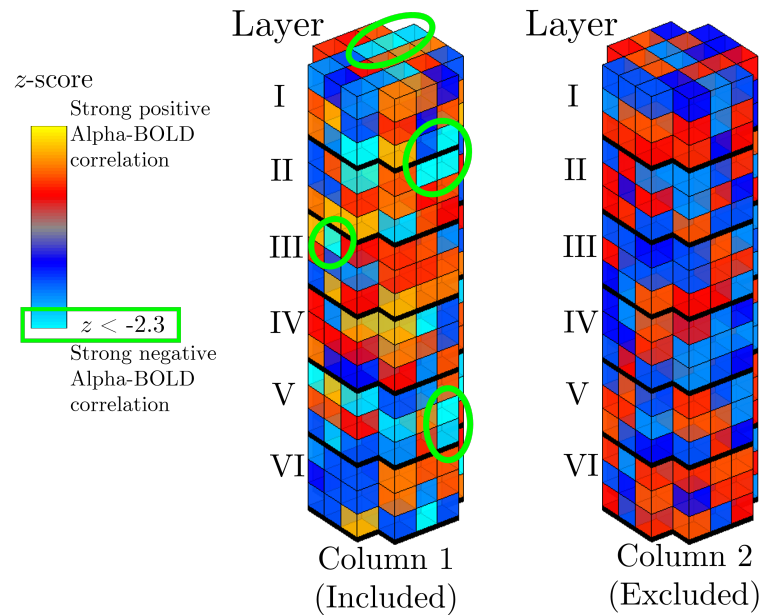


Figure 4.23: Schematic showing two example columns. Column 1 contains multiple voxels that have a significant negative alpha-BOLD correlation ($z < -2.3$ shown in light blue) whereas Column 2 has no significant negative alpha-BOLD correlations.

From this point on, when interrogating the data, the raw GLM β -weights are used instead of the z -stat map, with large positive β -weights corresponding to the strongest negative correlation between EEG alpha power and the BOLD response. The percentage of positive and negative β -weights within each column

was assessed. Since the whole column is in our analysis, it was important to exclude voxels within the column where the β -weights were likely to be dominated by noise, rather than brain activity. Section 4.6.4 outlines the method followed to assess exclusion of voxels from columns which are likely to reflect noise.

4.6.4 Determining a Noise Threshold for the β -weights

Noise is defined as a voxel within a column with a low amplitude β -weight. This definition arises as such a voxel is unlikely to be responding to the neuronal alpha signal of interest and to contribute to the pial draining vein effect which needs to be corrected for in GE-EPI BOLD. Therefore, the working hypothesis is that these noisy voxels should be excluded from the process of correcting the draining vein effect (outlined in Section 4.7). Three thresholds were assessed: i) no threshold, ii) 5% threshold of the absolute maximum β -weight ($\max |\beta|$) and iii) 10% threshold of the absolute maximum β -weight across all the remaining columns. Any β -weights that had a magnitude lower than this threshold were set to Not a Number (NaN) and therefore did not contribute to any further layer analyses. Figure 4.24 illustrates this process.

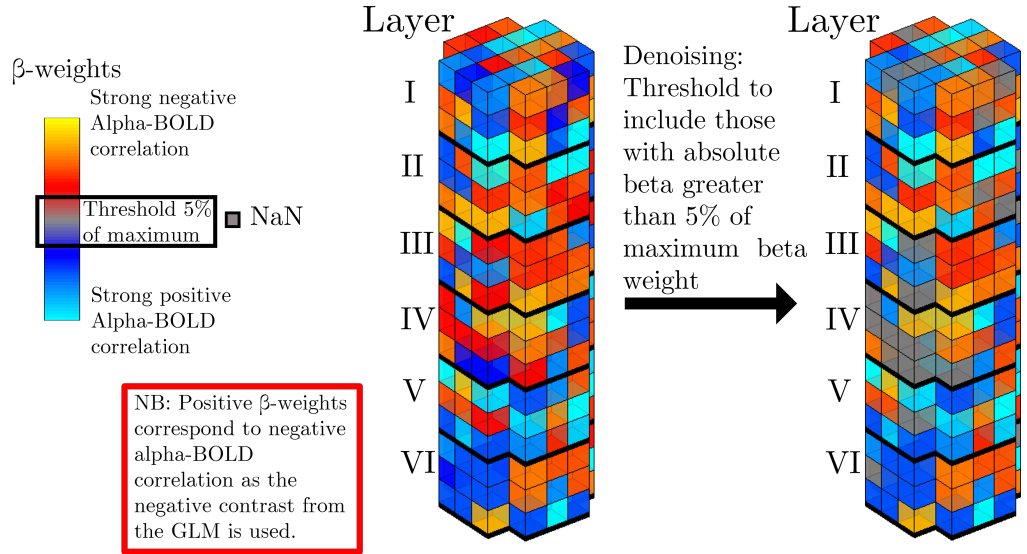


Figure 4.24: Schematic showing the application of a 5% threshold of the maximum absolute β to all the voxels in a column.

Figure 4.25 presents example histograms showing the composition of the a) positive β -weights (corresponding to negative z -stats) and b) negative β -weights (corresponding to positive z -stats) within each of the columns on applying the different noise thresholds (i, ii, iii). When (i) no noise threshold is applied, but the columns have been selected to contain at least one voxel with a significant ($z < -2.3$) positive β -weight, it can be seen that there are far more columns that contain a high percentage of positive β -weights than negative β -weights. However, there are still a large number of columns that contain 20 – 50% negative β -weights, as a column may contain a small cluster of significant positive β -weights with the majority of voxels having negative β -weights. On applying (ii) a threshold of 5% of the maximum β -weight over all the columns, the number of columns containing 20 – 50% negative β -weights is greatly reduced (Figure 4.25b.ii), suggesting these β -weights are likely to be noise. Whilst, the number of columns with a high percentage of positive β -weights remains high (Figure 4.25a.ii) on applying threshold (ii). On increasing the threshold to (iii) 10% of the maximum β -weight, nearly all of the columns contain 0 – 5% negative

β -weights above the threshold (Figure 4.25b.iii), however the number of columns with a high percentage of positive β -weights above the threshold has greatly reduced (Figure 4.25a.iii). This behaviour was seen across all nine subjects, see Appendix A.1. Therefore, a 5% threshold of the maximum β -weight over all columns, was used going forward to exclude those voxels which were believed to only be dominated by noise.

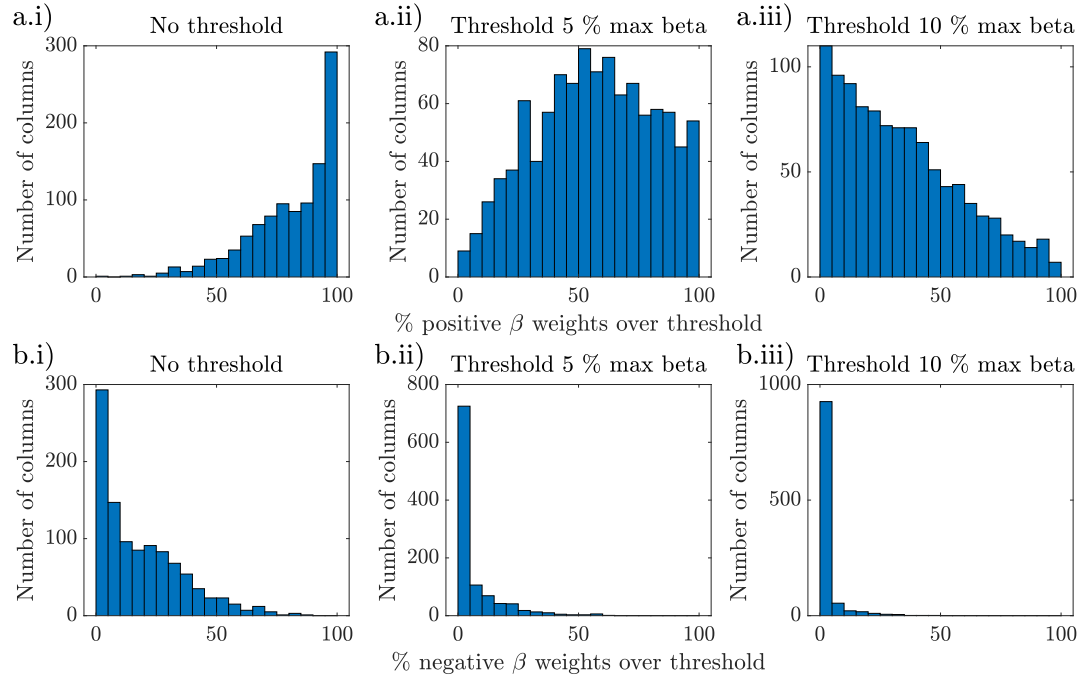


Figure 4.25: Histograms showing the percentage of (a) positive β -weight voxels, and (b) negative β -weight voxels across the three thresholding methods.

In addition to examining the composition of the β -weights within each column, the percentage of voxels that fell below the 5% of the maximum β -weight threshold within each of the six cortical layers was also assessed. Figure 4.26 shows that, as expected, for positive β -weights (a) there is a lower percentage of voxels that are below the threshold in the superficial layers than in the deeper layers. In comparison, there is a fairly uniform percentage across the layers of negative β -weights below the threshold (b). Also note the greater percentage of negative β -weight voxels that are below the threshold than positive

β -weight voxels in all layers. Similar patterns were seen across all nine subjects (see Appendix A.1). This provides further justification for the choice of the 5% of maximum β -weight threshold to exclude noisy β -weights.

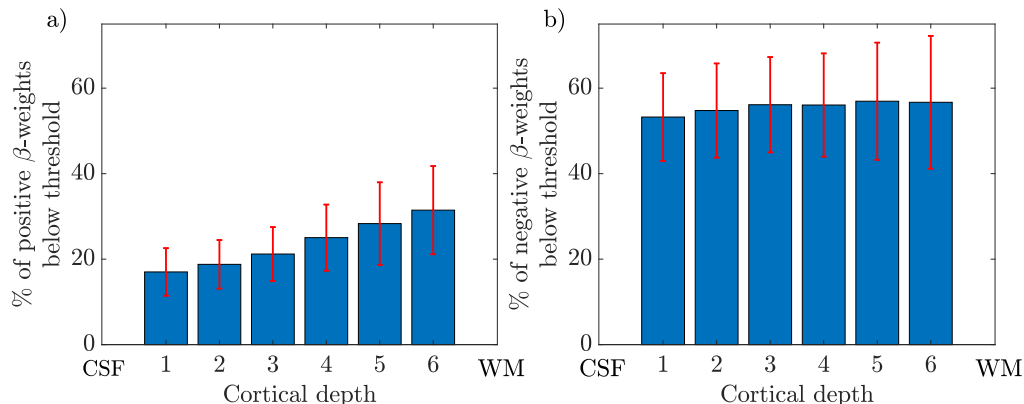


Figure 4.26: The distribution of β -weights below the 5% threshold for a) positive β -weights and negative b) β -weights across cortical depths. Error bars show the standard error on the mean across subjects.

4.6.5 Column size

Next, the impact of the numbers of columns was assessed on the layer analysis pipeline. Here, the main question was to determine the impact of the β -weights in each layer of each column on processing performed to remove draining vein effects. As described in Section 4.6.2, the column size was originally chosen such that when considered as a cylinder the diameter would be ~ 0.8 mm for columns with heights matching the GM cortical thickness of 2 – 3 mm. But with such small columns and a 5% noise threshold implemented (Section 4.6.4), it was possible for some columns to have layers that contain no β -weights. This is shown for a single subject in Figure 4.27. Over 40% of columns have no β -weights at cortical depth six which would have an impact on later analysis steps as corrections of the more superficial depths are dependent on the preceding deeper depths (see Section 4.7).

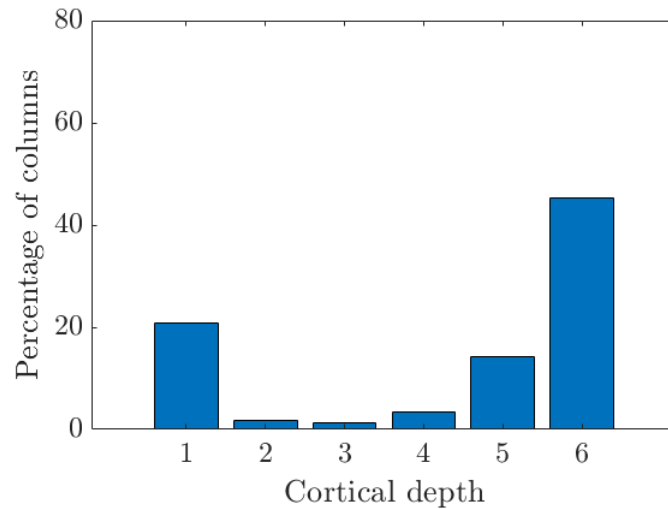


Figure 4.27: Percentage of columns with layers containing no β -weights after the 5% threshold has been applied within V1 for a single subject. This was calculated using the original 20,000 column size.

Therefore a range of numbers of columns were generated, from 4,000 to 20,000 columns, and the percentage of ‘full columns’ were calculated. A ‘full column’ was defined as a column containing β -weights in all six cortical layers.

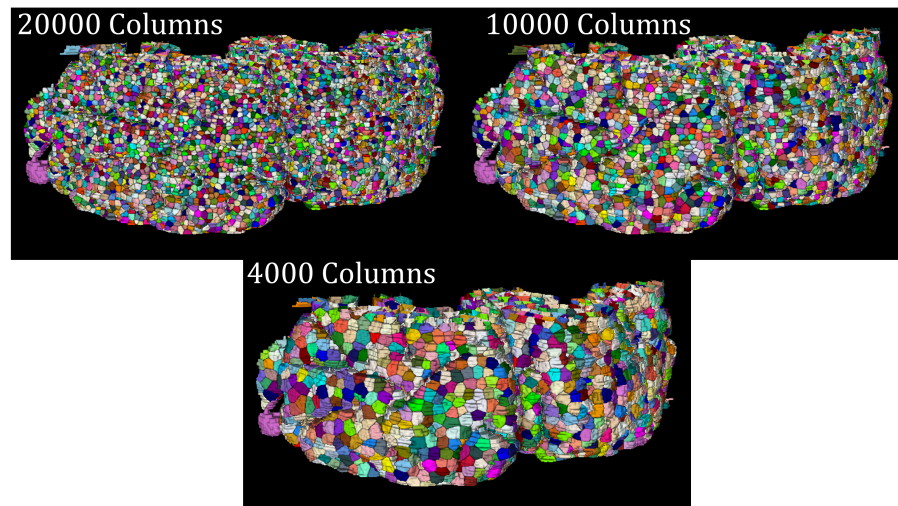


Figure 4.28: Volume view to show the difference in column size when different numbers of 20,000, 10,000 and 4,000 columns are generated across the GM ribbon.

Figure 4.29 shows, as expected, that the larger the columns (hence a smaller number of columns) the higher percentage of full columns. There is a slight reduction in the number of columns that have a value in every layer when only the positive β -weights are selected (right) for the layer profile calculation. Regardless of which β -weights are selected, the larger columns gave the best chance of having β -weights in every layer. Therefore the effect of the column size was taken forward into the future analysis steps for further investigation (see Section 4.7.3.1).

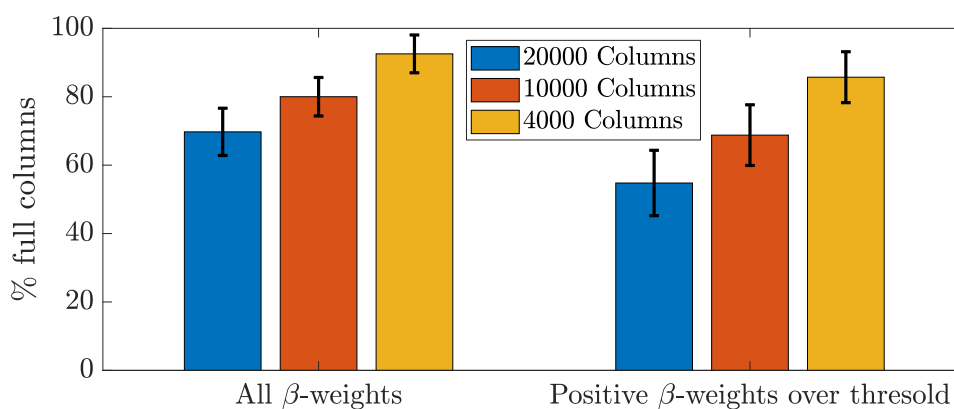


Figure 4.29: Percentage of ‘full columns’ for 4,000, 10,000 and 20,000 columns. This is shown at two stages in the analysis pipeline ‘All β -weights’ (left) considers all the columns after they have been filtered for those containing significant negative correlations ($z < -2.3$), and ‘Positive β -weights over threshold’ considers only the positive β -weights remaining in each column that would be used to calculate the layer profile. Error bars show the standard deviation between subjects.

4.7 Calculating layer profiles

Due to the sensitivity of GE-BOLD to draining vein effects (see Section 4.1), an increase in signal towards the pial surface is typically seen in layer profiles of GE-BOLD fMRI data. This section outlines the methods that can be used

to correct for such an effect, and then these methods are used to investigate the sensitivity to studying alpha-BOLD correlation.

4.7.1 Deveining Methods Background

A number of models have been proposed to correct the artifactual signal bias due to blood draining across the cortical surfaces. Here the most commonly employed models are applied to the data.

4.7.1.1 Method 1: Deveining using Linear Scaling

The simplest, linear offset model assumes that the macrovascular task independent signal is added to the layer-specific microvascular signal [155, 161]. A version of this model is implemented in the LayNii software library, as a linear scaling of the β -weights based on their cortical layer depth, with layers closer to the pial surface being reduced more than those at the GM/WM boundary.

$$I_{f_n} = I_{i_n} l_n, \quad (4.1)$$

where I_{i_n} and I_{f_n} are the β -weights in layer n before and after deveining and l_n is the fractional distance layer n is from the pial surface, equal to 0 at the pial surface and 1 at the WM/GM boundary. It is important to note that n has a single value for all voxels within a layer.

4.7.1.2 Method 2: Deveining using Linear Regression

An alternative implementation of the linear offset is to perform a simple linear regression on the final layer activation profile to remove the effect of draining veins.

$$I_{i_n} = a + bI_{f_n} + \epsilon, \quad (4.2)$$

where a is the y -intercept and b is the gradient of the layer profile and ϵ is the error.

4.7.1.3 Method 3: Deveining using Linear CBV scaling

This model requires an estimate of the voxel-wise Venous Cerebral Blood Volume (CBV_v). One method used in LayNii for this is to identify those voxels with the largest variance in an fMRI series and assume these voxels can be attributed to veins [162, 163]. Here, CBV_v was estimated for each subject by calculating the mean variance of the BOLD signal during the eyes closed periods for each run, and then taking the mean of the variance over runs. The CBV scaling model assumes the superficial macrovascular signal bias is due to increased vein density, therefore venous blood volume, in superficial layers [164, 165]. LayNiis implementation of this model calculates the mean CBV per layer, n , within each column, m , and adjusts the β -weights across the layers according to the following equation,

$$I_{f_{m,n}} = \frac{I_{i_{m,n}}}{CBV_{m,n}} n_{max}, \quad (4.3)$$

where $CBV_{m,n}$ is the mean CBV in layer n of column m and n_{max} is the maximum layer in the data.

4.7.1.4 Method 4: Deveining using Deconvolution

The final model, known as the leakage model, is the most physiologically grounded model. In this case it is assumed that each layer contains a mixture of neural signals from that specific layer along with signals from all preceding deeper layers [166–168]. This spatial signal subtraction, involves correcting the current layer in the column with a weighted sum across the preceding layers,

$$I_{f_n} = I_{i_n} - \sum_{k=n}^1 \lambda \left(\frac{I_{m,k}/n_{max}}{CBV_{m,n}} \right), \quad (4.4)$$

where k indicates previous layer numbers and λ is a scaling parameter that relates to the peak-to-tail ratio of layer-dependent point spread function (PSF), which was set to 0.25 corresponding to a normal estimated CBF [169]. CBV is calculated as described above for Method 4.7.1.3. It is important to note

that in this correction both the negative and positive β -weights are used, hence the thresholding process outlined in Section 4.6.4 is important so that the subtraction is not biased by noise.

4.7.2 Extracting layer profiles for the different deveining methods

After applying a noise threshold and correcting for the draining vein effect using different deveining methods, the β -weights were used to calculate layer profiles to show the variation of alpha-BOLD correlations across cortical depth. First the mean of all the positive β -weights in each layer was taken. Then profiles were combined across V1, V2 and V3. First the profile for the V1, V2 or V3 was normalised to the mean β value of the first cortical depth (at the CSF-GM boundary) and then the weighted average, according to the number of columns present in the V1, V2 and V3 ROIs, was calculated to give a layer profile over the whole active visual area.

Figure 4.30 shows the initial results of implementing each deveining method. Figure 4.30a shows the data with no correction, highlighting the expected increase towards the cortical surface. Figure 4.30b shows the result of the linear offset correction implemented in LayNii. The profile shows a decrease in signal towards the pial surface and an overall decrease in mean β -weight per layer and suggests this method has over-corrected the draining vein effect. Figure 4.30c shows the result of linear regression correction using in-house code. The profile shows two peaks in cortical depths 2 and 5 and as expected the overall amplitude of the profile is greatly reduced across all depths. The profile from the CBV scaling model is shown in Figure 4.30d, there is an overall amplitude increase throughout the entire profile but the increase in signal towards the pial surface is still present and in fact has been amplified. Figure 4.30e shows the leakage model deconvolution, with a reduced signal throughout the cortex and a slope towards the pial surface still appears to be present. However, this

method reveals a peak in the signal for cortical depths 1 – 3 and a dip in the signal for depths 4 – 6 of the cortex.

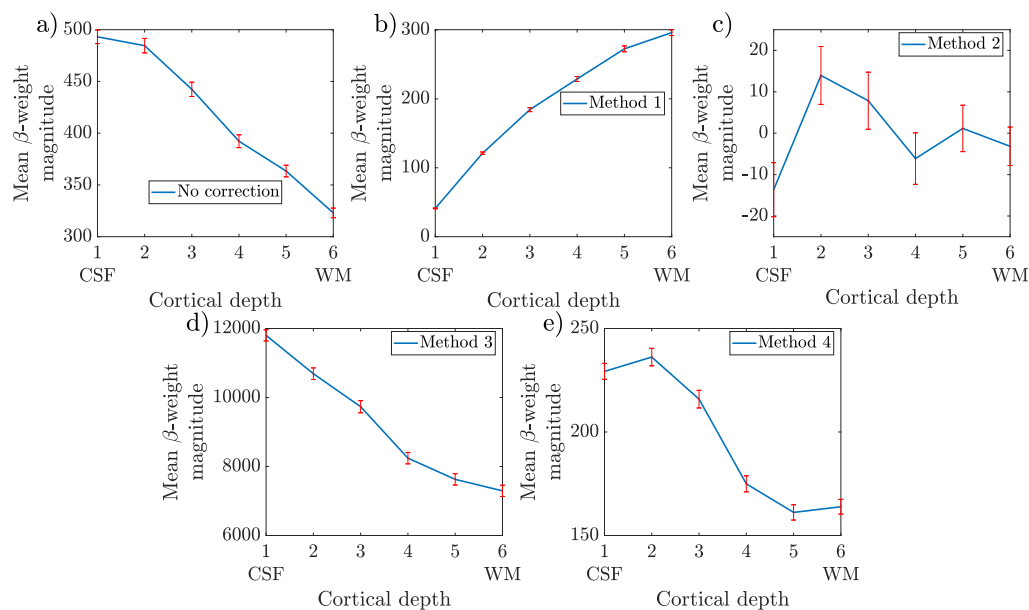


Figure 4.30: Effect of the different deconvolution methods on layer profiles from V1 shown for a single subject (Subject 1). Panel a) no correction of draining veins, Method 1: Linear Scaling, c) Method 2: Linear regression, d) Method 3: CBV scaling, and e) Method 4: Deconvolution. Error bars show the Standard Error on the Mean (SEM) for the mean β -weight across each cortical depth.

Figure 4.30 highlights that the different correction methods give different profiles. This is problematic if the correct profile is unknown, as is the case in this work. Method 4, the deconvolution method is the most physiologically based, but as seen from Equation 4.4 there are a number of assumptions made and constants used which may affect results. The sensitivity of this method to changing the choice of layers/columns and constants on the profile is shown in Figure 4.30e and whether this leads to a profile more similar to the profiles obtained using Methods 1 – 3 (Figures 4.30 b – d). It is also important to note at this point that this process of ‘deveining’ the GE-BOLD data is in effect an attempt to correct these data and make it more similar to methods such

as VASO which does not have this draining vein contribution. Therefore, a comparison between deveined GE-BOLD data and VASO data is another way to assess these correction methods, and this will be studied in Chapter 6.

4.7.3 Impact of analysis steps on the shape of the layer profile

Here, the effects of column size and method of averaging as well as parameters used in the deconvolution deveining method are assessed to establish their effect on the shape of the resultant layer profile.

4.7.3.1 Column Size

The effect of column sizes and denoising the β -weights were investigated in Section 4.6.5. This section looks at how the change in column size alters the shape of the layer profile. Figure 4.31 shows that the layer profile for the ‘Uncorrected’ data is a consistent shape for each column size, there is only a slight difference in the mean β -weight magnitude for each column size. The ‘Deveined’ layer profiles also have a consistent shape with the superficial depths having a higher mean β -weight before dipping in cortical depths 4 to 6.

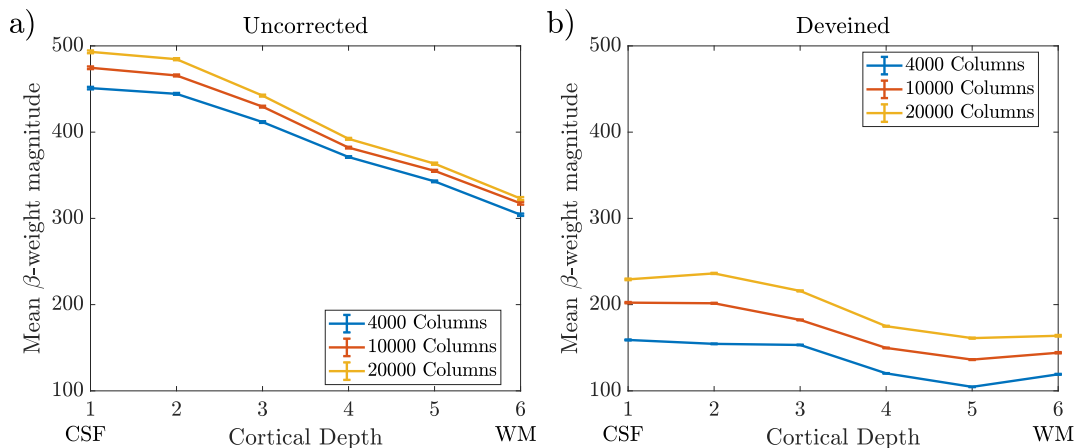


Figure 4.31: Layer profiles from V1 for a single subject shown for (a) ‘Uncorrected’ and (b) ‘Deveined’ data calculated as described in Section 4.7.2. The data were ‘deveined’ using the spatial deconvolution ‘leakage’ model (Method 4). Data is shown for 4,000, 10,000 and 20,000 columns. Error bars show the standard error on the mean (SEM) for the mean β -weight of each cortical depth.

In conclusion, this suggests that the profiles are not greatly affected by the size of the columns and therefore using the larger column size is preferable to maximise the presence of β -weights in all layers.

4.7.3.2 ‘Global Mean’ versus ‘Column Profile Mean’

Up until this point the method used to calculate the mean β -weight for each layer uses all the columns that are remaining after filtering for those containing voxels with significant ($z < -2.3$) negative alpha-BOLD correlations at once to produce one profile, this is called the ‘Global Mean’ method. An alternative approach is to calculate an individual layer profile for each column remaining after the filtering for those containing voxels with significant ($z < -2.3$) negative alpha-BOLD correlations and then average all of these column profiles together, this is referred to as the ‘Column Profile Mean’ method. The ‘Column Profile Mean’ method is likely to be more physiologically accurate but also more prone to noise.

Figure 4.32 shows the layer profile shape using the ‘Global Mean’ and ‘Column Profile Mean’ show very similar shapes for both the ‘Uncorrected’ (Figure 4.32a) and ‘Deveined’ (Figure 4.32b) data, regardless of at what stage the averaging across columns occurred during the analysis process.

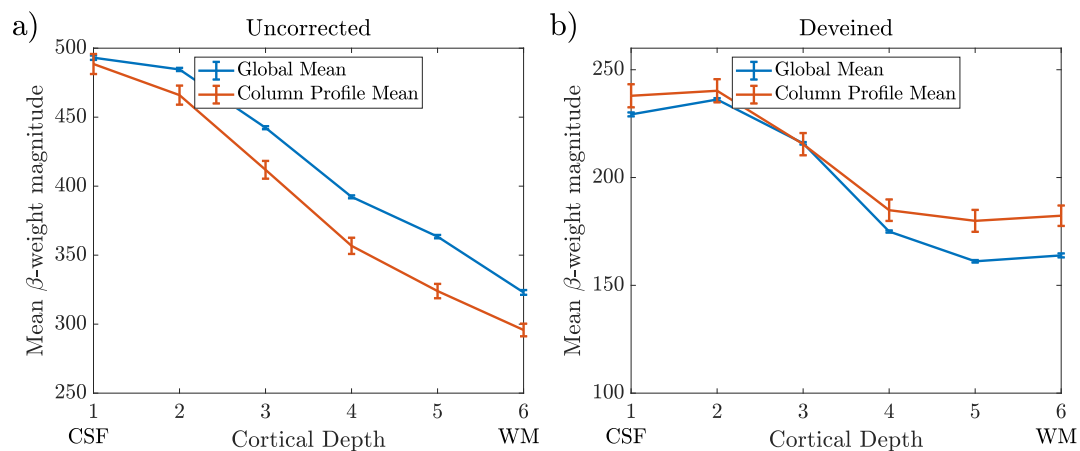


Figure 4.32: Layer profiles from the V1 region for a single subject shown for ‘Uncorrected’ (a) and ‘Deveined’ (b) GE-BOLD data. Blue and Orange lines indicate the ‘Global Mean’ and ‘Column Profile Mean’ methods respectively. Error bars show the standard error on the mean (SEM) for the mean β -weight of each cortical depth.

4.7.3.3 ‘Unmatched’ versus ‘Matched’ Method

So far, the layer profile calculation has used only voxels with positive β -weights, by thresholding before calculating the layer profiles for both the ‘Uncorrected’ and ‘Deveined’ data (See Section 4.7.2). After deveining, the β -weights in each layer are altered which may mean that β -weights that were > 0 are now < 0 . As a result the voxels which are used in calculating the layer profiles after deveining may be in spatially different locations to those voxels used to generate the ‘Uncorrected’ profile. I term this method ‘Unmatched’. An alternative is to use the same voxels for both the ‘Uncorrected’ and ‘Deveined’ layer profile calculation. The voxels used in the ‘Matched method’ are determined by the

positive β -weights before deveining. As a result the ‘Deveined’ layer profile will use different voxel locations between the ‘Unmatched’ and ‘Matched’ methods.

Figure 4.33 shows the layer profile shape using the ‘Unmatched’ and ‘Matched’ method. In Figure 4.33 the ‘Unmatched’ case shows high mean β -weights in superficial cortical depths 1 – 3 before dipping in the deeper depths. However, for the ‘Matched’ method the layer profile is at it’s lowest at cortical depth 1 and increases towards the middle depths 3 and 4 before increasing again through depths 5 and 6. As was seen in Figure 4.31, the profiles for each column size are offset with mean β -weight magnitude with column size.

It is difficult to know which of the deveined profiles is correct. The unmatched method was taken forward as this results in positive β -weights being used for the calculation of all profiles. This will be revisited in Chapter 6.

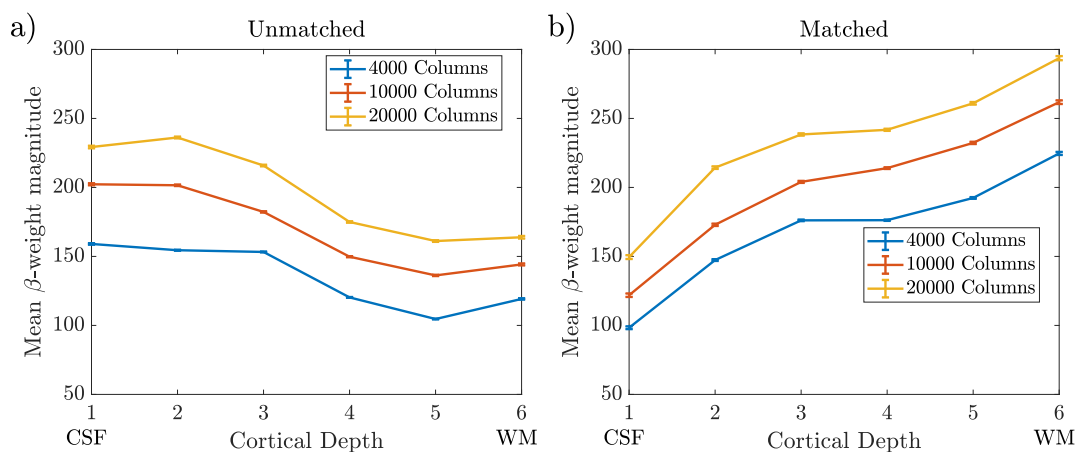


Figure 4.33: The ‘deveined’ layer profiles from V1 for a single subject calculated using ‘Unmatched’ (a) and ‘Matched’ (b) method. Blue, Orange and Yellow lines indicate the number of columns the GM ribbon was divided into for the analysis. Error bars show the standard error on the mean (SEM) for the mean β -weight of each cortical depth.

4.7.3.4 Choice of λ Value in Deconvolution Deveining Method

As seen in Equation 4.4, λ is a scaling parameter used in the deconvolution deveining method in LayNii [152] related to the layer-dependent point-spread-function (PSF). It reflects an estimate of the CBF.

Using 20,000 columns, the ‘Global Mean’ averaging method, and the ‘Unmatched’ method, the effect of λ in the deconvolution deveining method was investigated for values of λ of 0.2, 0.25, and 0.3, which corresponded to a plausible range previously reported [169].

Figure 4.34 shows that as expected at cortical depth 6 the profiles all have the same mean β -weight but they diverge as they move towards the superficial layers. This can be predicted from Equation 4.4, as λ is effectively scaling the amount that is subtracted from each depth so the cumulative effect by the time cortical depth 1 is reached will be greater. It is important to note however that the divergence of the profiles does not change the overall shape of the profile.

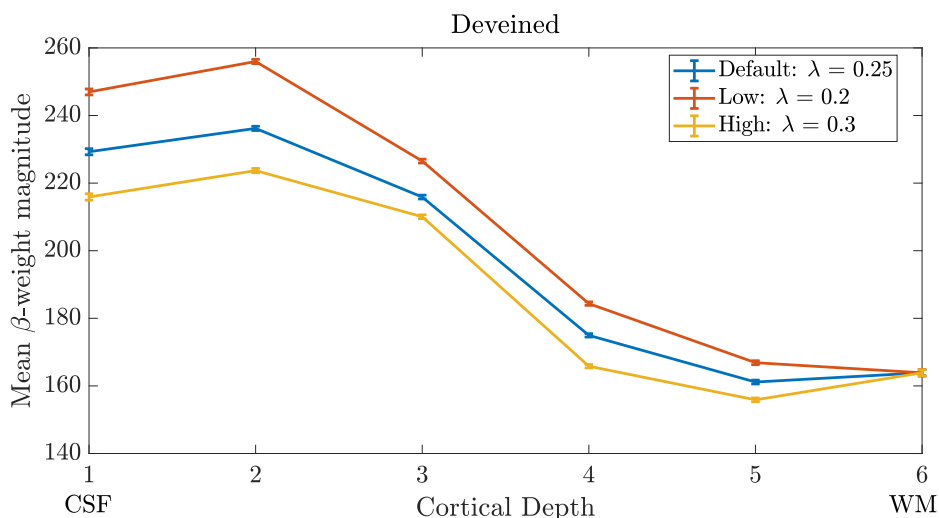


Figure 4.34: The ‘deveined’ layer profiles from the V1 region for a single subject calculated using 20,000 columns, the ‘Global Mean’ and the ‘Unmatched’ method shown for data ‘deveined’ using deconvolution with default ($\lambda = 0.25$), low ($\lambda = 0.25$) and high ($\lambda = 0.3$) λ values in LayNii. Error bars show standard error on the mean.

4.7.3.5 Effect of proximity to veins

As discussed earlier, and shown in Fracasso *et al* 2021, large draining veins impact layer dependent GE-BOLD, not only in those voxels that contain the veins themselves but also in surrounding voxels. When calculating profiles for each column using the ‘Column Profile Mean’ method (Section 4.7.3.2) it was also possible to assess how profiles were changed after deveining. Here this is shown for data analysed using 4,000 columns.

The uncorrected profile for each column was calculated and the gradient across cortical depth determined in MATLAB. This was then repeated for the deveined profile and the difference between each profiles gradient was calculated. In some cases, the profile completely flipped the gradient (shown in Figure 4.35) indicating an over correction from the deveining, potentially due to the presence of a nearby draining vein.

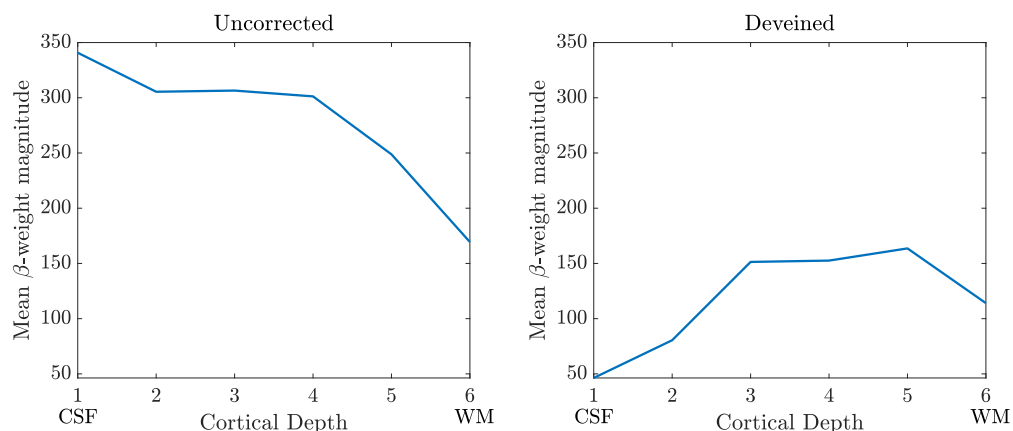


Figure 4.35: Example from one column where the gradient can be seen to flip from the ‘Uncorrected’ to the ‘Deveined’ profile.

Data was analysed such that each of the 4,000 columns now had a value for how much the gradient changed due to deveining correction. The columns were then classified into three groups of Bottom 25%, Middle 50% and Top 25% of gradient profile changes.

The optimal method to extract small veins from the 3D GE-EPI data was then assessed using either the multi-echo T_2^* data or raw 3D-EPI functional data. For the multi-echo 3D GE-EPI data acquired across 6 dynamics at a range of echo times (See Section 4.2), the data was averaged across each echo time (TE), and then concatenated. The multi-echo data was then fit to a monoexponential decay (Equation 4.5) to generate a weighted map of T_2^* and M_0 map,

$$M = M_0 \exp\left(-\frac{TE}{T_2^*}\right). \quad (4.5)$$

However, the resultant generated T_2^* map did not provide sufficient contrast to accurately automatically segment the veins (see Figure 4.36) likely due to spatial variation in noise due to the surface coils impacting the fit.

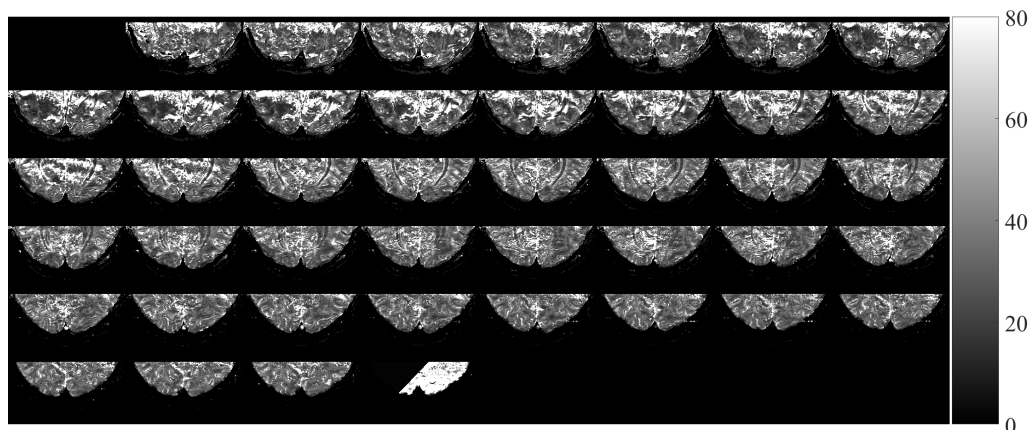


Figure 4.36: The weighted T_2^* map shown for all 44 axial slices for a single test subject (Subject 3).

Instead, a vein mask was generated from the functional 3D GE-EPI data from the EEG-fMRI session. All the dynamics of the central functional run that was used as the reference for coregistration were averaged to create a mean image. The mean image was smoothed using a Gaussian kernel with $\sigma = 2$ mm and the smoothed image was subtracted from the original mean image. An upper threshold was applied manually in FSLeaves to create a binary vein

mask that closely matched the extent of the veins visible in the mean functional image (as shown in Figure 4.37).

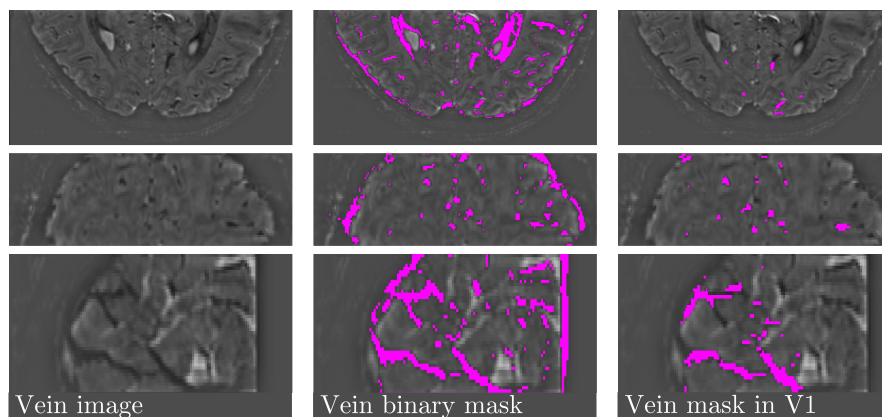


Figure 4.37: The generation of the vein mask shown axially (top), coronally (middle) and sagittally (bottom) for a single subject. Smoothed image subtracted from average 3D-EPI timecourse (left column), threshold by eye in FSLEyes (middle column), masked to V1 ROI and manually corrected (right column).

The resulting vein mask was then upsampled to 0.175 mm in plane and masked to include only the V1, V2 and V3 visual regions before being manually corrected in FSLEyes. Finally, the mask was upsampled to 0.175 mm isotropic resolution. Examples of vein masks for each subject can be seen in Appendix B.1.

Figure 4.38 illustrates the spatial correspondence in the gradient changes between the ‘Uncorrected’ and ‘Deveined’ profiles in each column and the vein mask. The percentage overlap of the vein mask with each of the profile gradient regions for each of the subjects was assessed as shown in Figure 4.39.

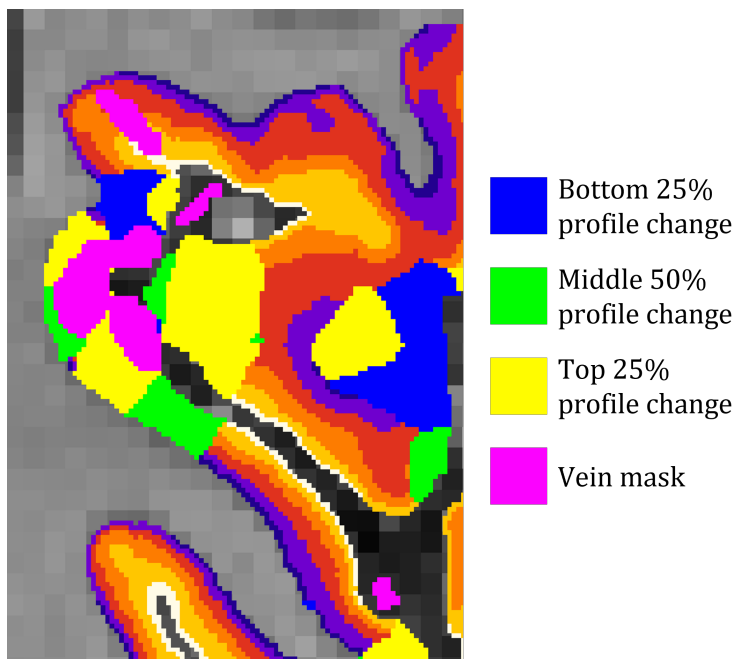


Figure 4.38: A section of the cortex shown with the equivolume layers, column profile change labels and vein mask overlaid onto the PSIR for a single subject.

Figure 4.39 shows that columns within the top 25% of most changed profiles overlap more with the vein mask than the middle 50% or bottom 25% of columns. $6.9 \pm 1.0\%$ of the Top 25% region overlaps with the vein mask, compared to $4.0 \pm 0.5\%$ for the Middle 50% region and the $4.7 \pm 0.9\%$ for the Bottom 25% region.

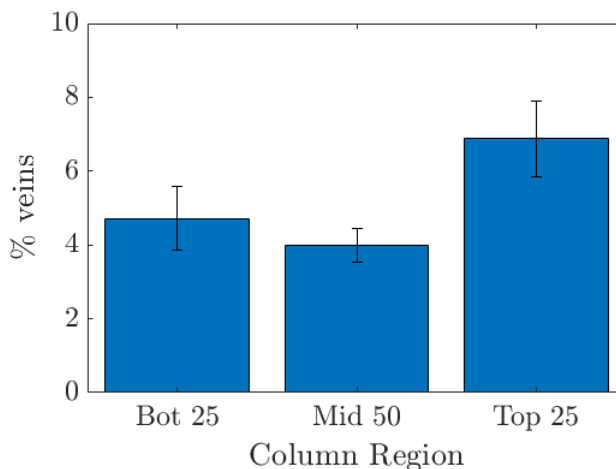


Figure 4.39: The percentage of each classified region that overlaps with the vein mask within V1 averaged over all nine subjects. Error bars show the standard error on the mean.

Obvious large veins were excluded during the manual correction of the GM mask before layer analysis but it is likely that veins are still present in the regions. Figure 4.39 shows that as expected, the majority of remaining veins are within the columns where the profiles are changed the most by the deveining process, this perhaps suggests that the deconvolution deveining method is working as required. Whilst it is clear that only a small percentage of overlap occurs even in the columns with the highest change in gradient (top 25%), if these are removed to try and remove the effect from large vessels and the layer profile is recalculated using the ‘Global Mean’ method (Section 4.7.3.3) then the resultant profile shown in Figure 4.40 is seen for the example subject investigated in this chapter. It can be seen for this subject this has a minimal effect.

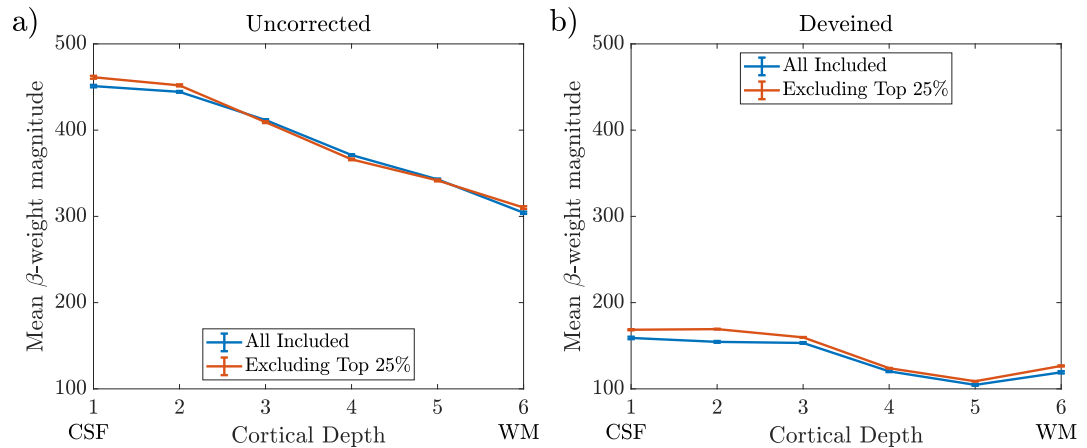


Figure 4.40: The layer profiles from the V1 region for a single subject ‘Uncorrected’ (a) and ‘Deveined’ (b). Blue indicates the profile including all available columns, Orange shows the profile resulting from excluding the columns with the highest change in profile gradient (top 25%). Error bars show the standard error on the mean (SEM) for the mean β -weight of each cortical depth.

Figure 4.40a shows that when excluding the top 25% of columns with the most changed profiles the uncorrected profile gradient is similar to the gradient profile containing all the columns. For the deveined profile shown in Figure 4.40b the signal in the superficial depths increases for the profile with the excluded top 25% of columns compared to the profile containing all columns but the overall shape of the profiles are the same. The effect of excluding the top 25% of columns with the most changed profiles impacted the layer profile shape differently for each subject (see Appendix B.2).

4.8 Discussion

The aim of this chapter was to develop methods to analyse layer-dependent 7 T EEG-fMRI data collected using a 3D GE-EPI readout with a view to assess the origins of human alpha oscillations. The acquired data were novel with the only other previous layer-dependent EEG-fMRI data being acquired at 3 T [1].

The analysis pipeline required precise motion correction and coregistration to align functional and structural data, the formation of EEG-fMRI regressors to find alpha-BOLD correlations, accurate segmentation and manual corrections to define the boundaries of the GM, and a GLM to define regions containing alpha-BOLD correlation, as well as a method for correcting the draining vein effect seen in GE-BOLD layer data. Multiple method options were assessed at different stages of the pipeline to understand their impact on the final layer profile, and to define the pipeline to be applied in Chapter 5.

In summary, the chosen pipeline is as follows and is shown in Figure 4.7. Motion correction and coregistration of the fMRI data are performed with a single concatenated transformation matrix, followed by B_0 distortion correction to align the functional and structural data. The EEG alpha power timecourses are convolved at 500 Hz with a HRF and downsampled to form regressors for the fixed effects GLM. Retinotopic mapping is used to define ROIs for visual regions V1, V2 and V3 with the assistance of an anatomical atlas for each subject. The retinotopy and EEG-fMRI structural data are coregistered and the resulting transform is applied to the V1, V2 and V3 ROIs which are upsampled and manually corrected.

The structural data are tissue segmented and upsampled for manual correction (avoiding large veins where possible) and labelling of the GM boundaries within the V1, V2 and V3 ROIs. The equivolume layers are calculated and 4,000 columns are generated across the GM ribbon. The columns within V1, V2 and V3 are filtered for those containing significant alpha-BOLD correlation and denoised using a threshold equal to 5% of maximum value in that visual region. The β -weights within the remaining columns are then deconvolved in LayNii using the spatial deconvolution leakage model using the default value $\lambda = 0.2$. The uncorrected and deconvolved layer profiles are then calculated from the mean of the positive β -weights within each layer using the ‘Unmatched’ and ‘Global Mean’ method.

The methods in this chapter have been developed with aim of applying them to layer dependent 7 T EEG-fMRI data to answer the question ‘*What is the origin of the EEG Alpha signal?*’. At the time of writing this thesis, we know of only one other layer dependent EEG-fMRI study for which two papers have been published [1, 86]. There is no standard pipeline for analysing such data. Table 4.8 compares the key chosen steps in our analysis pipeline against similar studies. The criteria for selection were papers published: 1) on layer dependent fMRI since 2018, 2) using only GE-BOLD and 3) focusing on the primary visual cortex.

Previous studies often use separate transforms when registering the fMRI timeseries with only four using a single combined transformation matrix [170–173]. 10 out of 13 studies use retinotopic mapping to functionally define ROIs of the primary visual cortex, with the remaining three using a brain atlas [172, 174] or labels from Freesurfer [159].

Some of the key differences in our chosen pipeline are: 1) the denoising threshold of the data – four other studies have implemented a denoising method using either the R^2 fit value from Population Receptive Field (pRF) mapping [175–177] or coherence level from the pRF mapping [171], 2) the use of an explicit vein mask, with some other studies using a minimum EPI signal threshold to achieve a similar effect, 3) deconvolving using deconvolution – only two other studies have implemented this [176, 177] with most studies relying on the difference between two task-based stimulus conditions.

A number of previous studies have used a method to select a subset of the data to be used for the layer dependent profiles, most choosing to select the voxels/vertices with the top N z -stats or t -stats.

From the comparison to other literature it can be seen that our analysis pipeline provides bespoke methods for layer dependent EEG-fMRI data with some overlap with prior work. Chapter 5 follows which applies the analysis pipeline to the full dataset.

Paper	Registration	Visual ROI	Denoising	Choice of Voxels	Deveining	λ
Scheeringa <i>et al</i> 2016	Separate	Retinotopic mapping	N/A	Top 10% of nodes based on T-stat	Exclude top 25% of T- stats	N/A
Fracasso <i>et al</i> 2018	One combined transform	Retinotopic mapping	N/A	Median T-stat >2 & GM thickness within 2.5–97.5 percentiles	Three linear gradient groups	N/A
Klein <i>et al</i> 2018	One combined transform	Retinotopic mapping	Coherence <25 th per- centile	12.5–87.5 percentile eccentricity	N/A	N/A
Gau <i>et al</i> 2020	One combined transform	Atlas	N/A	N/A	Median β -weight & Condition difference	N/A
Bergmann <i>et al</i> 2019	Separate transforms	Retinotopic mapping	R^2 pRF fit & mean BOLD signal thresh- old	R^2 threshold & pro- jected	SVM. Superficial sen- sitivity vs Deeper specificity trade-off	N/A
Zaretskaya <i>et al</i> 2020	Separate transforms	Atlas	N/A	<7.5° eccentricity from Benson atlas	Difference in condi- tions	N/A

Paper	Registration	Visual ROI	Denoising	Choice of Voxels	Deveining	λ
Vizioli <i>et al</i> 2020	Separate transforms	Retinotopic mapping	N/A	N/A	SVM. Difference in conditions	N/A
Navarro <i>et al</i> 2021	One combined transform	Retinotopic mapping	N/A	Structural/Functional alignment threshold	Difference in conditions	N/A
Marquadt <i>et al</i> 2018	Separate transforms	Retinotopic mapping	R^2 pRF fit & mean EPI signal threshold	N/A	Deconvolution	Weights from Markuerkiaga <i>et al</i> 2016
Marquadt <i>et al</i> 2020	Separate transforms	Retinotopic mapping	R^2 pRF fit & mean EPI signal threshold	Top 1,000 max z -stats columns	Deconvolution	Weights from Markuerkiaga <i>et al</i> 2016
Aitken <i>et al</i> 2020	Separate transforms	Freesurfer label	N/A	Localiser GLM activation mask & top 500 T-Stats mask	Reallocate ROIs so even contribution across layers	N/A
van Mourik <i>et al</i> 2021	Separate transforms	Retinotopic mapping	N/A	Top 600 activated vertices	N/A	N/A

Paper	Registration	Visual ROI	Denoising	Choice of Voxels	Deveining	λ
Haarsma <i>et al</i> 2022	Separate transforms	Freesurfer label	N/A	Localiser GLM activation mask & top 500 T-Stats mask	Difference in conditions	N/A

Table 4.1: A summary of the key analysis methods in related literature using GE-BOLD layer-fMRI in the primary visual cortex since 2018. The analysis steps relate to the methods I have assessed throughout this chapter.

Chapter 5

Assessing the origins of alpha oscillations

Abstract

Despite alpha oscillations playing a key role in cognition and brain function, the mechanisms generating these oscillations are poorly understood [45, 46, 70, 79–81]. Current work to investigate alpha generation is predominantly conducted on animals with intracranial LFP recordings. To translate these types of studies into human research there is a need to develop non-invasive methods to assess laminar alpha oscillations. In this chapter, layer dependent 7 T EEG-fMRI is used to address the question ‘*What is the origin of the EEG alpha signal?*’. The analysis pipeline optimised in Chapter 4 was implemented on 7 T EEG-fMRI data from ten healthy subjects during an eyes open, eyes closed paradigm. EEG alpha power timecourses were used to form regressors for the GLM analysis of the fMRI data to provide alpha-specific activation maps spatially specific to the grey matter of the primary visual cortex. Spatial deconvolution was implemented to ‘devein’ the alpha-BOLD layer profiles to correct for the known draining vein effect in GE-BOLD data [166–168, 180, 181]. After ‘deveining’, the mean layer profile across visual areas V1–3 across the subjects showed a dip in the middle cortical depths. This dip was contrary to the hypothesised generation of the alpha through bottom-up thalamocortical loops and suggested that EEG alpha is generated during top-down, feedback processing where corticocortical alpha is projected from higher brain regions and terminates in layers outside of layer IV. However, that is not stay that alpha is not driven by feed forward, bottom-up processing as it has been shown previously that prolonged, unchanging visual stimuli can result in layer profiles that are dominated by the deep and superficial layers [182].

This work was presented as a talk at the ISMRM UHF Workshop Lisbon 2022 ‘Laminar layer 7 T fMRI-EEG reveals human alpha oscillations are predominately from superficial and deep layers’; a digital poster at ISMRM 2022 ‘Laminar layer 7 T fMRI-EEG reveals human alpha oscillations are predominately from superficial and deep layers’; and a poster at OHBM

2022, Glasgow 'Layer 7 T fMRI-EEG: human alpha oscillations originate from visual cortex superficial and deep layers'.

5.1 Introduction

Alpha oscillations have been detectable in humans for many decades [9] and have been studied extensively in neuroscience and psychology. Modulations in alpha power have been linked to a range of cognitive tasks such as working memory [183], sensory perception [184] and motor control [185]. Despite alpha oscillations playing a key role in cognition and brain function, their generation mechanisms are poorly understood. As described in Section 3.3.1, opinions are divided between alpha being driven by bottom-up processes, top-down processes, or a combination of both.

To differentiate between top-down or bottom-up processing pathways and their role in alpha generation, methods are required that can measure alpha oscillations on a laminar level [46, 186, 187]. The vast majority of work investigating the origins of alpha oscillations has been conducted on animal models using invasive intracranial Current Source Density (CSD) and local field potential (LFP) recordings. In recent primate studies using LFP recordings, it has been shown that alpha activity in the primary visual cortex (V1) is highest in cortical layers IVC and VI, and is reduced across all cortical layers when attention is increased [187, 188]. In contrast to this, Buffalo *et al* studied LFP coherence across cortical depths in visual regions V1, V2 and V4 and found that the strongest alpha band coherence was in the deep cortical layers (layers V & VI) and that coherence and LFP power reduced during visual attention. These findings are important for improved understanding of alpha oscillations, but use techniques that are unsuitable for use in human neuroscience in healthy people as they are incredibly invasive and have limited spatial coverage.

Additionally, when measuring alpha oscillations using LFPs for intracranial EEG (icEEG), the reference electrode is in such close proximity to the measuring site that any global changes in alpha oscillations are experienced equally by both electrodes. This is in contrast to alpha measured on the scalp with EEG which can have a global reference, therefore detecting the global changes in alpha.

This more complete measure of alpha highlights the importance of assessing alpha using scalp EEG measures rather than from LFP icEEG.

To investigate the origins and functional significance of alpha oscillations in humans, a non-invasive method is needed to relate EEG alpha measured from the scalp to neuronal signals across the cortical depths. Chapter 3, outlined that fMRI BOLD contrast provides an indirect measure of neuronal activity and has been shown to correlate with alpha power [103]. In recent years, seminal work at 7 T has shown that the modulation of BOLD responses across the cortical layers can be measured to provide information on feedforward and feedback signalling mechanisms [77]. Therefore, combining EEG with layer BOLD fMRI at 7 T will provide a novel technique to study the localisation of neuronal activity and investigate the organisation and neural pathways of the human brain.

Previous work by Scheeringa *et al* [1, 86] details the acquisition and analysis of layer dependent simultaneous EEG-fMRI acquired at 3 T. The relationship between EEG alpha, beta and gamma oscillations and the BOLD response across different cortical layers during an attention task was investigated and it was found that alpha-band EEG power is negatively correlated to the BOLD response in both deep and superficial layers. Additionally, beta-band power was found to be negatively correlated to the BOLD response in the deep layers and gamma-band power was positively correlated to the superficial layers BOLD signal.

Following this work, moving to 7 T from 3 T [1] will provide increased sensitivity to changes across layers [87], which will be advantageous in investigating the source of the alpha signal. An understanding of the generating mechanisms of the alpha signal will provide the opportunity to use alpha oscillations as a biomarker for the efficacy of the attention system in attention disorders such as Attention Deficit Hyperactivity Disorder (ADHD). This work aims to lay the foundation for future studies on information processing and EEG-fMRI laminar measures.

In Chapter 4, an analysis pipeline was developed for layer analysis over large ROIs to study EEG-fMRI measures. Here this pipeline is applied across a group of subjects with the aim of answering the question ‘*What is the origin of the EEG Alpha signal?*’. In this Chapter, the analysis pipeline that was developed in Chapter 4 is applied to data from ten subjects, and layer results combined across subjects to study the origin of the alpha signal. Figure 4.6 summarises the different elements of the pipeline.

5.2 Assessing EEG data quality

The acquisition of EEG simultaneously with fMRI data at 7 T is especially challenging due to the large gradient, pulse and movement artefacts in the data caused by the high magnetic field [139]. Artefact correction did not form part of this PhD thesis, but for this chapter I did assess the quality of the cleaned EEG alpha timecourses for each subject. These were then to be used to generate model BOLD responses of the fMRI data for each subject in a fixed effects general linear model (GLM). Modulation of each individual’s EEG alpha power was assessed by performing a Fourier transform on the EEG timecourse collected during the eyes open and eyes closed periods, and comparing the resulting frequency power spectrum for each subject. Figure 5.1 shows the eyes open and eyes closed EEG spectra for each of the ten subjects.

Spectra of Subjects 3 – 9 show a noticeable increase in power in the alpha frequency range of 8 – 13 Hz for the eyes closed to eyes open periods confirming that alpha power has been modulated during the stimuli. Subject 1 shows a dramatic increase in power on eyes closed compared to eyes closed, indicating a strong modulation of alpha power. Subjects 2 and 10 show little to no difference in alpha power between eyes open and eyes closed periods.

To further assess the EEG data quality, all EEG-fMRI runs for each subject were concatenated and compared with a box car of the eyes open, eyes closed stimulus timings, as shown in Figure 5.2.

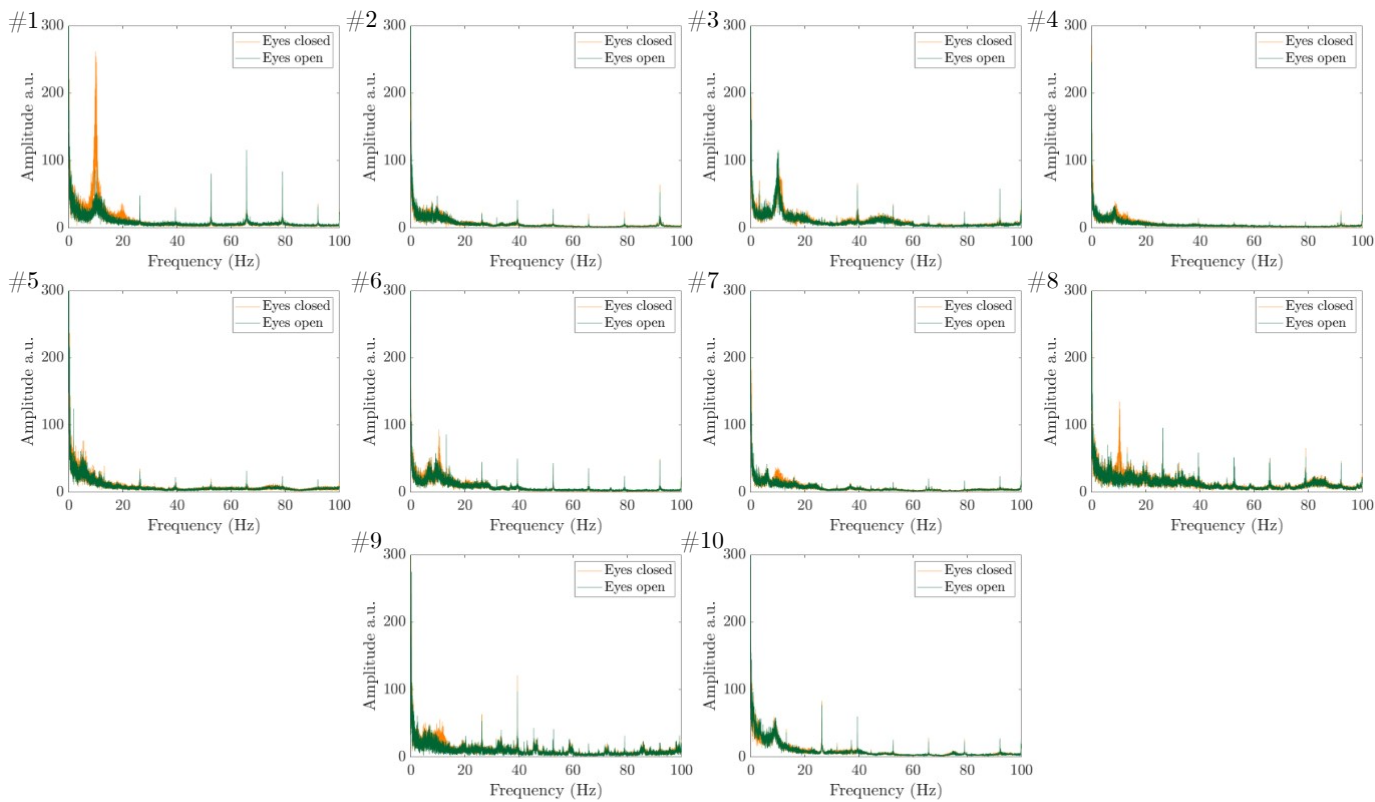


Figure 5.1: The EEG power spectrum from the Fourier transform of the EEG alpha power timecourse from the VE at the peak alpha power location during the eyes open (green) and eyes closed (yellow) periods, shown for each of the ten subjects. Subject numbers are denoted on the top left of each subplot.

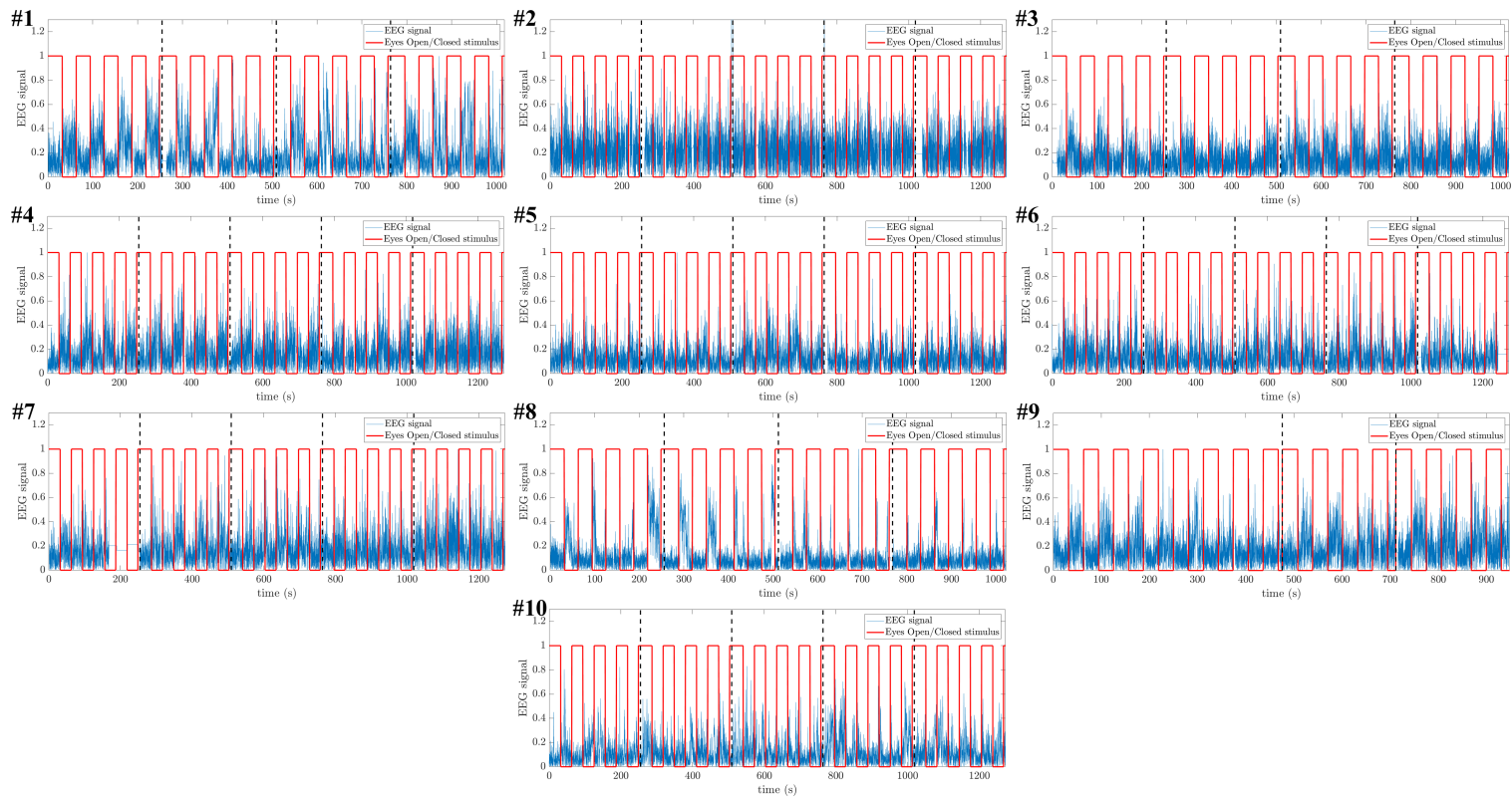


Figure 5.2: All runs (separated with black dashes) of the EEG alpha power timecourse from the VE at the peak alpha power location during the eyes open, eyes closed stimulus concatenated together (blue), with the stimulus timing box overlaid (red), shown for each of the 10 subjects. For the stimulus, periods of eyes open are denoted by a value of 1 and periods of eyes closed are denoted by value of 0. Subject numbers are denoted in the top left of each subplot. The first run for Subject 7 was excluded from further analyses as there was a ~ 80 s period at the end of this run where the signal had been replaced with the mean value from the location of the VE

For most subjects there can be seen to be a periodic pattern in the EEG alpha power that matched the timing of the 30 s eyes open 30 s eyes closed stimulus across most runs. An increase in EEG alpha power is seen during eyes closed periods compared to eyes open.

Subject 10 from this point onwards was excluded from further analyses, due to both the high noise level across all experimental runs, as shown in Figure 5.2, and the lack of alpha power modulation, as shown in Figure 5.1.

5.3 EEG alpha HRF Convolution

Figure 5.3 shows the result of the convolution of the EEG data with the HRF using the method described in Section 4.4.1 for each run for the remaining nine subjects (Subject 1 – 9). The plots show there was considerable variability in the alpha response across runs and subjects, as would be expected due to the spontaneous nature of the alpha band response. Each of these timecourses were used as regressors for GLMs to identify where in the visual cortex BOLD responses negatively correlated with the alpha signal (see Section 5.5)

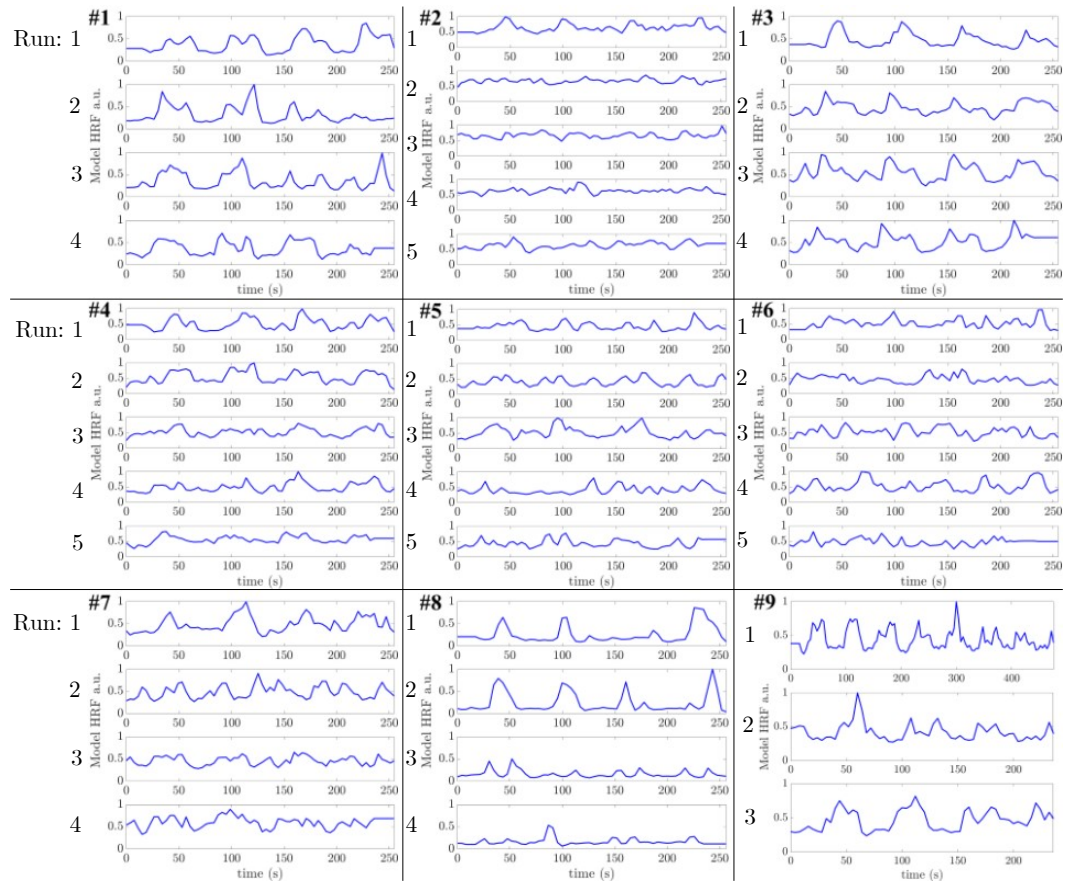


Figure 5.3: Each run of the ‘eyes open/eyes closed’ task for each of the nine subjects. The model paradigm derived from the preprocessed EEG data was convolved with a standard HRF at 500 Hz with a double gamma function (time to-peak = 6 s) and then downsampled to the volume TR. The number in the top left of each subplot denotes the subject.

5.4 Subject-specific Retinotopy

Retinotopy is commonly used to functionally define subject specific ROIs of the visual cortex. As shown in Chapter 4, it is the most common method for definition of the visual ROIs in studies using GE-BOLD layer fMRI in the primary visual cortex (Table 4.8). Here we show the results from implementing

standard retinotopic mapping methods (Section 4.4.4) on data for Subjects 1 – 9.

Figure 5.4 shows the cortical flat patches of the phase from the rotating wedges stimulus for each of the nine subjects, with the manually defined (informed by the Benson atlas) boundaries for V1, V2 and V3 overlaid. The rotating wedges phase maps were used to highlight the boundaries between each primary visual region.

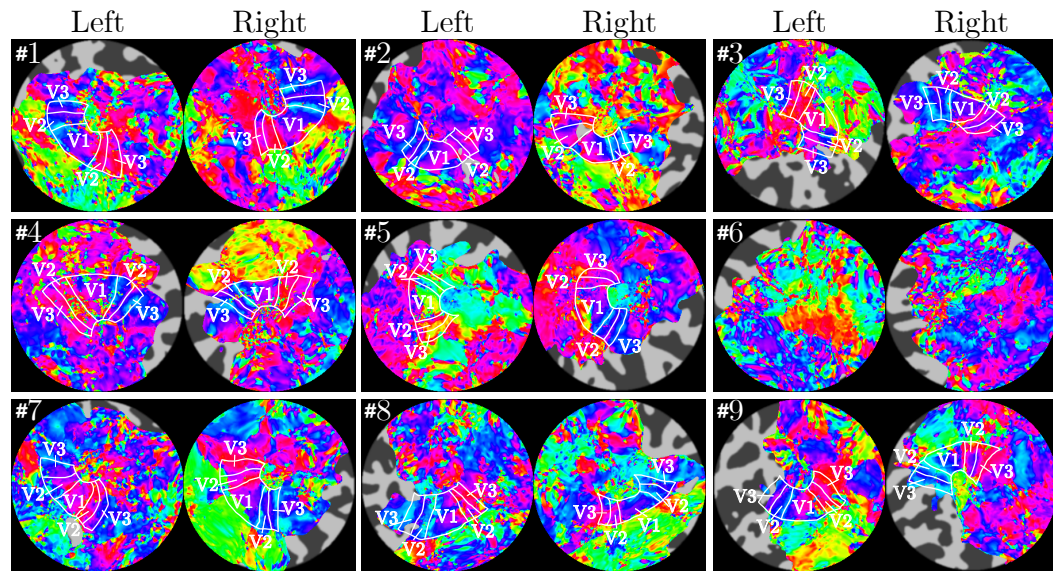


Figure 5.4: Retinotopic maps for Subjects 1 – 9 showing the phase flat map from the rotating wedges stimulus for the left and right hemisphere of the brain. Manually defined ROIs V1, V2 and V3 are overlaid in white.

Figure 5.5 shows the cortical flat patches of the phase from the expanding/contracting annuli stimulus for the same nine subjects, with the manually defined (informed by the Benson atlas) boundaries for V1, V2 and V3 overlaid in white. The expanding/contracting rings phase maps were used to identify the location of the fovea and the extent of each of the primary visual regions.

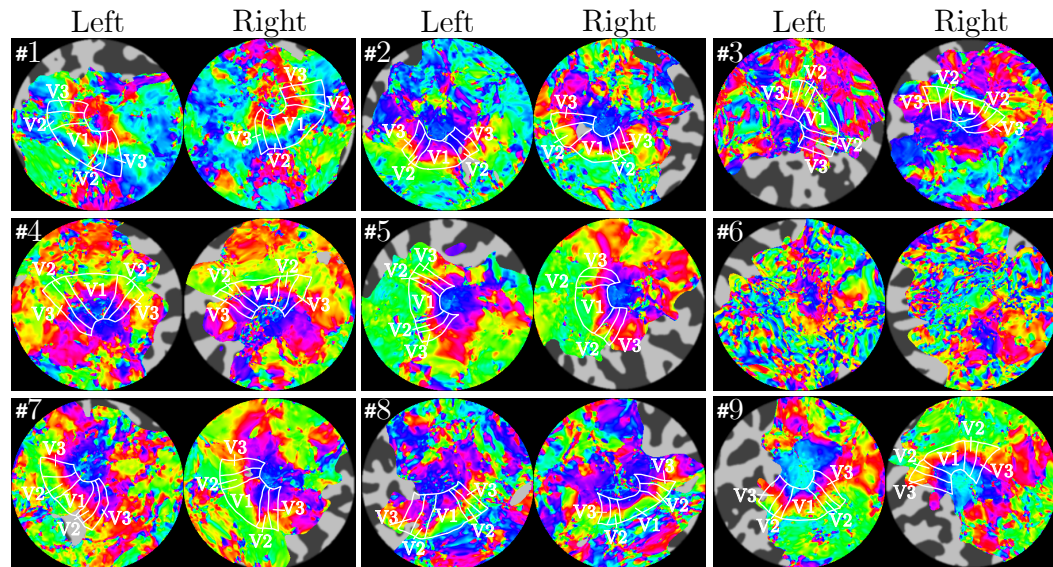


Figure 5.5: Retinotopic maps for Subjects 1 – 9 showing the phase flat map from the expanding/contracting annuli stimulus for the left and right hemisphere of the brain. Manually defined ROIs V1, V2 and V3 are overlaid in white.

It was possible to define V1, V2 and V3 for eight of the nine subjects manually from the reversals in the phase of the data using the Benson atlas only as a guide. The data quality for Subject 6 was too poor to define boundaries manually, so for this subject the definitions from the Benson atlas for V1, V2 and V3 ROIs were used. It was known that Subject 6 had a visual impairment (astigmatism) and this was the most likely cause for the poor quality of the retinotopy data [189]. After transformation from surface to volume space the visual ROIs were aligned to the functional data. The resulting ROIs for V1–3 are shown in Figure 5.6 for Subjects 1 – 9.

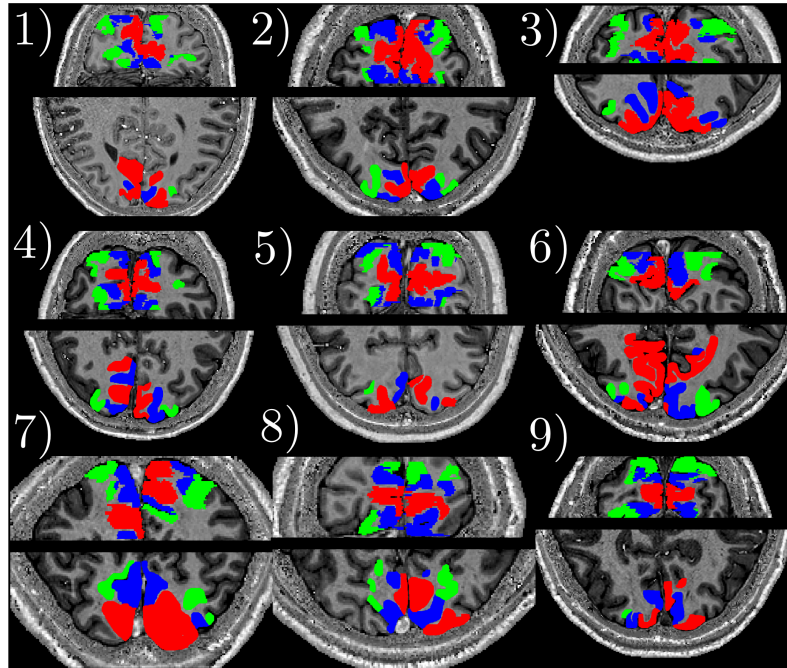


Figure 5.6: Primary visual regions V1 (red), V2 (blue) and V3 (green), as defined from the retinotopy, after being transformed into the native space of the functional EEG-fMRI data and upsampled to 0.175 mm isotropic spatial resolution. Results are shown in the coronal (top) and axial (bottom) view for each subject overlaid onto the partial head PSIR acquired during the functional EEG-fMRI scan session.

The final upsampled ROIs for each subject covered the calcarine sulcus and surrounding areas and there was no overlap between V1, V2 or V3. The extent of the ROIs defined using subject specific retinotopy were notably smaller compared to the Benson atlas which was used for Subject 6. This is likely to be due to the restricted visual FOV for subjects during the retinotopy visual stimuli due to the narrow bore of the 7 T scanner. In addition, Figure 5.6 shows the large inter-subject variability in the extent of each of the visual regions, demonstrating the value of performing subject specific retinotopy for the definition of V1–V3. The final upsampled ROIs for each of the subjects was

then used to define the region in which the cortical layers and columns were calculated (see Section 5.6).

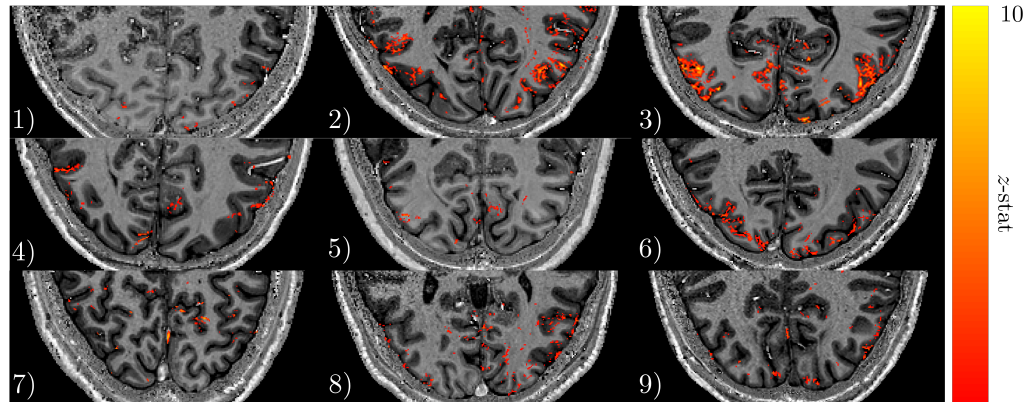
5.5 EEG-fMRI fixed effects General Linear Model (GLM)

A key challenge to the development of the analysis pipeline was the combination of the EEG and fMRI data. The chosen method was to model the BOLD response using the EEG alpha power timecourse convolved with a HRF which formed regressors to input into a fixed-effects GLM (see Section 4.10). This section compares the results of using the three different regressor inputs to the GLM analysis: 1) A boxcar of the stimulus timing of eyes open/closed convolved with a HRF, 2) The EEG alpha power timecourse regressors, and 3) Both the boxcar and EEG alpha power regressors with the EEG orthogonalised to the boxcar.

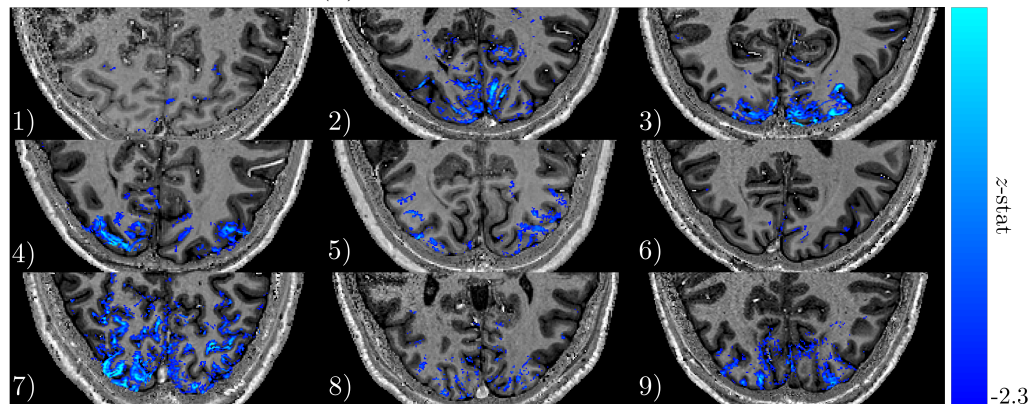
5.5.1 GLM using a Boxcar

Figures 5.7a and Figure 5.7b show the results of the GLM analysis (single slice shown for each subject), using a convolved boxcar to model the alpha-BOLD response for the positive contrast and negative contrast respectively. The boxcar was set to match the expected alpha power changes: with eyes open periods set to a value of 0, and eyes closed periods set to a value of 1. The z -stat maps are overlaid on the partial head PSIR for each of the 9 subjects. The positive contrast z -stat maps of the boxcar GLM (Figure 5.7a) show very sparse activation in the primary visual cortex across all subjects except for Subject 6. We believe subject six incorrectly followed the stimulus and had their eyes open when they should have been closed and vice versa. Subjects 2 and 3 show some activation in areas outside of the primary visual cortex.

For the negative contrast z -stat maps of the boxcar GLM (Figure 5.7b), it can be seen that Subjects 2, 3, 4, 5, 7 and 9 all show significant negative correlation of the convolved boxcar regressors with the BOLD response localised to the visual cortex and spatially specific to the grey matter. Due to their inverted responses to the stimulus prompts Subject 6 shows no activation in the primary visual cortex.



(a) Positive contrast z -stat map.



(b) Negative contrast z -stat map.

Figure 5.7: The z -stat maps resulting from the fixed effects GLM analysis over all runs for each subject using a boxcar of the stimulus timings convolved with a double gamma HRF as a regressor shown for (a) positive contrast and (b) negative contrast. z -stats are thresholded at $z < -2.3$ averaged over all runs, and cluster corrected, $p < 0.05$. Results are shown for a single slice for each subject.

Alpha oscillations are known to negatively correlate with the BOLD response so this result was expected, but it is important to also note the effect of non-alpha related brain activation due to visual stimulation. Thus using the boxcar regressor results in brain activation maps that may not be specific to the timings of the changes in alpha power. The next section looks at using the EEG regressors as modulations of the alpha-BOLD response.

5.5.2 GLM using EEG alpha regressors

Figure 5.8 shows the negative z -stat maps obtained using the EEG alpha power timecourses to model the alpha-BOLD response. These maps show activation that is more closely related to the timings of the alpha oscillations than a simple boxcar. All nine subjects show significant negative activation in the primary visual cortex that is spatially specific to the grey matter, with subjects 2, 3, 4, 5, 6, 7 and 9 all showing widespread activation. Note that the use of the EEG regressors has negated the incorrect timings of Subject 6 opening and closing their eyes and results in significant activation similar to that of the other subjects.

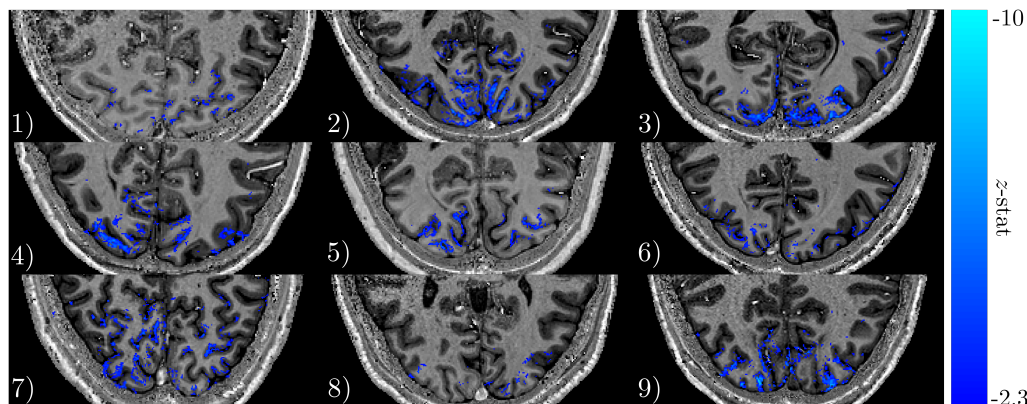
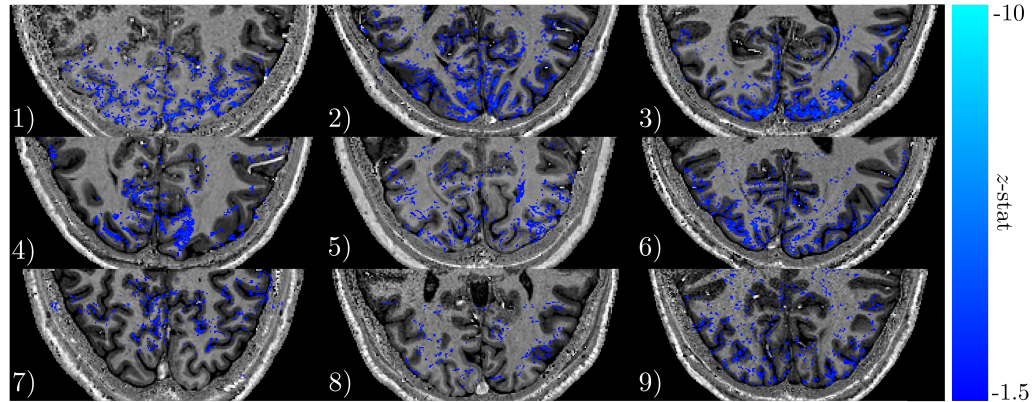


Figure 5.8: The negative contrast z -stat map resulting from the fixed effects GLM using the EEG alpha power timecourse convolved with a double gamma HRF as a regressor overlaid on the PSIR for each subject. A fixed effects analysis over all runs for each subject. z -stat maps are thresholded to $z < -2.3$ and cluster corrected $p < 0.05$. Results are shown for a single slice for each subject.

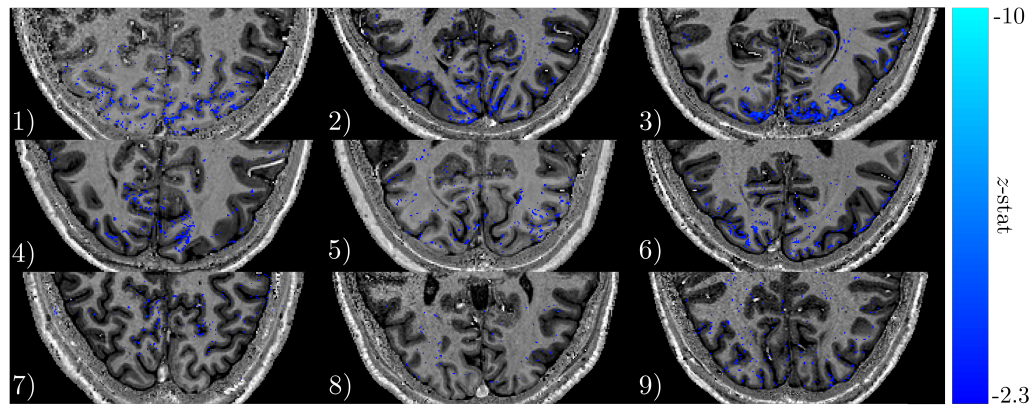
5.5.3 GLM using Regressor Orthogonalisation of boxcar and EEG regressors

To uncouple the BOLD activation due to simply opening and closing the eyes, and alpha-specific BOLD changes, the boxcar regressors were input into a fixed effects GLM with the EEG alpha regressors orthogonalised to them. By orthogonalising the regressors to one another they no longer share any descriptive variability. The corresponding z -stat maps for the orthogonalised EEG regressors are shown in Figures 5.9aa and 5.9ab with thresholds of $z < -1.5$ and $z < -2.3$ respectively. The threshold of $z < -1.5$ was also considered as the orthogonalisation of the regressors resulted in lower correlation between the modelled BOLD response and the data. Reassuringly the orthogonalised activation maps show the same pattern as seen in Figure 5.8. After orthogonalising to remove the large "step changes" in alpha power induced by the eyes open and

closed the z -stat threshold did need to be reduced to -1.5 from -2.3 to reveal the activation pattern. This is to be expected as the modulations induced by the change from eyes open to closed was far larger than alpha changes during each of the eye open/closed periods as can be seen from Figure 5.2.



(a) z -stat map with a threshold of $z < -1.5$



(b) z -stat map with a threshold of $z < -2.3$

Figure 5.9: The z -stat map resulting from the fixed effects GLM analysis over all runs for each subject using a convolved boxcar as the first regressor and the orthogonalised EEG alpha regressor as the second regressor thresholded at (a) $z < -1.5$ and (b) $z < -2.3$, and cluster corrected ($p < 0.05$). The orthogonalised alpha regressor response is shown here overlaid on the PSIR for a single slice for each subject.

Going forward, the z -stat maps from the non-orthogonalised EEG regressors are primarily used for calculation of the layer profiles. A comparison of the

layer profiles resulting from each regressor type will be shown at the end of this chapter in Section 5.7.

5.5.4 Timecourse analysis

A model free approach was considered to find areas of alpha-BOLD correlation. The mean fMRI timecourse from all voxels in V1, V2 or V3 was compared to the EEG alpha power regressors to look for modulations that match the expected alpha activation. It was found that for most subjects there was no discernible modulation in the mean fMRI timecourse across the visual regions V1, V2 or V3 and so a model free approach would be ineffective (see Appendix C.1).

In addition, the timecourses were also used to look at inter trial variability [190], the regressors formed from the EEG alpha power timecourse were compared with the fMRI timecourse of significantly correlated voxels ($z < -2.3$) within each visual region. As expected the regressors and mean fMRI timecourses were visually anti-correlated for all subjects. There was little variability between trials for the HRF modelled using the EEG alpha power timecourse for subjects 1, 3, 4, 8 and 9. There was a noticeable reduction in the regressor amplitude for later trials, likely due to habituation. When plotting the fMRI response for each trial against the corresponding EEG alpha power regressor all subjects except for subjects 1 and 4 showed a negative correlation between EEG alpha power regressor amplitude and fMRI response. Notably, Subject 1 had a very strong alpha power response and very weak BOLD responses which might explain the lack of negative correlation for this subject.

On visual inspection, the variability in the trials of the mean fMRI timecourse was greater for visual regions V2 and V3 compared to V1. Earlier trials had a shape that was more consistent with the expected BOLD response.

5.6 Defining layers and columns from structural scans

Another key challenge for this dataset was the alignment and segmentation of the structural data to create high quality GM boundary definitions. These boundary definitions were used for 1) the definition of cortical layers and 2) definition of cortical columns, as described in Section 4.6.

5.6.1 Layers

Figure 5.10 shows the results of the tissue segmentation, upsampling and manual correction of the PSIR structural data to result in six equivolume modelled layers for the 9 subjects. It should be noted that, on visual inspection, the most accurate areas are the areas corresponding to V1, V2 and V3 as defined by the retinotopic mapping as these were focused on during the manual correction of the grey matter and boundary definitions.

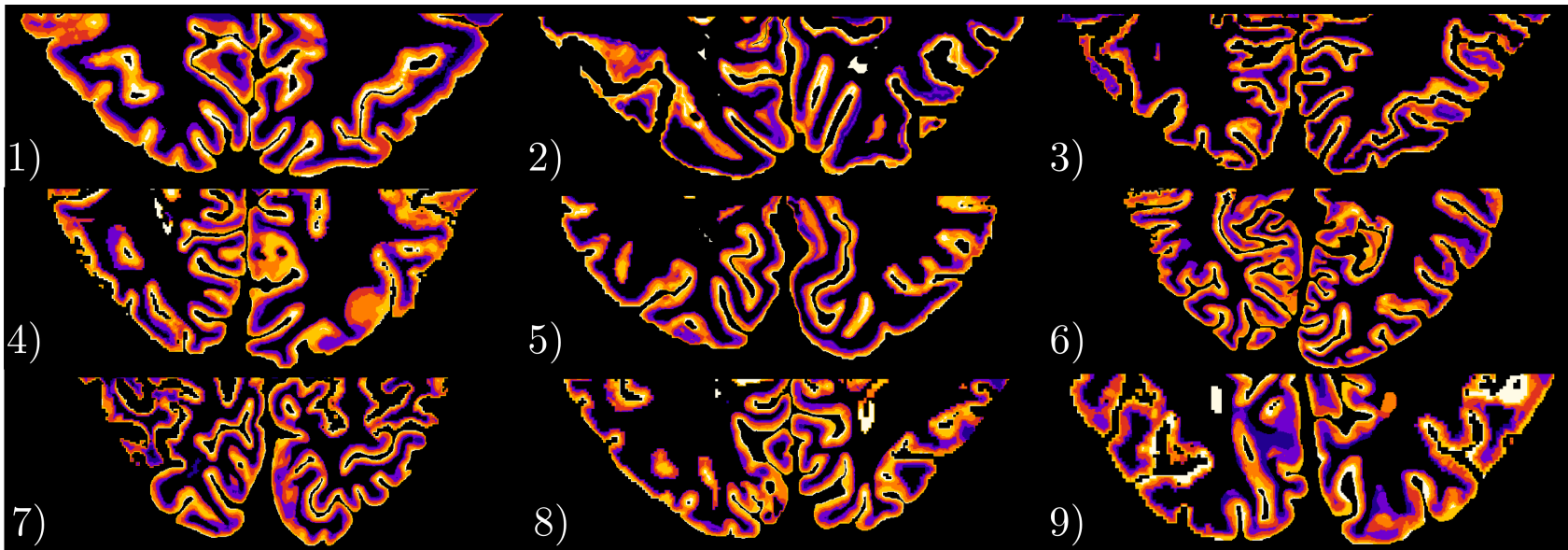


Figure 5.10: The six cortical layers modelled using the equivolume approach shown for an example single slice for each subject.

5.6.2 Columns

Figure 5.11 shows, for a given slice, the calculated cortical columns before filtering the columns for areas of alpha-BOLD activation, with 4000 columns over the entire cortical area for each of the nine subjects. Following assessment of column numbers in Chapter 4 Section 4.6.5, it was chosen to use 4000 columns. This was found to give the best chance of having β -weights in every layer for the ‘deveining’ of the data and the layer profile calculations.

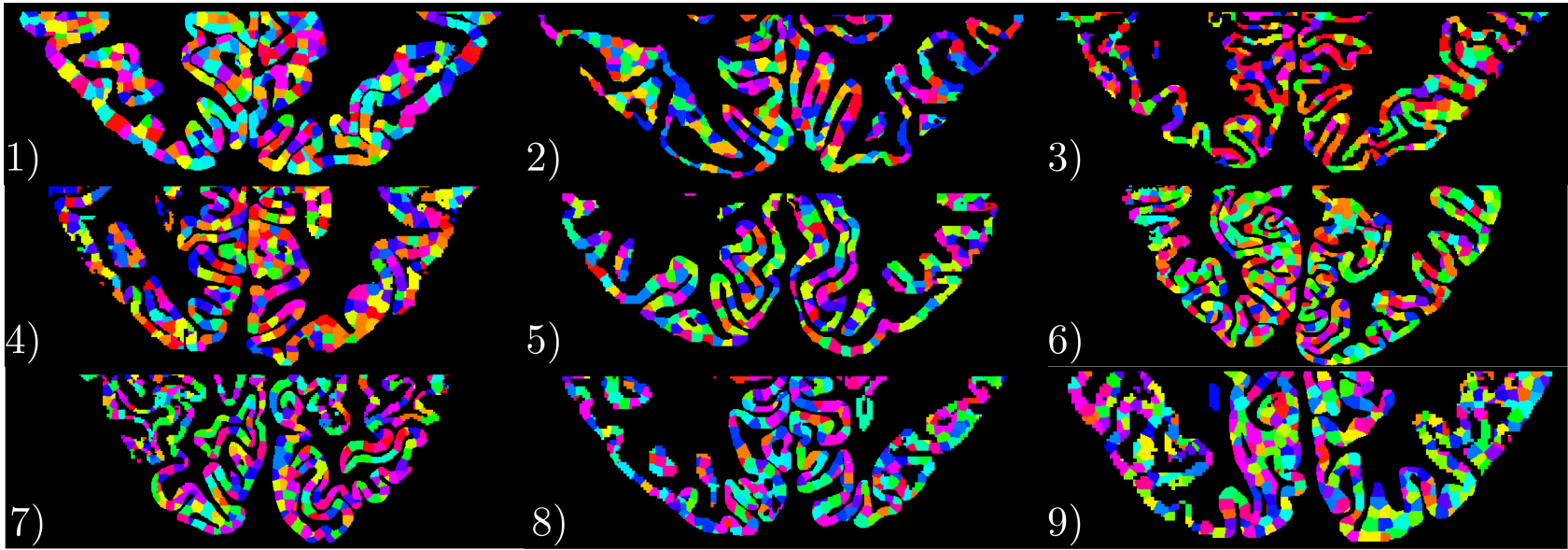


Figure 5.11: The 4000 cortical columns calculated across the whole GM ribbon shown for an example single slice for each subject.

5.7 Layer Profiles

By combining the functional and structural data, layer profiles can be calculated to show the variation of alpha-BOLD signal across cortical depths in the primary visual cortex. Figure 5.12 shows a) uncorrected and b) deconvolved profiles for the GLM using the EEG alpha power regressor with deconvolving implemented using deconvolution, as described in Section 4.30. This first analysis is performed without applying a 5% noise threshold to the data and not excluding the top 25% of columns with the most changed profiles. The uncorrected profiles in Figure 5.12a show the well documented increase in signal towards the pial surface due to draining veins seen in GE-BOLD data. After deconvolving (Figure 5.12b using the spatial deconvolution method there is a slight dip in the middle depths. There is some variance in profile shape between subjects but all subjects except for Subjects 1, 5 and 6 exhibit a ‘U’ shaped profile dipping in the middle depths. From a repeated measures ANOVA it was found that there was a significant trend ($p = 0.027$) across the cortical depths. Post-hoc t-tests revealed this is driven by cortical depths 4 ($p = 0.02$) and 5 ($p = 0.01$) being significantly lower than depth 6 and depth 3 being significantly ($p = 0.01$) lower than depth 1.

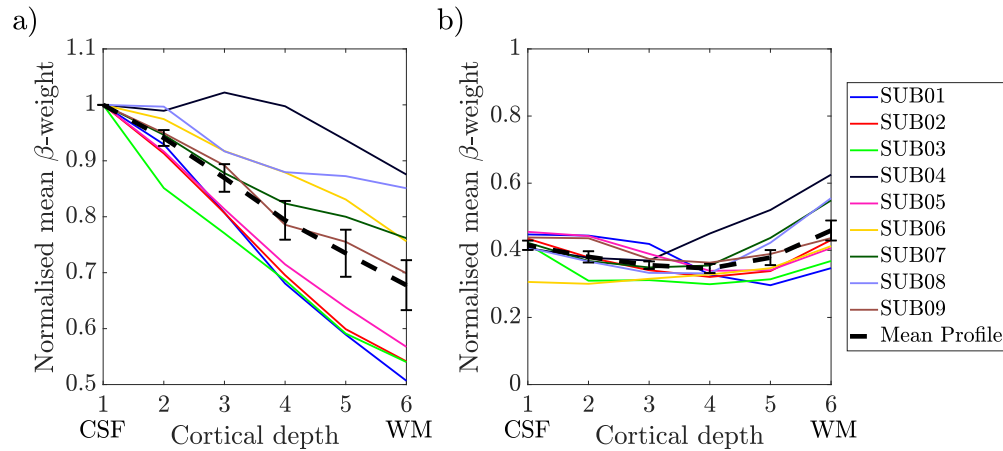


Figure 5.12: Layer profiles resulting from analysis without applying a 5% noise threshold to the data and not excluding the top 25% of columns with the most changed profiles. The weighted average over V1–3 of the variation in normalised β -weights over cortical depths for a) uncorrected layer profiles and b) deveined layer profiles. Individual subject profiles are shown with the mean over all subjects in black. Each subjects responses are normalised to the mean β -weight at depth 1 (CSF boundary) from before deveining. Error bars showing the standard error over subjects. CSF = cerebrospinal fluid; WM = white matter.

Figure 5.14 shows the layer profiles after implementing the optimal analysis methods described in Chapter 4. The analysis included using a 5% noise threshold, and excluding the top 25% of most change profiles. The deveined profiles shown in Figure 5.13 are shown as the average of all subjects for each visual ROI of V1, V2 and V3. Since the layer profiles for each visual region of V1, V2 and V3 exhibit no clear differences. The profiles were combined using a weighted average determined from the amount of activated cortical columns in each of the visual regions for the final layer profiles. The final layer profiles across V1–3 after deveining (Figure 5.14) using the optimal deconvolution method outlined in Chapter 4. This is shown for each subject. It can be seen that there is a dip in the response in the middle depths with cortical depths 4 and 5 being lower than depths 1 – 3 and 6. There is some variance in profile

shape between subjects but all subjects, except for Subject 6, have a 'U' shaped profile dipping in the middle depths. From a repeated measures ANOVA it was found that there was a significant trend ($p = 0.017$) across the cortical depths. Post-hoc t-tests revealed this is driven by cortical depths 3 ($p = 0.01$) and 4 ($p = 0.01$) being significantly lower than depth 1, and depth 5 being significantly ($p = 0.01$) lower than depth 6.

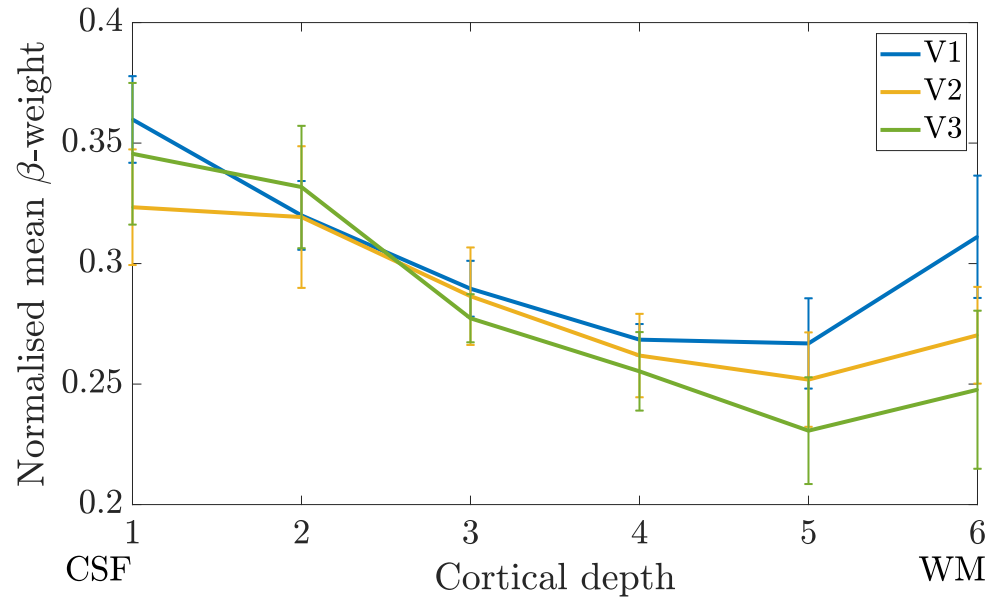


Figure 5.13: Layer profiles resulting from using the optimal analysis pipeline developed in Chapter 4. The variation in normalised β -weights over cortical depths for V1, V2 and V3 separately after deconvolving. Layer profiles averaged over subjects; error bars show the standard error over subjects. CSF = cerebrospinal fluid; WM = white matter.

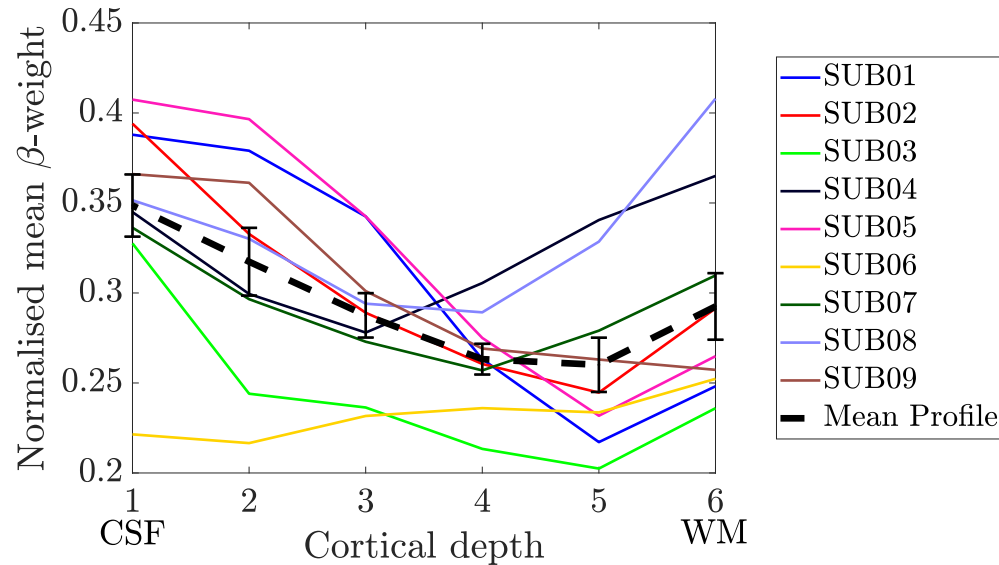


Figure 5.14: Layer profiles resulting from using the optimal analysis pipeline developed in Chapter 4. The weighted average over V1–3 of the variation in normalised β -weights over layers for deveined layer profiles. Individual subject profiles are shown with the mean over all subjects in black. Each subjects responses are normalised to the mean β -weight at depth 1 (CSF boundary) from before deveining. Error bars showing the standard error over subjects. CSF = cerebrospinal fluid; WM = white matter.

In Figure 5.15 layer profiles for the ‘deveined’ GE-BOLD for each regressor type outlined in Section 5.5 are shown. Each profile shows a similar ‘U’ shape, exhibiting a dip in the middle cortical depths. The dip for the boxcar regressor layer profile is slightly skewed towards the CSF boundary (cortical depth 1) compared to the the EEG and orthogonalised EEG regressors. From a repeated measures ANOVA on the orthogonalised EEG regressors layer profiles it was found that there was a significant trend ($p = 0.017$ for z -stat < -1.5 and $p = 0.012$ for z -stat < -2.3) across the cortical depths. Post-hoc t-tests for the orthogonalised EEG regressor (z -stat < -1.5) revealed this is driven by cortical depths 4 ($p = 0.02$) and 5 ($p = 0.01$) being significantly lower than depth 6 and depth 3 being significantly ($p = 0.01$) lower than depth 1. Post-hoc t-tests

for the orthogonalised EEG regressor ($z\text{-stat} < -2.3$) revealed this is driven by cortical depths 4 ($p = 0.02$) and 5 ($p = 0.01$) being significantly lower than depth 6, and depths 3 ($p = 0.01$) and 4 ($p = 0.02$) being significantly lower than depth 1.

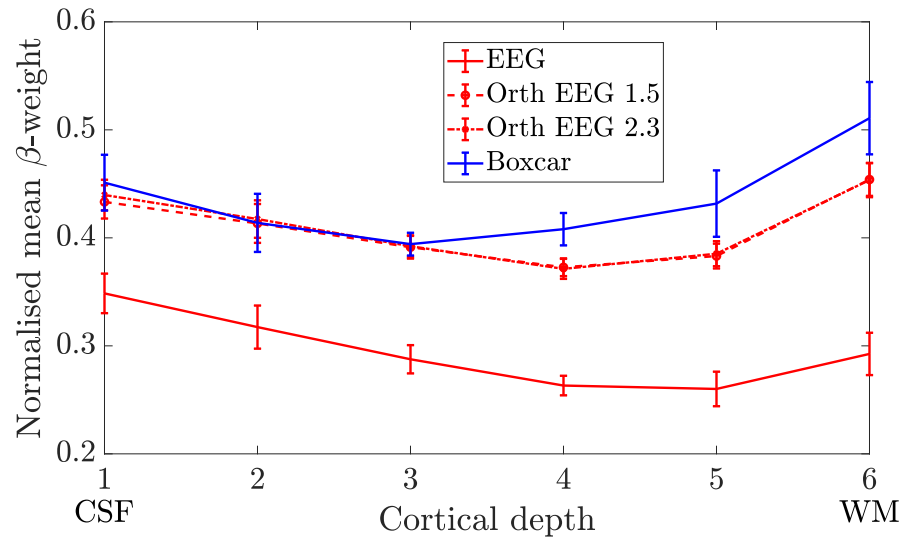


Figure 5.15: The variation in the GE-BOLD signal across cortical depths normalised to the CSF and averaged across V1–3 using different regressors in the GLM. Profiles for each regressor are given after deconvolving. Red lines show the profiles resulting from using the EEG informed regressors for the fixed effects GLM and the blue line shows the profile resulting from using a HRF convolved boxcar. Dashed lines show the results of orthogonalising the regressors with respect to one another for the fixed effects GLM.

5.8 Discussion

A novel layer-dependent EEG-fMRI dataset acquired using 3D GE-BOLD at 7 T during an eyes open/closed task was analysed using the bespoke pipeline developed in Chapter 4. The aim was to address the question ‘*What is the origin of the EEG alpha signal?*’.

First, the EEG data were successfully used to create regressors for use in the GLM analysis of the fMRI data. Data from nine of the ten subjects scanned could be used for subsequent analysis. One subject, Subject 10, was excluded due to poor EEG data quality. The fMRI data were accurately registered and aligned to the structural data. Alpha-BOLD correlations were calculated using regressors modelled from the EEG alpha power timecourse, as well as a boxcar, and orthogonalised boxcar and EEG regressors in a fixed effects GLM. The alpha-BOLD signals were negatively correlated, and spatially specific to the grey matter of the primary visual cortex, with the majority of subjects showing a good extent of activation. A separate retinotopic mapping scan was used to functionally define the visual areas V1, V2 and V3 for eight out of the remaining nine subjects, for one the Benson atlas was used. These subject specific visual ROIs aided the preparation of the structural data which were segmented and manually corrected to successfully define six cortical layers and 4000 cortical columns for all nine subjects.

Alpha-BOLD correlations across cortical depths were then calculated to assess which layers alpha oscillations were predominantly generated in, with cortical depths containing higher mean GLM β -weights corresponding to layers with higher alpha oscillation activity. The initial uncorrected profiles for all subjects showed the expected increase in signal towards the pial surface known as the draining vein effect. After correcting for this, using spatial deconvolution, a dip in the middle cortical depths is visible in the mean layer profile of all subjects across visual regions V1–3. A dip in the middle cortical depths is seen in the layer profiles resulting from using three different regressor types modelled from the EEG alpha power timecourse, a boxcar, or the orthogonalised boxcar and EEG regressors. By orthogonalising the boxcar and EEG regressors the shared descriptive variability is removed and hence the remaining variation in alpha-BOLD correlation across the layers is specific to alpha oscillation and not any other factors.

A dip in the middle cortical depths indicates that the BOLD signal was least well correlated with the EEG alpha regressors in the middle layers. This suggests that the middle layers are not the sole origin of the alpha signal and instead it can originate from deep and superficial layers. The superficial and deep layers, correspond to top-down, feedback processing [80]. The recruitment of top-down processing generates corticocortical alpha which predominantly terminates outside of layer IV [4]. This is contrary to what was hypothesised in Chapter 3, where it was stated that opening and closing the eyes would recruit bottom-up processing with thalamocortical feedforward alpha mostly terminating in layer IV [191, 192]. However, this result does align with the findings of van Kerkoerle *et al* in which they found that the alpha layer profile for a sustained visual stimuli was dominated by the deeper and superficial layers [182]. As our stimulus consisted of long 30 s periods of eyes open or eyes closed we could expect our alpha-BOLD layer profiles to exhibit a similar shape.

As the EEG signal is thought to result from dendritic PSPs in pyramidal neurons, one might expect that the EEG signal would be weighted by the cytoarchitecture of the cortical layers (see Section 3.3), with layers containing more pyramidal cells more likely to contribute to the detected EEG signals, therefore making certain layer profile shapes more likely. However, pyramidal neurons are present in all cortical layers except for layer I and pyramidal dendrites project away from the cell bodies and can synapse in other layers or regions of the cortex [193]. Therefore, the distribution of pyramidal cell bodies does not necessarily weight the EEG response. If the EEG signal is weighted to specific layers, CSD measures from depth electrodes (LFPs) would only receive currents in specific layers, but different layer profile shapes have been shown for EEG oscillatory responses in different frequency bands [46, 101].

Scheeringa *et al* also observed alpha-BOLD correlations in the deeper and superficial layers, however this was detected during a visual attention task which is known to be a top-down process and so alpha generation is expected from corticocortical loops terminating in layers outside of layer IV.

5.8.1 Limitations

One of the biggest challenges with this dataset was using the partial head PSIR acquired on the two surface array coils for the segmentation of the GM and the following modelling of the cortical layers. The two surface array coils were used to enable high SENSE acceleration factors in both the phase and slice encode directions for the 3D-EPI functional acquisitions in order to achieve a reasonable TR at sub-millimetre resolution. As such the surface coils provided high sensitivity for where they were placed (over the visual cortex) but the areas further from the coils were far noisier. The spatially varying noise was an issue when segmenting the PSIR into WM, GM and CSF, resulting in patchy tissues masks that required more manual editing, adding more time onto a very time consuming task. Alternatively, the 32 channel volume coil could have been used to acquire the data but to achieve the same spatial and temporal resolution there would be a significant drop in tSNR in the functional data as well as a large increase in the g-factor with the acceleration factors in the phase and slice direction resulting in spatially inhomogeneous noise amplification. This may be overcome by new advanced post-processing methods such as NORDIC [110] which are explored in Chapter 6 and may allow high resolution data with sufficient tSNR using a whole head RF coil.

An important element of a layer-fMRI study is having the best alignment between the structural and functional data. Functional EPI data are distorted due to B_0 field inhomogeneities and the low bandwidth in the phase encode direction causing frequency shifts, therefore pixel shifts, in the signal. It is possible to use either B_0 distortion correction or non-linear registrations to correct for these pixel shifts so that the functional and structural data are in the same ‘image’ space. But these come with compromises: 1) Applying additional registration transforms to the data is undesirable as it increases blurring and 2) using B_0 distortion correction is challenging as it requires an accurate B_0 field map and doesn’t account for changes in B_0 over time. To overcome these

issues, it is now possible to acquire T_1 mapping data with a 3D-EPI readout that matches the distortions of the 3D-EPI functional data [10], giving the option to segment the GM in native functional space. In Chapter 6 3D-IR-EPI T_1 mapping data are acquired to assess GM segmentation for VASO layer fMRI measures.

Another limitation was the limited FOV available to the subjects during the retinotopic mapping stimuli. This was due to the bore size of the 7 T MRI scanner being long and narrow limiting the visual angle. This resulted in the extent of the subject specific definitions of the visual ROIs being smaller than those of the Benson atlas.

The largest limiting factor of the data presented here is the removal of the draining vein effect from the GE-BOLD data using spatial deconvolution. The draining vein effect is a well documented artefact in layer fMRI profiles and there are multiple models describing it [166, 168, 169, 194]. ‘Deveining’ the GE-BOLD data using these models is challenging as it is dependent on excellent alignment between functional and structural data, a high quality GM segmentation, and a good estimation of CBV from the data. There is currently no gold standard so it is difficult to know if the GE-BOLD layer profile after ‘deveining’ is matching the true neuronal profile. There are multiple methods beside deconvolution available for implementation in LAYNII, however these methods do not produce layer profiles that agree with one another. To address the disparity on layer profile shapes resulting from different deveining methods a non-BOLD contrast could be acquired, such as vascular space occupancy (VASO), which isn’t sensitive to the draining vein effect and so should be a more accurate measure of the underlying neuronal signals. To test the viability of acquiring GE-BOLD data and implementing ‘deveining’ to achieve layer profiles closer to the true neuronal signals, VASO and GE-BOLD were acquired during a finger-tapping motor task and their layer profiles compared in Chapter 6.

Chapter 6

Denoising for the improved study of VASO and BOLD layer fMRI

Abstract

Vascular Space Occupancy (VASO) is an fMRI contrast that is becoming a popular alternative to Gradient-Echo Blood Oxygenation Level Dependent (GE-BOLD) contrast. As it is a T_1 based contrast, VASO does not suffer from the draining vein effect and therefore has better spatial specificity compared to GE-BOLD. However, VASO sequences have an inherently lower sensitivity than BOLD and hence a lower tSNR, making high spatial resolution acquisitions challenging. The recent development of NOise Reduction with DIstribution Corrected (NORDIC) PCA denoising enables significant gains in previously tSNR limited fMRI acquisitions. In this chapter, first the implementation of NORDIC as a tool to improve the tSNR of fMRI acquisitions is assessed. A high resolution VASO sequence is then optimised to measure layer-specific activation in the motor cortex at 7 T to compare the VASO depth profiles with GE-BOLD depth profiles following deveining. A motor task was selected as the hand knob region is good for bench marking layer-fMRI methods due its consistent folding pattern, it has a larger cortical thickness and a known layer activation profile. A finger-tapping paradigm was performed in 10 healthy volunteers to measure activation across the cortical depths. Significant activation was measured in the hand knob region of the motor cortex for both the BOLD and VASO contrast for all subjects. The mean BOLD profile exhibited the expected increase in activation towards the pial surface. The mean VASO profile consisted of a peak in the middle cortical depths, whilst the mean deveined BOLD layer profile was consistent with the VASO profile for depths 1–4 but diverged for depths 5 and 6. Finally, the implementation of NORDIC PCA on structural 3D IR-EPI T_1 mapping data is assessed. A small improvement in the fit is shown, reflected by increases in R^2 and narrowing of the FWHM of the GM and WM peaks. Greater improvements were seen for the WM which has greater thermal noise compared to the GM. The improvements were small but showed promise for the application of this to higher resolution T_1 mapping data

for the anatomical definition of layers where the contribution of thermal noise is greater.

6.1 Introduction

Vascular Space Occupancy (VASO) is an image contrast, first described over 20 years ago [195], that is sensitive to changes in total cerebral blood volume (CBV). VASO leverages the difference in T_1 relaxation time of blood and tissue to measure the changes in extravascular signals during brain activation. The changes in CBV due to vasodilation following neuronal activation are highly localised to the surrounding tissue, providing excellent spatial specificity. The greater signal localisation of VASO compared to the gradient echo (GE) BOLD signal, which suffers from spatial blurring due to the T_2^* effect from draining veins and thus larger signal at the pial surface (see Chapter 3), provides a good argument for VASO to be used for layer-dependent fMRI. This chapter will outline the testing of NORDIC PCA denoising for BOLD data before the implementation on VASO data, this is followed by the development of a high resolution VASO sequence which is used for a comparison of GE-BOLD and VASO for a layer-dependent motor fMRI study at 7 T. The chapter concludes with an assessment of the application of NORDIC to structural T_1 mapping data.

6.1.1 The Origin of VASO Contrast

VASO is an inversion recovery sequence that uses specific inversion timings such that the signal from the blood is nulled and the modulated signal from the tissue is retained. VASO was initially described by Lu *et al* in 2003 [195] who was investigating the extravascular contributions to the BOLD signal but unexpectedly observed a decrease in signal during activation. This provided a technique that was sensitive to CBV without the need for contrast agents, but that had much lower CNR compared to BOLD. At 7 T, the T_1 of blood is ~ 2100 ms [13, 196] and the T_1 of tissue is ~ 1950 ms [11, 12]. The convergence of the T_1 of blood and tissue when moving to higher field strengths reduces the CNR of VASO posing further challenges for layer-fMRI VASO. Venous

and arterial blood have similar T_1 [195] relaxation times so an optimised TI should achieve near-complete nulling of all blood and give the best estimation of total blood volume. After a non-selective inversion pulse, the null point – the time at which the magnetisation crosses zero differs for blood and tissue due to their differences in T_1 , see Figure 6.2. The VASO signal is acquired at the null point using a single shot, either a 2D-EPI with a 90° RF pulse per slice or a 3D-EPI using a train of RF pulses to excite a volume. Figure 6.1 describes the change in the magnetisation of blood and grey matter in a single voxel during a VASO acquisition. Initially the magnetisation, M_z , of blood and grey matter are inverted (Figure 6.1b), after an inversion time, TI_1 , the blood M_z is zero and is therefore nulled (Figure 6.1c) while the tissue signal has recovered quicker and is beyond the null point. During brain activation, the vessels in the capillary bed dilate, causing an increase in CBV. An increase in CBV means that there is a larger volume of nulled blood in the voxel that therefore does not contribute to the detected MR signal (Figure 6.1d), therefore the VASO signal decreases upon brain activation.

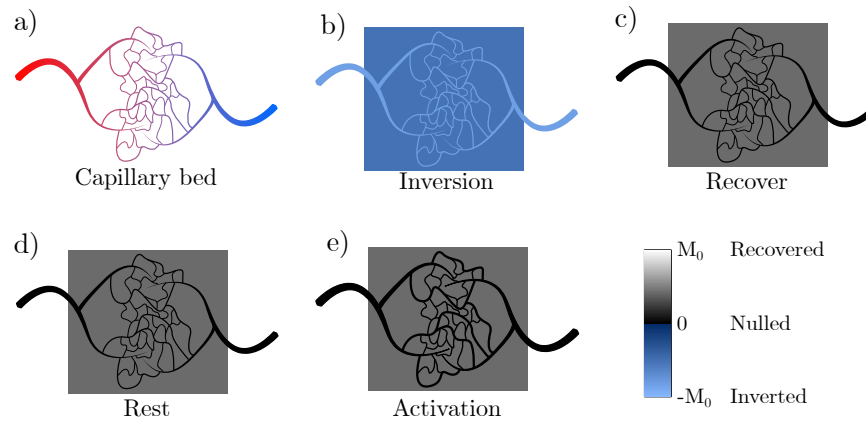


Figure 6.1: Schematic showing the change in the magnetisation, M_z , in a voxel during a VASO acquisition. b) M_z of the blood and grey matter is inverted. c) After inversion time TI_1 , M_z recovers faster for grey matter than blood and the MR signal from the blood is nulled. d) The brain tissue is at rest and the blood is nulled e) Upon activation the blood vessels dilate, the increased CBV results in an overall decrease in the detected MR signal.

Due to the T_2^* decay there is only a short window to acquire the signal, therefore it is challenging to acquire EPI images with large coverage and high spatial resolution in reasonable time. VASO sensitivity can be improved by using a higher field strength, which yields higher SNR, however this comes with additional challenges. As field strength increases, the T_1 of blood and tissue converge, reducing the tissue-blood signal difference received from the tissue at the nulling point for a non-selective VASO slab. In addition to this, the BOLD signal increases at higher field strength, enhancing the need for BOLD correction. Another challenge specifically for VASO acquisitions collected with high spatial resolution or large brain coverage is the change in intensity in the VASO signal across the readout due to the T_1 decay over long readout trains. For a 2D-EPI readout this will result in altered VASO sensitivity across each slice in the volume. For a 3D-EPI readout the VASO sensitivity will be constant over a volume but the flip angle for each segment in the readout in the image needs to be carefully adjusted to achieve constant magnetisation else blurring

occurs in the image. Gai *et al* used Variable Flip Angles (VFAs) for a 3D-EPI ASL acquisition [197], and showed that by using a range of flip angles across the 3D-EPI RF pulses the magnetisation of the grey matter can be maintained constant over the readout train, resulting in a reduced point spread function (PSF) for the acquired EPI data.

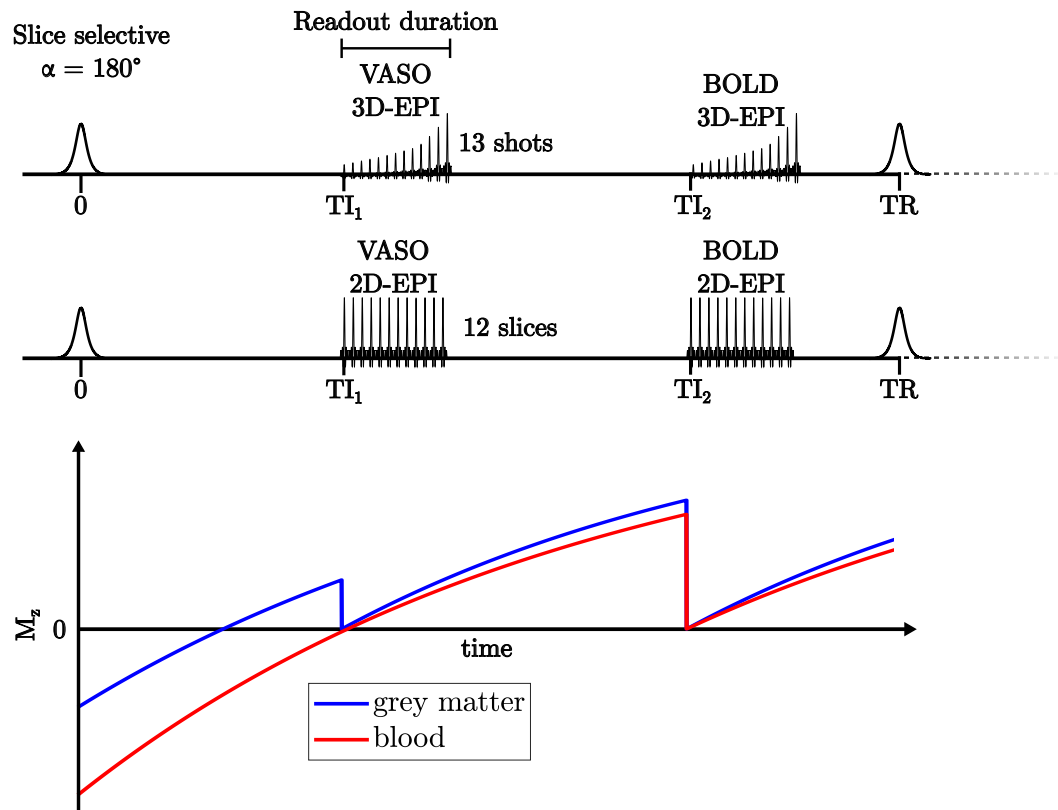


Figure 6.2: VASO pulse sequence diagram. The first readout at TI_1 acquires blood-nulled VASO data and the second readout at TI_2 acquires BOLD weighted data that can be used to correct the VASO data for T_2^* dependence. Shown is a 3D-EPI readout with 13 shots and a variable flip angle (top) and a 2D-EPI readout with 13 shots and a constant flip angle (middle). The recovery of the longitudinal magnetisation following a RF inversion pulse simulated for 7 T. Simulated using a T_1 of 2100 ms of blood and a T_1 of 1800 ms for grey matter and an inversion efficiency of 0.75.

Advances in the VASO sequence have been implemented to improve functional sensitivity. Work on cats at 9.4 T by Jin and Kim [198] proposed the use of a slice specific inversion at the start of the VASO sequence meaning that after each image acquisition the slab would be filled with fresh blood, hence replacing the steady-state blood magnetisation and increasing signal. Implementing slab inversion VASO (SI-VASO) improved CNR by an order of magnitude compared to the original VASO sequence. This study was also one of the first layer-dependent VASO studies to be performed.

In 2013, Huber *et al* further addressed the issues VASO has at high field strengths. Building on the SI-VASO method of Jin and Kim, they maximised the tissue magnetisation at the nulling point by applying multiple RF excitation pulses to saturate the tissue signal shortly before the slab inversion [199]. This results in the tissue magnetisation recovering to a larger magnitude before the blood nulling point and therefore a larger signal. Additionally, the period during which the RF excitation pulses are applied can be used to acquire BOLD contrast data which can then be later used to correct the BOLD contamination of the VASO signal. This sequence was termed slice saturation slab inversion VASO (SS-SI-VASO).

6.1.1.1 Correction of BOLD contamination in the VASO signal

As T_2^* changes with activation, it is important to factor out signal changes due to T_2^* changes from the VASO signal so that what remains is solely proportional to changes in CBV. This correction is achieved by normalising the signal acquired at the blood nulling point (TI_1), S_n , to the signal acquired at blood-not-nulled readout (TI_2), S_{nn} . When the not-nulled image is acquired at TI_2 the relative longitudinal magnetisation, M_z , of the GM and blood are very similar, therefore it is assumed the M_z of parenchyma (blood and tissue), $M_{z,GM,n}$, is constant and independent of brain activation. It assumed that at high field strengths the T_2^* of parenchyma and extravascular tissue are equal so after division, the effects of T_2^* and hence the BOLD response are cancelled out.

$$\frac{S_n}{S_{nn}} = \frac{M_{z,GM,n} \exp\left(-\frac{TE}{T_{2,GM}^*}\right)}{M_{z,par,nn} \exp\left(-\frac{TE}{T_{2,par}^*}\right)} \approx \frac{M_{z,GM,n}}{const} \sim 1 - CBV \quad (6.1)$$

It is important to note that this division method only corrects for the extravascular contributions to the BOLD signal change which accounts for 90% of the total BOLD signal change at 7 T [200].

6.1.2 Applications of VASO

In recent years, the development of VASO has continued, predominantly focusing on validation and comparison to layer-dependent BOLD fMRI methods. As a result it is gaining popularity as a technique for layer-dependent fMRI studies. Seminal work by Huber *et al* compared the VASO and BOLD signal across cortical depths in humans during a finger-tapping task at 7 T [116]. The expected double peak pattern of neuronal activity in M1 of the motor cortex was seen for the VASO data but not for the BOLD data, this was compared to layer profiles from animal models seen in the literature. This work highlighted the specificity and reproducibility of VASO CBV measures and also its lower sensitivity to draining veins compared to GE-BOLD.

Further comparisons of BOLD and VASO have been conducted to take advantage of VASOs greater spatial specificity compared to BOLD. Oliveira *et al* used VASO-fMRI at 7 T to assess digit representations resulting from BOLD and VASO contrasts during a finger-tapping task [201]. They found that VASO-CBV measures resulted in less overlap between digit representations than BOLD and that other selectivity measures were also improved.

Layer-dependent VASO fMRI has also been applied to a patient group with focal hand dystonia [202]. This work found that for dystonia affected hemispheres there is a breakdown in ordered digit representations in the primary somatosensory cortex. The layer analysis revealed that in dystonia affected primary motor cortices there was increased fMRI activity in layers II and III

(associated with cortico-cortical input) compared to relatively weaker activity in layers V and VI (associated with output).

The application of layer-dependent VASO to neuroscience has mostly consisted of tasks that stimulate the primary motor, somatosensory or visual cortex. Recent work on the human somatosensory cortex at 7 T by Yu *et al* investigated laminar activation during sensory input and predictive feedback using VASO [203]. They found that during sensory input, the middle layers showed the highest activation while prediction inputs led to higher activity in the superficial and deep layers being observed. These findings agreed with the previously hypothesised thalamic feedforward processing during sensory input and the cortico-cortical feedback processing during predictive processing.

6.2 Implementation of NORDIC denoising

Observing layer dependent signals is challenging due to the inherently low signal-to-noise ratio (SNR) of the MR acquisitions used (BOLD, ASL, VASO), when pushing to high spatial resolution. There are a number of pre-processing stages that can be used to improve the effective image SNR of the imaging data, but it is important to do so without compromising the temporal SNR and spatial resolution of the data. Spatial smoothing is a tried and tested way to increase SNR, however for high spatial resolution layer-specific fMRI data this would be detrimental, as in this situation spatial localisation of signals is paramount [204].

Multiple methods have been developed which aim to increase SNR by denoising using principle component analysis (PCA) [205–207]. Currently a popular method is the Marchenko-Pastur PCA (MP-PCA) [208]. This method implements a local patch based PCA on the magnitude MR data. A threshold for the singular value decomposition components is calculated analytically using random matrix theory by using the tail of the spectrum of singular values. The

threshold leads to the removal of the components that have little contribution to the variance of the data.

In 2021 Moeller *et al.* proposed a new method known as NOise Reduction with DIstribution Corrected (NORDIC) PCA [110] has been published which builds on MP-PCA. This provides a data driven approach for the thresholding of the singular values. This has been shown to provide impressive improvements in image SNR for diffusion [110] MRI and temporal SNR for functional MRI [111] data. It is important to note that the noise in MR magnitude images is not Gaussian but Rician or non-central χ^2 distributed [209], as shown in Figure 6.3a, therefore the effectiveness of noise reduction techniques that are based on Gaussian assumptions are reduced.

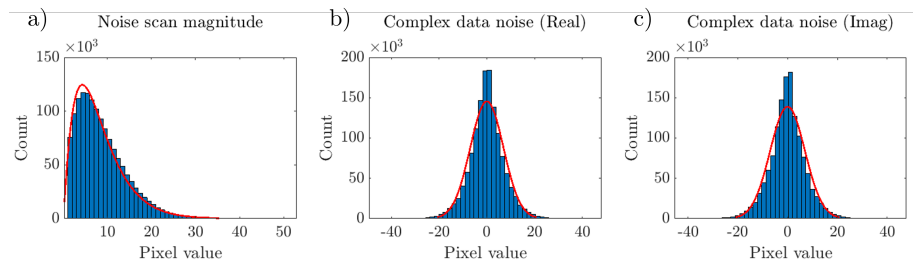


Figure 6.3: Histograms showing the distribution of pixel intensity values in the noise scan of an MRI dataset. The (a) magnitude data clearly shows a non-Gaussian, non-zero mean distribution, whereas the (b) real and (c) imaginary components of the complex data have zero-mean Gaussian distributions.

NORDIC PCA is a method that ensures the removed noise components are independent and are identically distributed as zero-mean Gaussians by using the complex data. With these constraints, an objective parameter-free threshold can be calculated which results in the removal of noise that is indistinguishable from Gaussian noise. NORDIC PCA requires both magnitude and phase data to be acquired along with a noise scan collected with no RF. The NORDIC analysis pipeline prepares the MRI data using the following steps: (1) Combining the magnitude and phase MR data to construct complex real and imaginary data

in which the noise distribution is zero-mean Gaussian (as shown in Figure 6.3b and 6.3c); (2) Mapping the spatially varying noise to spatially uniform noise using the parallel imaging g-factor; and (3) Calculating the threshold for singular values explicitly from the noise spectrum of the MRI data. In terms of fMRI data, NORDIC should be effective at removing thermal noise but not physiological noise from the timeseries.

The next sections outline work on implementing NORDIC on BOLD data collected on a 7 T Philips Achieva MR scanner.

6.2.1 Implementation of NORDIC on Philips data

As a first test, the 3D-EPI protocol used in Chapter 4 (with the two 16-channel receive surface coils) was acquired at rest for 40 dynamics + 1 noise scan using the 32-channel NOVA receive head coil with high SENSE factors in both the phase and slice (P&S) directions with a TR of 3.8 s. Acquiring this data on the 32-channel NOVA receive head coil rather than the receive surface coils hugely reduced the image (and temporal) SNR and the high SENSE factors would result in large g-factor noise amplification, thus testing the limits of NORDIC.

NORDIC was available online on GitHub (https://github.com/SteenMoeller/NORDIC_Raw) to download and implement in MATLAB. The NORDIC code provided options to run with or without phase data, with or without a noise dynamic and the patch size for the local PCA data could also be set. Upon inspection of the 3D-EPI data, after applying NORDIC denoising using the magnitude and phase data, including a noise dynamic and the default patch size, it was clear that NORDIC had failed and removed the majority of the signal in the image. Until this point in time, NORDIC had been developed and tested on data from Siemens scanners, but not Philips data. It was likely that the differences in handling the data acquired on the different vendors were causing these issues, and so this was discussed with the developer (Dr Steen Moeller).

On closer inspection, the issue with the Philips data was found to result from irregularities in the calculation of the g-factor within NORDIC. This led to the threshold calculated from the noise spectrum being far too high and the majority of PCA components being removed from the data. Despite the Philips data being collected with a large dynamic range of 2×10^5 , the noise scan of this data had a poor dynamic range, with only ~ 50 unique values with large steps between each value, as shown in Figure 6.4. NORDIC had been developed such that it expected continuous integer values from 0 to 4096, as is generated by Siemens scanners, so the large steps in the Philips data were causing NORDIC to fail.

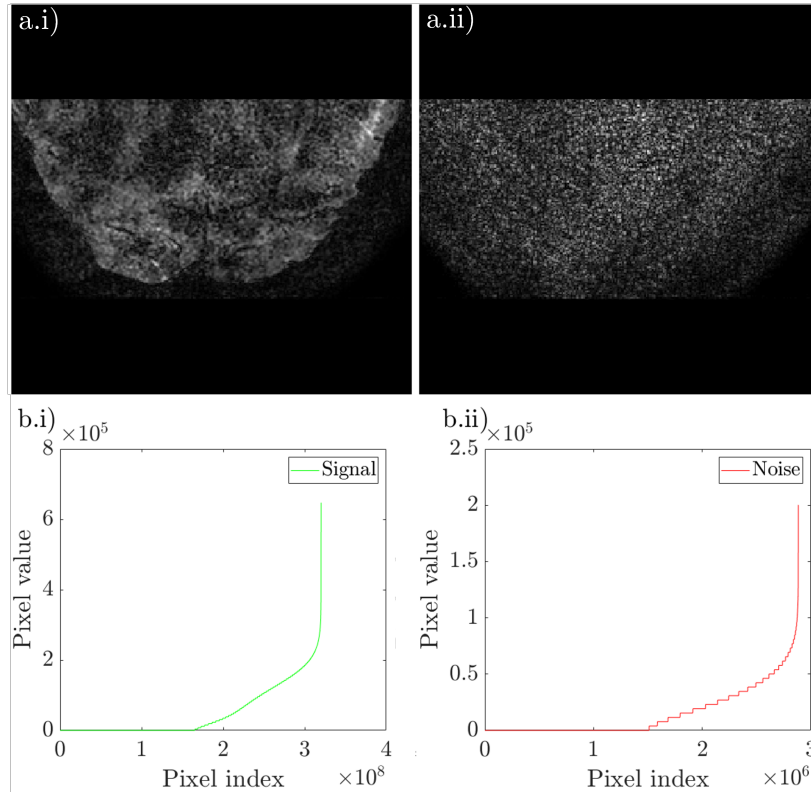


Figure 6.4: Plots showing a) a single dynamic of the the 0.8 mm isotropic 3D-EPI data for the signal (a.i) and the noise dynamic (a.ii), and b) pixel value versus pixel index for the signal (b.i) and the noise (b.ii) acquired using the 32-channel NOVA receive head coil. It was found that NORDIC failed to correct this dataset, leading to the loss of the majority of the signal from the image.

The issue of poor dynamic range was solved by changing the Scan Control Parameter (SCP), ‘SNR Maxima’ on the Philips system. The initial 3D-EPI acquisition was acquired with a default SCP of ‘SNR Maxima’ of 600 which gave a large step size, and could not be corrected. By changing the ‘SNR Maxima’ SCP to 100 and collecting a new dataset this increased the number of unique noise values. This is shown for a more standard 1.5 mm isotropic 2D-EPI dataset in Figure 6.5. For this dataset, the number of unique signal values in the image data increased from 298 for ‘SNR Maxima = 600’ to 1726 for ‘SNR Maxima = 100’. The number of unique noise values increased from

38 for ‘SNR Maxima = 600’ to 134 for ‘SNR Maxima = 100’. The large steps between values that caused NORDIC to fail were corrected for in the NORDIC code by dividing the input data by the step size between the values. In addition, the SCP ‘Noise Clip Factor’ was also changed from the default value of 1.15 to 0.01 to ensure the data was not tightly clipped to remove background noise.

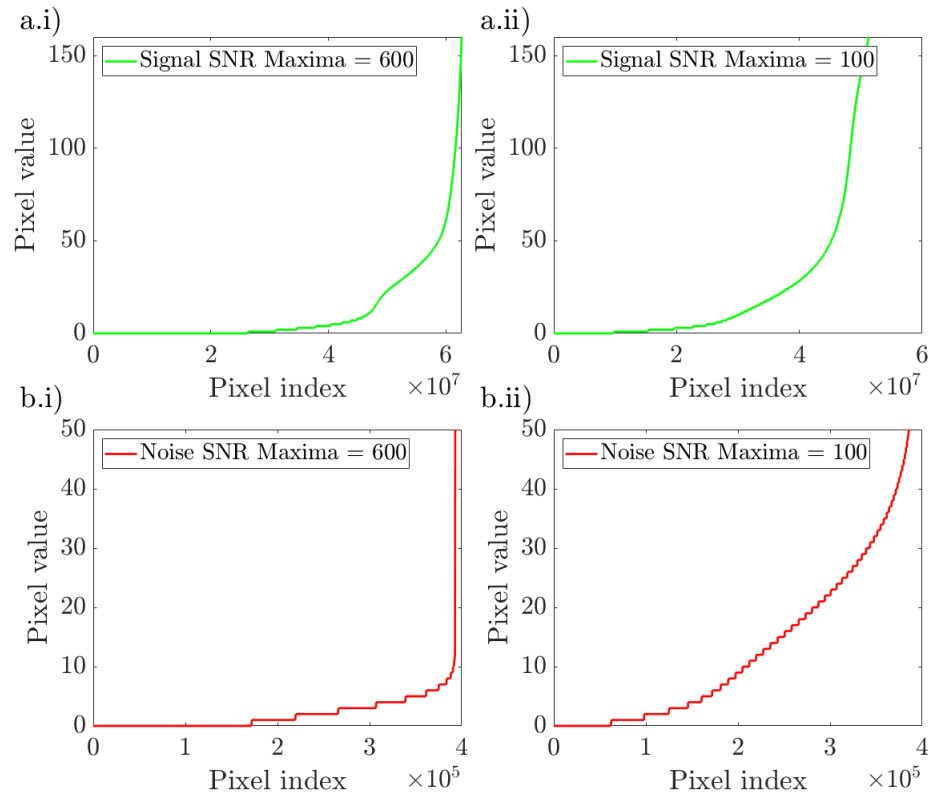


Figure 6.5: Pixel value versus pixel index for the (a) signal and (b) noise for the 1.5 mm isotropic 2D-EPI data acquired with ‘SNR Maxima’ set to (i) 600 and (ii) 100.

6.2.2 Testing NORDIC implementation in different SNR regimes

A small pilot study was then run to test the adaptations to the NORDIC code and setting of the SCPs. For this, 2D-EPI datasets (spatial resolution of 1.5 mm isotropic and SENSE 2) were acquired at a range of flip angles (FA) to adjust

the image SNR in a defined way. By deliberately acquiring low FA data that is dominated by thermal noise, as opposed to physiological noise, we could imitate the thermal noise dominated regime of high spatial resolution fMRI. Functional finger-tapping task data were acquired to assess the impact of NORDIC PCA on the image and temporal SNR, and the detection of the BOLD response.

6.2.2.1 Methods

A simple left hand finger-tapping paradigm was designed to induce brain activation in the motor cortex. The subject lay supine in the scanner bore and viewed a projector screen with prism glasses. The subject was prompted to ‘TAP’ or ‘REST’ by commands displayed on the projector screen. Each run began with a 20 s ‘REST’ period followed by ten blocks of 10 s ‘TAP’, 20 s ‘REST’ (see Figure 6.6).

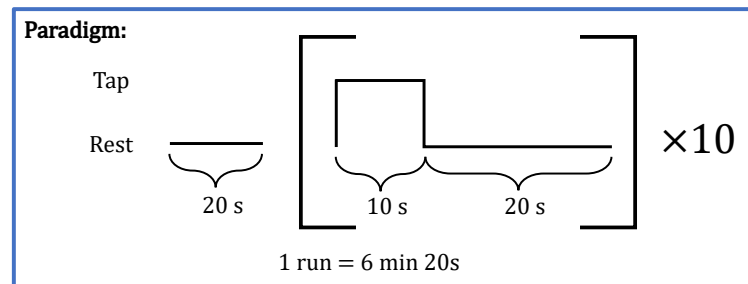


Figure 6.6: Finger-tapping paradigm used to stimulate the motor cortex.

2D gradient echo EPI (GE-EPI) data were collected during the finger-tapping task using the 32-channel receive NOVA head coil. Sequence parameters comprised 1.5 mm isotropic resolution, TE/TR = 27/2000 ms, matrix size 128×126 , no multiband, SENSE 2 (reconstructed matrix = 128×128), 24 slices in an axial orientation. Datasets were collected at a range of flip angles of 5° , 10° , 20° , 40° , 60° , 80° to change the image SNR of the acquisition. A single scan consisted of 161 volumes with the final volume being a noise scan collected with no RF and no gradients, resulting in a scan duration of 5 min 22 s. For the acquisitions the SCPs of ‘SNR Maxima’ and ‘SNR clip factor’ were

set to 100 and 0.01 respectively and both the magnitude and phase data were saved. NORDIC correction was then applied to each of the datasets. The iSNR, variance and tSNR across volumes were computed pre- and post- NORDIC. iSNR was calculated by dividing the mean of all the magnitude dynamics by the mean of a patch of background signal outside the brain and corrected for the Rician distribution of MR noise by multiplying by 0.655 [210]. tSNR was calculated by dividing the mean of all dynamics by the standard deviation across dynamics.

The 2D GE-EPI data were motion corrected (FSL FLIRT) and input into a fixed-effects GLM. Regressors for the GLM were calculated using a boxcar of the stimulus convolved with a double gamma HRF (time-to-peak of 6 s). The GLM produced z -stat maps which were thresholded at $z > 3.1$ and cluster corrected ($p < 0.05$). A small ROI covering the hand knob region of the motor cortex in the right hemisphere was hand drawn to assess changes in z -stats pre- and post- NORDIC. Within this ROI the mean and maximum z -stat was calculated and the number of voxels with $z > 3.1$ were counted.

6.2.2.2 Results

Figure 6.7 shows the iSNR pre- and post- NORDIC across each of the flip angles. Increases in iSNR post NORDIC are seen for all flip angles, with the higher FA data (80° , 30° , 20°) having a greater absolute increase in iSNR than the lower FA data (10° , 5° , 2°). The increases in iSNR are seen in the GM and near the surface of the brain. For fMRI studies, a key measure is the change in the variance across volumes, and the resultant tSNR.

Figure 6.8 shows a map of the variance in the signal over time for each flip angle pre- (Figure 6.8a) and post- (Figure 6.8b) NORDIC correction. For the FA 5° data, before NORDIC there is a high variance across the entire brain, indicating a dominance of thermal noise. After NORDIC, the regions of high variance are localised to the cortical GM, indicating the removal of thermal noise and that physiological noise is now the dominant source of variance. For

higher flip angles, pre- NORDIC high variance is mostly localised to the cortical GM with less evidence of thermal noise throughout the WM. Post NORDIC, the high variance due to physiological noise is still present in the GM but there is a reduction in variance across the WM, indicating a reduction in thermal noise.

Figure 6.9 shows the tSNR, pre- and post- NORDIC for each of the flip angles. Increases in tSNR post NORDIC are seen for each of the flip angles, with the lower FA data (2° , 5° , 10°) showing a greater increase than the higher FA data (20° , 30° , 80°), as was seen in the variance maps above in Figure 6.8. As expected, the increases in tSNR are seen predominantly in the WM and are greatest towards the centre of the brain.

Figure 6.10 shows the z -stat maps from the fixed effects GLM in response to a finger-tapping task pre- and post- NORDIC for each FA. Increases in activation are seen post-NORDIC for all FAs. Higher FA (above the thermal noise limit) z -stat maps see little improvement when inspected visually, in keeping with lower gains of tSNR, whilst the lower FA data see notable improvements, especially the 5° and 2° flip angles.

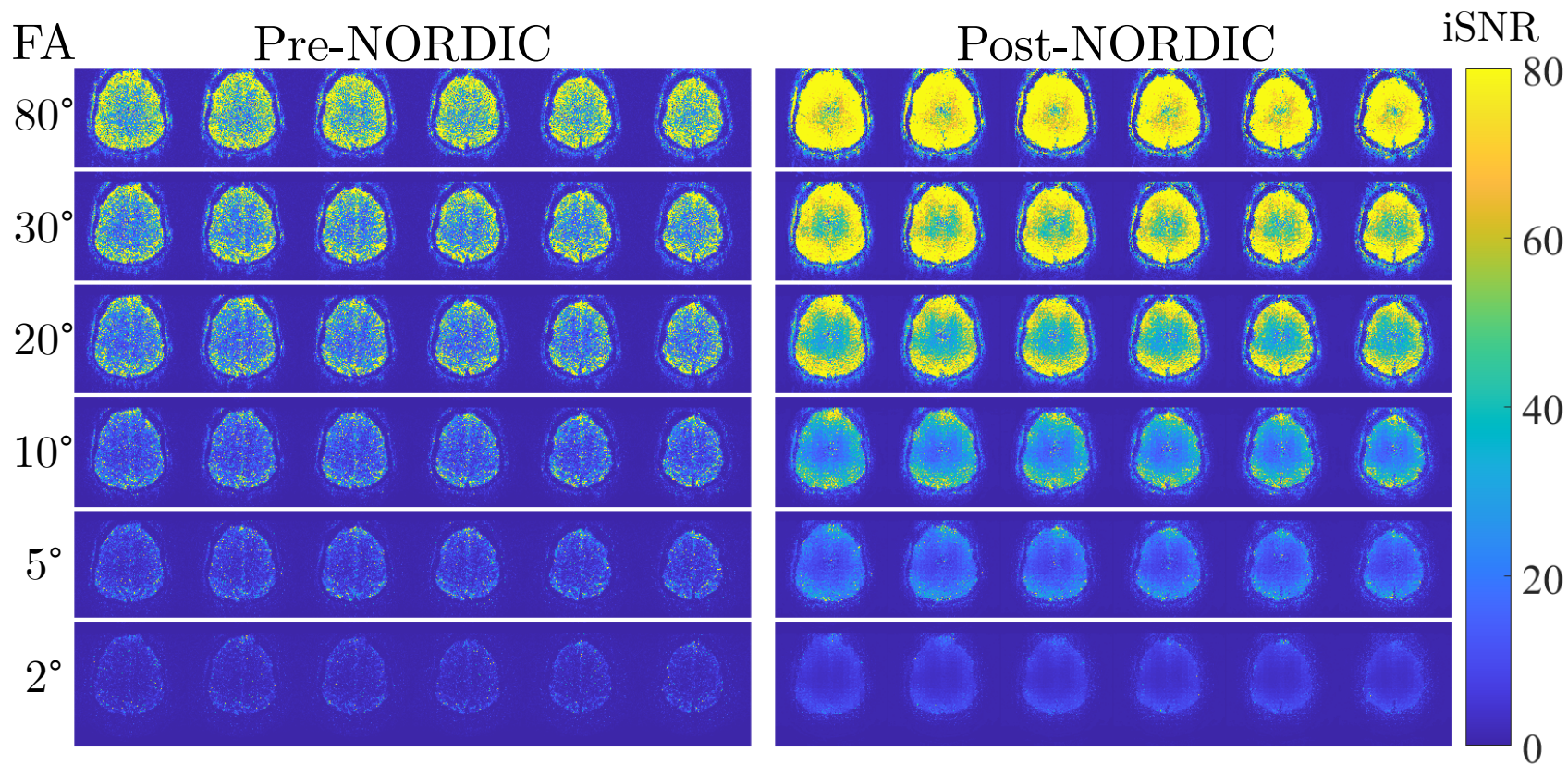


Figure 6.7: *iSNR* for a subset of the 2D-EPI 1.5 mm isotropic slices covering the motor cortex. Data shown for each flip angle (FA) pre- (left) and post- (right) NORDIC correction.

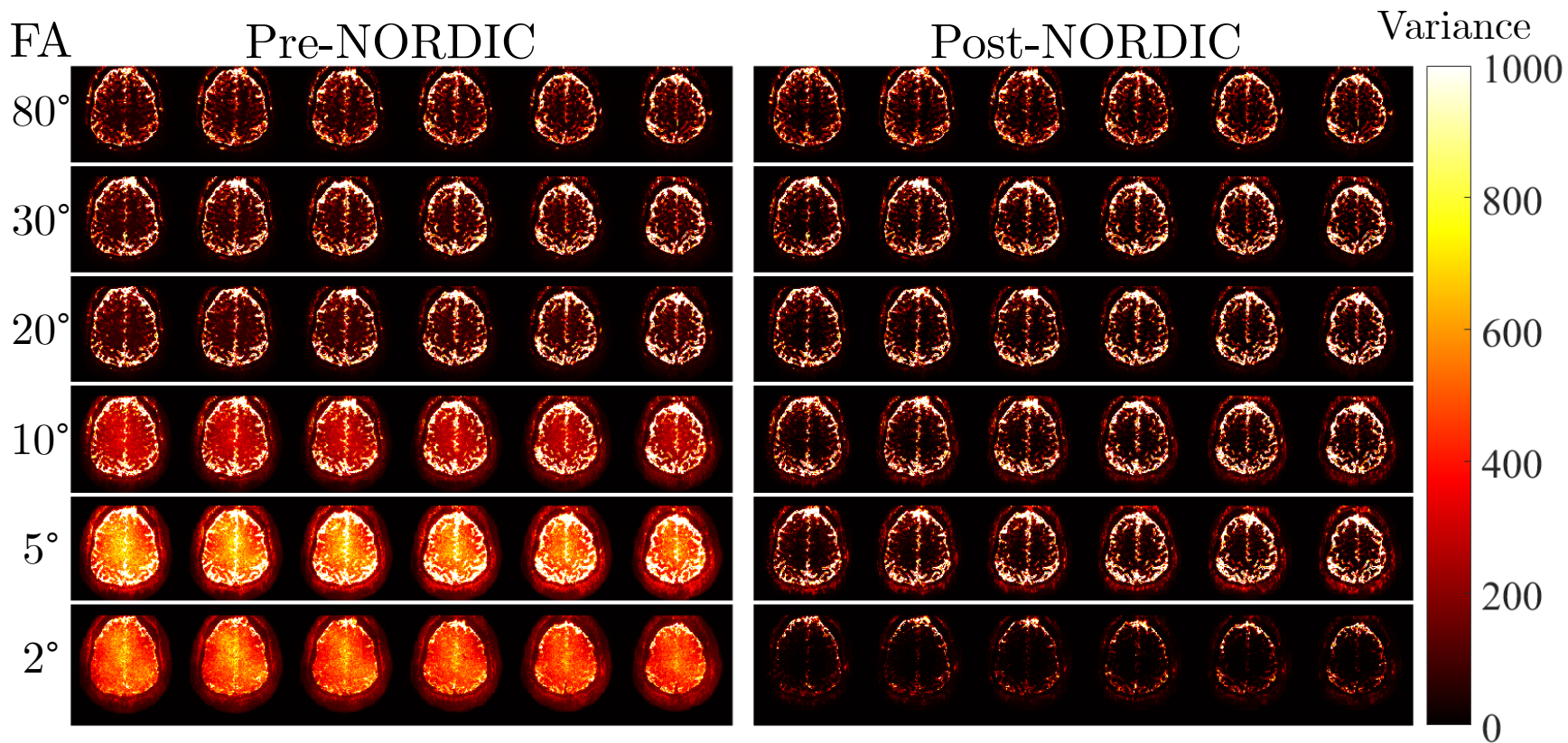


Figure 6.8: Temporal variance for a subset of the 2D-EPI 1.5 mm isotropic slices covering the motor cortex shown for each flip angle (FA) pre- (left) and post- (right) NORDIC.

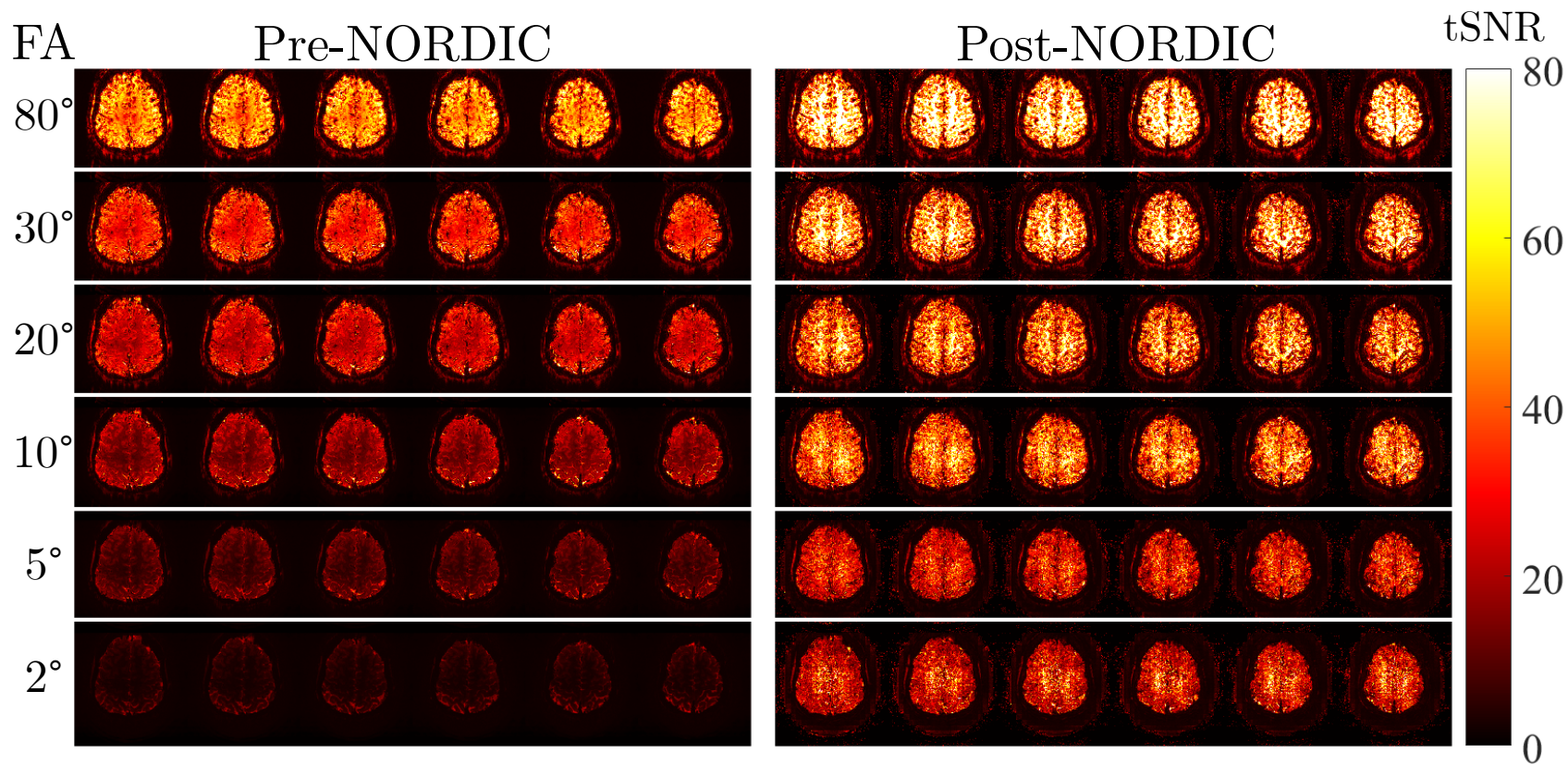


Figure 6.9: $tSNR$ for a subset of 2D-EPI 1.5 mm isotropic slices covering the motor cortex shown for each flip angle (FA) pre (left) and post (right) NORDIC.

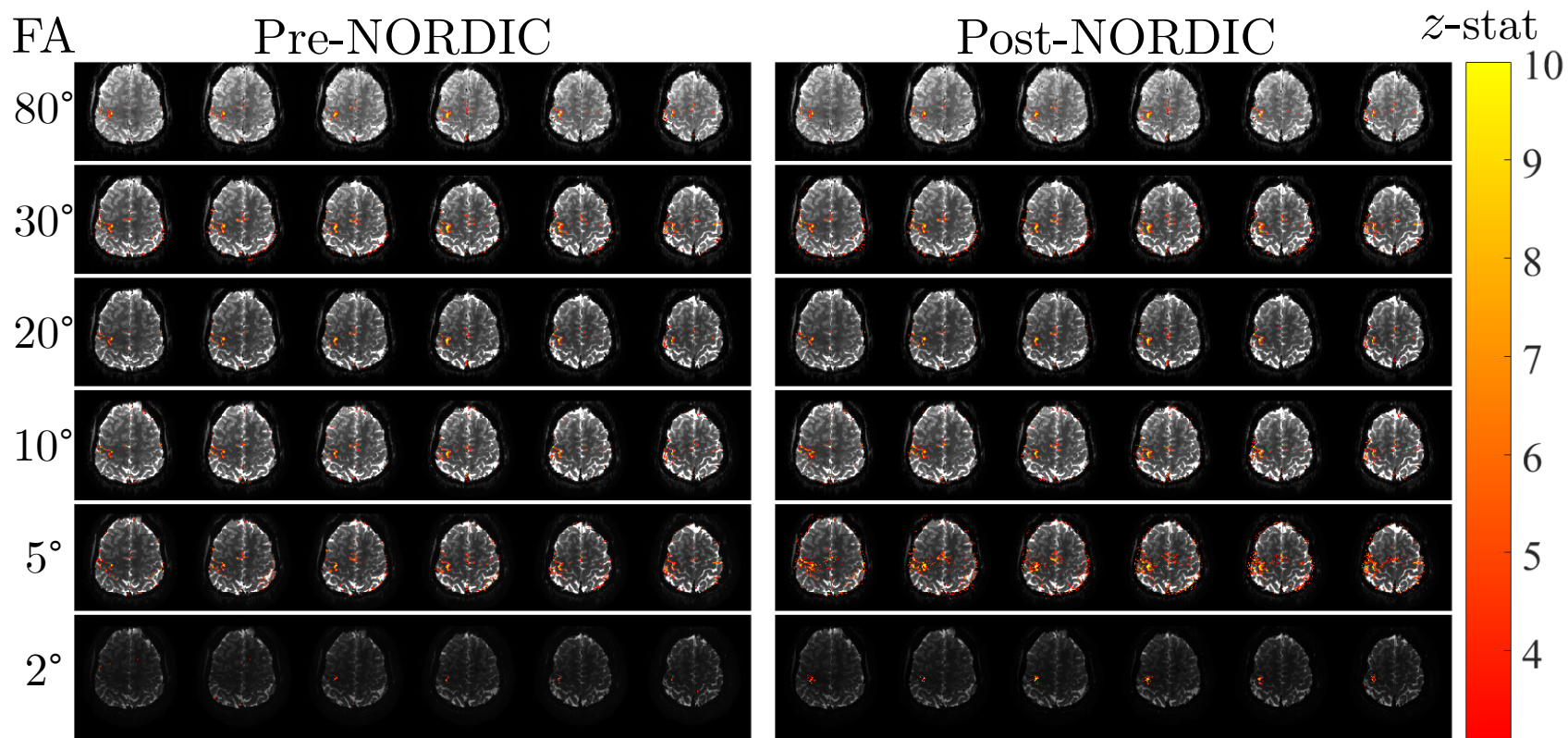


Figure 6.10: z -stat maps from the GLM analysis with a $z > 3.1$ threshold, and cluster corrected, $p < 0.05$, overlaid on the mean 2D GE-EPI image for a subset of slices covering the motor cortex shown for each flip angle (FA) pre- and post-NORDIC.

Figure 6.11 shows the quantitative improvements in the z -stat maps from Figure 6.10. Figure 6.11a shows the hand drawn ROI in the motor cortex used to compare the maximum, mean and extent of z -stats between the different FA scans. Figure 6.11b shows the increase in mean z -stat in the motor cortex ROI post NORDIC, with a greater increase for FA 2° , 5° and 10° than FA 20° , 30° and 80° . A similar finding can be seen for the maximum z -stat within the ROI (shown in Figure 6.11c) with the lower FA having much higher maximum z -stats after NORDIC than before. The spatial extent of the z -stats over the $z > 3.1$ threshold also increases to a greater extent for the lower FA than the higher FA, with FA 80° showing no increase in spatial extent between pre- and post- NORDIC.

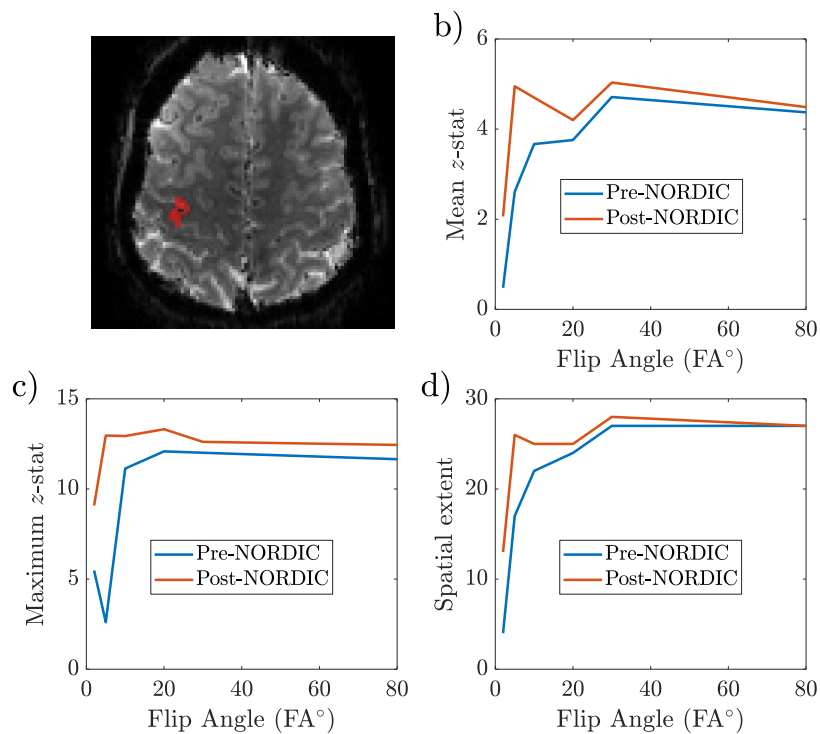


Figure 6.11: Quantitative fMRI metrics in the motor ROI pre- and post-NORDIC. Data is shown for: a) Mean z -stat b) Maximum z -stat and c) Spatial extent of $z > 3.1$ across flip angles.

Figure 6.12 shows the impact of NORDIC on the timecourse of the voxels within the ROI in Figure 6.11. Looking at the mean timecourse within the ROI, the highest similarity between the pre and post NORDIC data is seen for the 80° and 30° flip angles. Despite the fact the timecourses have been calculated by averaging across multiple voxels, there are still notable differences in the timecourses for the 2° and 5° flip angle data. For the lower flip angles the temporal variance in the timecourse is visibly reduced post NORDIC and the timecourses look very similar to the 30° and 80° timecourses. Importantly, the integrity of the denoised timecourses for the higher flip angles has not been effected. That is to say that NORDIC appears not to be removing physiological signal of interest. However, it would be good to conduct further timecourse analysis [211] to assess this in future.

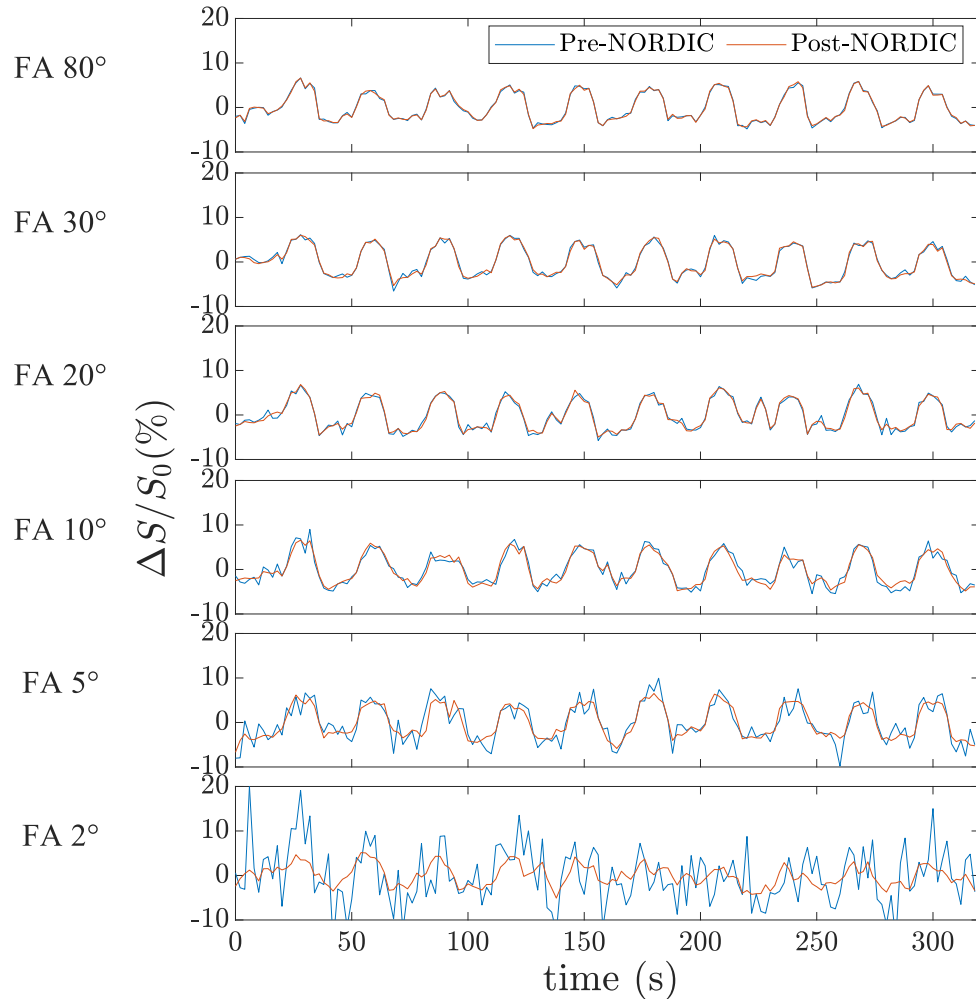


Figure 6.12: Mean timecourse as percentage change from baseline from the motor ROI pre- (blue) and post- (orange) NORDIC shown for all flip angles.

6.2.2.3 Discussion

It has been shown that for 1.5 mm isotropic 2D GE-EPI data collected with a low FA, a regime where thermal noise dominates, after NORDIC correction there is a large reduction in temporal variance across the entire brain. The largest reductions in temporal variance are seen in the white matter. Areas of remaining high variance arise due to physiological noise localised to the GM. At higher FAs, where physiological noise is dominant, there is little reduction

in variance seen in the GM but a small reduction is seen in the WM, again indicating that thermal noise is being removed.

When applying NORDIC PCA to the 1.5 mm isotropic GE-BOLD fMRI data acquired at a range of FAs, the resulting activation maps are seen to increase in both z -stat and spatial extent for low FAs where the data is in the high thermal noise regime, but little to no change is seen for higher FAs which have far less thermal noise. Reduction in the temporal variance for the lower FAs can be seen when visually inspecting the mean timecourse from within the ROI. For the higher FAs with less thermal noise there is little difference between the timecourse pre- and post- NORDIC which also indicates that NORDIC is not removing any physiological signal of interest. The increase in temporal SNR from implementing NORDIC and the resultant improvement in the BOLD z -stat maps opens up opportunities to acquire data at higher spatial resolution that was previously heavily SNR limited due to thermal noise. The improvements for this Philips data are in agreement with those previously seen with Siemens data [111] and therefore confirms that NORDIC PCA denoising can be applied to our data going forward.

6.2.3 NORDIC implementation for high resolution 2D and 3D-EPI

To achieve higher spatial resolution with suitable coverage of the region of interest whilst maintaining a TR that is suitable for capturing the BOLD response, techniques such as 2D-EPI multiband imaging and 3D-EPI, SENSE and Halfscan (HS) are often required [20, 21]. But these can have implications on how well NORDIC denoising performs and the resultant corrected data. MB and SENSE lead to increases in the g-factor, whilst scans using HS acquire a reduced percentage of the phase data. Both the g-factor and phase data are important components of the NORDIC PCA method. The next section

investigates how NORDIC performs when implemented on sequences using 3D-EPI and 2D-EPI with multiband and the trade off of SENSE and halfscan.

6.2.3.1 Methods

Three datasets were acquired over the visual cortex with 1 mm isotropic spatial resolution using the 32-channel receive NOVA head coil: (1) 3D-EPI with sequence parameters: 1 mm isotropic resolution, $TE/TR/TR_{vol} = 32/76/4600$ ms, constant FA of 28° , matrix size 148×148 , SENSE 2.5×2.5 (reconstructed matrix = 224×224), no HS, 36 slices in an axial orientation. Here the 3D-EPI are acquired with a constant FA so the signal reaches a steady state over the long TR, maintaining a good point spread function (PSF), (2) 2D-EPI with sequence parameters: 1 mm isotropic resolution, $TE/TR = 30/2000$ ms, constant FA of 75° , matrix size 148×145 , MB 2, SENSE 3 (reconstructed matrix = 160×160), no HS, 36 slices in an axial orientation; (3) 2D-EPI with sequence parameters: 1 mm isotropic resolution, $TE/TR = 28/2000$ ms, constant FA of 75° , matrix size 148×146 , MB 2, SENSE 2.5 (reconstructed matrix = 160×160), HS 0.8, 36 slices in an axial orientation. Each dataset consisted of 41 volumes with the final volume being a noise scan collected with no RF and no gradients. Both the magnitude and phase data were saved, and the SCPs of ‘SNR Maxima’ and ‘SNR clip factor’ were set to 100 and 0.01 respectively. A summary of the acquisitions is shown in Table 6.1. In this context, the readout duration is defined as the time taken to acquire the stack of slices as illustrated in Figure 6.14a.

Acquisition	Resolution	FOV	SENSE	Slices	MB	HS	Readout duration (ms)
3D-EPI	1 mm iso	224×224	2.5×2.5	36	NA	none	1000
2D-EPI	1 mm iso	160×160	3	36	2	none	1000
2D-EPI	1 mm iso	160×160	2	36	2	0.8	1000

Table 6.1: A summary of the EPI data acquired to assess the impact of 2D MB, and 3D-EPI SENSE, and HS on NORDIC PCA denoising.

The tSNR for each sequence was calculated pre- and post- NORDIC. In addition, the g-factor map calculated by NORDIC to spatially normalise the noise scan was inspected.

6.2.3.2 Results

Figure 6.13 shows the tSNR pre- and post- NORDIC alongside the g-factor map for each acquisition. Prior to NORDIC the 3D-EPI data has the highest tSNR. All acquisitions show an increase in tSNR after NORDIC, with the largest increase seen for the 2D-EPI data without HS. The 3D-EPI data has SENSE acceleration in both the phase and slice direction resulting in a high acceleration factor, a high g-factor region and area of lower tSNR in the central axial slices of the acquisition. As expected, the 2D-EPI with HS 0.8 has a lower g-factor map magnitude than SENSE factor of 3 no HS. Note for these 2D-EPI MB2 acquisitions the g-factor maps exhibit a larger g-factor magnitude in the top half of slices compared to the bottom half.

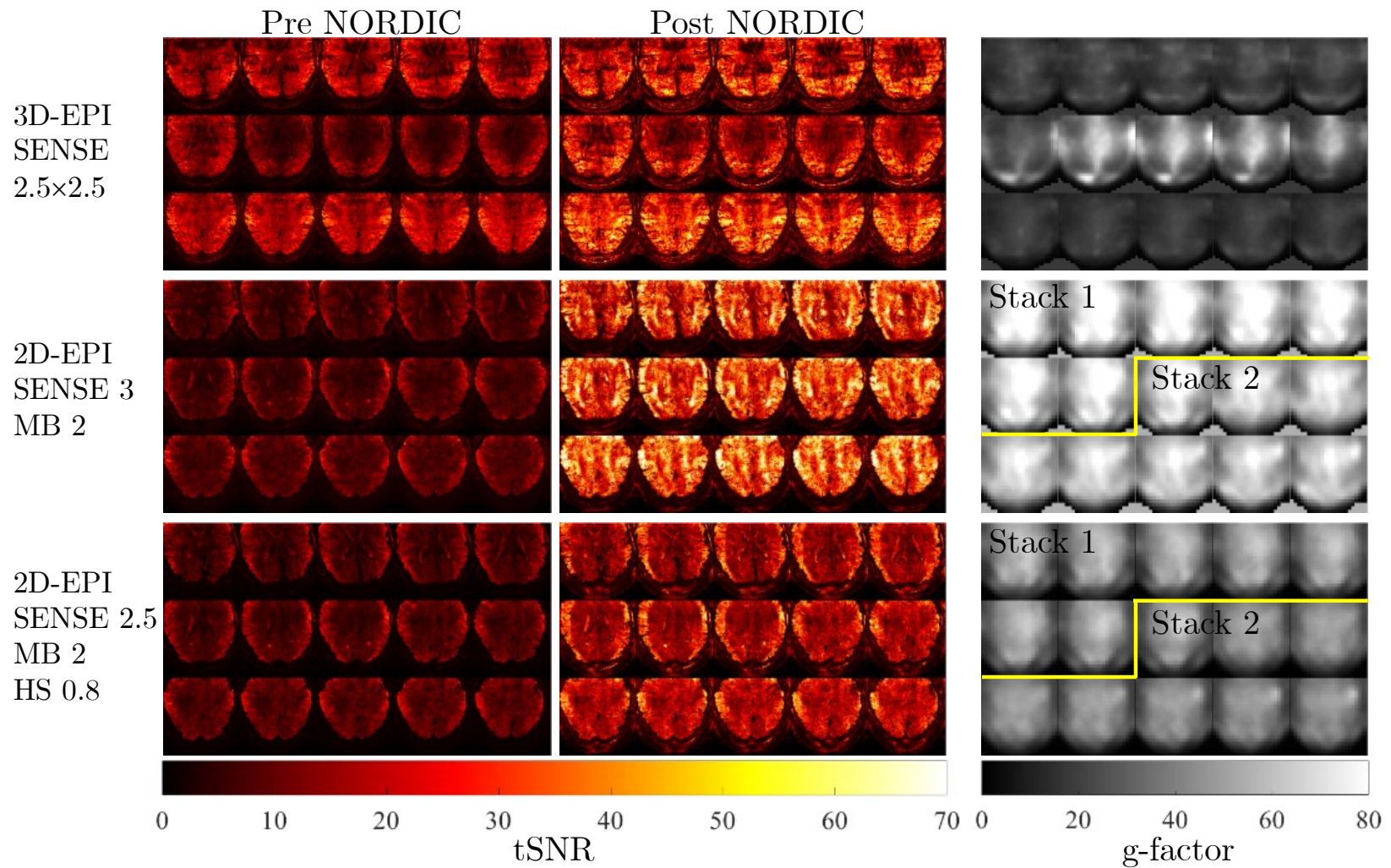


Figure 6.13: t SNR maps pre- (left) and post- (middle) NORDIC for a subset of slices for the 3D-EPI (top), 2D-EPI without HS (middle) and 2D-EPI with HS (bottom) acquisitions. The g -factor calculated by NORDIC is shown for a subset of slices in the right column.

6.2.3.3 Discussion

NORDIC can remove thermal noise and improve the tSNR of high resolution fMRI data acquired with both 2D and 3D EPI readouts with different image acceleration factors. The g-factor map for the 3D-EPI scheme with SENSE 2.5×2.5 highlighted a region where there was a reduction in tSNR in the data, suggesting that the SENSE acceleration was too high and impacting data quality. For both the 2D-EPI acquisitions, the g-factor maps had a higher magnitude in the top half of slices, this is likely to be due to the use of a MB factor of 2 and there not being sufficient spacing between the two slice stacks with the number of slices and a thickness of 1 mm. Having the two stacks so close together results in ghosting of one stack onto the other. This data illustrates these are important considerations before performing a study. The remainder of this chapter uses a 3D-EPI acquisition optimised for use in a VASO layer-specific fMRI experiment.

6.3 Implementation of 1 mm VASO for layer fMRI

Layer dependent fMRI using GE-BOLD acquisitions suffers from signal blurring towards the pial surface due to draining veins (see Chapter 4 and 5) and the resulting layer profiles are dependent on the accuracy of the models used to correct the data. To achieve higher specificity of the fMRI signal a VASO sequence can be acquired. This section outlines the development and optimisation of a VASO sequence for use in layer-dependent fMRI. Figure 6.14 shows the VASO scheme comprising an initial slice selective inversion followed by a variable flip angle 3D-EPI VASO readout at TI_1 (set to the blood-nulling time), followed by a second variable flip angle 3D-EPI readout at TI_2 , with a final delay before the next slice selective inversion.

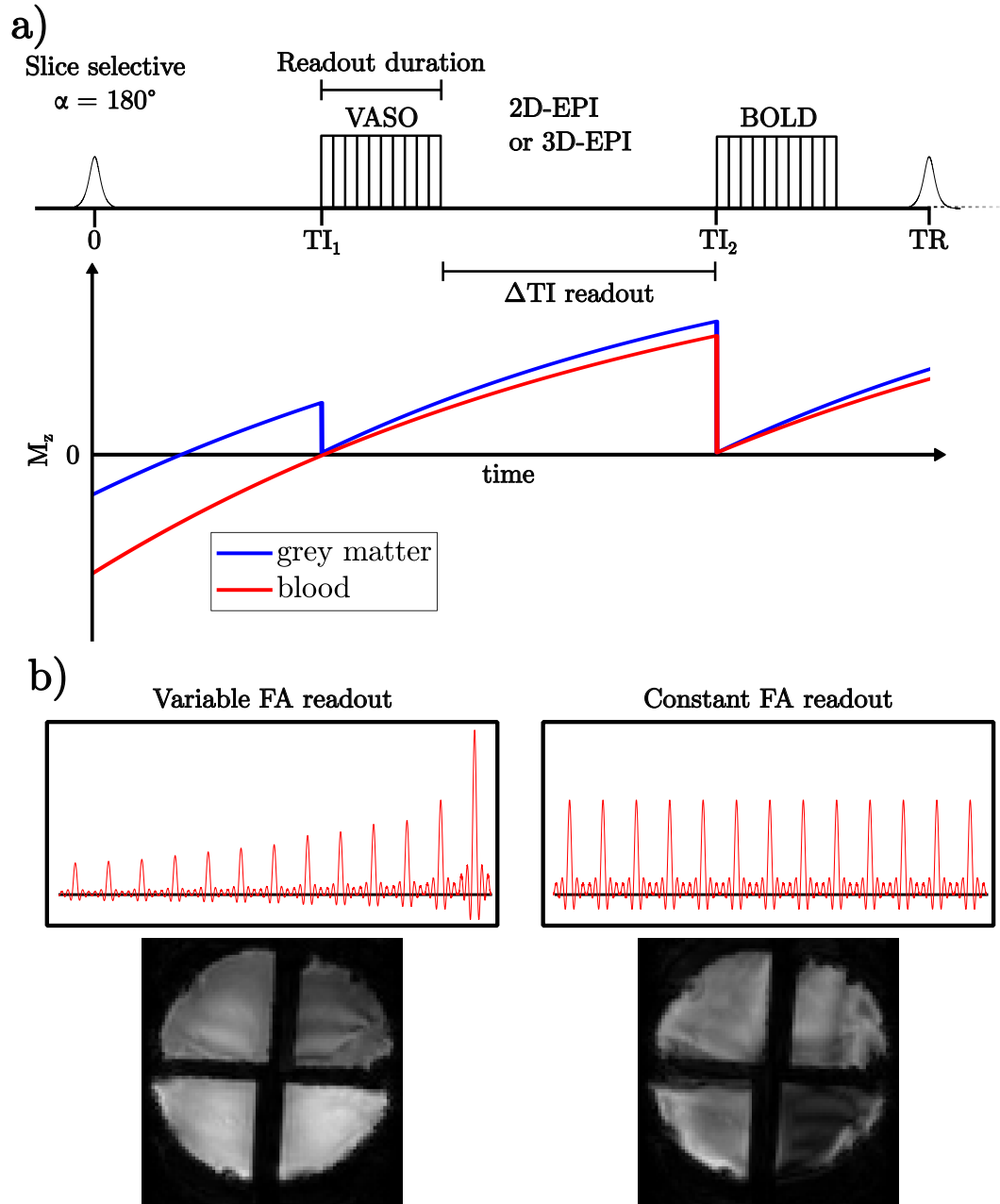


Figure 6.14: a) VASO pulse sequence diagram. The first 3D-EPI readout at T_{I1} acquires blood-nulled VASO data and the second 3D-EPI readout at T_{I2} acquires BOLD weighted data that can be used to correct the VASO data for T_2^* dependence. The typical parameters are $T_{I1} = 1050$ ms, $T_{I2} = 2400$ ms, and a volume TR of 5000 ms. b) A comparison of a phantom image acquired with a variable flip angle 3D-EPI compared to constant flip angle 3D-EPI readout which leads to blurring. The phantom contained agar quadrants of differing T_1 .

6.3.1 Comparison of VASO sequences

First the implementation of NORDIC was assessed on a 1.5 mm isotropic VASO-ASL-BOLD sequence [212] including an additional pair of readouts with a non-selective inversion to enable the calculation of a CBV and CBF contrasts. This sequence had been developed prior to this PhD. A motor task is used for the testing throughout this chapter and was selected for the layer-fMRI BOLD and VASO comparison as the hand knob region is good for benchmarking layer-fMRI methods due to its consistent folding pattern, its larger cortical thickness and having a known layer activation. Specifically at 7 T, the transmit head coil has limited coverage of lower brain regions for the inversion slab used in the VASO sequence. By acquiring in the motor cortex it is easier to achieve a uniform non-selective inversion. VASO data were collected during a simple finger tapping task consisting of 6 blocks of 18 s ‘ON’ 36 s ‘OFF’. A VASO-ASL-BOLD sequence was acquired with a 3D-EPI variable flip angle (VFA) readout with sequence parameters as follows: $1.4 \times 1.4 \times 1.5$ mm resolution, $TE/TR = 37/18$ ms, $TR_{\text{volume}} = 6$ s, with 13 segments with variable FAs (18° , 19° , 20° , 22° , 24° , 26° , 28° , 33° , 35° , 39° , 41° , 52° , 90°) to maintain a steady state and reduce blurring, matrix size 104×101 , SENSE 2.5 (reconstructed matrix = 112×112), no HS, 12 slices in an axial orientation. The additional aCBV and CBF contrasts of the VASO-ASL-BOLD sequence were dropped moving forwards as the additional repeat of the sequence with a non-selective inversion on alternate volumes requires a TR that is two times longer than a typical VASO sequence.

Following this, the optimum VASO sequence parameters to allow a 1 mm isotropic spatial resolution to be achieved were investigated. When increasing the in-plane spatial resolution or increasing the slice coverage, the readout duration (shown in Figure 6.14) increases, resulting in one of two things: 1) If the volume TR is kept constant, the temporal spacing between the VASO readout and BOLD readout (ΔTI readout) is reduced, as a result there is

less time for the signal to recover after the VASO readout leading to reduced BOLD CNR or, 2) If the gap between the VASO and BOLD readouts (ΔTI readout), is kept constant this comes at the expense of increasing the volume TR. Here, when optimising the VASO sequence, the temporal spacing between the VASO and BOLD readouts (ΔTI readout) was kept constant at 1450 ms. To counteract the increase in volume TR, increasing the SENSE acceleration factor and halfscan factor were employed to reduce the readout duration. A variety of combinations of stack size, SENSE factor and halfscan were used to optimise the VASO sequence, which was constrained to provide good coverage of the motor cortex, a volume TR of ~ 5 seconds, and minimal artefacts.

Three sequences were considered, as outlined in Table 6.2. All sequences were acquired at 1 mm isotropic resolution with a FOV of 154×154 and a TE of 20 ms, using a VFA 3D-EPI readout, with FAs of ($18^\circ, 19^\circ, 20^\circ, 22^\circ, 24^\circ, 26^\circ, 28^\circ, 33^\circ, 35^\circ, 39^\circ, 41^\circ, 52^\circ, 90^\circ$) across 13 segments for the 12 slice acquisitions, and FAs of ($15^\circ, 16^\circ, 17^\circ, 18^\circ, 19^\circ, 19^\circ, 20^\circ, 21^\circ, 22^\circ, 23^\circ, 24^\circ, 26^\circ, 28^\circ, 30^\circ, 32^\circ, 36^\circ, 41^\circ, 50^\circ, 90^\circ$) across the 19 segments for the 18 slice acquisition. Each sequence was first acquired on a phantom, before testing on a head. All sequences were tested with a stack of 12 or 18 slices, except for Sequence 1 which could only be collected with 12 slices within the required volume TR of < 5 s.

Sequence	SENSE	HS	TE (ms)	Readout duration (ms)		Dynamic TR (ms)
				12 slices	18 slices	
1	2.5	none	40	1057	1604	4800/6000
2	2.5	0.75	20	798	1225	4200/5050
3	3	0.75	19	700	1120	4000/4800

Table 6.2: Summary of each of the 1 mm isotropic VASO sequences considered during the optimisation.

6.3.1.1 Analysis of VASO sequences

Each readout of the 1.5 mm isotropic VASO data were denoised using NORDIC PCA. The VASO data were corrected for BOLD T_2^* contamination by dividing each volume by the corresponding BOLD volume. tSNR maps for both the BOLD and corrected VASO, were calculated by dividing the temporal mean of all volumes by the temporal standard deviation over all volumes. The VASO and BOLD data were each input into a fixed effects GLM. The BOLD data were input with regressors modelled using a standard HRF convolved with a boxcar of the stimulus timings. The VASO data used the same model design but a negative contrast was assessed as the VASO signal decreases on activation. The mean of the timecourses from significantly correlated ($z > 3.1$) voxels within the the activation mask was calculated for the BOLD and BOLD corrected VASO data. The mean timecourses were highpass filtered and converted into % signal change in order to compare BOLD and VASO timecourses.

6.3.2 Results of VASO sequences

Results of the ~ 1.5 mm isotropic resolution VASO tests are shown in Figures 6.15 & 6.16. tSNR was used to assess the data quality and the effect of using NORDIC PCA on the data. Pre-NORDIC the mean tSNR for the BOLD signal was 19.5 and for the VASO signal was 16.3. Post-NORDIC the tSNR maps visually show an increase across the brain. Quantitatively their mean tSNR values also increase with a BOLD tSNR of 20.5 and VASO tSNR of 18.7. At this 1.5 mm resolution a small gain in activation is seen in the z -stat maps post-NORDIC. Figure 6.16 shows the mean timecourse of all voxels with significant correlations ($z > 3.1$) for the BOLD and VASO data pre- and post- NORDIC. The BOLD timecourse has a % signal change of $\sim 10\%$ during the stimuli compared to $\sim 3\%$ for the VASO. As expected, the VASO signal is anti-correlated to the BOLD signal and reduces during brain activation. NORDIC denoising has marginally improved the BOLD timecourse, resulting in

a larger % signal change in the timecourse. There are no visible improvements post-NORDIC for the VASO timecourse.

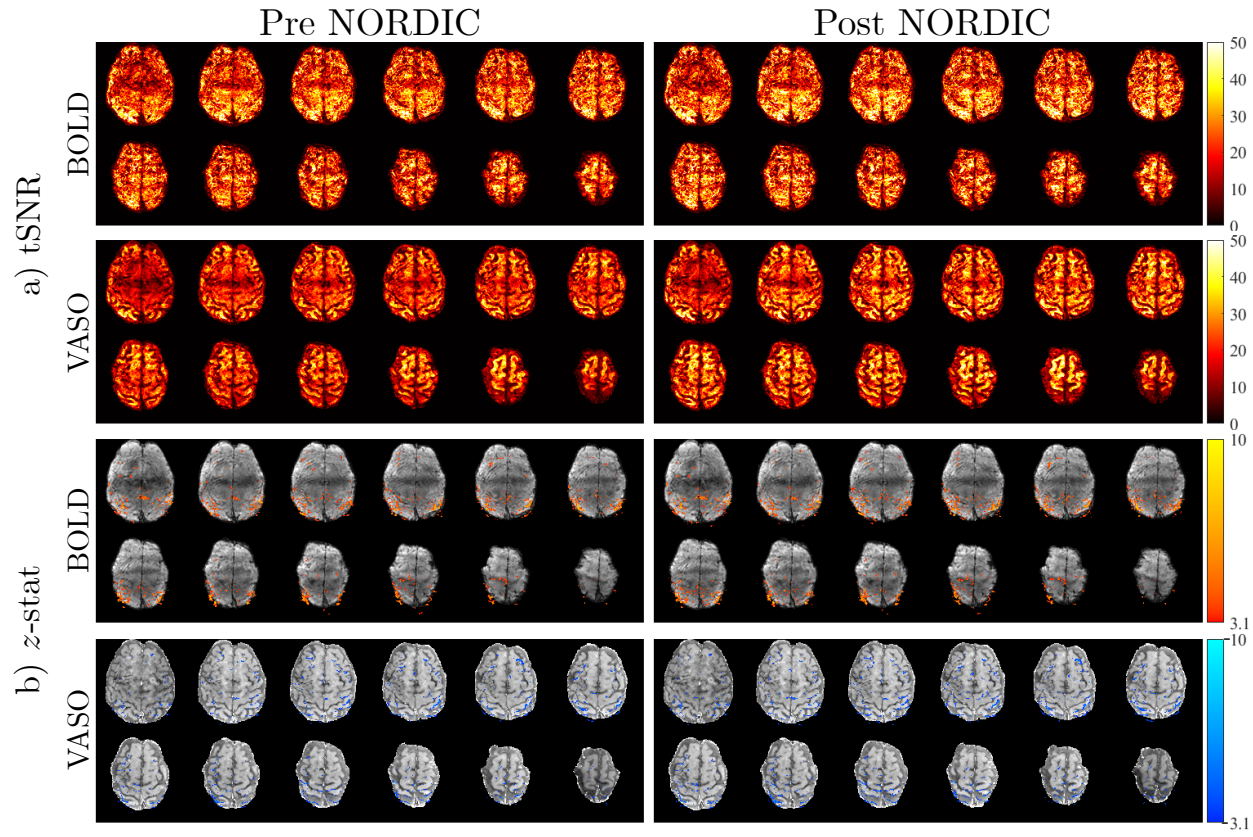


Figure 6.15: a) $tSNR$ maps pre- (left) and post- (right) NORDIC for the 3D-EPI BOLD and VASO acquisitions at $1.4 \times 1.4 \times 1.5$ mm^3 . b) Activation maps for BOLD and BOLD corrected VASO resulting from a fixed effects GLM, $z > 3.1$, cluster corrected, $p > 0.05$.

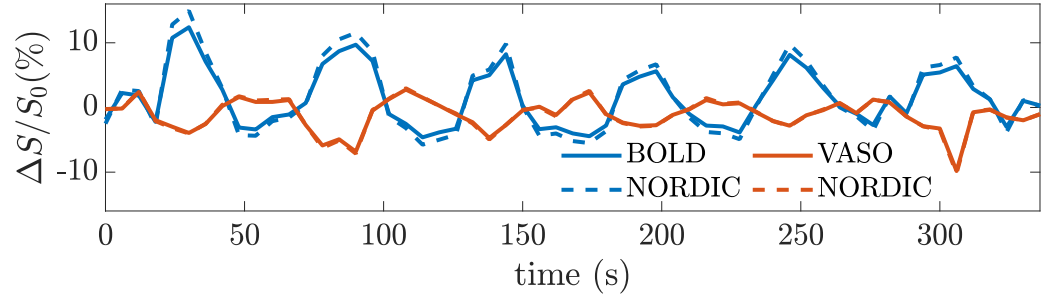


Figure 6.16: The mean timecourse as % signal change from the significantly correlated voxels ($z > 3.1$) for the pre- and post-NORDIC 3D-EPI BOLD and BOLD corrected VASO data.

Figure 6.17 shows the 1 mm isotropic VASO sequence on a quadrant phantom of differing T_1 for VASO Sequence 1 (Table 6.2). The image intensity can be seen to be uniform across all slices, good contrast between each compartment of the phantom, and no large distortions or artefacts, although there is some ringing artefacts visible due to SENSE. For a stack of 12 slices the volume TR is 4.8 s, however on increasing the stack coverage to 18 slices the volume TR increased to 6 s, too long for our desired applications. Thus Sequence 1 was only considered for the initial scans on phantoms, and was ruled out from this point on due to the long volume TR for the 18 slice coverage.

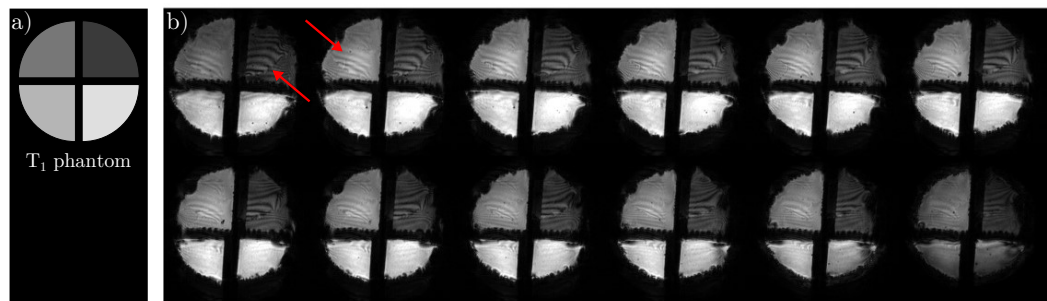


Figure 6.17: a) Phantom with agar quadrants of differing T_1 used to evaluate sequences. b) The signal from the VASO readout the parameters for Sequence 1 in Table 6.2. Data acquired for 12 slices, SENSE 2.5, no HS and a TE of 40 ms. Red arrows indicate an examples of SENSE ringing artefacts.

Figure 6.18 shows the VASO signal for Sequences 2 and 3 (Table 6.2). After introducing a HS factor of 0.75, on visual inspection the image quality has not been effected. There are still some areas with SENSE artefacts, these are reduced in the 18 slice acquisitions. Figure 6.19 shows the VASO signal for Sequence 2 and 3 for the 12 and 18 slice acquisitions. The data quality between SENSE 2.5 and 3 is visually comparable. Image intensity is uniform across all slices except for the first and last slices of the acquisitions. Figure 6.20 shows the in-vivo signal for the corresponding BOLD readout for Sequence 2 and 3 for 12 and 18 slice acquisitions. The data quality between SENSE 2.5 and 3 is visually comparable. Image intensity is uniform across all slices except for the first and last slices of the acquisitions. A SENSE artefact can be seen in the lower right corner of most slices (red arrows) for both the SENSE 2.5 (Sequence 2) and SENSE 3 (Sequence 3) acquisitions, which is reduced for the 18 slice acquisition compared to the 12 slice acquisition.

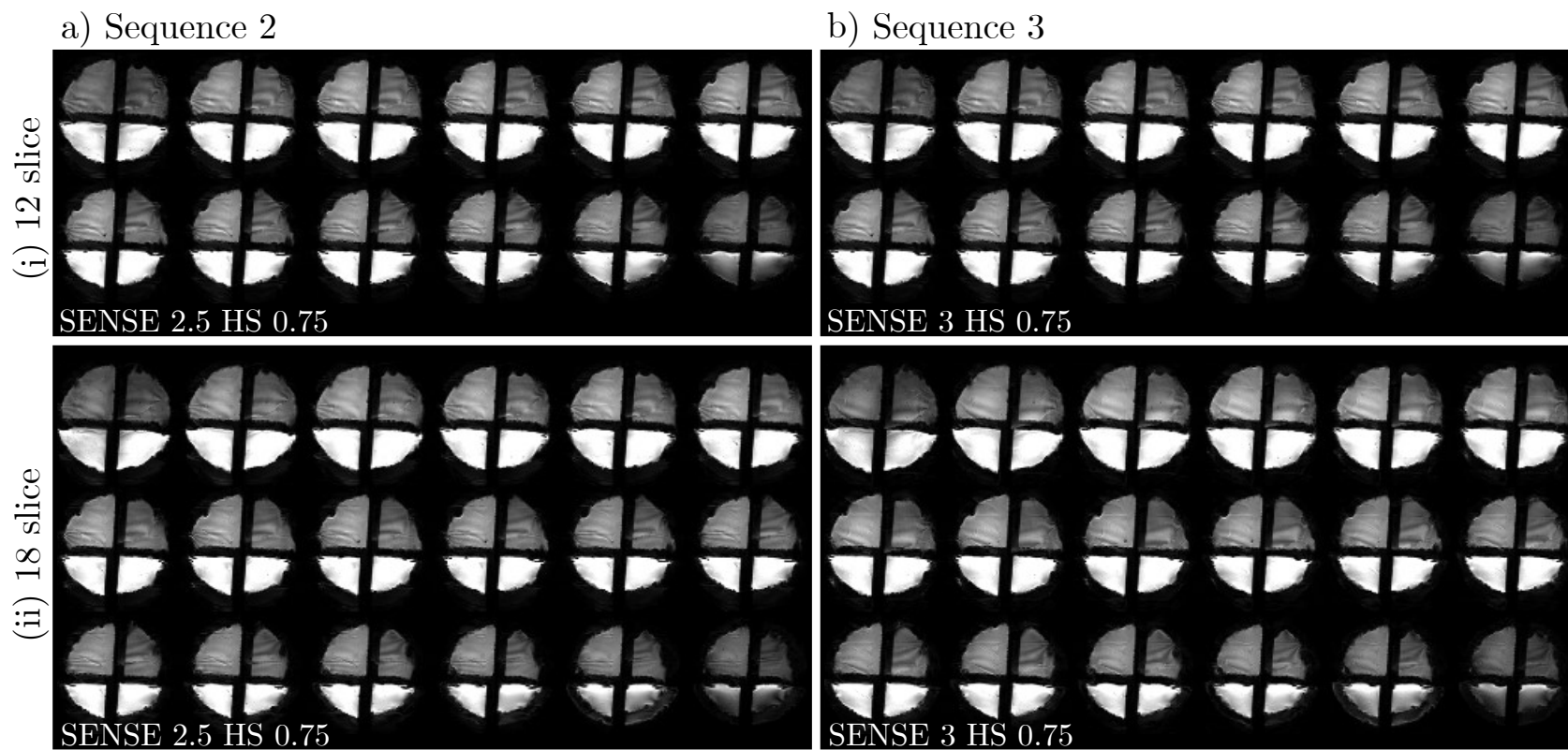


Figure 6.18: The VASO signal for the Sequences 2 (a) and 3 (b) from Table 6.2 shown for 12 (i) and 18 (ii) slice acquisitions of a phantom.

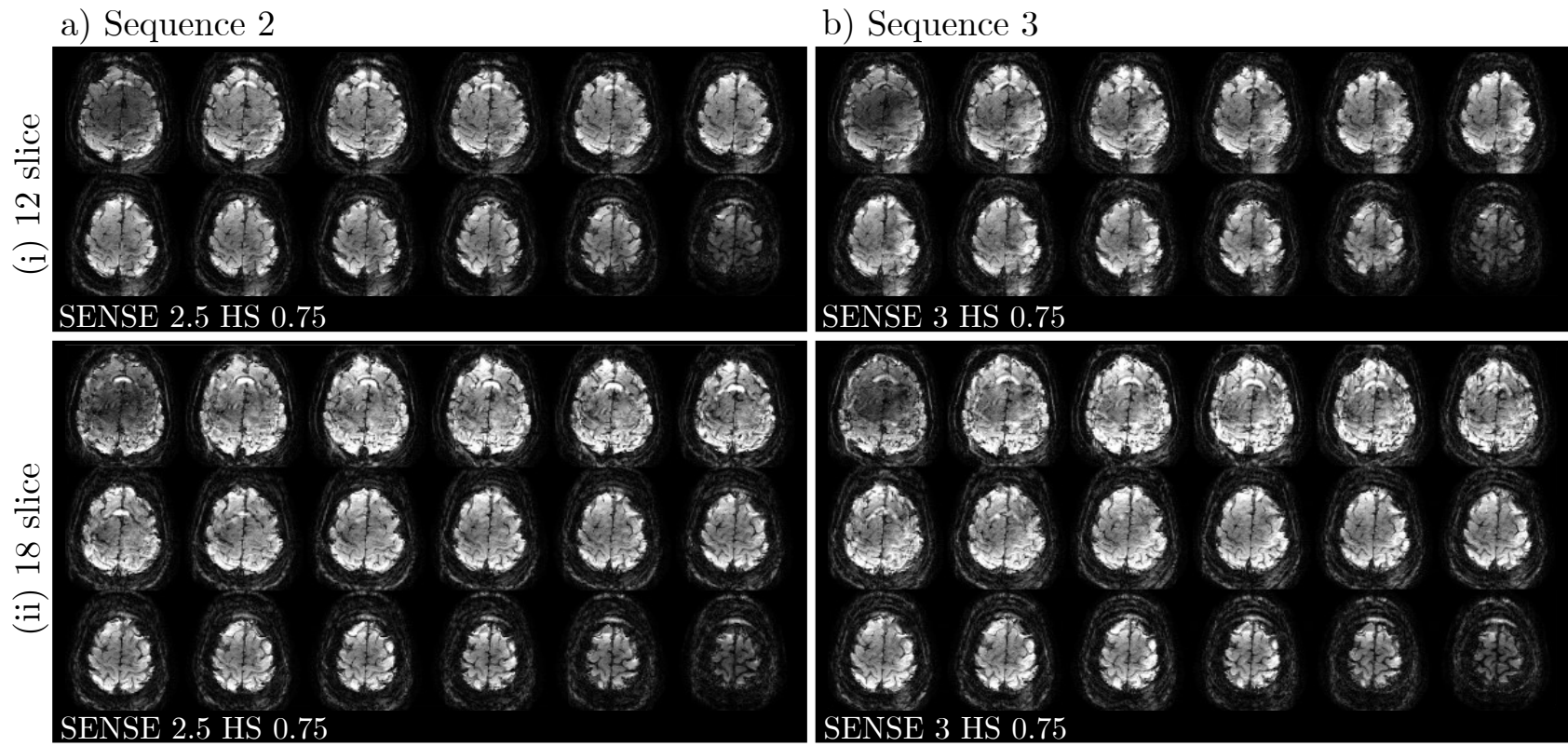


Figure 6.19: The signal of the VASO readout for Sequence 2 (a) and 3 (b) from Table 6.2 shown for (i) 12 and (ii) 18 slice acquisitions of the brain.

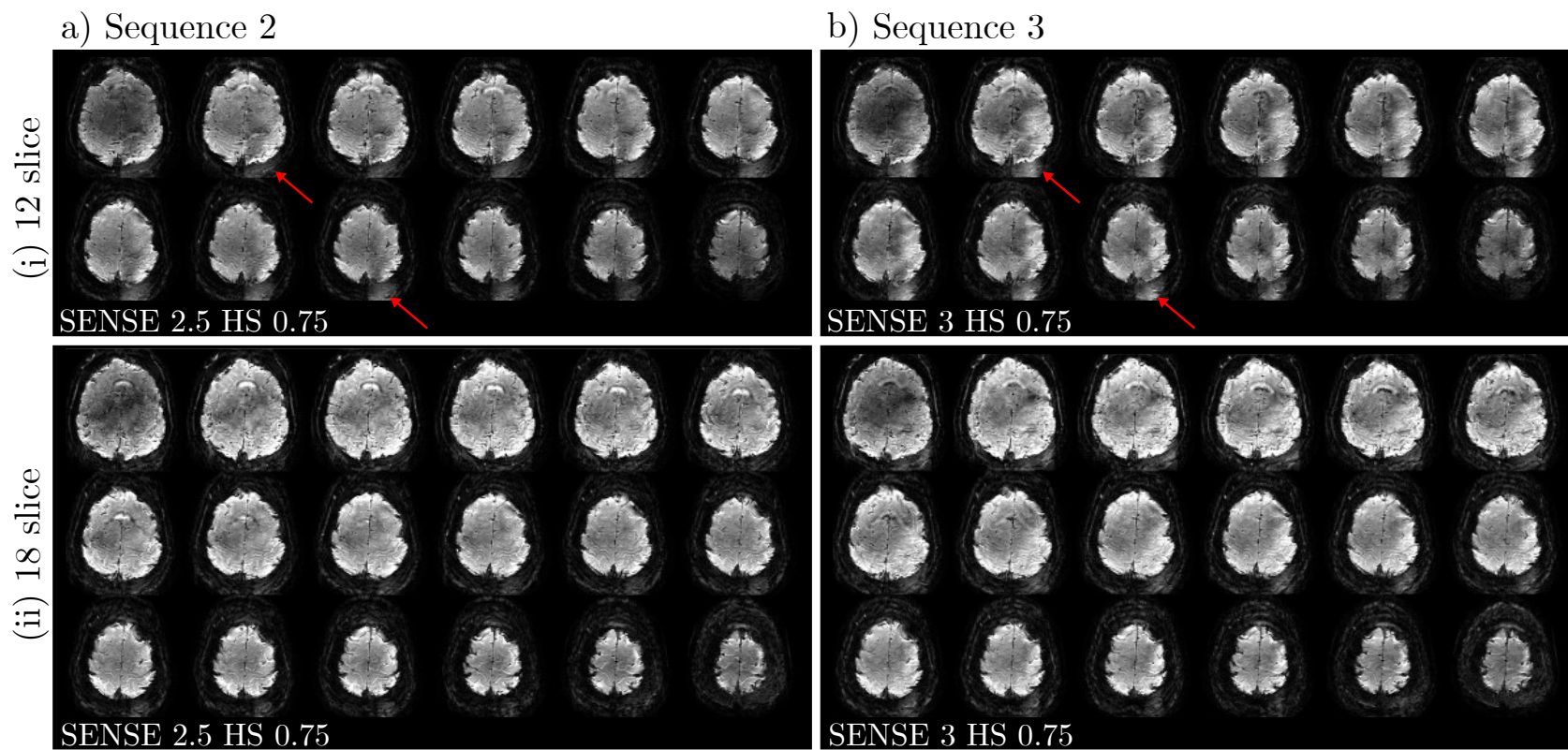


Figure 6.20: The signal for the BOLD readout for Sequences 2 (a) and 3 (b) from Table 6.2 shown for (i) 12 and (ii) 18 slice acquisitions of the brain. Red arrows indicate examples of a SENSE artefact.

Sequence 3 (SENSE 3, HS 0.75, 18 slices) was therefore selected for use in a layer dependent fMRI VASO study on the motor cortex as this provided suitable image quality, a TE of 20 ms, and good coverage, in a TR of < 5 s.

6.3.3 Optimisation of TI_1 for 1 mm VASO

After optimising the sequence the next step was to assess sensitivity to the functional changes in the VASO signal. The sensitivity to the VASO signal is dependent on how well the blood signal has been nulled compared to the grey matter, and so it is important that TI_1 is optimised to match the required blood nulling point. The initial acquisition acquired at 1.5 mm isotropic resolution used a TI_1 of 1050 ms but the contrast for the blood nulling point shifts dependent on the 3D-EPI readout time and the recovery. To determine the optimal TI_1 value for the 1 mm VASO sequence, a simple finger-tapping experiment was run on a single subject using Sequence 3 and altering the TI_1 across a range of values ($TI_1 = 1100, 1150, 1200, 1250, 1300, 1350, 1400, 1450$ ms). The subject lay supine in the scanner bore and viewed a projector screen with prism glasses. The subject was prompted to ‘TAP’ or ‘REST’ on the projector screen. Each run began with a 20 s ‘REST’ period followed by six blocks of 40 s ‘TAP’, 20 s ‘REST’. This resulted in one run of a given TI_1 , consisting of 76 dynamics + 1 noise dynamic for use with NORDIC, taking 6 min 20 s to collect. The full set of TI_1 values were acquired sequentially over 3 scan sessions starting with 1100 ms.

NORDIC PCA denoising was applied to the VASO data and BOLD data which were then motion corrected (FSL, FLIRT) and each dynamic of the VASO data was divided by the corresponding BOLD dynamic, to correct for the BOLD contamination of the VASO signal [199]. The VASO and BOLD data were each input into a fixed effects GLM. The BOLD data were input with regressors modelled using a standard HRF convolved with a boxcar of the stimulus timings. The VASO data used the same model design but a negative

contrast was assessed as the VASO signal decreases on activation. Both GLMs were run with the motion parameters included as nuisance regressors.

Figure 6.21 shows the results from the fixed effects GLM for the VASO data collected across a range of TI_1 values, shown for a) Pre-NORDIC denoising and b) Post-NORDIC denoising. Upon visual inspection the shorter TI_1 of 1100 and 1150 ms show a greater extent of activation in the motor cortex compared to compared to TI_1 of 1200 and 1250 ms. The z -stat maps for the longest TI_1 ($TI_1 = 1300, 1350, 1400$ and 1450 ms) are not shown as there was no significant activation in the motor cortex for these data at $z > 2.3$. Figure 6.22 shows the corresponding results from the fixed effects GLM of the BOLD data for the VASO sequence. As expected, there is little difference in the extent and magnitude of the z -stat maps for each of the TI_1 values, with all showing a strong activation in the motor cortex. The denoised BOLD data shows greater BOLD responses. Comparing Figure 6.22b to 6.22a, NORDIC has improved both the extent and magnitude of the z -stat maps for all TI_1 .

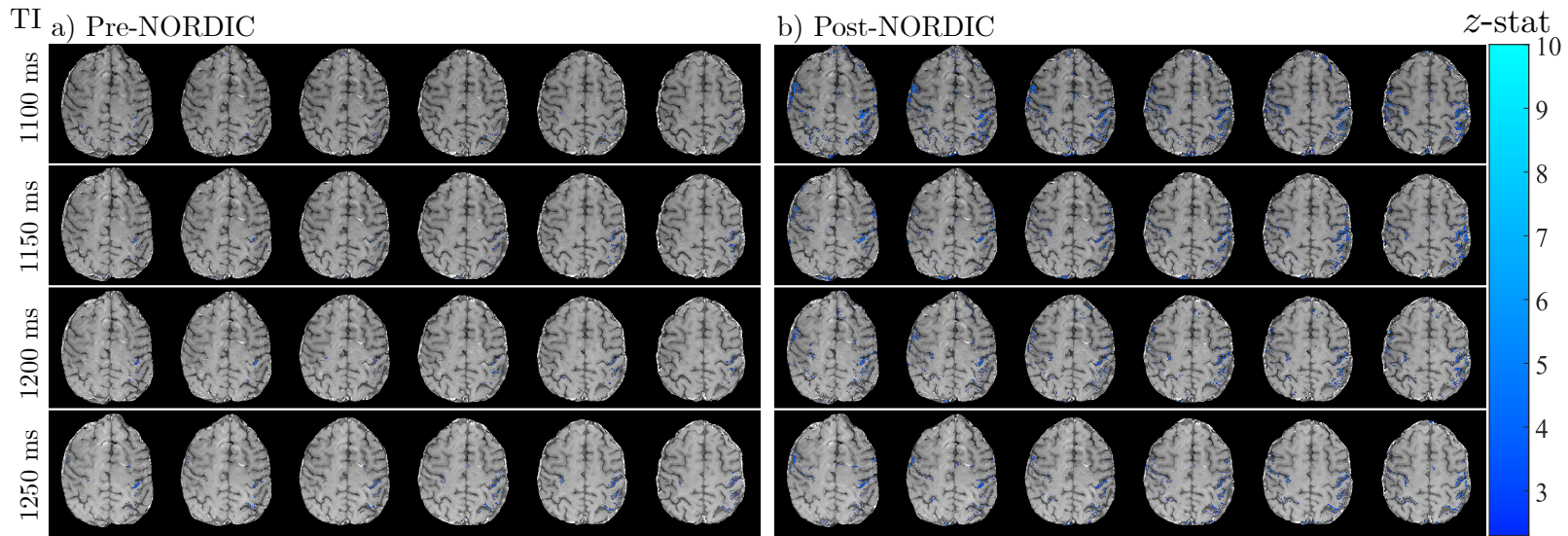


Figure 6.21: z -stat maps from the fixed effects GLM of the VASO signal for a range inversion times ($TI_1 = 1100, 1150, 1200, 1250$ ms) overlaid on a subset of slices of the mean BOLD corrected VASO timeseries. Data shown for a) pre-NORDIC denoising and b) post-NORDIC denoising. z -stat maps are thresholded to $z > 2.3$ and cluster corrected $p < 0.05$.

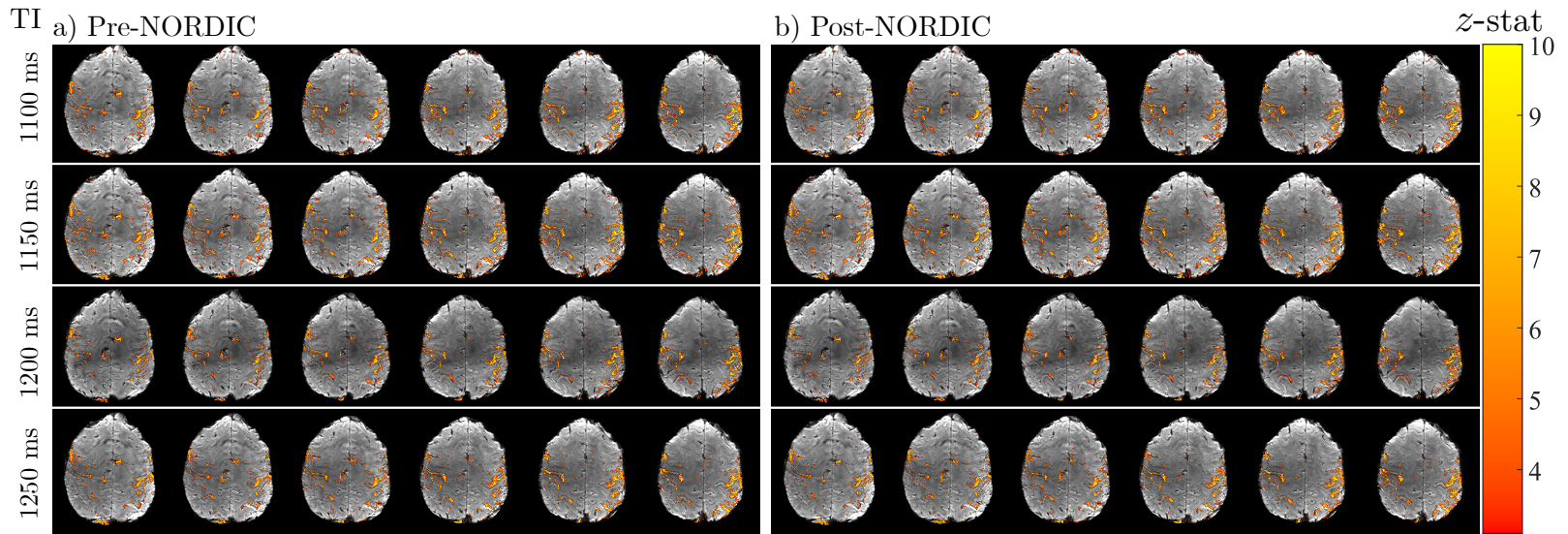


Figure 6.22: z -stat maps from the fixed effects GLM of the BOLD signal for a range inversion times ($TI_1 = 1100, 1150, 1200, 1250$ ms) overlaid on a subset of slices of the mean BOLD timeseries. Data shown for a) pre-NORDIC denoising and b) post-NORDIC denoising. z -stat maps are thresholded to $z > 3.1$ and cluster corrected $p < 0.05$.

The z -stat maps indicated the best sensitivity to the VASO signal for $TI_1 = 1100$ ms and $TI_1 = 1150$ ms with each also giving a strong BOLD response. The optimal TI_1 for the VASO readout of 1150 ms was taken forward to study layer dependent responses in the motor cortex in the next section.

6.4 High resolution VASO for layer dependent measures in the motor cortex

6.4.1 Methods

This study was conducted with approval from the local ethics committee and complied with the Code of Ethics of the World Medical Association (Declaration of Helsinki). 10 healthy volunteers (1 female) with a mean age 26.7 ± 3.8 years participated in this study. Each subject gave written, informed consent before participation.

6.4.1.1 Experimental Paradigm

A simple finger-tapping paradigm was designed to induce brain activation in the motor cortex. Subjects lay supine in the scanner bore and viewed a projector screen with prism glasses. Subjects were prompted to ‘TAP’ or ‘REST’ on the projector screen. Each run began with a 20 s ‘REST’ period followed by six blocks of 40 s ‘TAP’, 20 s ‘REST’ (see Figure 6.23). Four runs were acquired per subject. Before entering the scanner subjects were directed to tap each finger to the thumb sequentially, starting with the second digit and moving to the fifth digit and returning back to the second digit on both hands during each ‘TAP’ period.

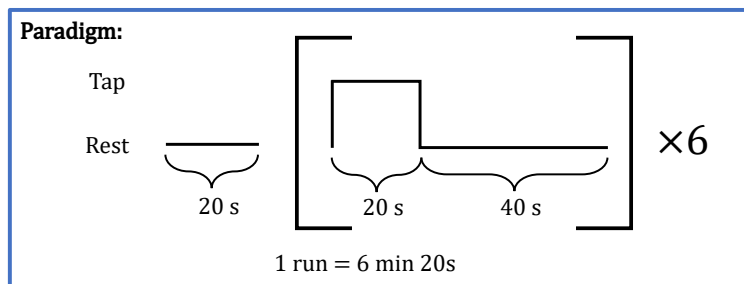


Figure 6.23: Finger-tapping paradigm used to stimulate the somatosensory cortex.

6.4.1.2 Data Acquisition

All MRI data were acquired on a 7 T Phillips Achieva MR scanner (Phillips Medical Systems, Best, Netherlands) using a 32-channel volume transmit/receive coil (Nova Medical, Wilmington, USA).

VASO data: Data were collected using a 32-channel receive/transmit coil using a 3D-EPI VFA VASO sequence with (Sequence 3 Table 6.2) with: 1 mm isotropic resolution, TE/TR = 19/52 ms, FA = 15 – 90°, TR_{volume} = 5 s, TI₁=1150 ms, TI₂=3720 ms, BW in EPI frequency = 1023 Hz, acquired matrix size 156×153 (AP×RL), SENSE 3 (AP) (reconstructed matrix = 320 × 320), HS = 0.75, 18 slices in an axial orientation. A single scan consisted of 77 volumes, with the final volume being a noise dynamic, resulting in a scan duration of ~6 minutes. Four functional scans were acquired for each subject. The functional runs were acquired sequentially, following the survey scans and B_0 -field map.

Resting State BOLD (rsBOLD): This was acquired to be used as a measure for the Amplitude of Low Frequency Fluctuations (ALFF), an estimate of CBV_v used for the deconvolving of the functional BOLD data (see Chapter 4, Section 4.7). The rsBOLD data were acquired using a 3D GE-EPI sequence with: 1 mm isotropic resolution, TE/TR = 19/52 ms, FA = 15 – 90°, TR_{volume} = 1.5 s, BW in EPI frequency = 1245.0 Hz, acquired matrix size 156×153 (AP×RL), SENSE 3 (AP) (reconstructed matrix = 320 × 320), Halfscan = 0.75, 18 slices

in an axial orientation. A single scan consisted of 100 volumes, with the final volume being a noise dynamic. This resulted in a scan duration of ~ 2.5 minutes. Prior to the fMRI acquisition, a B_0 -field map was acquired (TR = 20 ms, TE = 5.92 ms, Δ TE = 1 ms, 4 mm isotropic resolution, 64×64 matrix, 40 slices, FA = 25° , SENSE factor 2) for local image-based (IB) shimming over the region of interest for the fMRI data acquisition to limit field perturbations in B_0 . A B_0 -field map was then collected using the same shims as used for local IB shimming such that this could be later used for distortion correction of the VASO 3D-EPI fMRI dataset.

Anatomical data: Scans were collected for the creation of a vein mask using a Fast Low Angle Shot (FLASH) sequence with: $0.5 \times 0.5 \times 1$ mm acquired resolution (reconstructed to $0.48 \times 0.48 \times 1$ mm), 308×308 matrix, TE/TR = 20/564 ms, 32 slices, SENSE: 2 (RL), MB: 2. For GM segmentation, a phase-sensitive inversion recovery (PSIR) sequence was acquired [141]: $0.7 \times 0.7 \times 1$ mm acquired resolution (reconstructed to $0.47 \times 0.47 \times 1$ mm), 320×320 matrix, TI = 725/2150 ms, TE/TR = 2.8/6.3 ms, 158 slices, SENSE: 3 (RL). In addition, a T_1 mapping dataset with distortions and geometry matched to the VASO data, were acquired using a 3D IR-EPI sequence with 1 mm isotropic resolution (TE = 18 ms, EPI factor = 51, 15 shots, TI = [0, 100, 200, 300, 400, 500, 600, 700, 900, 1100, 1400, 1900, 2900, 3900 ms], field-of-view (FOV) = 154 (AP) \times 154 (RL) \times 18 (FH), SENSE = 3 (AP)). The final shot was acquired as a noise scan for NORDIC denoising prior to T_1 mapping (see Section 6.5).

6.4.1.3 fMRI Processing

The VASO and corresponding BOLD images were each motion corrected using the same method as described in Chapter 4 Section 4.4.2. In brief, the motion transformation matrices between and within runs for the correction of all VASO volumes to the central dynamic of the entire session were concatenated and applied in a single step. Following this, each dynamic of the VASO

data was divided by the corresponding BOLD dynamic, to correct for BOLD contamination of the VASO signal [199]. Unlike the data in Chapter 4, it was decided to keep the functional data in its native space and warp the structural data to the functional space as this reduces the number of times the data is resampled and hence the amount of blurring [3].

The functional VASO and BOLD responses were modelled. A single model for the BOLD response, was created using a boxcar of the stimulus timecourse convolved with a haemodynamic response function (HRF) (double gamma, time-to-peak of 6s). The VASO data used the same model but a negative contrast was used as VASO signal decreases with brain activation. No time shifts were implemented for the BOLD and VASO models as the stimulus had very long ‘on’ and ‘off’ periods. The effect of a 2.5 s delay between the BOLD and VASO readouts during a 40 s ‘on’ period would be negligible.

At the first-level, for each run, the main effect of the VASO responses regressor and motion parameters as regressors of no interest were modelled in a GLM (FEAT, FSL). For each subject the average response was calculated across all runs using a second-level fixed-effects analysis to produce the z -stat map across all runs per subject. A threshold of $|z| = 2.3$ was applied to all z -stats and cluster correction ($p < 0.05$) performed. The main effect of the BOLD responses regressor and motion parameters as regressors of no interest were modelled in a GLM (FEAT, FSL). For each subject the average response was calculated across all runs using a second-level fixed-effects analysis to produce the z -stat map across all runs per subject. A threshold of $|z| = 3.1$ was applied to all z -stats and cluster correction ($p < 0.05$) performed.

In preparation for the layer analysis, both the thresholded z -stats maps and non-thresholded z -stats maps for the VASO and BOLD were upsampled to 0.175 mm isotropic resolution using spline interpolation [3]. To counteract the slight smoothing from spline interpolation, a threshold of $|z| = 2.3$ and $|z| = 3.1$ were applied to the VASO and BOLD z -stats.

The rsBOLD data were motion corrected and coregistered to the 2nd VASO BOLD functional run (FSL FLIRT). The ALFF was calculated using Analysis of Functional NeuroImages (AFNI) (3dRSFC) with a frequency range of 0.01–0.08 Hz. In preparation for the layer analysis, the resulting ALFF map was upsampled to 0.175 mm isotropic resolution using spline interpolation.

6.4.1.4 Structural Processing

The PSIR data, comprising magnitude and phase images at two delays (TI = 725 ms/TI = 2150 ms), were combined to form a field-bias corrected PSIR image. A brain mask was generated using the same method used in Chapter 4. Brain extraction on the PSIR data was performed by taking the magnitude image acquired at TI = 2168 ms from the PSIR dataset and skull stripping using BET2 in FSL [146]. The resultant image then underwent two erosion iterations using FSL, and was viewed in FSLeyes, and any manual correction of the brain mask performed.

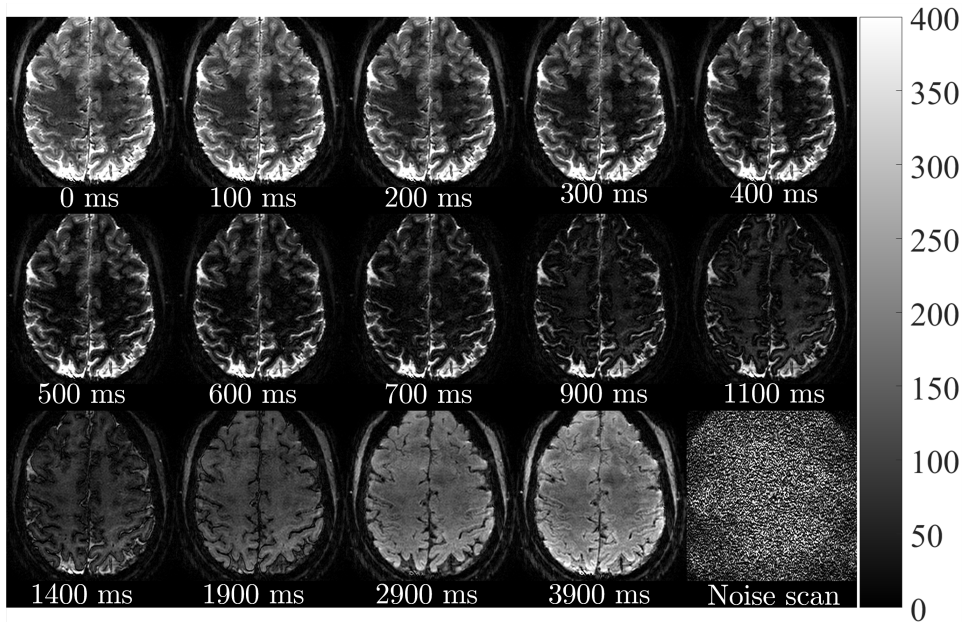


Figure 6.24: A single central slice of the 3D T_1 mapping acquisition from one subject shown for the 15 dynamics across a range of inversion times (TI) of 100 – 3900 ms and the final noise scan. This data is used to fit to a T_1 map (see Section 6.5.2).

For T_1 mapping, first the polarity of the magnitude data shown in Figure 6.24 was corrected using the phase data. A T_1 map was computed by fitting the data to an inversion recovery curve. The T_1 maps (Figure 6.25) were originally generated to be used to segment the GM ribbon in the same space as the functional VASO data. After segmentation into four tissue types, a GM binary mask was created from the partial volume effect (PVE) GM map. However, the binary GM mask was not of sufficient quality to be used to assess layers with the VASO data. As the T_1 mapping data consisted of 14 shots at a range of TIs, these provided multiple contrasts that could be used for the registration of the PSIR to the VASO data as an alternative.

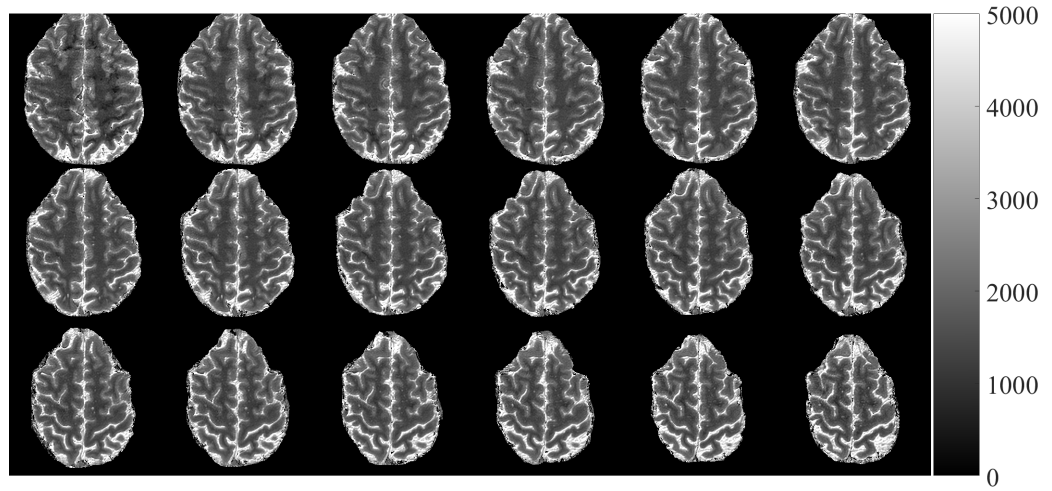


Figure 6.25: 1 mm isotropic T_1 map generated following NORDIC denoising of the data. 18 axial slices shown for an example subject.

The 13th shot of the T_1 data was similar in contrast to the 2nd PSIR magnitude image (TI = 2150 ms) and the 14th shot of the T_1 data (TI = 3900 ms) was most similar to the temporal mean image of the 2nd run of the VASO functional data, to which all the functional runs were motion corrected to for all subjects. Therefore, these T_1 shots were used to transform the field-bias corrected PSIR into the same space as the VASO data. This first involved a linear transform to move the PSIR as close as possible to the VASO data, then a non-linear warp was performed for the final alignment. All transforms were applied using spline interpolation and the final transformation matrices were combined and applied as one transform to minimise blurring. The registration is described below and shown in Figure 6.26.

The 13th shot of the T_1 data (TI = 2900 ms) was registered to the 2nd PSIR magnitude image (TI = 2150 ms) using a rigid body transform (FSL, FLIRT). The 14th shot of the T_1 data (TI = 3900 ms) was registered to the mean image of the 2nd VASO functional run using an affine transform (FSL, FLIRT). The inverse of the rigid body transformation matrix was concatenated with the affine transformation matrix to create a combined linear transformation matrix and then applied to the 2nd PSIR magnitude image (TI = 725 ms) to move it as close as possible to the VASO data. The affine transformation matrix was also applied to the computed T_1 map for later alignment of the FLASH data.

The resulting PSIR from the linear transform was then warped to the mean image of the 2nd VASO functional run (Advanced Normalisation Tools (ANTs), `antsRegistrationSyN`) and the non-linear warp field saved. Finally the linear transformation matrix and the non-linear warp field were combined and applied to the field-bias corrected PSIR data in one step.

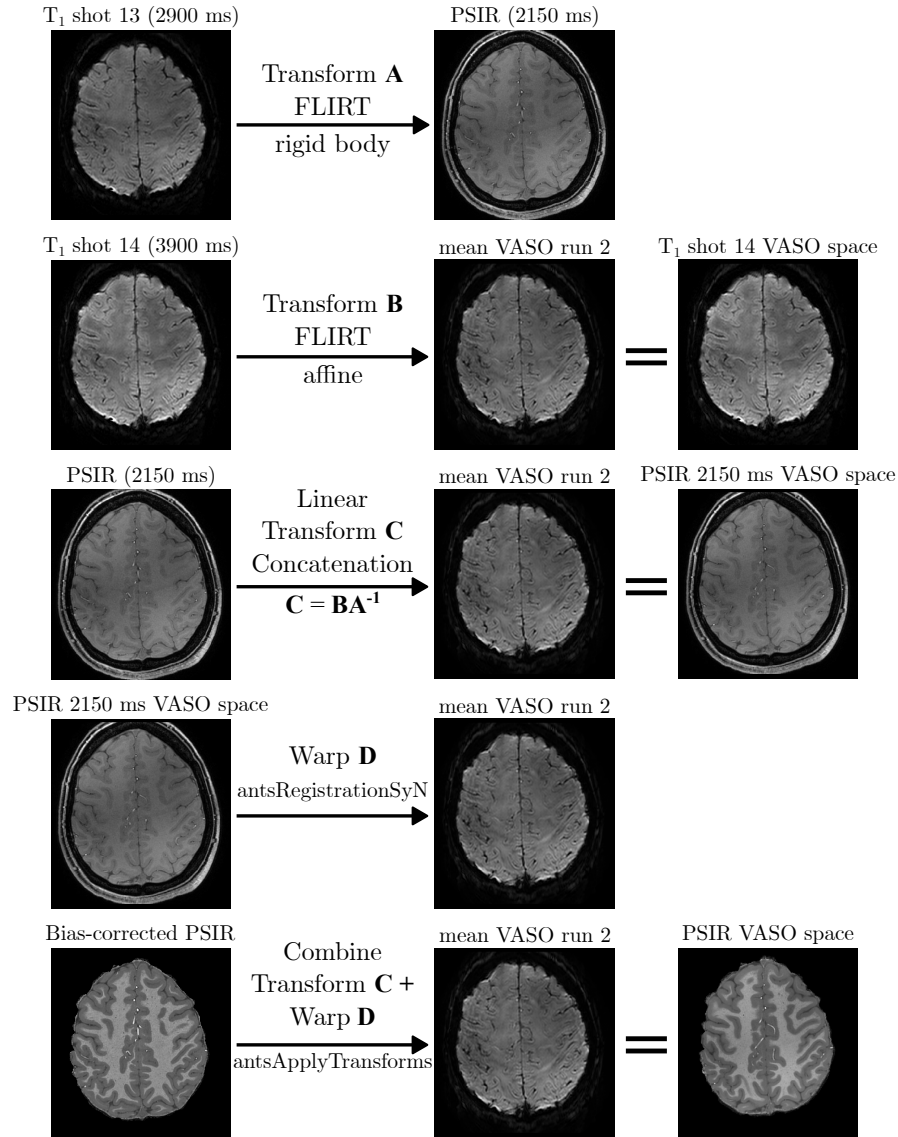


Figure 6.26: Schematic detailing the linear and non-linear registration of the structural data to the functional VASO data.

The warped PSIR data, now in VASO space, was upsampled to 0.175 mm isotropic in-plane and 1 mm through-plane resolution using spline interpolation was segmented into three tissue types (FSL FAST), the GM binary mask was created from the partial volume effect (PVE) GM map. The GM mask was visually inspected and cropped to a region of interest (ROI) that contained the hand knob region – manually identified by its distinctive Ω or ϵ shape for

each subject. The cropped GM mask was then overlaid onto the warped PSIR and the mean image of the BOLD corrected VASO data and edited manually in itk-SNAP. The final GM mask was then upsampled to 0.175 mm isotropic using spline interpolation and the blocky shape through slices was smoothed using in house code implemented in Python. A labelled ‘rim’ file was then produced using in house code that labelled the CSF/GM boundary with ‘1’, the GM/WM boundary with ‘2’ and the GM ribbon with ‘3’. The rim file was used to generate 6 cortical layers using the equivolume approach (LayNii LN2_LAYERS; see also Chapter 4, Section 4.6.1). Subsequently, the ‘mid GM’ output from LN2_LAYERS was used to generate 300 columns across the GM in the hand knob region (LayNii, LN2_COLUMNS).

The FLASH data were bias field corrected (SPM) and brain extracted (FSL BET) before being registered to the subjects VASO-registered T_1 map using non-linear registration (ANTs, `antsRegistrationSyN`). The FLASH data were upsampled to 0.175 mm isotropic using spline interpolation. To create a vein mask, an upper threshold of 2000 was applied to each subjects registered FLASH data, any value above 2000 was set to 0 and anything below was set to 1.

6.4.1.5 Layer profiles

Any columns that contained veins, defined from the FLASH vein mask, were removed. The remaining columns within the cropped GM mask were used as the ROI for the calculation of the layer profiles and the deveining of the BOLD data. The unthresholded z -stats from the BOLD data were deveined using the spatial deconvolution method (LayNii, LN2_DEVEIN) [169], see Chapter 4 Section 4.7. The layer profiles were calculated for uncorrected BOLD, deveined corrected BOLD and VASO by taking the mean of the unthresholded z -stats in each layer within the column ROI.

6.4.2 Results

Figure 6.27 shows the z -stats for VASO ($z < -2.3$) and BOLD ($z > 3.1$) within a defined ROI of the motor cortex. There is significant activation in the hand knob region of the motor cortex across all subjects for both VASO and BOLD contrasts. As expected, the BOLD contrast z -stats have larger magnitudes in the superficial layers of the grey matter, due to the draining vein effect, and a larger spatial extent compared to VASO. The largest VASO z -stats are predominantly in the middle layers of the grey matter. For Subjects 1, 2, 3, 4, 9 and 10 a double peak pattern is visible across the GM in the BOLD z -stat images [116]. The double peak pattern represents a peak in the superficial layers corresponding to cortical input and a peak in the deep layers corresponding to cortical output to the spinal cord for the movement to executed.

Figure 6.28 shows the BOLD, corrected BOLD and VASO layer profiles for each of the 10 subjects. The BOLD profile for all 10 subjects exhibits the expected increase in activation towards the pial surface due to the draining vein effect. The VASO profile for Subjects 1 – 7 exhibit a single peak shape, with the middle cortical depths 3 and 4 having a higher mean z -stat than the deeper and superficial depths. The VASO profiles for Subjects 8, 9 and 10 show an increase towards the pial surface, however the slope of the profile is less than that of the BOLD profile. The corrected BOLD profiles exhibit an increase from the CSF towards the WM for Subjects 1 – 5. For Subject 6 the corrected BOLD exhibits a single peak shape, which peaks at depth 5, and for Subject 9 the corrected BOLD exhibits a single peak at depths 2 and 3.

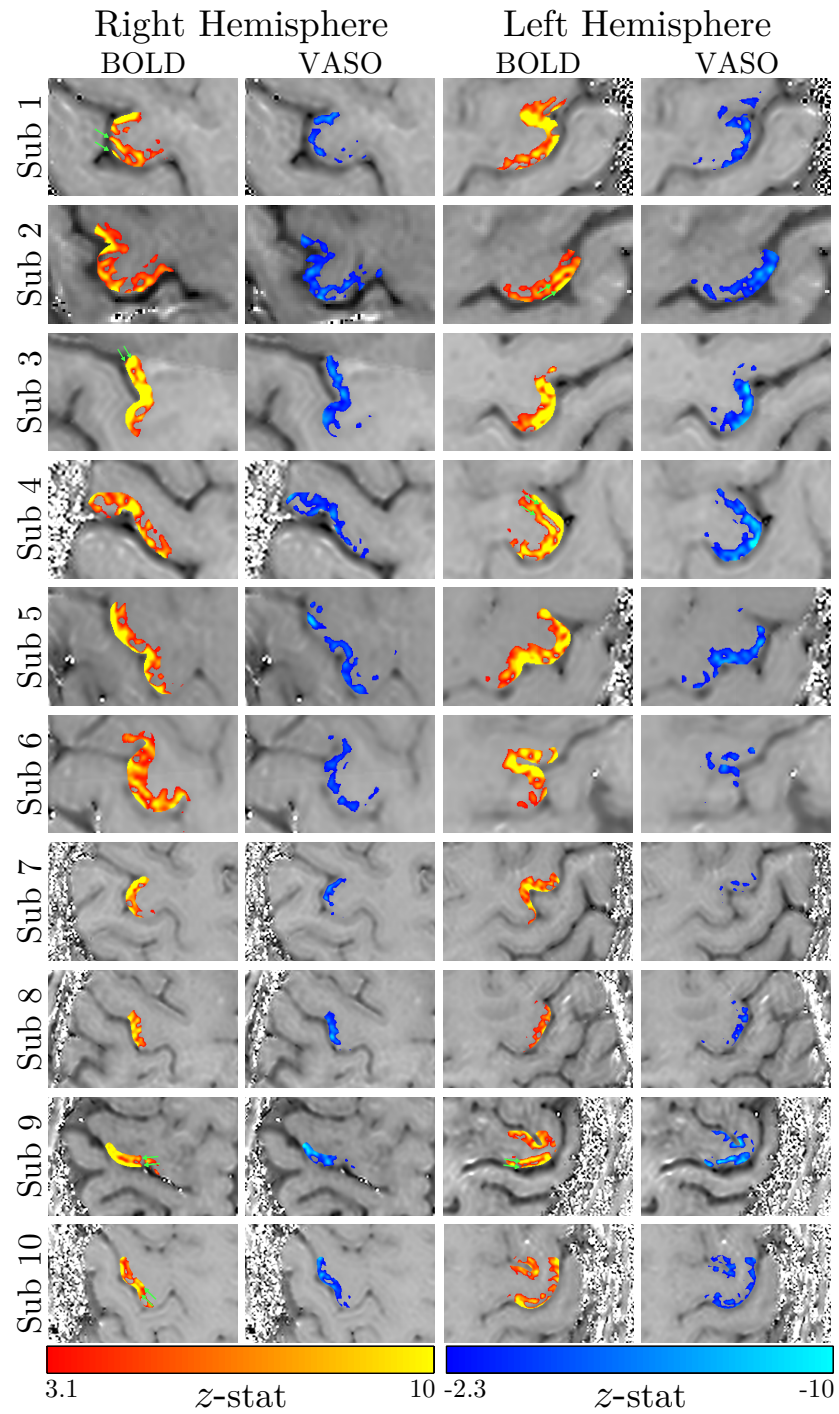


Figure 6.27: z -stat maps from the fixed effects GLM of the VASO and BOLD data. Overlaid on the mean BOLD corrected VASO image in the hand knob ROI. z -stat maps are thresholded at $z > 3.1$ for BOLD and $z < -2.3$ for VASO, and cluster corrected $p < 0.05$. Data shown for both hemispheres for all subjects.

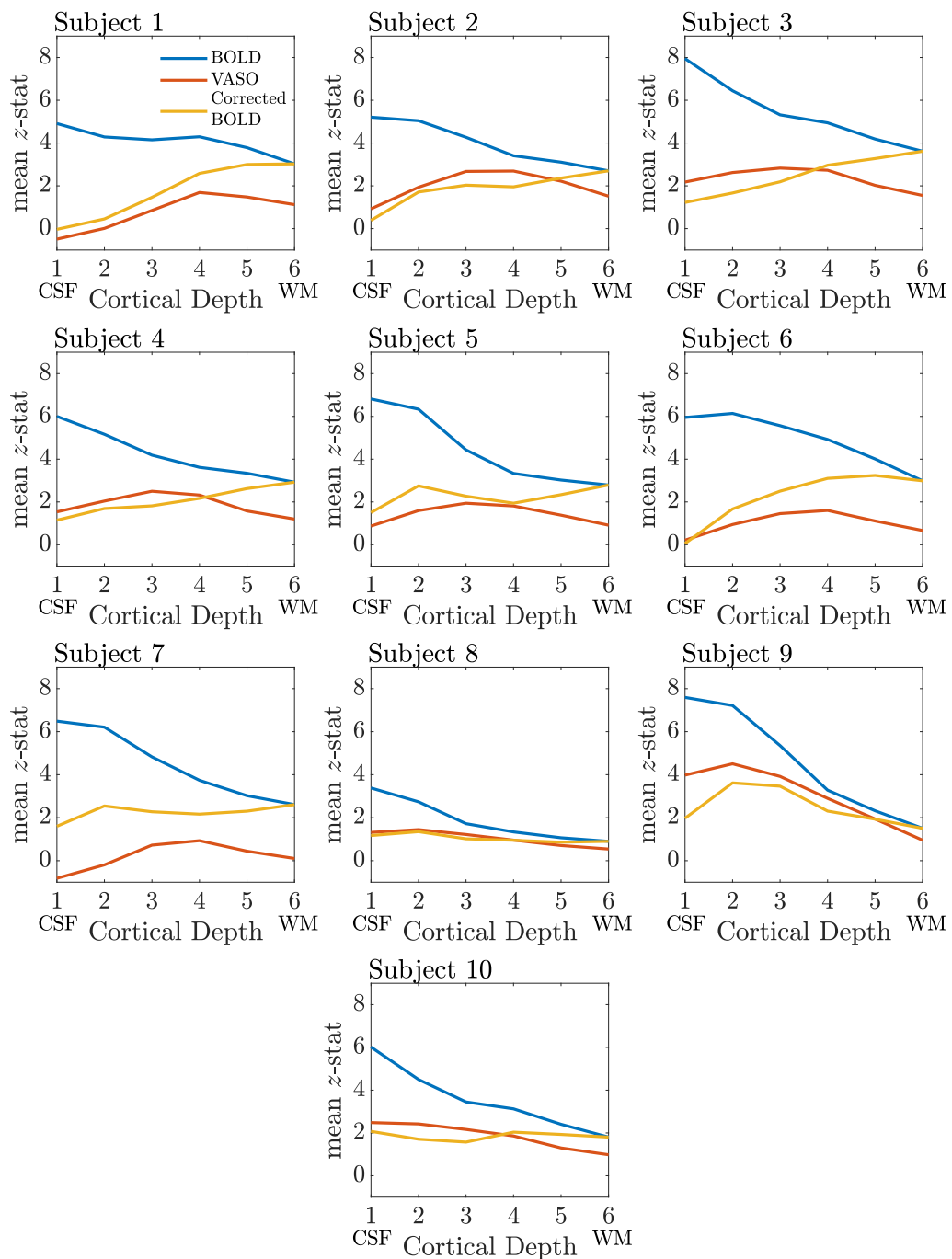


Figure 6.28: Layer profiles resulting from the mean unthresholded z -stat from each equivolume layer for BOLD, VASO and BOLD corrected using spatial deconvolution deconvolving.

Figure 6.29 shows the mean profile over all subjects for the BOLD, corrected BOLD and VASO. The BOLD profiles shows a linear increase from the WM towards the pial surface (CSF), highlighting the draining vein effect in the GE-BOLD data. The mean VASO profile shows a peak in the middle cortical depths, depth 2 is significantly higher than depth 1 ($p < 0.001$); Depth 3 higher than depths 1 ($p < 0.001$), 5 ($p < 0.016$) and 6 ($p < 0.002$); Depth 4 higher than depths 5 ($p < 0.001$) and 6 ($p < 0.001$); and depth 5 being higher than depth 6 ($p < 0.001$). The corrected BOLD mean profile shows a slope from the CSF/GM boundary (depth 1) towards the GM/WM boundary (depth 6).

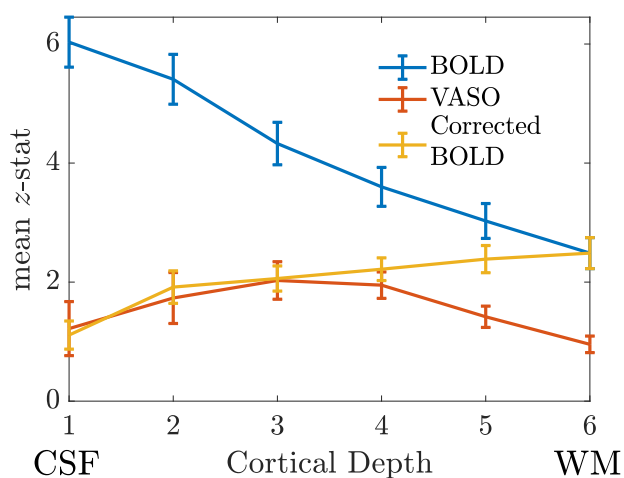


Figure 6.29: Layer profile for BOLD, corrected BOLD and VASO. Data shows mean over all subjects, and errorbars show SEM over subjects.

6.4.3 Discussion

An optimised 1 mm isotropic 3D-EPI VASO sequence has been used to measure layer-specific activation in the motor cortex during a finger-tapping task. The z -stat maps for both BOLD and VASO show significant activation in the hand knob region in the motor cortex. BOLD data yielded higher z -stats and a larger spatial extent than VASO, with higher activation being detected in the superficial layers compared to the deeper layers. The higher specificity of VASO

resulted in the peak activation being in the middle layers. In some subjects, a double peak/stripe pattern was seen in the z -stat maps of the BOLD data, this was not visible for the VASO data.

The VASO profiles for seven subjects showed a single peak pattern, with activation peaking in the middle depths. The same profile shape for both the BOLD and VASO data was seen in the layer profiles calculated from the mean across all subjects.

The expected shape of the VASO layer profile is a double peak pattern, as shown in Figure 6.30 taken from Huber *et al* 2015, thought to correspond to increased activity in the thalamocortical input layer V, in addition to increased activity in corticocortical input layers II and III. The grey shaded area in Figure 6.30 corresponds to the cortical GM region which is equivalent to the cortical depths 1 – 6 in Figure 6.29.

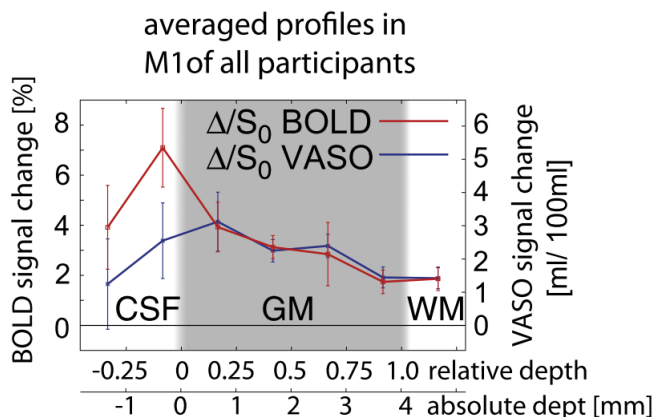


Figure 6.30: BOLD and VASO signal in M1 of the motor cortex. Showing an increase in signal at the pial surface for BOLD and a double peak in the VASO data [116].

The mostly likely explanation as to why only a single peak was seen in our data is that the resolution is too coarse, and so the two peaks merge into a single peak. In addition, the double peak pattern generated by finger to thumb pinching is located on the anterior side of the hand knob region [213, 214] and

the handknob ROIs used in this analysis covered both the anterior and posterior regions. Double peaks/stripes were seen in the BOLD z -stat maps of some subjects, but were no longer prominent in the layer profiles after averaging over the entire handknob ROI.

The BOLD profile corrected using spatial deconvolution was compared with the VASO profile. The resultant corrected BOLD profiles for five subjects showed an increase in signal from the CSF to WM, suggesting over correction of the profiles, as also seen in Chapter 4, Section 4.7.3.5. Two subjects had profiles that presented a peak in activity in the middle depths, similar to the shape of the VASO profile.

When comparing the mean layer profiles across subjects, the VASO and corrected BOLD profiles exhibit a similar shape from cortical depths 1–4, but diverge from depth 5, with the corrected BOLD continuing to increase towards the GM/WM boundary at depth 6 and the VASO profile decreasing towards depth 6. In Chapter 4 it was suggested that the deconvolving processing may over-correct the GE-BOLD data, resulting in a profile that linearly increases from the GM/CSF boundary towards the GM/WM boundary. In fact it may actually be the case that the deeper layers are being under-corrected and remaining too high after deconvolving. Currently, the VASO layer profiles provide the best description of the expected cortical layer activity, but with further exploration of deconvolving parameters and strategies it could become viable to solely acquire GE-BOLD data. Using GE-BOLD contrast for layer-fMRI would allow the use of shorter TRs as only a single readout is required per volume and no inversion times are needed. Alternatively, higher spatial resolution GE-BOLD data could be acquired using the TRs currently used to acquire VASO layer-fMRI data.

6.4.4 Future Work

In future work, the VASO sequence will be optimised further to achieve sub-millimetre spatial resolution. This can be achieved by increasing the SENSE acceleration factor or increasing the level of Halfscan applied (i.e. reducing

the amount of k-space data acquired), which would enable the acquisition of higher spatial resolution within the same TR. Additionally, the delay between the VASO readout and BOLD readout (Δ TI readout) can be reduced allowing for longer readouts to acquire higher spatial resolution. Reducing Δ TI readout will reduce the SNR of the measured BOLD response this should not be an issue as the BOLD data from the 1 mm isotropic VASO sequence were not SNR limited.

This will provide more voxels across the cortical depths to study the representation of the underlying neuronal activity. For tasks where temporal resolution is not of importance the spatial resolution can be significantly increased by implementing multishot 3D-EPI acquisitions at the expense of an increased volume TR e.g <0.5 mm with 2 shots which doubles volume TR.

Further work is needed to validate and optimise the deconvolution of GE-BOLD data such that the BOLD activation layer profile matches the VASO layer profile. GE-BOLD would provide greater sensitivity than VASO, combating the lower tSNR, if the draining vein effect could be accurately corrected for.

It should be noted that the development and implementation of VASO reaches further than fMRI studies, but can also be used to study glioma tumor detection and grading [215, 216], as an alternative to contrast based gadolinium methods.

6.5 NORDIC implementation for T_1 mapping structural measures

The final section assesses if any gains are made by also applying NORDIC to T_1 mapping data. High-resolution T_1 mapping of the human brain can be used to measure myelination to assess changes during brain development [217], characterise demyelination in clinical conditions [218], and perform in-vivo cortical parcellation [219]. However, high resolution T_1 mapping can become SNR limited. For example, whole brain 2D measures which provide improved

point-spread function but lower SNR than 3D schemes [10], or for high resolution partial brain 3D T_1 mapping schemes used to provide structural measures with the same coverage and distortions as functional data, such as when using vascular-space-occupancy (VASO) for layer evaluation [203, 220, 221]. NORDIC PCA denoising provides substantial SNR improvements for fMRI, VASO and diffusion data [110, 111]. Here the benefit of applying NORDIC PCA denoising to the 3D-EPI T_1 mapping dataset is evaluated.

6.5.1 Aim

To determine whether NORDIC results in a reduction in noise across the TIs of T_1 mapping acquisitions leading to improved fitting, and more precise T_1 measures in brain tissue. Improvements of using NORDIC PCA denoising were assessed for each subject by calculating improvement to the fit and interrogating the GM and WM peak heights and FWHM of the T_1 map tissue types.

6.5.2 Methods

3D T_1 mapping data were collected on ten subjects acquired with a 3D IR-EPI as described in in Section 6.4.1.2. NORDIC correction was applied to the magnitude and phase data (MATLAB, Mathworks) using a $5 \times 5 \times 5$ patch size. To compute T_1 -maps, the polarity of the magnitude data was first corrected using the phase data, and T_1 values were fit to an inversion recovery.

$$M = M_0 \left(1 - 2 \exp \left(-\frac{t}{T_1} \right) \right) \quad (6.2)$$

where M is the longitudinal magnetisation, M_0 is the initial magnetisation, and t is the inversion time.

To assess improvements from applying NORDIC denoising to the T_1 mapping the following metrics were assessed: T_1 difference map, R^2 difference map and GM/WM peak full width half maximum (FWHM). The corrected T_1 maps were subtracted from the uncorrected T_1 maps to calculate the T_1 difference map,

and similarly the difference in the coefficient of determination, R^2 , from the T_1 fit was determined by subtracting the R^2 maps.

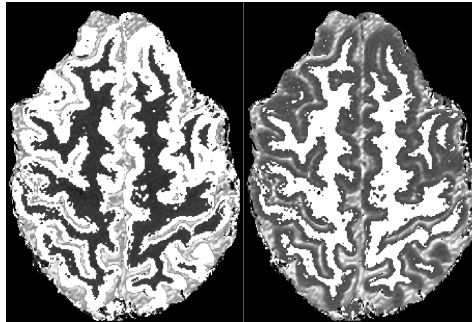


Figure 6.31: Segmentation of T_1 map using FSL FAST. Showing GM (left) and WM (right)

The uncorrected T_1 maps were segmented into grey matter, white matter and CSF masks using FSL FAST [134]; these were used as ROIs to compare the T_1 and R^2 differences. The T_1 values in the GM, WM and CSF were plotted as histograms with 300 bins in the range 0 - 5000. The height and FWHM of the GM and WM peak was calculated using MATLAB `findpeaks`.

6.5.3 Results

Figure 6.32 shows the difference in T_1 map data pre- and post-NORDIC. There are localised T_1 differences across all subjects, with greater T_1 differences in the WM, as shown in Figure 6.32a and b. The majority of T_1 differences for the WM are in the range 0 – 15 ms and for the GM 0 – 12 ms. Figure 6.32c and d shows the distribution of R^2 from the T_1 fitting. There is a small improvement of R^2 across the brain with the T_1 fit improving more in the WM than in the GM. There is an increase in R^2 around the outside/surface of the brain but this is an artefact and isn't considered when calculating R^2 improvements in the GM and WM. Data that has been denoised using NORDIC before fitting leads to a larger number of voxels with higher R^2 values, indicating that the T_1 fit

has improved. Shown in Table 6.3 the mean R^2 percentage improvement across the WM is $0.18 \pm 0.07\%$ and for the GM it is $0.14 \pm 0.08\%$.

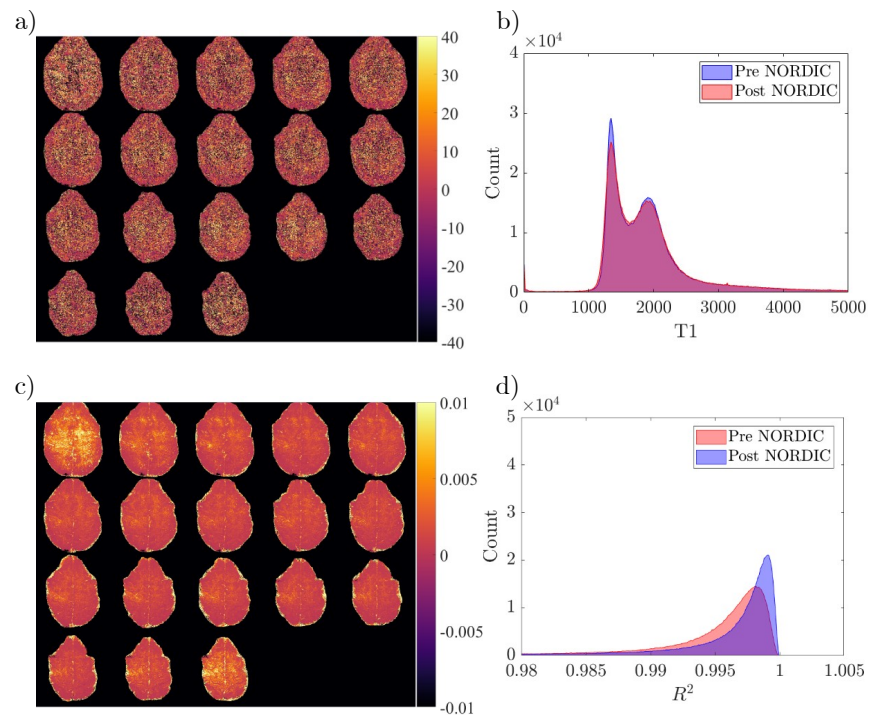


Figure 6.32: a) The difference in the 1 mm isotropic 3D-EPI T_1 values calculated from subtracting the T_1 map generated from the original data from the T_1 map generated following NORDIC denoising of the data. b) Histograms of T_1 values for data with and without NORDIC denoising. Data shown for an example subject. c) Difference in R^2 map shown across all 18 slices for a single subject. d) Distribution of R^2 values from the T_1 fitting using the original data (red) and the NORDIC denoised data (blue), shown for a single subject.

Subject		R^2		% Difference
		Pre-NORDIC	Post-NORDIC	
1	GM	0.9891	0.9909	0.18
	WM	0.9864	0.9888	0.25
2	GM	0.9694	0.9721	0.28
	WM	0.9749	0.9776	0.28
3	GM	0.9931	0.9939	0.08
	WM	0.9910	0.9922	0.12
4	GM	0.9936	0.9946	0.09
	WM	0.9926	0.9939	0.13
5	GM	0.9943	0.9955	0.12
	WM	0.9918	0.9935	0.18
6	GM	0.9888	0.9898	0.10
	WM	0.9890	0.9904	0.15
7	GM	0.9796	0.9825	0.29
	WM	0.9744	0.9770	0.27
8	GM	0.9903	0.9910	0.07
	WM	0.9822	0.9836	0.14
9	GM	0.9821	0.9832	0.12
	WM	0.9765	0.9782	0.18
10	GM	0.9971	0.9976	0.05
	WM	0.9961	0.9968	0.07
Group	GM	0.9878	0.9891	0.14±0.08
	WM	0.9855	0.9872	0.18±0.07

Table 6.3: Mean R^2 values in the GM and WM from the T_1 fitting of original and NORDIC denoised data.

Figure 6.33 shows the T_1 values from within the WM and GM showing sharper peaks for the T_1 data after NORDIC, with the WM peak sharpened

more than the GM peak. Table 6.4 shows the peak FWHM for GM and WM for each subject. The mean WM peak FWHM reduced by $7.4 \pm 5.8\%$ and the mean GM peak FWHM reduced by $3.0 \pm 1.0\%$.

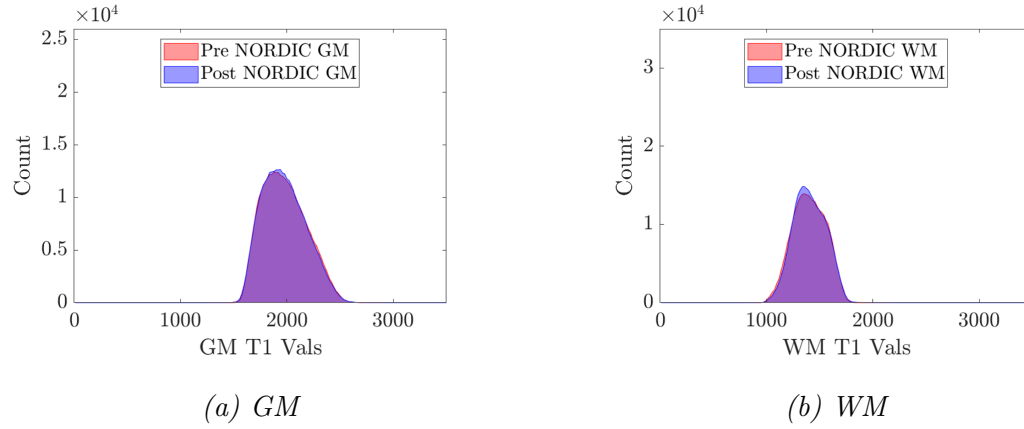


Figure 6.33: GM and WM peak pre/post NORDIC

Subject		Peak FWHM		% Difference
		Pre-NORDIC	Post-NORDIC	
1	GM	590.	574	2.80
	WM	425	398	6.4
2	GM	458	447	2.4
	WM	669	650	2.8
3	GM	591	575	2.6
	WM	293	256	12.8
4	GM	593	579	2.4
	WM	360	327	9.3
5	GM	585	561	4.0
	WM	271	217	19.7
6	GM	510	495	3.0
	WM	389	375	3.6
7	GM	609	601	1.4
	WM	385	362	6.0
8	GM	628	614	2.1
	WM	432	422	2.3
9	GM	523	501	4.3
	WM	523	521	0.5
10	GM	488	466	4.5
	WM	347	311	10.3
Group	GM	557	541	3.0 ± 1.0
	WM	410	384	7.4 ± 5.8

Table 6.4: FWHM of GM/WM peaks pre- and post- NORDIC denoising.

6.5.4 Discussion

The improvement in T_1 maps can also be seen in the increase in R^2 from the T_1 fitting, with the percentage improvement of R^2 being greater for WM than GM. The largest differences were seen in the sharpening of the histogram peaks for T_1 values in the GM and WM (Table 6.4). The reduction in the FWHM for both the GM and WM peak represents better tissue delineation, useful when using segmentation tools. These differences are all reasonably small, but do indicate some benefits to implementing NORDIC on T_1 mapping data. For this assessment the acquired data were 1 mm isotropic, and at this resolution the data were not in the SNR limited regime. For future layer studies with sub-millimeter resolutions the benefits of NORDIC will be more apparent.

6.6 Conclusion

This Chapter has shown that NORDIC PCA is an effective denoising method for BOLD, VASO and T_1 mapping data which are dominated by thermal noise. For optimal implementation of NORDIC, care should be taken when acquiring data with high SENSE acceleration factors and/or a high degree of HS [211] as these impact the g-factor and phase of the data which are key components for NORDIC denoising. In addition, the acquired noise dynamic must contain a high enough number of unique noise values so that NORDIC can calculate an accurate estimate of the noise floor from the data.

A VASO sequence was optimised for the acquisition of layer-specific measures during a motor task at 1 mm isotropic resolution. This was used to acquire data on 10 subjects during a finger-tapping task. The data were analysed to produce mean layer profiles across subjects for BOLD, ‘deveined’ corrected BOLD and VASO. The BOLD layer profile exhibited the well documented increase in activation towards the pial surface due to the draining vein effect. The VASO profile exhibited a peak in the middle cortical depths, likely due to insufficient

resolution to distinguish the expected double peak. The corrected BOLD profile shape was similar to the VASO profile for cortical depths 1–4 but diverged at depths 5–6, suggesting that deveining was under-correcting in deeper layers rather than over-correcting in superficial layers, as was suggested in Chapter 4. Further work is needed to increase the spatial resolution of the VASO sequence to acquire sub-millimetre resolution. In addition, further comparisons between VASO and corrected GE-BOLD are needed to validate the ‘deveining’ method.

Finally, NORDIC PCA was implemented on T_1 mapping data with matched geometry to VASO to assess if it can improve structural measures for layer definition. Improvements were seen in R^2 , indicating a better fit for the T_1 values, and narrowing of the FWHM for the GM and WM peaks. Greater improvements in R^2 and FWHM were seen for WM compared to GM. The improvements were small but indicate that acquisitions with higher spatial resolution for improved layer segmentation, would see greater improvements.

Chapter 7

Conclusion

7.1 Key Findings

The work in this thesis has developed methods for the analysis and interrogation of layer-specific EEG-fMRI data (Chapters 4 and 5), and the acquisition of layer-specific VASO-BOLD measures, together with the assessment of the ‘deveining’ method for correcting layer-specific GE-BOLD data.

In Chapter 4 a pipeline was developed for the analysis of previously acquired layer-dependent simultaneous 7 T EEG-fMRI data using a high resolution gradient echo 3D-EPI readout in response to an eyes open eyes closed task. The EEG and fMRI data were combined by calculating the regressors for use in the fMRI GLM by convolving the EEG alpha power timecourse with a standard HRF. The 3D-EPI fMRI data were distortion corrected to match the structural space and then motion corrected and coregistered using a single combined transformation to minimise blurring, optimising the alignment between the structural and functional data. Subject specific ROIs for V1, V2 and V3 were generated using retinotopic mapping. The structural data were then segmented and manually corrected to create a grey matter mask that was used to calculate six equivolume layers and 4000 cortical columns. Alpha-BOLD correlations were calculated by inputting the fMRI data into a fixed effects GLM with the EEG

regressors. The areas of interest were determined by selecting columns within visual areas V1, V2 and V3 that contained significant negative alpha-BOLD correlations. The initial layer profiles from these areas exhibited an increase in alpha-BOLD correlation towards the pial surface, resulting from the draining vein effect caused by ascending veins blurring the BOLD signal towards the cortical surface. Linear scaling, CBV scaling, linear regression and spatial deconvolution were all assessed for ‘deveining’ the GE-BOLD data to produce layer profiles. It was concluded that spatial deconvolution was the preferred method due to it being the most physiologically grounded model, taking into account baseline CBF measures estimated from the amplitude of low frequency fluctuations (ALFF) of the GE-BOLD fMRI data. In addition to the deveining methods, multiple analysis steps were assessed to determine the impact they had on the final layer profile shape. The steps considered were: the level of noise thresholding for the alpha-BOLD β -weights, the size of the columns used for region selection and ‘deveining’ of the GE-BOLD data, the ‘ λ ’ parameter for ‘deveining’, orthogonalisation of regressors for the GLM, and finally the method of layer profile calculation. A threshold of 5% was used to denoise the data as this provided a compromise of removing voxels deemed to be noise but keep a large percentage of the voxels containing negative alpha-BOLD correlations. For the column size, it was found that 4000 columns should be used to reduce the amount of column layers containing no alpha-BOLD correlation data. Columns containing empty layers impacted the deveining calculation as the model works by subtracting previous layer contributions from the current layer, so reducing the number of empty layers results in better deveining. The default value for ‘ λ ’ was used as each subjects CBF in the visual cortex was not considered to be abnormal. Finally, the layer profiles were calculated using the ‘Unmatched’ with the ‘Global mean’ method (Section 4.7.3.3).

Chapter 5 details the application of the optimal pipeline developed in Chapter 4 to EEG-fMRI layer data collected in 10 healthy subjects, with the aim of improving the understanding of the origins of human alpha oscillations. The

variation in alpha-BOLD correlation across cortical depths was assessed across subjects. As expected, the uncorrected GE-BOLD data showed alpha-BOLD correlations that increased towards the pial surface. Following ‘deveining’ using spatial deconvolution it was found that there was a significant dip in cortical depths 4 and 5 in the mean layer profile across V1, V2 and V3 over all subjects. This dip was similar when different GLM regressors were used, with the ‘EEG only’ regressor being skewed more towards the white matter (WM) surface compared to the ‘orthogonalised EEG’ regressor profile. This indicates that the orthogonalised EEG and boxcar regressors in the pipeline would be the most effective for analysing layer-specific EEG-fMRI data.

The alpha-BOLD layer profile dipping in the middle layers suggests cortico-cortical sources of alpha oscillations during the eyes open eyes closed paradigm. Alpha oscillations terminating in layers outside of layer IV of the cortex indicates top-down processing, which is contrary to the hypothesis that alpha oscillations are generated via thalamocortical mechanisms during an eyes open eyes closed task. However, our findings do agree with those seen in monkeys during a sustained visual stimulus [182]. The conclusions from Chapter 5 highlighted the need for further validation of deveining methods, which led to the work conducted in Chapter 6.

Chapter 6 first focuses on the denoising of high resolution BOLD and VASO data, for comparison of layer-specific profiles for VASO activation and ‘deveined’ BOLD activation. The relatively new denoising method of NORDIC PCA was assessed and implemented on high resolution 2D-EPI BOLD data collected at a range of flip angles to study a range of image and temporal SNR values. This was followed by the application to a VASO finger-tapping task to study layer profiles of VASO and BOLD. A 1 mm isotropic resolution VASO sequence was optimised for use in a finger-tapping task in the motor cortex. NORDIC is shown to be a helpful tool for the denoising of data that has high thermal noise, leading to improvements in image and temporal SNR of high resolution functional data. Layer-specific VASO-BOLD data were acquired on 10 healthy

subjects during a finger-tapping task and data were analysed using parts of the pipeline developed in Chapter 4. A key difference was the generation of the cortical layers in native VASO space. Significant VASO and BOLD activation was seen in the handknob region of the motor cortex for all 10 subjects, with some BOLD z -stat maps showing a double peak pattern across the cortex. The resulting mean layer profiles over all subjects were compared. The uncorrected BOLD profiles exhibited the expected increase towards the pial surface. The VASO profiles showed a single peak in the middle cortical depths, however the expected double peak was not seen. This is most likely due to the spatial resolution of the data being too coarse, causing the peaks to merge together. The corrected ‘deveined’ BOLD exhibited a profile shape similar to the VASO profile for cortical depths 1 – 4 but the profiles diverge for depths 5 and 6. This is potentially due to an under correction of the BOLD data in the deeper layers.

Finally, NORDIC is applied to T_1 mapping data to assess the improvements for layer specific structural measures. A small improvement was seen in both the wellness of fit R^2 and the FWHM of the grey matter and white matter peaks, with white matter showing more improvement due to its higher level of thermal noise. It was concluded that NORDIC improvements would be greater for higher resolution T_1 mapping data. It is recommended that a noise dynamic should be acquired and both the magnitude and phase data saved when performing T_1 mapping so that NORDIC denoising can be implemented on the complex data. Further investigation on the optimal NORDIC patch size for T_1 mapping data is needed. In addition, 3D-EPI-IR T_1 mapping data will provide structural measures with the same distortions as the functional BOLD and VASO data so that grey matter masks can be generated in the native functional space. This would avoid the spatial smoothing that is introduced by coregistering and warping the functional and structural data to each other.

7.2 Future Directions

In future the pipeline developed for layer-specific EEG-fMRI could be used to study EEG alpha oscillations during more complex paradigms to further advance our understanding of alpha generating mechanisms [183, 222, 223].

The application of NORDIC to high resolution VASO data provided good tSNR so that layer specific activation could be seen. Going forwards, layer specific EEG-fMRI could be performed using the VASO-BOLD sequence. This would remove the prior limitation of having to correct for the draining vein effect and also provide improved spatial localisation. If it can be approved from a safety perspective at 7 T, layer-specific EEG-fMRI using VASO-BOLD will also give further insight into the coupling between electrophysiological brain activity and the corresponding haemodynamics. Additionally, the 1 mm VASO sequence will be optimised further with the use of multishot 3D-EPI readouts explored for use in high resolution studies, for example to study layer alpha-BOLD and alpha-CBV correlations to uncover whether alpha oscillations are strictly attentional. Finally, further work is needed to validate the spatial deconvolution deveining method, by comparing different implementations of the model.

Work has also been conducted to assess the feasibility of layer-fMRI at 3 T [224, 225]. Protocols have been developed for both VASO [225] and GE-BOLD [224] that can be implemented in conjunction with NORDIC denoising to improve the heavily SNR limited data. Acquiring layer EEG-fMRI at 3T would greatly improve the quality of the EEG data as amplitude of motion artefacts and pulse artefacts would reduce due to the lower B_0 field strength. In addition, motion artefacts can be further reduced by using EEG caps with carbon wire loops enabling improved artefact removal [226]. With improved EEG data quality it may be possible to look at other frequency bands such as beta [49, 56, 58] or gamma [46, 59, 60] and their relationship with the haemodynamics of the brain on a laminar level. Layer EEG-fMRI at 3 T would enable wider

spread adoption of these methods as 3 T scanners are more readily available and the challenges of EEG-fMRI at 7T [139] would be circumvented.

Other MR techniques such as Diffusion Weighted (DW) fMRI [227], line scanning [228], or Direct Imaging of Neuronal Activity (DIANA) [229] could be considered in future to measure neuronal activity. DW-fMRI aims to measure neuronal activity via a decrease in the apparent diffusion coefficient upon activation corresponding to the swelling of cortical cells [230]. To date, DW-fMRI remains controversial [231] and has not been widely adopted. On the other hand, line scanning is a popular method for high temporal resolution imaging across the cortical layers [228, 232, 233]. Line scanning acquisitions enable TRs on the order of ~ 100 ms by removing the need for phase encoding gradients that would typically be present in a 2D-EPI acquisition for example. This results in the signal from the 2D plane collapsing down to solely the frequency encode direction. Therefore, the acquisition requires saturation pulses to null as much signal from outside the imaged line as possible. Line scanning is suitable for measuring layer activation from a predetermined, specific area of the cortex, for example sections of the hand knob in M1 or S1. Line scanning would be difficult to implement when activation is more disperse and less spatially predictable as was shown to be the case for alpha-BOLD correlations in Chapter 5. Finally, DIANA [229] is a technique similar to line scanning which aims to directly measure neuronal activity (via changes in T_1) at a temporal resolution of 5 ms. This is achieved by repeatedly acquiring a line of k -space during 1 trial of the stimulus, then repeatedly acquiring the next line of k -space during the next trial of the stimulus and so forth. However, DIANA remains controversial due to limited understanding of the physiological underpinnings of the neuronal cell changes that give rise to the MR signal change and there are a growing number of questions about the reproducibility of the methods [234].

References

1. Scheeringa, R., Koopmans, P. J., Van Mourik, T., Jensen, O. & Norris, D. G. The relationship between oscillatory EEG activity and the laminar-specific BOLD signal. eng. *Proceedings of the National Academy of Sciences of the United States of America* **113**, 6761–6766. doi:10.1073/pnas.1522577113 (2016).
2. Ogawa, S., Lee, T. M., Kay, A. R. & Tank, D. W. Brain magnetic resonance imaging with contrast dependent on blood oxygenation. *Proceedings of the National Academy of Sciences of the United States of America* **87**, 9868. doi:10.1073/PNAS.87.24.9868 (1990).
3. Huber, L. *Unwanted spatial blurring during resampling* 2018. <https://1ayerfmri.com/2018/03/23/unwanted-spatial-blurring-during-resampling/>.
4. Felleman, D. J. & Van Essen, D. C. Distributed hierarchical processing in the primate cerebral cortex. *Cerebral Cortex*. doi:10.1093/cercor/1.1.1 (1991).
5. Gotman, J. & Pittau, F. Combining EEG and fMRI in the study of epileptic discharges. *Epilepsia* **52**, 38–42. doi:10.1111/J.1528-1167.2011.03151.X (2011).
6. Tatum, W. O. *et al.* Clinical utility of EEG in diagnosing and monitoring epilepsy in adults. *Clinical Neurophysiology* **129**, 1056–1082. doi:10.1016/J.CLINPH.2018.01.019 (2018).

7. Van Houdt, P. J. *et al.* EEG-fMRI correlation patterns in the presurgical evaluation of focal epilepsy: A comparison with electrocorticographic data and surgical outcome measures. *NeuroImage* **75**, 238–248. doi:10.1016/J.NEUROIMAGE.2013.02.033 (2013).
8. Smith, S. J. M. EEG in the diagnosis, classification, and management of patients with epilepsy. *Journal of Neurology, Neurosurgery & Psychiatry* **76**, ii2 LP –ii7. doi:10.1136/jnnp.2005.069245 (2005).
9. Berger, H. Über das Elektrenkephalogramm des Menschen. *Archiv für Psychiatrie und Nervenkrankheiten* **87**, 527–570. doi:10.1007/BF01797193/METRICS (1929).
10. Sanchez Panchuelo, R. M., Mougin, O., Turner, R. & Francis, S. T. Quantitative T1 mapping using multi-slice multi-shot inversion recovery EPI. *NeuroImage* **234**, 117976. doi:10.1016/J.NEUROIMAGE.2021.117976 (2021).
11. Rooney, W. D. *et al.* Magnetic field and tissue dependencies of human brain longitudinal 1H2O relaxation in vivo. *Magnetic Resonance in Medicine* **57**, 308–318. doi:10.1002/MRM.21122 (2007).
12. Wright, P. J. *et al.* Water proton T1 measurements in brain tissue at 7, 3, and 1.5T using IR-EPI, IR-TSE, and MPRAGE: Results and optimization. *Magnetic Resonance Materials in Physics, Biology and Medicine* **21**, 121–130. doi:10.1007/S10334-008-0104-8/METRICS (2008).
13. Rane, S. D. & Gore, J. C. Measurement of T1 of human arterial and venous blood at 7 T. *Magnetic Resonance Imaging* **31**, 477–479. doi:10.1016/J.MRI.2012.08.008 (2013).
14. Lauterbur, P. C. Image Formation by Induced Local Interactions: Examples Employing Nuclear Magnetic Resonance. *Nature* **1973** **242**, 190–191. doi:10.1038/242190a0 (1973).

-
15. Mansfield, P. & Grannell, P. K. NMR 'diffraction' in solids? *Journal of Physics C: Solid State Physics* **6**, L422. doi:10.1088/0022-3719/6/22/007 (1973).
 16. Garroway, A. N., Grannell, P. K. & Mansfield, P. Image formation in NMR by a selective irradiative process. *J. Phys. C: Solid State Phys* **7** (1974).
 17. Kumar, A., Welti, D. & Ernst, R. R. NMR Fourier Zeugmatography. *JOURNAL OF MAGNETIC RESONANCE* **18**, 69–83 (1975).
 18. Mansfield, P. Multi-planar image formation using NMR spin echoes. **10**. doi:10.1088/0022-3719/10/3/004 (1977).
 19. Rzedzian, R. *et al.* REAL-TIME NUCLEAR MAGNETIC RESONANCE CLINICAL IMAGING IN PAEDIATRICS. *The Lancet* **322**, 1281–1282. doi:[https://doi.org/10.1016/S0140-6736\(83\)91153-4](https://doi.org/10.1016/S0140-6736(83)91153-4) (1983).
 20. Feinberg, D. A., Hale, J. D., Watts, J. C., Kaufman, L. & Mark, A. Halving MR imaging time by conjugation: demonstration at 3.5 kG. <https://doi.org/10.1148/radiology.161.2.3763926> **161**, 527–531. doi:10.1148/RADIOLOGY.161.2.3763926 (1986).
 21. MacFall, J. R., Pelc, N. J. & Vavrek, R. M. Correction of spatially dependent phase shifts for partial Fourier imaging. *Magnetic Resonance Imaging* **6**, 143–155. doi:10.1016/0730-725X(88)90444-4 (1988).
 22. Pruessmann, K. P., Weiger, M., Scheidegger, M. B. & Boesiger, P. SENSE: Sensitivity Encoding for Fast MRI. *Magnetic resonance in medicine* **42**, 952–962 (1999).
 23. Griswold, M. A. *et al.* Generalized autocalibrating partially parallel acquisitions (GRAPPA). *Magnetic Resonance in Medicine* **47**, 1202–1210. doi:10.1002/MRM.10171 (2002).

-
24. Robson, P. M. *et al.* Comprehensive quantification of signal-to-noise ratio and g-factor for image-based and k-space-based parallel imaging reconstructions. *Magnetic resonance in medicine* **60**, 895–907. doi:10.1002/MRM.21728 (2008).
 25. Larkman, D. J. *et al.* Use of Multicoil Arrays for Separation of Signal from Multiple Slices Simultaneously Excited. doi:10.1002/1522-2586 (2001).
 26. Moeller, S. *et al.* Multiband Multislice GE-EPI at 7 Tesla, With 16-Fold Acceleration Using Partial Parallel Imaging With Application to High Spatial and Temporal Whole-Brain fMRI. *Magn Reson Med* **63**, 1144–1153. doi:10.1002/mrm.22361 (2010).
 27. Hennel, F. Multiple-shot echo-planar imaging. *Concepts in Magnetic Resonance* **9**, 43–58. doi:https://doi.org/10.1002/(SICI)1099-0534(1997)9:1<43::AID-CMR4>3.0.CO;2-N (1997).
 28. Gao, J. H. & Liu, H. L. Inflow effects on functional MRI. *NeuroImage* **62**, 1035–1039. doi:10.1016/J.NEUROIMAGE.2011.09.088 (2012).
 29. Mugler III, J. P. & Brookeman, J. R. Three-dimensional magnetization-prepared rapid gradient-echo imaging (3D MP RAGE). *Magnetic Resonance in Medicine* **15**, 152–157. doi:10.1002/mrm.1910150117 (1990).
 30. Kasai, K. *et al.* Neuroanatomy and neurophysiology in schizophrenia. *Neuroscience Research* **43**, 93–110. doi:10.1016/S0168-0102(02)00023-8 (2002).
 31. Torres, F. & Hutton, J. T. Clinical Neurophysiology of Dementia. *Neurologic Clinics* **4**, 369–386. doi:10.1016/S0733-8619(18)30975-7 (1986).
 32. Neher, E. & Sakmann, B. The Patch Clamp Technique. *Scientific American* **266**, 44–51 (1992).

-
33. Cogan, S. F. Neural Stimulation and Recording Electrodes. *Annual Review of Biomedical Engineering* **10**, 275–309. doi:10.1146/annurev.bioeng.10.061807.160518 (2008).
 34. Legatt, A. D., Arezzo, J. & Vaughan, H. G. Averaged multiple unit activity as an estimate of phasic changes in local neuronal activity: effects of volume-conducted potentials. *Journal of Neuroscience Methods* **2**, 203–217. doi:10.1016/0165-0270(80)90061-8 (1980).
 35. Cohen, D. Magnetoencephalography: Evidence of Magnetic Fields Produced by Alpha-Rhythm Currents. *Science* **161**, 784–786. doi:10.1126/SCIENCE.161.3843.784 (1968).
 36. Noachtar, S. & Rémi, J. The role of EEG in epilepsy: A critical review. *Epilepsy & Behavior* **15**, 22–33. doi:10.1016/J.YEBEH.2009.02.035 (2009).
 37. Ogawa, S. *et al.* *Intrinsic signal changes accompanying sensory stimulation: Functional brain mapping with magnetic resonance imaging* tech. rep. (1992), 5951–5955.
 38. Bandettini, P. A., Wong, E. C., Hinks, R. S., Tikofsky, R. S. & Hyde, J. S. Time course EPI of human brain function during task activation. *Magnetic Resonance in Medicine* **25**, 390–397. doi:10.1002/MRM.1910250220 (1992).
 39. Kwong, K. K. *et al.* Dynamic magnetic resonance imaging of human brain activity during primary sensory stimulation. *Proceedings of the National Academy of Sciences* **89**, 5675–5679. doi:10.1073/PNAS.89.12.5675 (1992).
 40. Hamalainen, M., Hari, R., Ilmoniemi, R. J., Knuutila, J. & Lounasmaa, O. V. Magnetoencephalography theory, instrumentation, and applications to noninvasive studies of the working human brain (1993).

-
41. Kirschstein, T. & Köhling, R. What is the source of the EEG? *Clinical EEG and neuroscience* **40**, 146–149. doi:10.1177/155005940904000305 (2009).
 42. Knyazev, G. G. Motivation, emotion, and their inhibitory control mirrored in brain oscillations. *Neuroscience & Biobehavioral Reviews* **31**, 377–395. doi:10.1016/J.NEUBIOREV.2006.10.004 (2007).
 43. Murphy, M. *et al.* Source modeling sleep slow waves. *Proceedings of the National Academy of Sciences of the United States of America* **106**, 1608–1613. doi:10.1073/PNAS.0807933106/SUPPL{_}FILE/0807933106SI.PDF (2009).
 44. Shirvalkar, P. & Bahar, A. S. The Multiple Origins and Laminar Topography of the Hippocampal Theta Rhythm. *The Journal of Neuroscience* **29**, 7111. doi:10.1523/JNEUROSCI.1528-09.2009 (2009).
 45. Hughes, S. W. *et al.* Synchronized oscillations at α and θ frequencies in the lateral geniculate nucleus. *Neuron* **42**, 253–268. doi:10.1016/S0896-6273(04)00191-6 (2004).
 46. Buffalo, E. A., Fries, P., Landman, R., Buschman, T. J. & Desimone, R. Laminar differences in gamma and alpha coherence in the ventral stream. *Proceedings of the National Academy of Sciences of the United States of America* **108**, 11262–11267. doi:https://doi.org/10.1073/pnas.1011284108 (2011).
 47. Leventhal, D. K. *et al.* Basal Ganglia Beta Oscillations Accompany Cue Utilization. *Neuron* **73**, 523–536. doi:10.1016/J.NEURON.2011.11.032 (2012).
 48. Jensen, O. *et al.* On the human sensorimotor-cortex beta rhythm: Sources and modeling. *NeuroImage* **26**, 347–355. doi:10.1016/J.NEUROIMAGE.2005.02.008 (2005).

-
49. Sherman, M. A. *et al.* Neural mechanisms of transient neocortical beta rhythms: Converging evidence from humans, computational modeling, monkeys, and mice. *Proceedings of the National Academy of Sciences of the United States of America* **113**, E4885–E4894. doi:10.1073/PNAS.1604135113/SUPPL_{_}FILE/PNAS.1604135113.SAPP.PDF (2016).
 50. Buzsáki, G. & Wang, X. J. Mechanisms of Gamma Oscillations. *Annual Review of Neuroscience* **35**, 203–225. doi:10.1146/ANNUREV-NEURO-062111-150444 (2012).
 51. Harmony, T. *et al.* EEG delta activity: an indicator of attention to internal processing during performance of mental tasks. *International Journal of Psychophysiology* **24**, 161–171. doi:10.1016/S0167-8760(96)00053-0 (1996).
 52. Klimesch, W., Schimke, H. & Schwaiger, J. Episodic and semantic memory: an analysis in the EEG theta and alpha band. *Electroencephalography and Clinical Neurophysiology* **91**, 428–441. doi:10.1016/0013-4694(94)90164-3 (1994).
 53. Manuel De Vega, X. *et al.* Sentential Negation Might Share Neurophysiological Mechanisms with Action Inhibition. Evidence from Frontal Theta Rhythm. *The Journal of Neuroscience*. doi:10.1523/JNEUROSCI.3736-15.2016 (2016).
 54. Webster, K. & Ro, T. Visual Modulation of Resting State α Oscillations. *eNeuro* **7**. doi:10.1523/ENEURO.0268-19.2019 (2020).
 55. Sokoliuk, R. *et al.* Two Spatially Distinct Posterior Alpha Sources Fulfill Different Functional Roles in Attention. *The Journal of Neuroscience* **39**, 7183. doi:10.1523/JNEUROSCI.1993-18.2019 (2019).
 56. Pfurtscheller, G., Stancák, A. & Neuper, C. Post-movement beta synchronization. A correlate of an idling motor area? *Electroencephalography and Clinical Neurophysiology* **98**, 281–293. doi:10.1016/0013-4694(95)00258-8 (1996).
-

-
57. Xiao, R. & Ding, L. EEG resolutions in detecting and decoding finger movements from spectral analysis. *Frontiers in Neuroscience* **9**, 308. doi:10.3389/FNINS.2015.00308 (2015).
 58. Qi, H. Post-Movement Beta Rebound Is Related to Movement Connection. *World Journal of Neuroscience* **12**, 93–104. doi:10.4236/WJNS.2022.122010 (2022).
 59. Gross, J., Schnitzler, A., Timmermann, L. & Ploner, M. Gamma oscillations in human primary somatosensory cortex reflect pain perception. *PLoS Biol* **5**, 133. doi:10.1371/journal.pbio.0050133 (2007).
 60. Osipova, D. *et al.* Theta and Gamma Oscillations Predict Encoding and Retrieval of Declarative Memory. *Journal of Neuroscience* **26**, 7523–7531. doi:10.1523/jneurosci.1948-06.2006 (2006).
 61. Bauer, M., Oostenveld, R., Peeters, M. & Fries, P. Tactile Spatial Attention Enhances Gamma-Band Activity in Somatosensory Cortex and Reduces Low-Frequency Activity in Parieto-Occipital Areas. *The Journal of Neuroscience* **26**, 490–501. doi:10.1523/JNEUROSCI.5228-04.2006 (2006).
 62. Bear, M. F. *Neuroscience : exploring the brain* Enhanced f. eng (eds Connors, B. W. & Paradiso, M. A.) (Jones & Bartlett Learning, 2016).
 63. Brodmann, K. *Vergleichende Lokalisationslehre der Grosshirnrinde in ihren Prinzipien dargestellt auf Grund des Zellbaues* (Johann Ambrosius Barth, Leipzig, 1909).
 64. Buckner, R. L., Kelley, W. M. & Petersen, S. E. Frontal cortex contributes to human memory formation. *Nature Neuroscience* 1999 2:4 **2**, 311–314. doi:10.1038/7221 (1999).
 65. Shomstein, S., Lee, J. & Behrmann, M. Top-down and bottom-up attentional guidance: Investigating the role of the dorsal and ventral parietal

-
- cortices. *Experimental Brain Research* **206**, 197–208. doi:10.1007/S00221-010-2326-Z/FIGURES/6 (2010).
66. Ojanen, V. *et al.* Processing of audiovisual speech in Broca's area. *NeuroImage* **25**, 333–338. doi:10.1016/J.NEUROIMAGE.2004.12.001 (2005).
67. Guo, Z. J. *et al.* Brain areas activated by uncertain reward-based decision-making in healthy volunteers. *Neural Regeneration Research* **8**, 3344. doi:10.3969/J.ISSN.1673-5374.2013.35.009 (2013).
68. Thompson, R. F. *The brain : a neuroscience primer* 2nd ed. eng (eds Atkinson, R. C., Gardner, L. & Thompson, R. F.) (Worth Publishers, New York, 1993).
69. Schüz, A. & Braitenberg, V. in *International Encyclopedia of the Social & Behavioral Sciences* (eds Smelser, N. J. & Baltes, P. B.) 1634–1640 (Elsevier, Oxford, 2001). doi:10.1016/B0-08-043076-7/03443-4.
70. Hanslmayr, S., Gross, J., Klimesch, W. & Shapiro, K. L. The role of alpha oscillations in temporal attention. *Brain Research Reviews* **67**, 331–343. doi:10.1016/j.brainresrev.2011.04.002 (2011).
71. Jensen, O., Gelfand, J., Kounios, J. & Lisman, J. E. Oscillations in the alpha band (9-12 Hz) increase with memory load during retention in a short-term memory task. *Cerebral Cortex* **12**, 877–882. doi:10.1093/cercor/12.8.877 (2002).
72. Klimesch, W., Doppelmayr, M., Schwaiger, J., Auinger, P. & Winkler, T. 'Paradoxical' alpha synchronization in a memory task. *Cognitive Brain Research* **7**, 493–501. doi:10.1016/S0926-6410(98)00056-1 (1999).
73. Ramón y Cajal, S. *Comparative Study of the Sensory Areas of the Human Cortex* (Clark University, 1899).
74. Gregory, R. L. (L. *The intelligent eye* eng (Weidenfeld & Nicolson, London, 1970).
-

-
75. Koopmans, P. J., Barth, M. & Norris, D. G. Layer-specific BOLD activation in human V1. *Human Brain Mapping* **31**, 1297–1304. doi:10.1002/hbm.20936 (2010).
76. Lawrence, S. J. *et al.* Laminar Organization of Working Memory Signals in Human Visual Cortex. *Current Biology* **28**, 3435–3440. doi:10.1016/j.cub.2018.08.043 (2018).
77. Olman, C. A. *et al.* Layer-Specific fMRI Reflects Different Neuronal Computations at Different Depths in Human V1. *PLOS ONE* **7**, e32536. doi:10.1371/JOURNAL.PONE.0032536 (2012).
78. Adrian, E. D. & Matthews, B. H. C. The Berger Rhythm: Potential changes from the Occipital lobes in man. *Brain* **57**, 355–385. doi:10.1093/brain/57.4.355 (1934).
79. Lopes da Silva, F. Neural mechanisms underlying brain waves: from neural membranes to networks. *Electroencephalography and Clinical Neurophysiology* **79**, 81–93. doi:10.1016/0013-4694(91)90044-5 (1991).
80. Von Stein, A., Chiang, C. & König, P. Top-down processing mediated by interareal synchronization. *Proceedings of the National Academy of Sciences of the United States of America* **97**, 14748–14753. doi:10.1073/pnas.97.26.14748 (2000).
81. Klimesch, W., Sauseng, P. & Hanslmayr, S. EEG alpha oscillations: The inhibition–timing hypothesis. *Brain Research Reviews* **53**, 63–88. doi:10.1016/J.BRAINRESREV.2006.06.003 (2007).
82. Da Silva, F. H., van Lierop, T. H., Schrijer, C. F. & van Leeuwen, W. S. Organization of thalamic and cortical alpha rhythms: spectra and coherences. *Electroencephalography and clinical neurophysiology* **35**, 627–639. doi:10.1016/0013-4694(73)90216-2 (1973).

-
83. Lopes Da Silva, F. H. & Storm Van Leeuwen, W. The cortical source of the alpha rhythm. *Neuroscience Letters* **6**, 237–241. doi:10.1016/0304-3940(77)90024-6 (1977).
84. Lopes da Silva, F. H., Vos, J. E., Mooibroek, J. & van Rotterdam, A. Relative contributions of intracortical and thalamo-cortical processes in the generation of alpha rhythms, revealed by partial coherence analysis. *Electroencephalography and Clinical Neurophysiology* **50**, 449–456. doi:10.1016/0013-4694(80)90011-5 (1980).
85. Silva, L. R., Amitai, Y. & Connors, B. W. Intrinsic oscillations of neocortex generated by layer 5 pyramidal neurons. *Science (New York, N. Y.)* **251**, 432–435. doi:10.1126/science.1824881 (1991).
86. Scheeringa, R. *et al.* Relating neural oscillations to laminar fMRI connectivity in visual cortex. *Cerebral Cortex*. doi:10.1093/CERCOR/BHAC154 (2022).
87. Van der Zwaag, W. *et al.* fMRI at 1.5, 3 and 7 T: Characterising BOLD signal changes. *NeuroImage* **47**, 1425–1434. doi:10.1016/J.NEUROIMAGE.2009.05.015 (2009).
88. Ogawa, S. *et al.* Functional brain mapping by blood oxygenation level-dependent contrast magnetic resonance imaging. A comparison of signal characteristics with a biophysical model. *Biophysical Journal* **64**, 803–812. doi:10.1016/S0006-3495(93)81441-3 (1993).
89. Boxerman, J. L., Hamberg, L. M., Rosen, B. R. & Weisskoff, R. M. Mr contrast due to intravascular magnetic susceptibility perturbations. *Magnetic Resonance in Medicine* **34**, 555–566. doi:10.1002/MRM.1910340412 (1995).
90. Hu, X. & Yacoub, E. The story of the initial dip in fMRI. *NeuroImage* **62**, 1103–1108. doi:10.1016/J.NEUROIMAGE.2012.03.005 (2012).

-
91. Parkes, L. M. *et al.* Quantifying the spatial resolution of the gradient echo and spin echo BOLD response at 3 Tesla. *Magnetic resonance in medicine* **54**, 1465–1472. doi:10.1002/MRM.20712 (2005).
 92. Ives, J. R., Warach, S., Schmitt, F., Edelman, R. R. & Schomer, D. L. Monitoring the patient's EEG during echo planar MRI. *Electroencephalography and Clinical Neurophysiology* **87**, 417–420. doi:[https://doi.org/10.1016/0013-4694\(93\)90156-P](https://doi.org/10.1016/0013-4694(93)90156-P) (1993).
 93. Mulert, C. & Lemieux, L. *EEG-fMRI : physiological basis, technique, and applications* 539 (Springer, 2010).
 94. Allen, P. J., Polizzi, G., Krakow, K., Fish, D. R. & Lemieux, L. Identification of EEG events in the MR scanner: The problem of pulse artifact and a method for its subtraction. *NeuroImage* **8**, 229–239. doi:10.1006/NIMG.1998.0361 (1998).
 95. Mullinger, K., Debener, S., Coxon, R. & Bowtell, R. Effects of simultaneous EEG recording on MRI data quality at 1.5, 3 and 7 tesla. *International Journal of Psychophysiology* **67**, 178–188. doi:10.1016/J.IJPSYCHO.2007.06.008 (2008).
 96. Yan, W. X., Mullinger, K. J., Geirsdottir, G. B. & Bowtell, R. Physical modeling of pulse artefact sources in simultaneous EEG/fMRI. *Human Brain Mapping* **31**, 604–620. doi:10.1002/hbm.20891 (2010).
 97. Yan, W. X., Mullinger, K. J., Brookes, M. J. & Bowtell, R. Understanding gradient artefacts in simultaneous EEG/fMRI. *NeuroImage* **46**, 459–471. doi:10.1016/j.neuroimage.2009.01.029 (2009).
 98. Jansen, M. *et al.* Motion-related artefacts in EEG predict neuronally plausible patterns of activation in fMRI data. *NeuroImage*. doi:10.1016/j.neuroimage.2011.06.094 (2012).

-
99. Portnova, G. V. *et al.* Correlation of BOLD signal with linear and non-linear patterns of EEG in resting state EEG-informed fMRI. *Frontiers in Human Neuroscience* **11**, 654. doi:10.3389/FNHUM.2017.00654/BIBTEX (2018).
100. Lachaux, J. P. *et al.* Relationship between task-related gamma oscillations and BOLD signal: New insights from combined fMRI and intracranial EEG. *Human Brain Mapping* **28**, 1368. doi:10.1002/HBM.20352 (2007).
101. Scheeringa, R. *et al.* Neuronal Dynamics Underlying High- and Low-Frequency EEG Oscillations Contribute Independently to the Human BOLD Signal. *Neuron* **69**, 572–583. doi:10.1016/J.NEURON.2010.11.044 (2011).
102. Laufs, H. *et al.* Electroencephalographic signatures of attentional and cognitive default modes in spontaneous brain activity fluctuations at rest. *Proceedings of the National Academy of Sciences of the United States of America* **100**, 11053–11058. doi:10.1073/PNAS.1831638100/SUPPL{_}FILE/1638FIG5.JPG (2003).
103. Moosmann, M. *et al.* Correlates of alpha rhythm in functional magnetic resonance imaging and near infrared spectroscopy. *NeuroImage* **20**, 145–158. doi:10.1016/S1053-8119(03)00344-6 (2003).
104. Meltzer, J. A., Negishi, M., Mayes, L. C. & Constable, R. T. Individual differences in EEG theta and alpha dynamics during working memory correlate with fMRI responses across subjects. *Clinical Neurophysiology* **118**, 2419–2436. doi:10.1016/J.CLINPH.2007.07.023 (2007).
105. Biswal, B., Yetkin, F. Z., Haughton, V. M. & Hyde, J. S. Functional Connectivity in the Motor Cortex of Resting Human Brain Using Echo-Planar MRI. doi:10.1002/mrm.1910340409 (1995).
106. Starck, T. *et al.* Resting state fMRI reveals a default mode dissociation between retrosplenial and medial prefrontal subnetworks in ASD despite
-

- motion scrubbing. *Frontiers in Human Neuroscience* **7**, 802. doi:10.3389/FNHUM.2013.00802 (2013).
107. Goldman, R. I., Stern, J. M., Jerome Engel, J. & Cohen, M. S. Simultaneous EEG and fMRI of the alpha rhythm. *Neuroreport* **13**, 2487. doi:10.1097/01.WNR.0000047685.08940.D0 (2002).
108. Laufs, H. *et al.* EEG-correlated fMRI of human alpha activity. *NeuroImage* **19**, 1463–1476. doi:10.1016/S1053-8119(03)00286-6 (2003).
109. Benson, N. C. & Winawer, J. Bayesian analysis of retinotopic maps. *eLife* **7**, 1–29. doi:10.7554/eLife.40224 (2018).
110. Moeller, S. *et al.* NOise reduction with DIstribution Corrected (NORDIC) PCA in dMRI with complex-valued parameter-free locally low-rank processing. *NeuroImage* **226**. doi:10.1016/j.neuroimage.2020.117539 (2021).
111. Vizioli, L. *et al.* Lowering the thermal noise barrier in functional brain mapping with magnetic resonance imaging. *Nature Communications* **2021 12:1** **12**, 1–15. doi:10.1038/s41467-021-25431-8 (2021).
112. Glover, G., Li, T.-Q. & Ress, D. Image-based method for retrospective correction of physiological motion effects in FMRI: RETROICOR. *Magnetic Resonance in Medicine* **44**, 162–167. doi:10.1002/1522-2594(200007)44:1<162::AID-MRM23>3.0.CO;2-E (2000).
113. Polimeni, J. R., Fischl, B., Greve, D. N. & Wald, L. L. Laminar analysis of 7T BOLD using an imposed spatial activation pattern in human V1. *NeuroImage* **52**, 1334–1346. doi:10.1016/j.neuroimage.2010.05.005 (2010).
114. Koopmans, P. J., Barth, M., Orzada, S. & Norris, D. G. Multi-echo fMRI of the cortical laminae in humans at 7 T. *NeuroImage* **56**, 1276–1285. doi:10.1016/J.NEUROIMAGE.2011.02.042 (2011).

-
115. Siero, J. C., Petridou, N., Hoogduin, H., Luijten, P. R. & Ramsey, N. F. Cortical depth-dependent temporal dynamics of the BOLD response in the human brain. *Journal of Cerebral Blood Flow and Metabolism* **31**, 1999–2008. doi:10.1038/JCBFM.2011.57/ASSET/IMAGES/LARGE/10.1038{_}JCBFM.2011.57-FIG2.JPEG (2011).
116. Huber, L. *et al.* Cortical lamina-dependent blood volume changes in human brain at 7 T. *NeuroImage* **107**, 23–33. doi:10.1016/J.NEUROIMAGE.2014.11.046 (2015).
117. Lund, J. S. Anatomical Organization of Macaque Monkey Striate Visual Cortex. *Annual Review of Neuroscience* **11**, 253–288. doi:10.1146/ANNUREV.NE.11.030188.001345 (1988).
118. Callaway, E. M. LOCAL CIRCUITS IN PRIMARY VISUAL CORTEX OF THE MACAQUE MONKEY. *Annual Review of Neuroscience* **21**, 47–74. doi:10.1146/ANNUREV.NEURO.21.1.47 (1998).
119. Lawrence, S. J., Formisano, E., Muckli, L. & de Lange, F. P. *Laminar fMRI: Applications for cognitive neuroscience* 2019. doi:10.1016/j.neuroimage.2017.07.004.
120. Huber, L. *Layer fMRI papers* 2018. <https://layerfmri.com/category/layer-fmri-papers/>.
121. Iamshchinina, P. *et al.* Perceived and mentally rotated contents are differentially represented in cortical depth of V1. *Communications Biology* **4**. doi:10.1038/s42003-021-02582-4 (2021).
122. Akbari, A., Bollmann, S., Ali, T. S. & Barth, M. Modelling the depth-dependent VASO and BOLD responses in human primary visual cortex. *Human Brain Mapping*, 1–31. doi:10.1002/hbm.26094 (2022).
123. Kemper, V. G. *et al.* Sub-millimeter T2 weighted fMRI at 7 T: Comparison of 3D-GRASE and 2D SE-EPI. *Frontiers in Neuroscience* **9**, 163. doi:10.3389/FNINS.2015.00163/BIBTEX (2015).
-

-
124. Taso, M., Munsch, F., Zhao, L. & Alsop, D. C. Regional and depth-dependence of cortical blood-flow assessed with high-resolution Arterial Spin Labeling (ASL). *Journal of Cerebral Blood Flow and Metabolism* **41**, 1899–1911. doi:10.1177/0271678X20982382/FORMAT/EPUB (2021).
125. Brant-Zawadzki, M., Gillan, G. D. & Nitz, W. R. MP RAGE: A three-dimensional, T1-weighted, gradient-echo sequence - Initial experience in the brain. *Radiology* **182**, 769–775. doi:10.1148/radiology.182.3.1535892 (1992).
126. Marques, J. P. *et al.* MP2RAGE, a self bias-field corrected sequence for improved segmentation and T1-mapping at high field. *NeuroImage* **49**, 1271–1281. doi:10.1016/J.NEUROIMAGE.2009.10.002 (2010).
127. Hou, P., Hasan, K. M., Sitton, C. W., Wolinsky, J. S. & Narayana, P. A. Phase-Sensitive T1 Inversion Recovery Imaging: A Time-Efficient Interleaved Technique for Improved Tissue Contrast in Neuroimaging. *AJNR: American Journal of Neuroradiology* **26**, 1432 (2005).
128. Huber, L. *et al.* Layer-dependent functional connectivity methods. *Progress in Neurobiology* **207**, 101835. doi:10.1016/J.PNEUROBIO.2020.101835 (2021).
129. Goense, J., Bohraus, Y. & Logothetis, N. K. fMRI at High Spatial Resolution: Implications for BOLD-Models. *Frontiers in Computational Neuroscience* **10**, 66. doi:10.3389/FNCOM.2016.00066 (2016).
130. Huber, L., Uludağ, K. & Möller, H. E. *Non-BOLD contrast for laminar fMRI in humans: CBF, CBV, and CMRO2* 2019. doi:10.1016/j.neuroimage.2017.07.041.
131. Kim, S. G. & Ogawa, S. Biophysical and physiological origins of blood oxygenation level-dependent fMRI signals. *Journal of Cerebral Blood Flow & Metabolism* **32**, 1188. doi:10.1038/JCBFM.2012.23 (2012).
-

-
132. Feinberg, D. A. *et al.* Multiplexed Echo Planar Imaging for Sub-Second Whole Brain fMRI and Fast Diffusion Imaging. *PLOS ONE* **5**. doi:10.1371/JOURNAL.PONE.0015710 (2010).
133. McRobbie, D. W., Moore, E. A., Graves, M. J. & Prince, M. R. *MRI from Picture to Proton* 93–94. doi:10.1017/9781107706958 (Cambridge University Press, 2017).
134. Jenkinson, M., Beckmann, C. F., Behrens, T. E., Woolrich, M. W. & Smith, S. M. FSL. *NeuroImage* **62**, 782–790. doi:10.1016/J.NEUROIMAGE.2011.09.015 (2012).
135. Ashburner, J. & Friston, K. Multimodal image coregistration and partitioning - A unified framework. *NeuroImage* **6**, 209–217. doi:10.1006/NIMG.1997.0290 (1997).
136. Dale, A. M., Fischl, B. & Sereno, M. I. Cortical Surface-Based Analysis. *NeuroImage* **9**, 179–194. doi:10.1006/nimg.1998.0395 (1999).
137. Andreou, C. *et al.* Theta and high-beta networks for feedback processing: a simultaneous EEG–fMRI study in healthy male subjects. *Translational Psychiatry 2017 7:1* **7**, e1016–e1016. doi:10.1038/tp.2016.287 (2017).
138. Moeller, F. *et al.* Simultaneous EEG-fMRI in drug-naive children with newly diagnosed absence epilepsy. *Epilepsia* **49**, 1510–1519. doi:10.1111/J.1528-1167.2008.01626.X (2008).
139. Mullinger, K., Brookes, M., Stevenson, C., Morgan, P. & Bowtell, R. Exploring the feasibility of simultaneous electroencephalography/functional magnetic resonance imaging at 7 T. *Magnetic Resonance Imaging* **26**, 968–977. doi:10.1016/J.MRI.2008.02.014 (2008).
140. Mullinger, K., Morgan, P. & Bowtell, R. Improved artifact correction for combined electroencephalography/functional MRI by means of synchronization and use of vectorcardiogram recordings. *Journal of Magnetic Resonance Imaging* **27**, 607–616. doi:10.1002/JMRI.21277 (2008).
-

-
141. Mougin, O. *et al.* Imaging gray matter with concomitant null point imaging from the phase sensitive inversion recovery sequence. eng. *Magnetic Resonance in Medicine* **76**, 1512–1516. doi:10.1002/mrm.26061 (2016).
142. Gardner, J. L., Merriam, E. P., Movshon, J. A. & Heeger, D. J. *Maps of visual space in human occipital cortex are retinotopic, not spatiotopic*. Gardner, Justin L.: Department of Psychology, New York University, 6 Washington Place, 8th Floor, New York, NY, US, 10003, justin@cns.nyu.edu, 2008. doi:10.1523/JNEUROSCI.5476-07.2008.
143. Gardner, J. L., Merriam, E. P., Schluppeck, D. & Larsson, J. *MGL: Visual psychophysics stimuli and experimental design package* 2018. doi:http://doi.org/10.5281/zenodo.1299497.
144. Oostenveld, R., Fries, P., Maris, E. & Schoffelen, J. M. FieldTrip: Open source software for advanced analysis of MEG, EEG, and invasive electrophysiological data. *Computational Intelligence and Neuroscience*. doi:10.1155/2011/156869 (2011).
145. Brookes, M. J., Mullinger, K. J., Stevenson, C. M., Morris, P. G. & Bowtell, R. Simultaneous EEG source localisation and artifact rejection during concurrent fMRI by means of spatial filtering. *NeuroImage* **40**, 1090–1104. doi:10.1016/J.NEUROIMAGE.2007.12.030 (2008).
146. Smith, Stephen M *et al.* Advances in functional and structural MR image analysis and implementation as FSL. *Neuroimage*. doi:10.1016/j.neuroimage.2004.07.051 (2004).
147. Wandell, B. A., Dumoulin, S. O. & Brewer, A. A. Visual field maps in human cortex. *Neuron* **56**, 366–383. doi:10.1016/j.neuron.2007.10.012 (2007).
148. Van der Kouwe, A. *et al.* Whole brain segmentation: automated labeling of neuroanatomical structures in the human brain. *Neuron* (2002).

-
149. Engel, S. A. The development and use of phase-encoded functional MRI designs. *NeuroImage* **62**, 1195–1200. doi:10.1016/J.NEUROIMAGE.2011.09.059 (2012).
150. Engel, S. A. *et al.* fMRI of human visual cortex. *Nature* **369**, 525 (1994).
151. Schira, M. M., Tyler, C. W., Breakspear, M. & Spehar, B. The foveal confluence in human visual cortex. *Journal of Neuroscience* **29**, 9050–9058. doi:10.1523/JNEUROSCI.1760-09.2009 (2009).
152. Huber, L. *et al.* LAYNII: A software suite for layer-fMRI. *bioRxiv*, 1–20. doi:10.1101/2020.06.12.148080 (2020).
153. Bok, S. T. *A quantitative analysis of the structure of the cerebral cortex* (Noord-Hollandsche Uitg. Mij., 1936).
154. Waehnert, M. D. *et al.* Anatomically motivated modeling of cortical laminae. *NeuroImage* **93**, 210–220. doi:10.1016/j.neuroimage.2013.03.078 (2014).
155. Huber, L. & Gulban, O. F. *Equi-voluming: The Anakin Skywalker of layering algorithms* 2020. <https://layerfmri.com/2020/04/24/equivol/>.
156. Mountcastle, V. B. Modality and topographic properties of single neurons of cat's somatic sensory cortex. *Journal of neurophysiology* **20**, 408–434. doi:10.1152/jn.1957.20.4.408 (1957).
157. Buxhoeveden, D. P. & Casanova, M. F. The minicolumn hypothesis in neuroscience. *Brain* **125**, 935–951. doi:10.1093/brain/awf110 (2002).
158. Cheong, O. *et al.* Farthest-polygon Voronoi diagrams. *Computational Geometry: Theory and Applications* **44**, 234–247. doi:10.1016/j.comgeo.2010.11.004 (2011).
159. Aitken, F. *et al.* Prior expectations evoke stimulus-specific activity in the deep layers of the primary visual cortex. *PLOS Biology* **18**, e3001023. doi:10.1371/JOURNAL.PBIO.3001023 (2020).
-

-
160. Haarsma, J., Deveci, N., Corbin, N., Callaghan, M. F. & Kok, P. Perceptual expectations and false percepts generate stimulus-specific activity in distinct layers of the early visual cortex. *bioRxiv*, 2022.04.13.488155. doi:10.1101/2022.04.13.488155 (2022).
161. Fracasso, A., Dumoulin, S. O. & Petridou, N. Point-spread function of the BOLD response across columns and cortical depth in human extra-striate cortex. *Progress in Neurobiology* **202**, 102034. doi:10.1016/j.pneurobi.2021.102034 (2021).
162. Kazan, S. M. *et al.* Physiological basis of vascular autocalibration (VasA): Comparison to hypercapnia calibration methods. *Magnetic Resonance in Medicine* **78**, 1168–1173. doi:10.1002/mrm.26494 (2017).
163. Kannurpatti, S. S. & Biswal, B. B. Detection and scaling of task-induced fMRI-BOLD response using resting state fluctuations. *NeuroImage* **40**, 1567–1574. doi:10.1016/j.neuroimage.2007.09.040 (2008).
164. Guidi, M., Huber, L., Lampe, L., Gauthier, C. J. & Möller, H. E. Lamina-dependent calibrated BOLD response in human primary motor cortex. *NeuroImage* **141**, 250–261. doi:10.1016/j.neuroimage.2016.06.030 (2016).
165. Kashyap, S., Ivanov, D., Havlicek, M., Poser, B. A. & Uludağ, K. Impact of acquisition and analysis strategies on cortical depth-dependent fMRI. *NeuroImage* **168**. doi:10.1016/j.neuroimage.2017.05.022 (2018).
166. Havlicek, M. & Uludağ, K. A dynamical model of the laminar BOLD response. *NeuroImage* **204**. doi:10.1016/j.neuroimage.2019.116209 (2020).
167. Markuerkiaga, I., Marques, J. P., Gallagher, T. E. & Norris, D. G. Estimation of laminar BOLD activation profiles using deconvolution with a physiological point spread function. *Journal of Neuroscience Methods* **353**. doi:10.1016/j.jneumeth.2021.109095 (2021).
-

-
168. Heinzle, J., Koopmans, P. J., den Ouden, H. E., Raman, S. & Stephan, K. E. A hemodynamic model for layered BOLD signals. *NeuroImage* **125**, 556–570. doi:10.1016/j.neuroimage.2015.10.025 (2016).
169. Markuerkiaga, I., Barth, M. & Norris, D. G. A cortical vascular model for examining the specificity of the laminar BOLD signal. *NeuroImage* **132**, 491–498. doi:10.1016/J.NEUROIMAGE.2016.02.073 (2016).
170. Fracasso, A., Luijten, P. R., Dumoulin, S. O. & Petridou, N. Laminar imaging of positive and negative BOLD in human visual cortex at 7 T. *NeuroImage* **164**. doi:10.1016/j.neuroimage.2017.02.038 (2018).
171. Klein, B. P. *et al.* Cortical depth dependent population receptive field attraction by spatial attention in human V1. *NeuroImage* **176**, 301–312. doi:10.1016/J.NEUROIMAGE.2018.04.055 (2018).
172. Gau, R., Bazin, P. L., Trampel, R., Turner, R. & Noppeney, U. Resolving multisensory and attentional influences across cortical depth in sensory cortices. *eLife* **9**. doi:10.7554/eLife.46856 (2020).
173. Navarro, K. T., Sanchez, M. J., Engel, S. A., Olman, C. A. & Weldon, K. B. Depth-dependent functional MRI responses to chromatic and achromatic stimuli throughout V1 and V2. *NeuroImage* **226**, 117520. doi:10.1016/J.NEUROIMAGE.2020.117520 (2021).
174. Zaretskaya, N. *et al.* Eye-selective fMRI activity in human primary visual cortex: Comparison between 3 T and 9.4 T, and effects across cortical depth. *NeuroImage* **220**, 117078. doi:10.1016/J.NEUROIMAGE.2020.117078 (2020).
175. Bergmann, J., Morgan, A. T. & Muckli, L. Two distinct feedback codes in V1 for ‘real’ and ‘imaginary’ internal experiences. *bioRxiv*, 664870. doi:10.1101/664870 (2019).

-
176. Marquardt, I., Schneider, M., Gulban, O. F., Ivanov, D. & Uludağ, K. Cortical depth profiles of luminance contrast responses in human V1 and V2 using 7 T fMRI. *Human Brain Mapping* **39**, 2812–2827. doi:10.1002/HBM.24042 (2018).
177. Marquardt, I. *et al.* Feedback contribution to surface motion perception in the human early visual cortex. *eLife* **9**, 1–28. doi:10.7554/ELIFE.50933 (2020).
178. Vizioli, L. *et al.* Multivoxel Pattern of Blood Oxygen Level Dependent Activity can be sensitive to stimulus specific fine scale responses. *Scientific Reports 2020 10:1* **10**, 1–18. doi:10.1038/s41598-020-64044-x (2020).
179. Mourik, T. v., Koopmans, P. J., Bains, L. J., Norris, D. G. & Jehee, J. F. Investigation of layer specific BOLD in the human visual cortex during visual attention. *bioRxiv*, 2021.02.07.430129. doi:10.1101/2021.02.07.430129 (2021).
180. Kim, S. G. & Ugurbil, K. High-resolution functional magnetic resonance imaging of the animal brain. *Methods* **30**, 28–41. doi:10.1016/S1046-2023(03)00005-7 (2003).
181. Zhao, F., Wang, P. & Kim, S. G. Cortical depth-dependent gradient-echo and spin-echo BOLD fMRI at 9.4T. *Magnetic Resonance in Medicine* **51**, 518–524. doi:10.1002/MRM.10720 (2004).
182. Van Kerkoerle, T. *et al.* Alpha and gamma oscillations characterize feedback and feedforward processing in monkey visual cortex. *Proceedings of the National Academy of Sciences of the United States of America* **111**, 14332–14341. doi:https://doi.org/10.1073/pnas.14027731 (2014).
183. Lenartowicz, A. *et al.* Alpha modulation during working memory encoding predicts neurocognitive impairment in ADHD. *Journal of child psychology and psychiatry, and allied disciplines* **60**, 917. doi:10.1111/JCPP.13042 (2019).

-
184. Sabate, M., Llanos, C., Enriquez, E., Gonzalez, B. & Rodriguez, M. Fast modulation of alpha activity during visual processing and motor control. *Neuroscience* **189**, 236–249. doi:10.1016/J.NEUROSCIENCE.2011.05.011 (2011).
185. Zhou, Y. J., Iemi, L., Schoffelen, J. M., de Lange, F. P. & Haegens, S. Alpha Oscillations Shape Sensory Representation and Perceptual Sensitivity. *The Journal of Neuroscience* **41**, 9581. doi:10.1523/JNEUROSCI.1114-21.2021 (2021).
186. Saalman, Y. B., Pinsk, M. A., Wang, L., Li, X. & Kastner, S. The pulvinar regulates information transmission between cortical areas based on attention demands. *Science (New York, N.Y.)* **337**, 753–756. doi:10.1126/SCIENCE.1223082 (2012).
187. Maier, A., Adams, G. K., Aura, C. & Leopold, D. A. Distinct superficial and deep laminar domains of activity in the visual cortex during rest and stimulation. *Frontiers in Systems Neuroscience* **4**, 31. doi:10.3389/FNSYS.2010.00031/ (2010).
188. Bollimunta, A., Mo, J., Schroeder, C. E. & Ding, M. Neuronal mechanisms and attentional modulation of corticothalamic α oscillations. *The Journal of neuroscience : the official journal of the Society for Neuroscience* **31**, 4935–4943. doi:10.1523/JNEUROSCI.5580-10.2011 (2011).
189. Elbel, G.-K., Kaufmann, C., Schaefer, S., Buser, A. & Auer, D. P. Refractive Anomalies and Visual Activation in Functional Magnetic Resonance Imaging (fMRI): A Versatile and Low-Cost MR-Compatible Device to Correct a Potential Confound. *J. Magn. Reson. Imaging* **15**, 101–107. doi:10.1002/jmri.10031 (2002).
190. Duann, J.-R. *et al.* Single-Trial Variability in Event-Related BOLD Signals. doi:10.1006/nimg.2001.1049 (2002).

-
191. Mumford, D. On the computational architecture of the neocortex. I. The role of the thalamo-cortical loop. *Biological cybernetics* **65**, 135–145. doi:10.1007/BF00202389 (1991).
192. Thomson, A. M. & Bannister, A. P. Interlaminar Connections in the Neocortex. *Cerebral Cortex* **13**, 5–14. doi:10.1093/CERCOR/13.1.5 (2003).
193. Benavides-Piccione, R., Rojo, C., Kastanauskaite, A. & Defelipe, J. Variation in Pyramidal Cell Morphology Across the Human Anterior Temporal Lobe. *Cerebral Cortex (New York, NY)* **31**, 3592. doi:10.1093/CERCOR/BHAB034 (2021).
194. Uludağ, K. & Havlicek, M. Determining laminar neuronal activity from BOLD fMRI using a generative model. *Progress in Neurobiology* **207**, 102055. doi:10.1016/J.PNEUROBIO.2021.102055 (2021).
195. Lu, H., Golay, X., Pekar, J. J. & Van Zijl, P. C. Functional magnetic resonance imaging based on changes in vascular space occupancy. *Magnetic Resonance in Medicine* **50**, 263–274. doi:10.1002/MRM.10519 (2003).
196. Zhang, X. *et al.* In vivo blood T1 measurements at 1.5 T, 3 T, and 7 T. *Magnetic Resonance in Medicine* **70**, 1082–1086. doi:10.1002/MRM.24550 (2013).
197. Gai, N. D., Talagala, S. L. & Butman, J. A. Whole-brain cerebral blood flow mapping using 3D echo planar imaging and pulsed arterial tagging. *Journal of Magnetic Resonance Imaging* **33**, 287–295. doi:10.1002/JMRI.22437 (2011).
198. Jin, T. & Kim, S. G. Improved cortical-layer specificity of vascular space occupancy fMRI with slab inversion relative to spin-echo BOLD at 9.4 T. *NeuroImage* **40**, 59–67. doi:10.1016/J.NEUROIMAGE.2007.11.045 (2008).

-
199. Huber, L. *et al.* Slab-selective, BOLD-corrected VASO at 7 Tesla provides measures of cerebral blood volume reactivity with high signal-to-noise ratio. *Magnetic Resonance in Medicine* **72**, 137–148. doi:10.1002/MRM.24916 (2014).
200. Donahue, M. J. *et al.* Blood oxygenation level-dependent (BOLD) total and extravascular signal changes and $\Delta R2^*$ in human visual cortex at 1.5, 3.0 and 7.0 T. *NMR in biomedicine* **24**, 25–34. doi:10.1002/NBM.1552 (2011).
201. De Oliveira, Í. A., Siero, J. C., Dumoulin, S. O. & van der Zwaag, W. Improved Selectivity in 7 T Digit Mapping Using VASO-CBV. *Brain topography* **36**, 23–31. doi:10.1007/S10548-022-00932-X (2023).
202. Huber, L., Kassavetis, P., Gulban, O. F., Hallett, M. & Horovitz, S. G. Laminar VASO fMRI in focal hand dystonia patients. *Dystonia* **2**. doi:10.3389/DYST.2023.10806 (2023).
203. Yu, Y. *et al.* Layer-specific activation of sensory input and predictive feedback in the human primary somatosensory cortex. *Science Advances* **5**. doi:10.1126/SCIADV.AAV9053/SUPPL{_}FILE/AAV9053{_}SM.PDF (2019).
204. Stelzer, J., Lohmann, G., Mueller, K., Buschmann, T. & Turner, R. Deficient approaches to human neuroimaging. *Frontiers in Human Neuroscience* **8**, 462. doi:10.3389/FNHUM.2014.00462/BIBTEX (2014).
205. Kay, K. N., Rokem, A., Winawer, J., Dougherty, R. F. & Wandell, B. A. GLMdenoise: a fast, automated technique for denoising task-based fMRI data. *Frontiers in neuroscience* **7**. doi:10.3389/FNINS.2013.00247 (2013).
206. Caballero-Gaudes, C. & Reynolds, R. C. Methods for cleaning the BOLD fMRI signal. *NeuroImage* **154**, 128–149. doi:10.1016/J.NEUROIMAGE.2016.12.018 (2017).
-

-
207. Lund, T. E., Madsen, K. H., Sidaros, K., Luo, W. L. & Nichols, T. E. Non-white noise in fMRI: Does modelling have an impact? *NeuroImage* **29**, 54–66. doi:10.1016/J.NEUROIMAGE.2005.07.005 (2006).
208. Veraart, J. *et al.* Denoising of diffusion MRI using random matrix theory. *NeuroImage* **142**, 394–406. doi:10.1016/j.neuroimage.2016.08.016 (2016).
209. Gudbjartsson, H. & Patz, S. The Rician distribution of noisy MRI data (vol 34, pg 910, 1995). *Magnetic Resonance in Medicine* **36**, 332 (1996).
210. Henkelman, R. M. Measurement of signal intensities in the presence of noise in MR images. *Medical Physics* **12**, 232–233. doi:10.1118/1.595711 (1985).
211. Dowdle, L. T. *et al.* Evaluating increases in sensitivity from NORDIC for diverse fMRI acquisition strategies. *NeuroImage* **270**, 119949. doi:10.1016/J.NEUROIMAGE.2023.119949 (2023).
212. Sanchez Panchuelo, R. M., Turner, R. & Francis, S. *Simultaneous assessment of total CBV, aCBV and BOLD measures at 7 Tesla in motor and somatosensory cortices in Proceedings of the International Society of Magnetic Resonance in Medicine* (2017).
213. Terumitsu, M., Fujii, Y., Suzuki, K., Kwee, I. L. & Nakada, T. Human primary motor cortex shows hemispheric specialization for speech. *Neuroreport* **17**, 1091–1095. doi:10.1097/01.WNR.0000224778.97399.C4 (2006).
214. Huber, L. *et al.* High-resolution CBV-fMRI allows mapping of laminar activity and connectivity of cortical input and output in human M1. *Neuron* **96**, 1253. doi:10.1016/J.NEURON.2017.11.005 (2017).
215. Donahue, M. J. *et al.* Evaluation of Human Brain Tumor Heterogeneity using MRI with Multiple T1-based Signal Weighting Approaches. *Magnetic Resonance in Medicine* **59**, 336. doi:10.1002/MRM.21467 (2008).
-

-
216. Wei, R. L. & Wei, X. T. Advanced Diagnosis of Glioma by Using Emerging Magnetic Resonance Sequences. *Frontiers in Oncology* **11**, 3072. doi:10.3389/FONC.2021.694498/BIBTEX (2021).
217. Eminian, S., Hajdu, S. D., Meuli, R. A., Maeder, P. & Hagmann, P. Rapid high resolution T1 mapping as a marker of brain development: Normative ranges in key regions of interest. *PLoS ONE* **13**. doi:10.1371/JOURNAL.PONE.0198250 (2018).
218. Vrenken, H. *et al.* Whole-Brain T1 Mapping in Multiple Sclerosis: Global Changes of Normal-appearing Gray and White Matter. *Radiology* **240**, 811–820. doi:10.1148/RADIOL.2403050569 (2006).
219. Haast, R. A., Ivanov, D., Formisano, E. & Uludağ, K. Reproducibility and reliability of quantitative and weighted T1 and T2* mapping for myelin-based cortical parcellation at 7 tesla. *Frontiers in Neuroanatomy* **10**, 112. doi:10.3389/FNANA.2016.00112/BIBTEX (2016).
220. Huber, L. *et al.* Sub-millimeter fMRI reveals multiple topographical digit representations that form action maps in human motor cortex. *bioRxiv*. doi:10.1101/457002 (2018).
221. Liu, T. T. *et al.* Layer-specific, retinotopically-diffuse modulation in human visual cortex in response to viewing emotionally expressive faces. *Nature Communications 2022 13:1* **13**, 1–15. doi:10.1038/s41467-022-33580-7 (2022).
222. Limbach, K. & Corballis, P. M. Alpha-power modulation reflects the balancing of task requirements in a selective attention task. *Psychophysiology* **54**, 224–234. doi:10.1111/PSYP.12774 (2017).
223. Lenartowicz, A., Mazaheri, A., Jensen, O. & Loo, S. K. Aberrant Modulation of Brain Oscillatory Activity and Attentional Impairment in Attention-Deficit/Hyperactivity Disorder. *Biological Psychiatry: Cognitive Neuroscience and Neuroimaging* **3**, 19–29. doi:10.1016/J.BPSC.2017.09.009 (2018).
-

-
224. Knudsen, L. *et al.* Improved sensitivity and microvascular weighting of 3T laminar fMRI with GE-BOLD using NORDIC and phase regression. *NeuroImage* **271**, 120011. doi:10.1016/J.NEUROIMAGE.2023.120011 (2023).
225. Huber, L. *et al.* Evaluating the capabilities and challenges of layer-fMRI VASO at 3T. *Aperture Neuro* **3**, 1–17. doi:10.52294/001C.85117 (2023).
226. Van der Meer, J. N. *et al.* Carbon-wire loop based artifact correction outperforms post-processing EEG/fMRI corrections—A validation of a real-time simultaneous EEG/fMRI correction method. *NeuroImage* **125**, 880–894. doi:10.1016/J.NEUROIMAGE.2015.10.064 (2016).
227. Le Bihan, D., Urayama, S. I., Aso, T., Hanakawa, T. & Fukuyama, H. Direct and fast detection of neuronal activation in the human brain with diffusion MRI. *Proceedings of the National Academy of Sciences of the United States of America* **103**, 8263–8268. doi:10.1073/PNAS.0600644103/SUPPL{_}FILE/00644FIG7.PDF (2006).
228. Raimondo, L. *et al.* Robust high spatio-temporal line-scanning fMRI in humans at 7T using multi-echo readouts, denoising and prospective motion correction. *Journal of Neuroscience Methods* **384**, 109746. doi:10.1016/J.JNEUMETH.2022.109746 (2023).
229. Toi, P. T. *et al.* In vivo direct imaging of neuronal activity at high temporospatial resolution. *Science* **378**, 160. doi:10.1126/science.adk4448 (2022).
230. Darquié, A., Poline, J. B., Poupon, C., Saint-Jalmes, H. & Le Bihan, D. Transient decrease in water diffusion observed in human occipital cortex during visual stimulation. *Proceedings of the National Academy of Sciences of the United States of America* **98**, 9391–9395. doi:10.1073/PNAS.151125698/ASSET/3AB72BCE-5183-4B2C-8D47-2574413D0E94/ASSETS/GRAPHIC/PQ1511256005.JPEG (2001).

231. Bai, R., Stewart, C. V., Plenz, D. & Basser, P. J. Assessing the sensitivity of diffusion MRI to detect neuronal activity directly. *Proceedings of the National Academy of Sciences of the United States of America* **113**, E1728–E1737. doi:10.1073/PNAS.1519890113 (2016).
232. Yu, X., Qian, C., Chen, D. Y., Dodd, S. J. & Koretsky, A. P. Deciphering laminar-specific neural inputs with line-scanning fMRI. *Nature Methods* *2013 11:1* **11**, 55–58. doi:10.1038/nmeth.2730 (2013).
233. Heij, J. *et al.* A selection and targeting framework of cortical locations for line-scanning fMRI. *Human Brain Mapping* **44**, 5471–5484. doi:10.1002/HBM.26459 (2023).
234. Choi, S.-H. *et al.* No Replication of Direct Neuronal Activity-related (DIANA) fMRI in Anesthetized Mice. *bioRxiv*. doi:10.1101/2023.05.26.542419 (2023).

Appendix A

Denoising β -weights

A.1 Determining the Noise Threshold of the β -weights

Individual subject results for the composition of positive and negative β -weights in each column following the application of different levels of noise thresholds. Figures A.1 to A.8 correspond to the results for subjects 2 – 9.

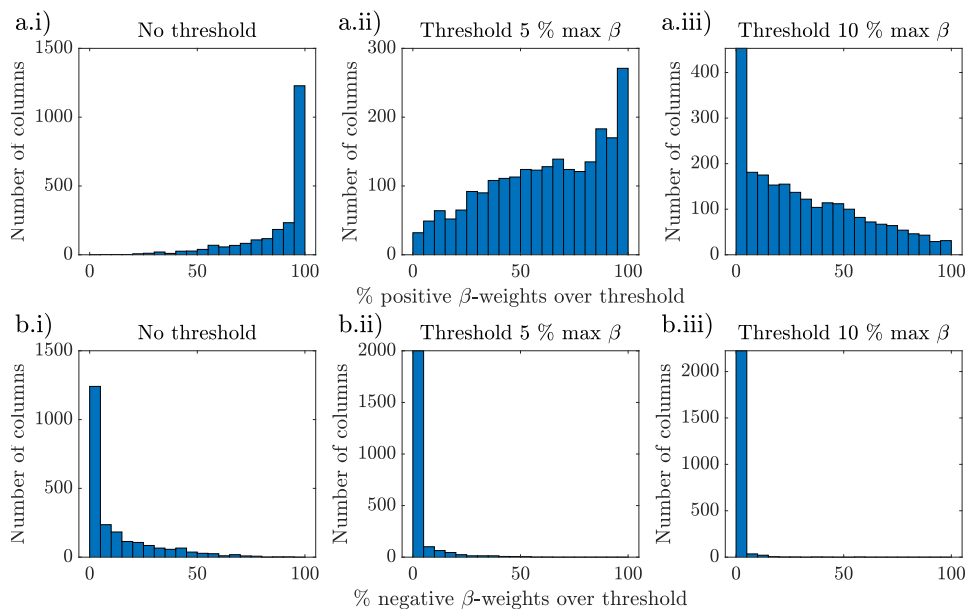


Figure A.1: Histograms showing the percentage of (a-c) positive β -weight voxels that are over the threshold within each column, and (d-f) negative β -weight voxels that are over the threshold within each column for Subject 2.

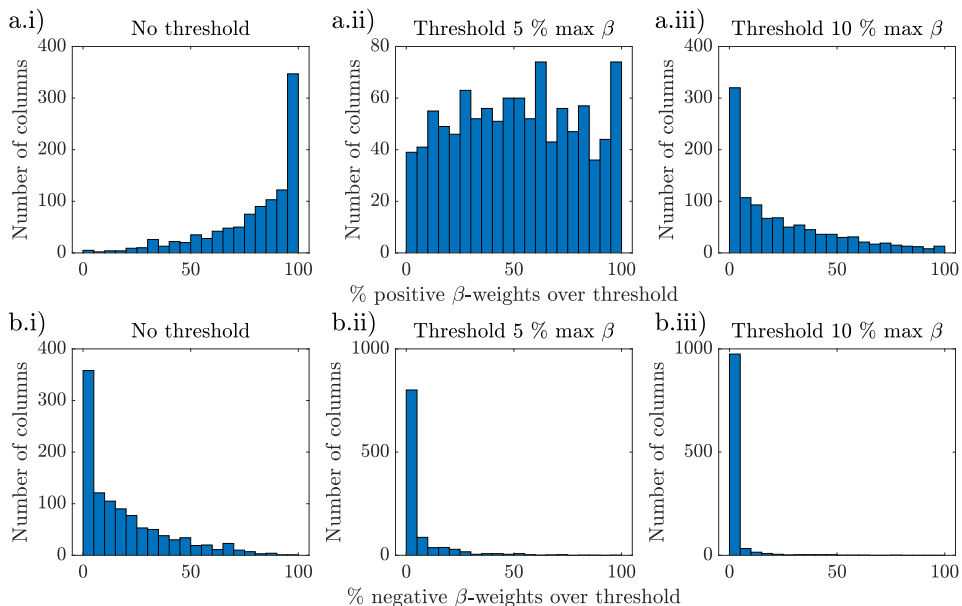


Figure A.2: Histograms showing the percentage of (a-c) positive β -weight voxels that are over the threshold within each column, and (d-f) negative β -weight voxels that are over the threshold within each column Subject 3.

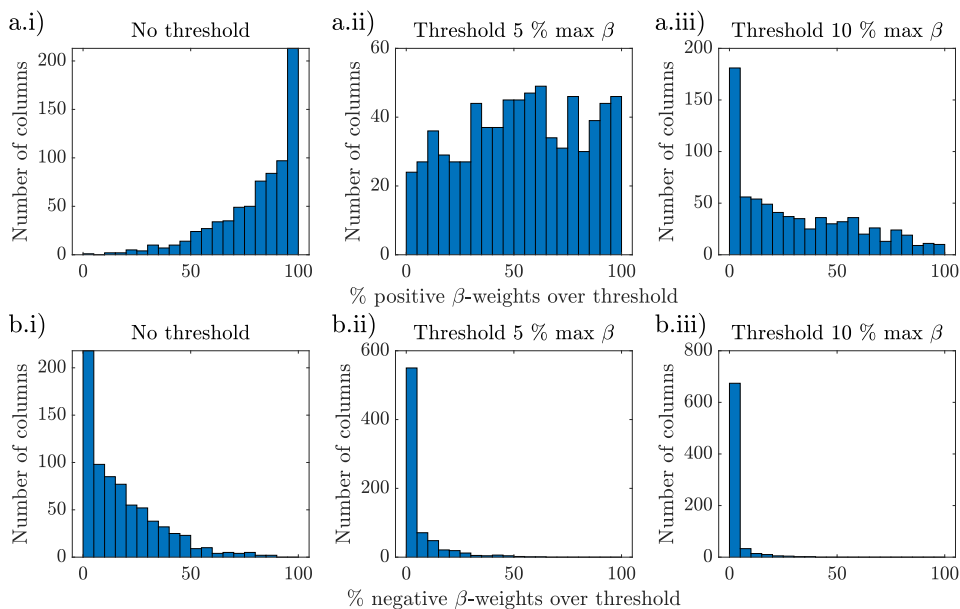


Figure A.3: Histograms showing the percentage of (a-c) positive β -weight voxels that are over the threshold within each column, and (d-f) negative β -weight voxels that are over the threshold within each column Subject 4.

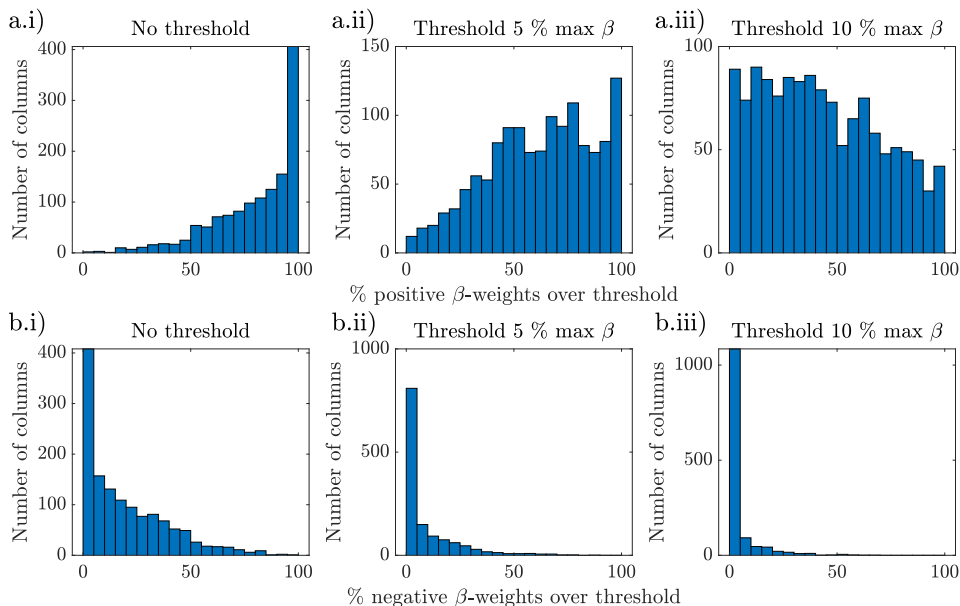


Figure A.4: Histograms showing the percentage of (a-c) positive β -weight voxels that are over the threshold within each column, and (d-f) negative β -weight voxels that are over the threshold within each column Subject 5.

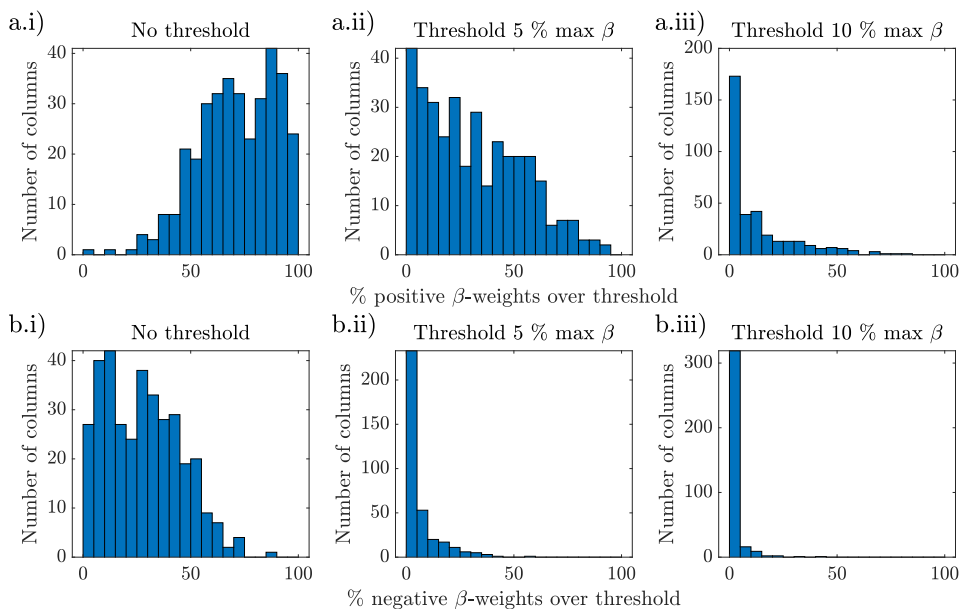


Figure A.5: Histograms showing the percentage of (a-c) positive β -weight voxels that are over the threshold within each column, and (d-f) negative β -weight voxels that are over the threshold within each column Subject 6.

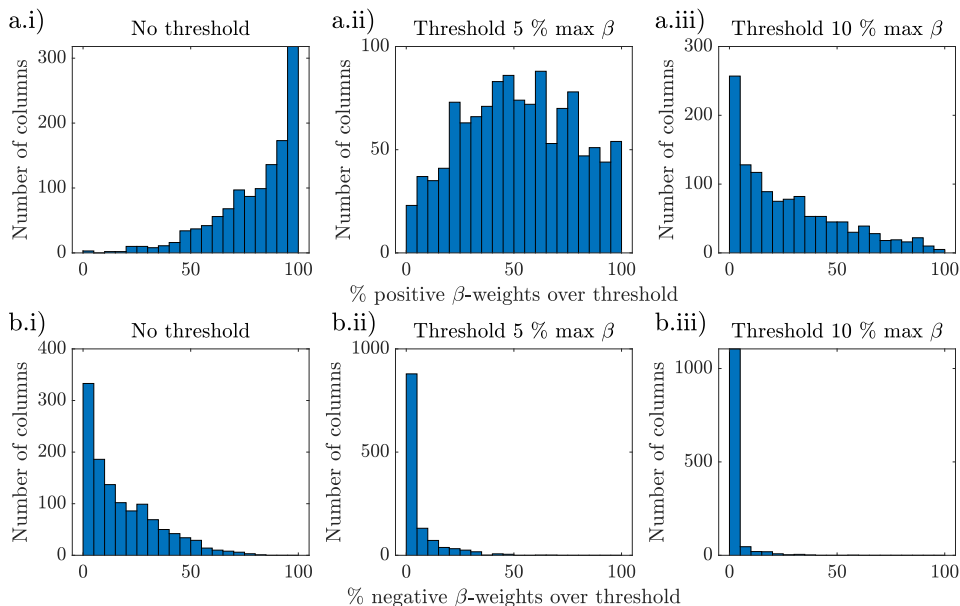


Figure A.6: Histograms showing the percentage of (a-c) positive β -weight voxels that are over the threshold within each column, and (d-f) negative β -weight voxels that are over the threshold within each column Subject 7.

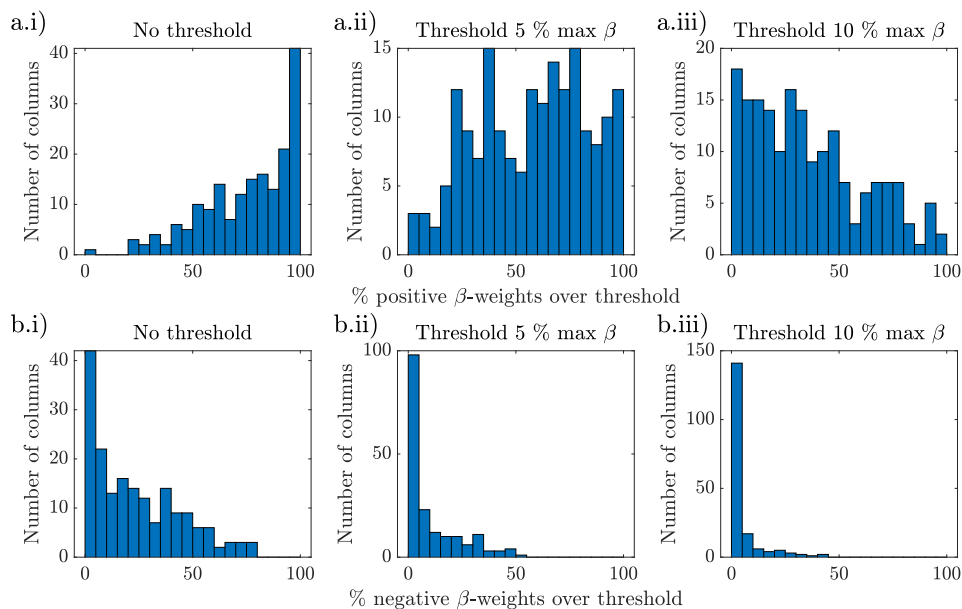


Figure A.7: Histograms showing the percentage of (a-c) positive β -weight voxels that are over the threshold within each column, and (d-f) negative β -weight voxels that are over the threshold within each column Subject 8.

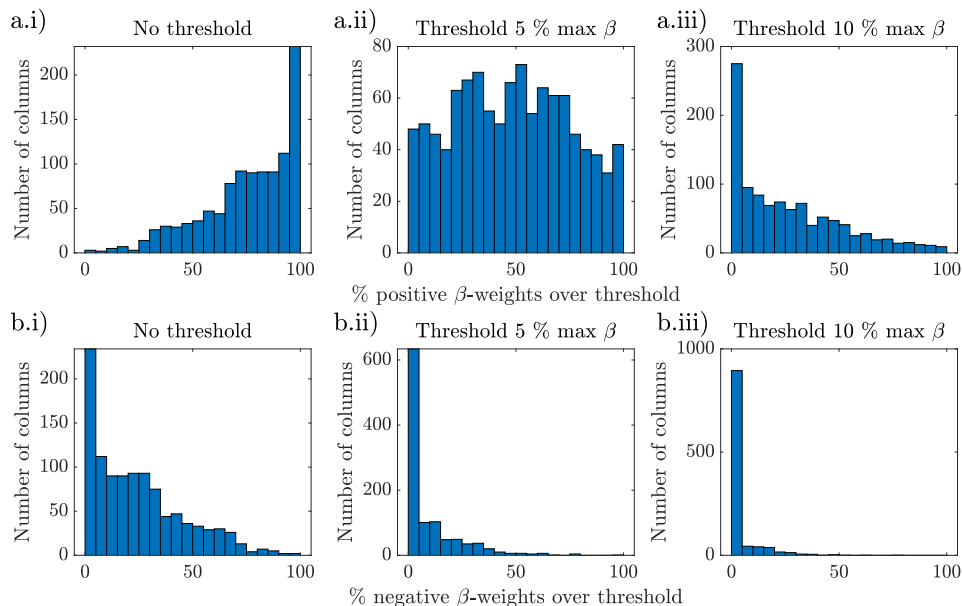


Figure A.8: Histograms showing the percentage of (a-c) positive β -weight voxels that are over the threshold within each column, and (d-f) negative β -weight voxels that are over the threshold within each column Subject 9.

Individual subject results for the percentage of voxels that fell below the 5% of the maximum β -weight threshold within each of the six cortical layers. Figures A.9 to A.17 correspond to the results for Subjects 1 – 9. Visually all subjects show a 3:1 ratio of positively to negatively correlated voxels below the threshold per layer. This holds true even for Subject 8 showed a reduced % of both positive and negative voxels below the threshold due to their reduced response. The reduced response can be seen in Figure 5.8 where the fewest significant negatively correlated voxels of all subjects are evident.

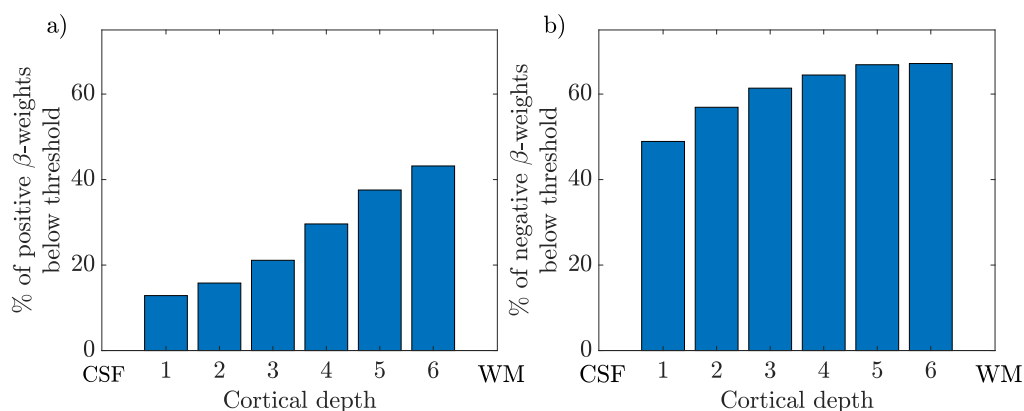


Figure A.9: The distribution across layers for β -weights below the 5% threshold for positive β -weights (a) and negative β -weights (b) across cortical depths for Subject 1.

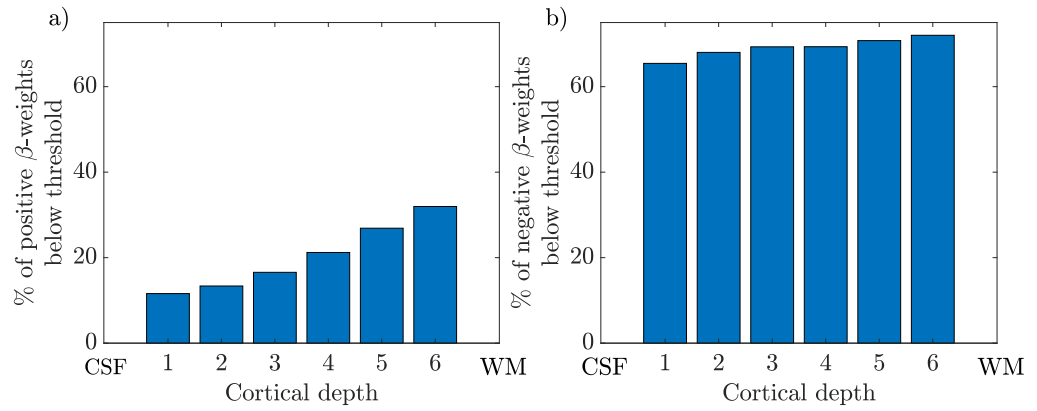


Figure A.10: The distribution across layers for β -weights below the 5% threshold for positive β -weights (a) and negative β -weights (b) for Subject 2.

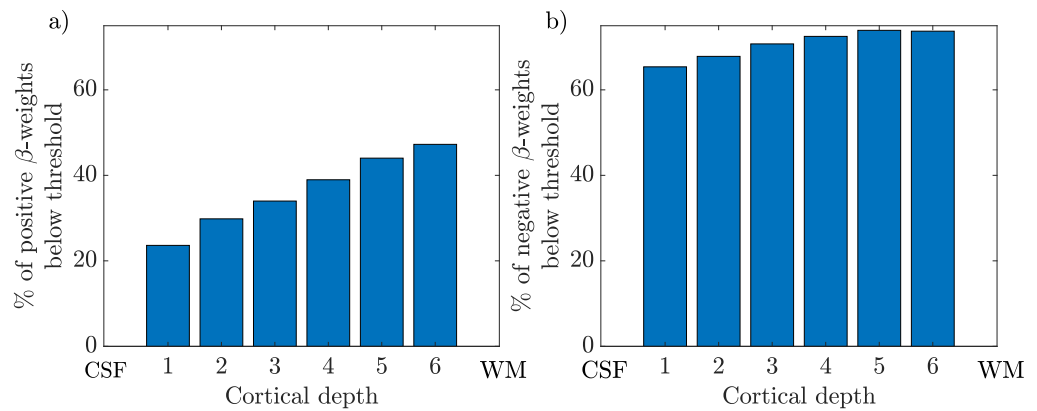


Figure A.11: The distribution across layers for β -weights below the 5% threshold for positive β -weights (a) and negative β -weights (b) for Subject 3.

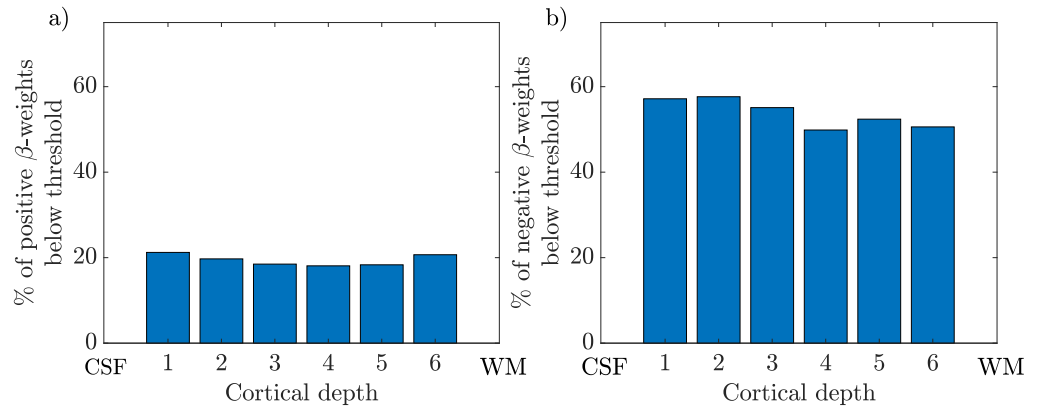


Figure A.12: The distribution across layers for β -weights below the 5% threshold for positive β -weights (a) and negative β -weights (b) for Subject 4.

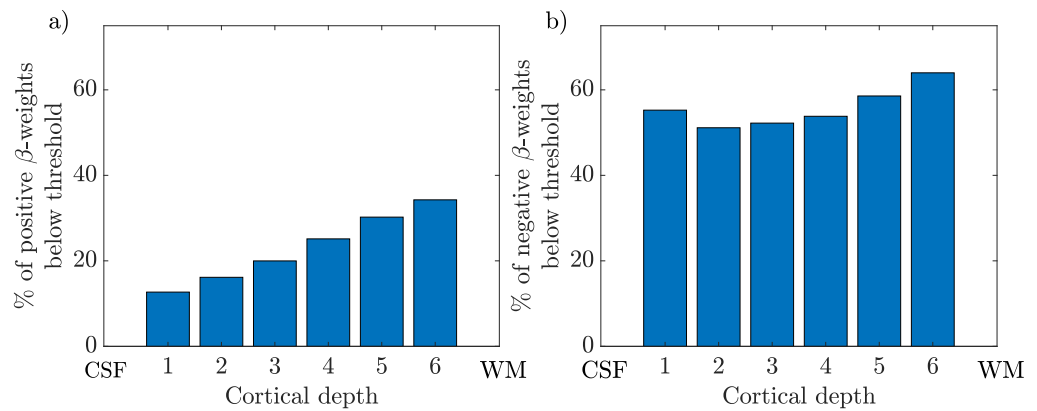


Figure A.13: The distribution across layers for β -weights below the 5% threshold for positive β -weights (a) and negative β -weights (b) for Subject 5.

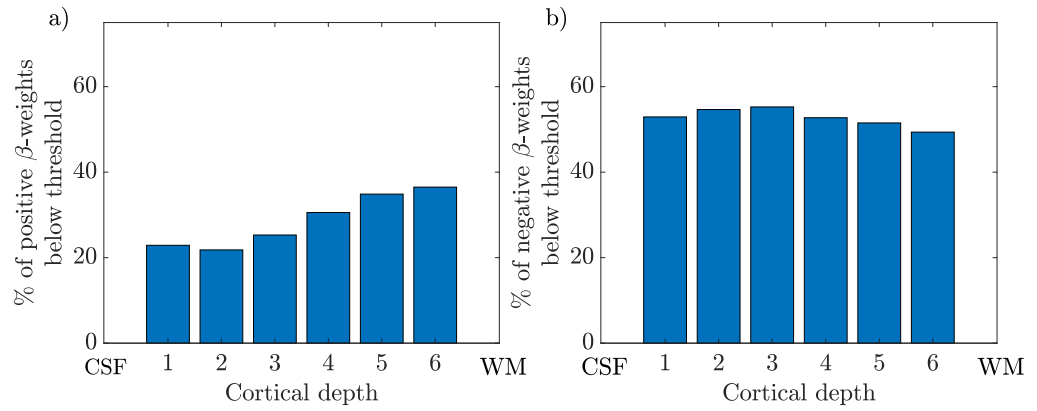


Figure A.14: The distribution across layers for β -weights below the 5% threshold for positive β -weights (a) and negative β -weights (b) for Subject 6.

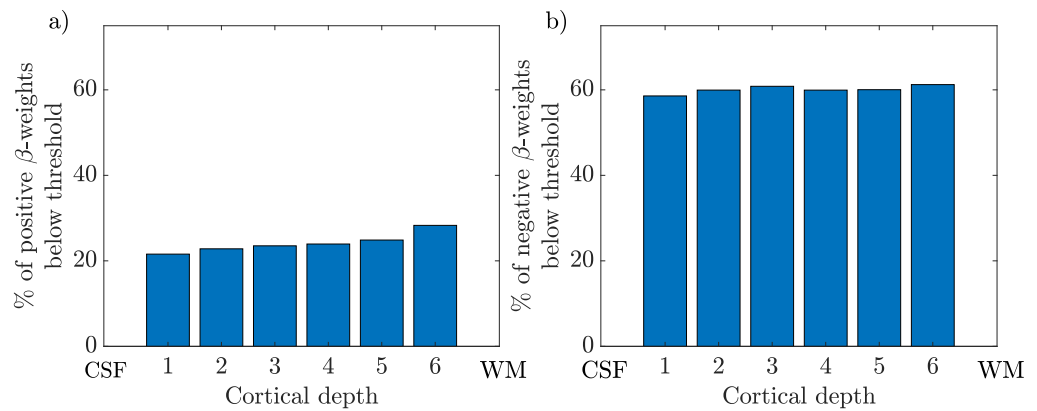


Figure A.15: The distribution across layers for β -weights below the 5% threshold for positive β -weights (a) and negative β -weights (b) for Subject 7.

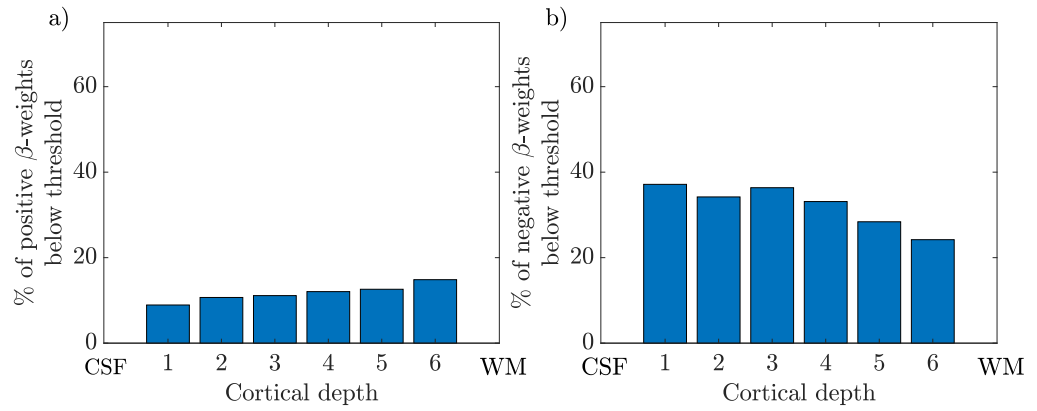


Figure A.16: The distribution across layers for β -weights below the 5% threshold for positive β -weights (a) and negative β -weights (b) for Subject 8.

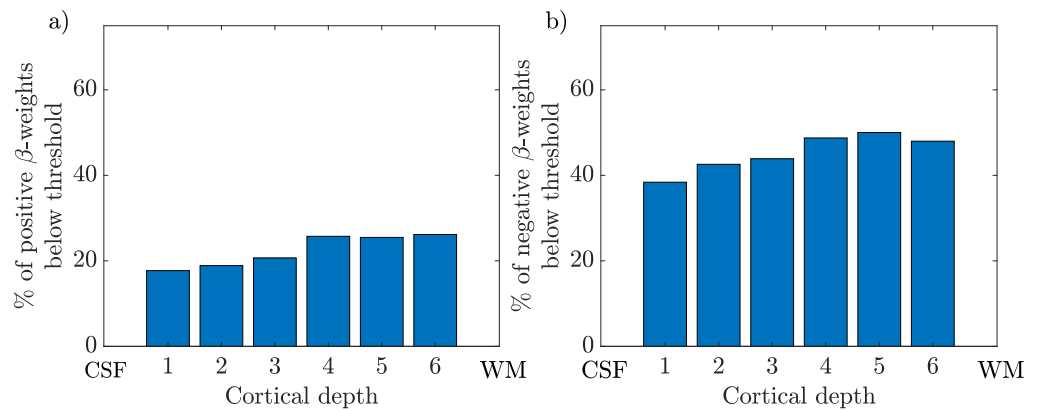


Figure A.17: The distribution across layers for β -weights below the 5% threshold for positive β -weights (a) and negative β -weights (b) for Subject 9.

Appendix B

Vein masks

B.1 Masking the veins from the fMRI data

Veins were easily identified as areas of low signal intensity in the functional 3D-EPI data and once masked they could be used to study the impact of ‘deveining’ on the layer fMRI data. Figure B.1 shows an example axial and coronal slice of the vein mask calculated by thresholding the central 3D-EPI functional run, using the methods described in Section 4.7.3.5 overlaid for each subject on their individual PSIR.

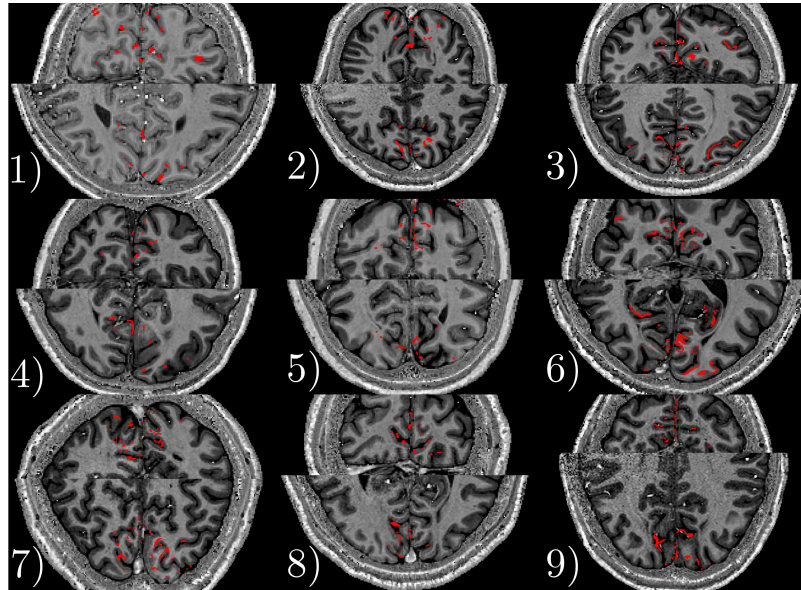


Figure B.1: Vein mask (red) calculated by thresholding the central functional 3D-EPI run of the session overlaid onto the PSIR shown axially and coronally for each subject.

B.2 Effect of veins on layer profiles

Individual subject results showing a comparison of layer profiles including all columns or layer profiles excluding the top 25% of most most change columns profiles for (a) uncorrected and (b) deveined data. Figures B.2 to B.9 correspond to the results for subjects 2 – 9.

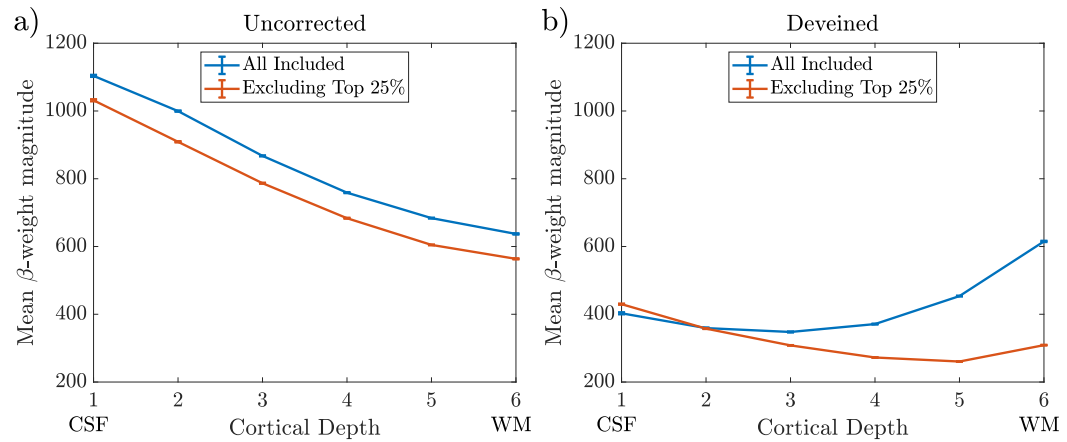


Figure B.2: The layer profiles from the V1 region for Subject 2 ‘Uncorrected’ (a) and ‘Deveined’ (b). Blue indicates the profile including all available columns, Orange shows the profile resulting from excluding the columns with the highest change in profile gradient (top 25%). Error bars show the standard error on the mean (SEM) for the mean β -weight of each cortical depth.

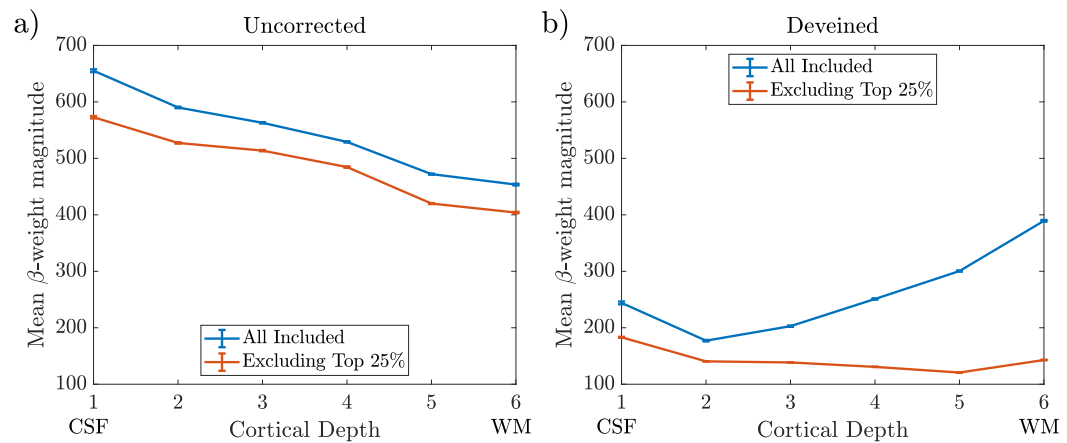


Figure B.3: The layer profiles from the V1 region for Subject 3 ‘Uncorrected’ (a) and ‘Deveined’ (b). Blue indicates the profile including all available columns, Orange shows the profile resulting from excluding the columns with the highest change in profile gradient (top 25%). Error bars show the standard error on the mean (SEM) for the mean β -weight of each cortical depth.

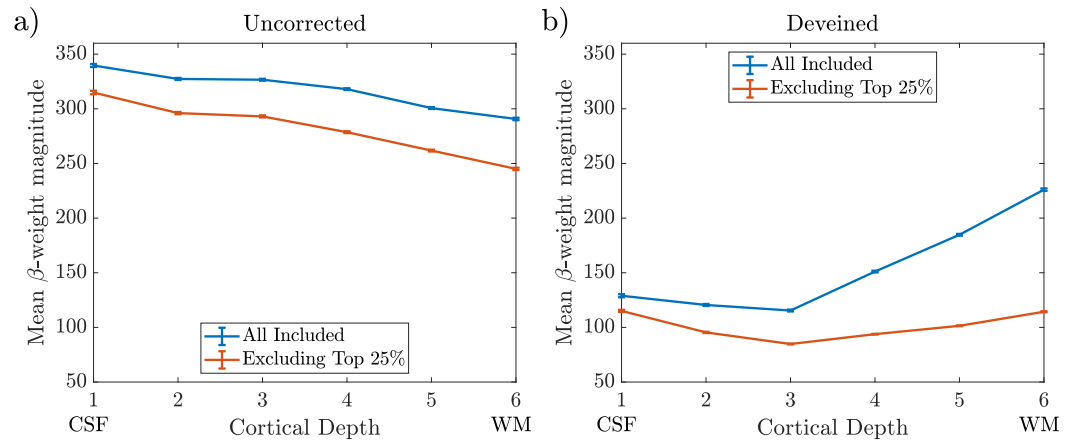


Figure B.4: The layer profiles from the V1 region for Subject 4 ‘Uncorrected’ (a) and ‘Deveined’ (b). Blue indicates the profile including all available columns, Orange shows the profile resulting from excluding the columns with the highest change in profile gradient (top 25%). Error bars show the standard error on the mean (SEM) for the mean β -weight of each cortical depth.

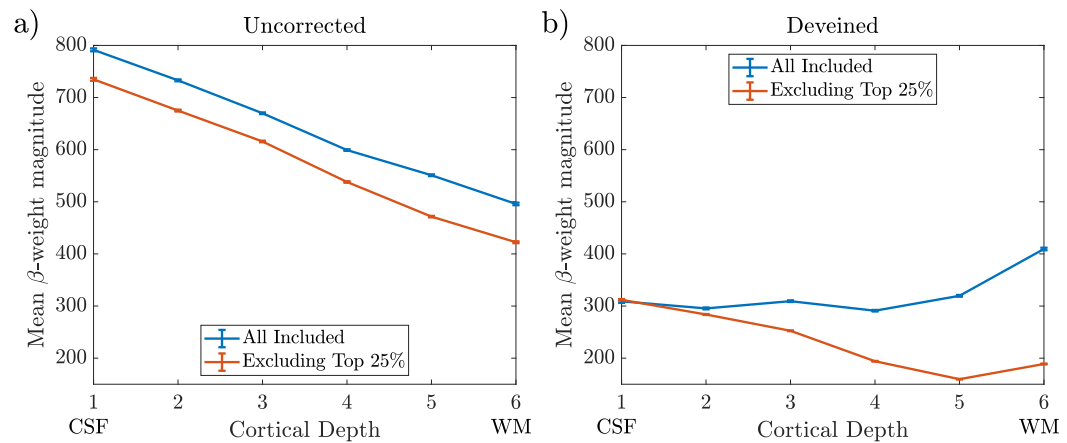


Figure B.5: The layer profiles from the V1 region for Subject 5 ‘Uncorrected’ (a) and ‘Deveined’ (b). Blue indicates the profile including all available columns, Orange shows the profile resulting from excluding the columns with the highest change in profile gradient (top 25%). Error bars show the standard error on the mean (SEM) for the mean β -weight of each cortical depth.

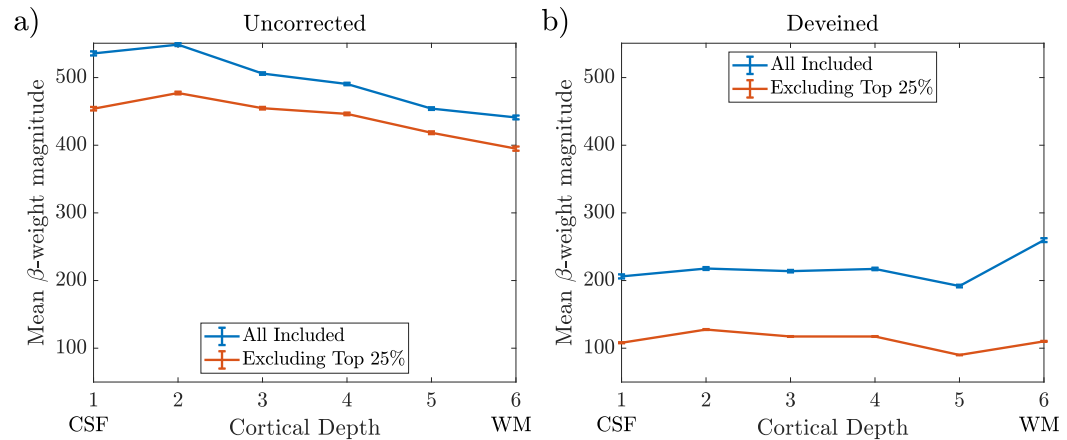


Figure B.6: The layer profiles from the V1 region for Subject 6 ‘Uncorrected’ (a) and ‘Deveined’ (b). Blue indicates the profile including all available columns, Orange shows the profile resulting from excluding the columns with the highest change in profile gradient (top 25%). Error bars show the standard error on the mean (SEM) for the mean β -weight of each cortical depth.

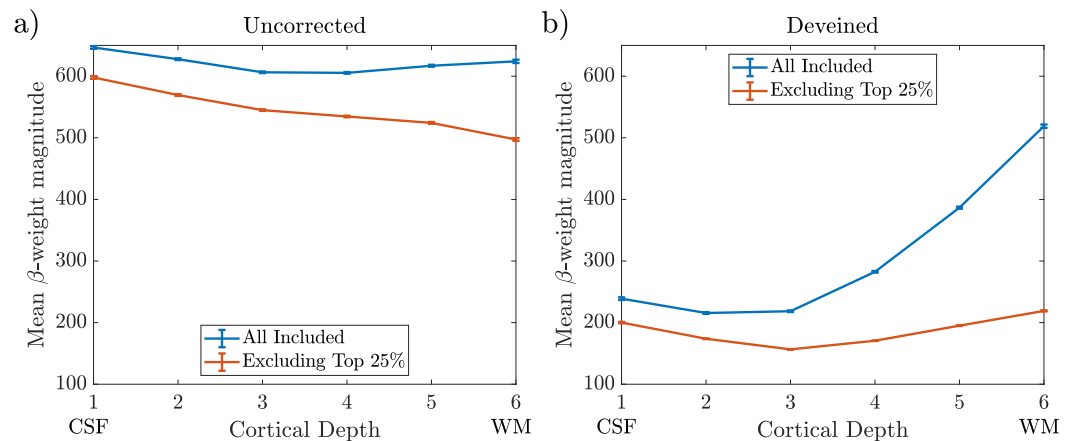


Figure B.7: The layer profiles from the V1 region for Subject 7 ‘Uncorrected’ (a) and ‘Deveined’ (b). Blue indicates the profile including all available columns, Orange shows the profile resulting from excluding the columns with the highest change in profile gradient (top 25%). Error bars show the standard error on the mean (SEM) for the mean β -weight of each cortical depth.

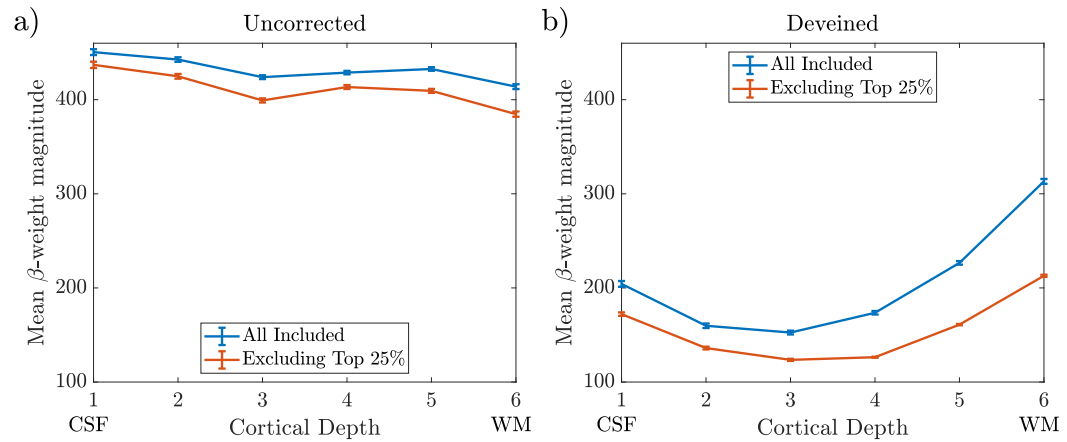


Figure B.8: The layer profiles from the V1 region for Subject 8 ‘Uncorrected’ (a) and ‘Deveined’ (b). Blue indicates the profile including all available columns, Orange shows the profile resulting from excluding the columns with the highest change in profile gradient (top 25%). Error bars show the standard error on the mean (SEM) for the mean β -weight of each cortical depth.

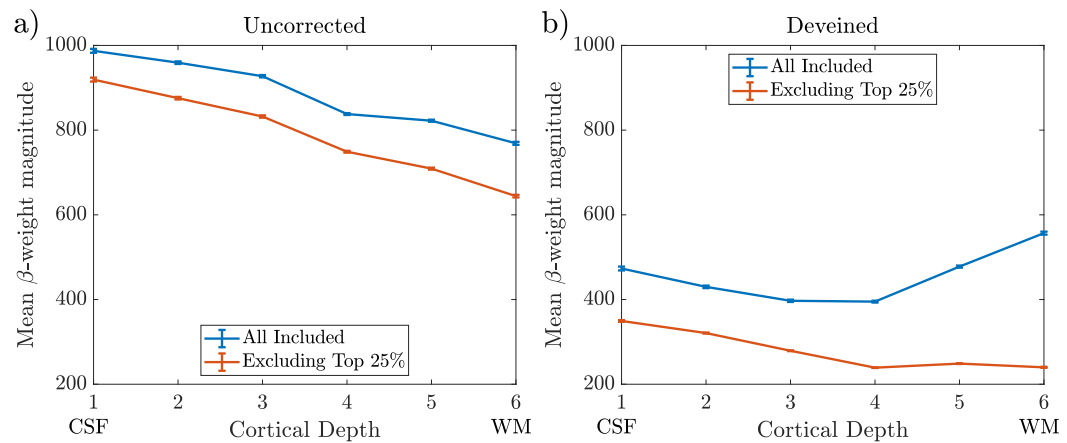


Figure B.9: The layer profiles from the V1 region for Subject 9 ‘Uncorrected’ (a) and ‘Deveined’ (b). Blue indicates the profile including all available columns, Orange shows the profile resulting from excluding the columns with the highest change in profile gradient (top 25%). Error bars show the standard error on the mean (SEM) for the mean β -weight of each cortical depth.

Appendix C

Timecourse analysis

C.1 Comparison of the EEG alpha power and fMRI BOLD response

Individual subject results showing a comparison of (a) the EEG alpha regressor convolved with a standard double gamma HRF and (b) the mean timecourse from the voxels in the V1 ROI (blue), the significant negatively correlated voxels from the GLM using the EEG alpha power timecourse convolved with with a standard double gamma HRF as regressors (orange) and the significant negatively correlated voxels from the GLM using a boxcar convolved with with a standard double gamma HRF as regressors (yellow). Figures C.1 to C.27 correspond to the results for V1, V2 and V3 for in order for each subject 1 – 9.

The variation in BOLD response driven by EEG alpha power on a trial by trial basis is shown in Figure C.28. The mean timecourse of significant negatively correlated ($z < -2.3$) fMRI voxels within V1 is plotted against the EEG alpha power regressor for each corresponding trial period.

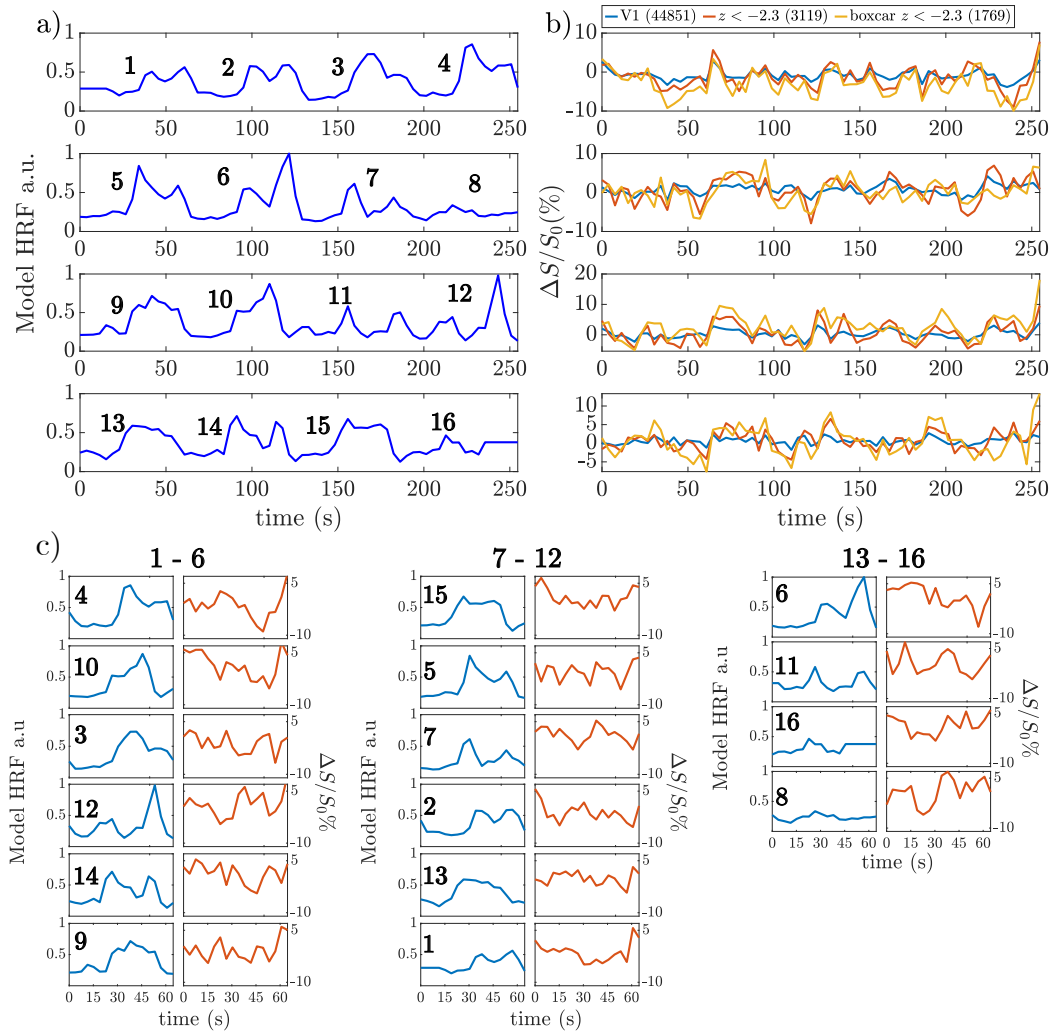


Figure C.1: Comparison of a) the EEG alpha power informed regressors and b) the fMRI timecourse from all voxels in V1 (blue), significant negatively correlated voxels ($z < -2.3$) when using the EEG regressors (orange) and significant negatively correlated voxels ($z < -2.3$) when using the boxcar regressors (yellow). In brackets are the number of voxels that are contributing to each mean timecourse plotted. c) Shows the regressors from a) (blue) split into single eyes open/closed periods ($\sim 65s$) and ranked from largest response to smallest response. The corresponding fMRI period is shown next to it in orange. The numbers in bold correspond to the response numbers in a). Shown for Subject 1.

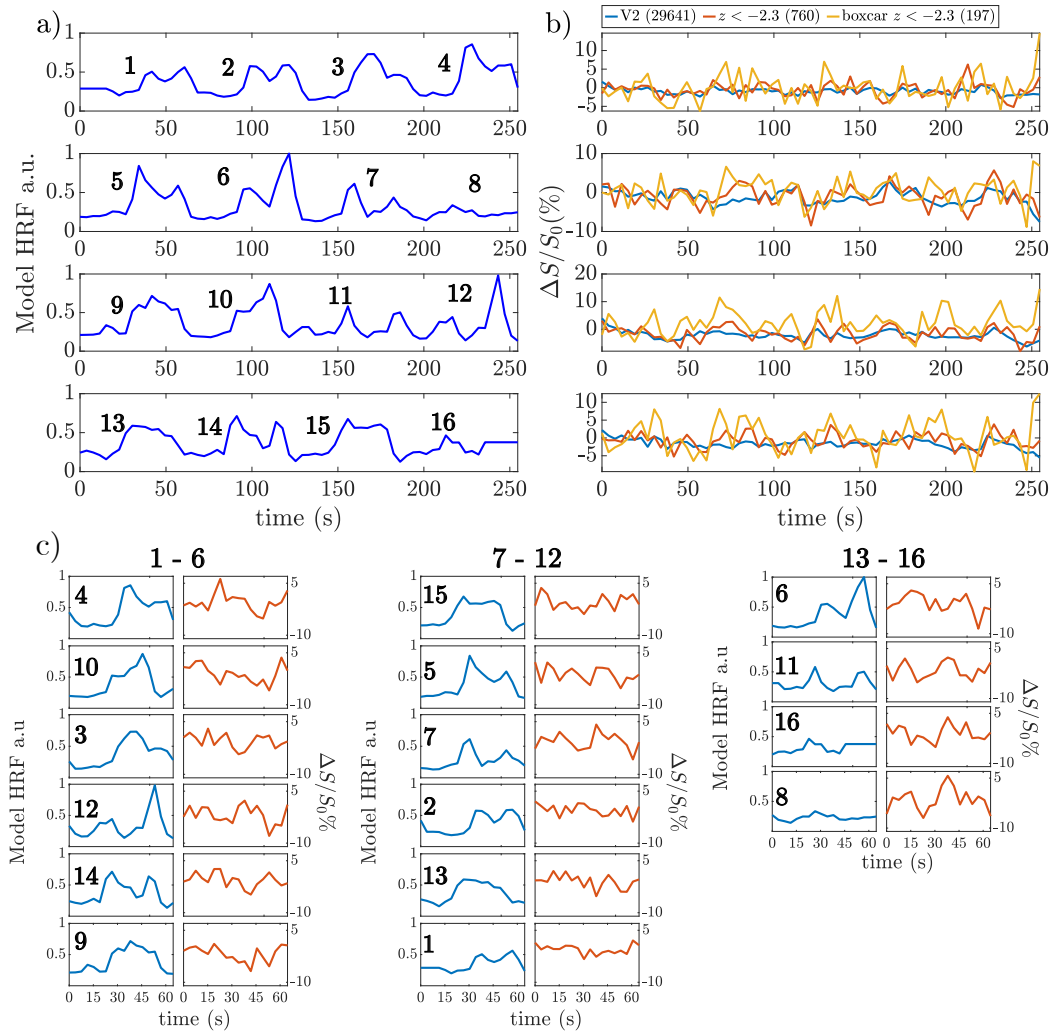


Figure C.2: Comparison of a) the EEG alpha power informed regressors and b) the fMRI timecourse from all voxels in V2 (blue), significant negatively correlated voxels ($z < -2.3$) when using the EEG regressors (orange) and significant negatively correlated voxels ($z < -2.3$) when using the boxcar regressors (yellow). In brackets are the number of voxels that are contributing to each mean timecourse plotted. c) Shows the regressors from a) (blue) split into single eyes open/closed periods ($\sim 65s$) and ranked from largest response to smallest response. The corresponding fMRI period is shown next to it in orange. The numbers in bold correspond to the response numbers in a). Shown for Subject 1.

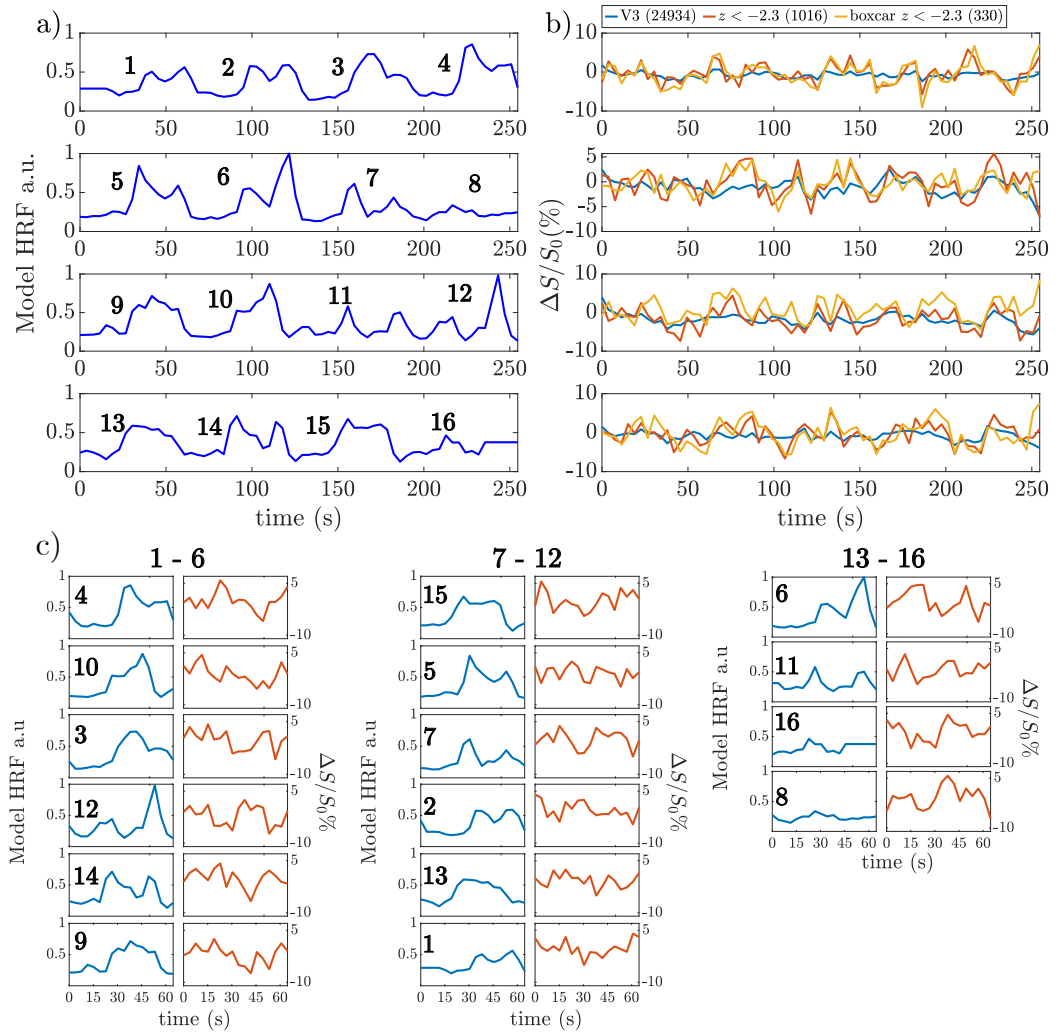


Figure C.3: Comparison of a) the EEG alpha power informed regressors and b) the fMRI timecourse from all voxels in V3 (blue), significant negatively correlated voxels ($z < -2.3$) when using the EEG regressors (orange) and significant negatively correlated voxels ($z < -2.3$) when using the boxcar regressors (yellow). In brackets are the number of voxels that are contributing to each mean timecourse plotted. c) Shows the regressors from a) (blue) split into single eyes open/closed periods ($\sim 65s$) and ranked from largest response to smallest response. The corresponding fMRI period is shown next to it in orange. The numbers in bold correspond to the response numbers in a). Shown for Subject 1.

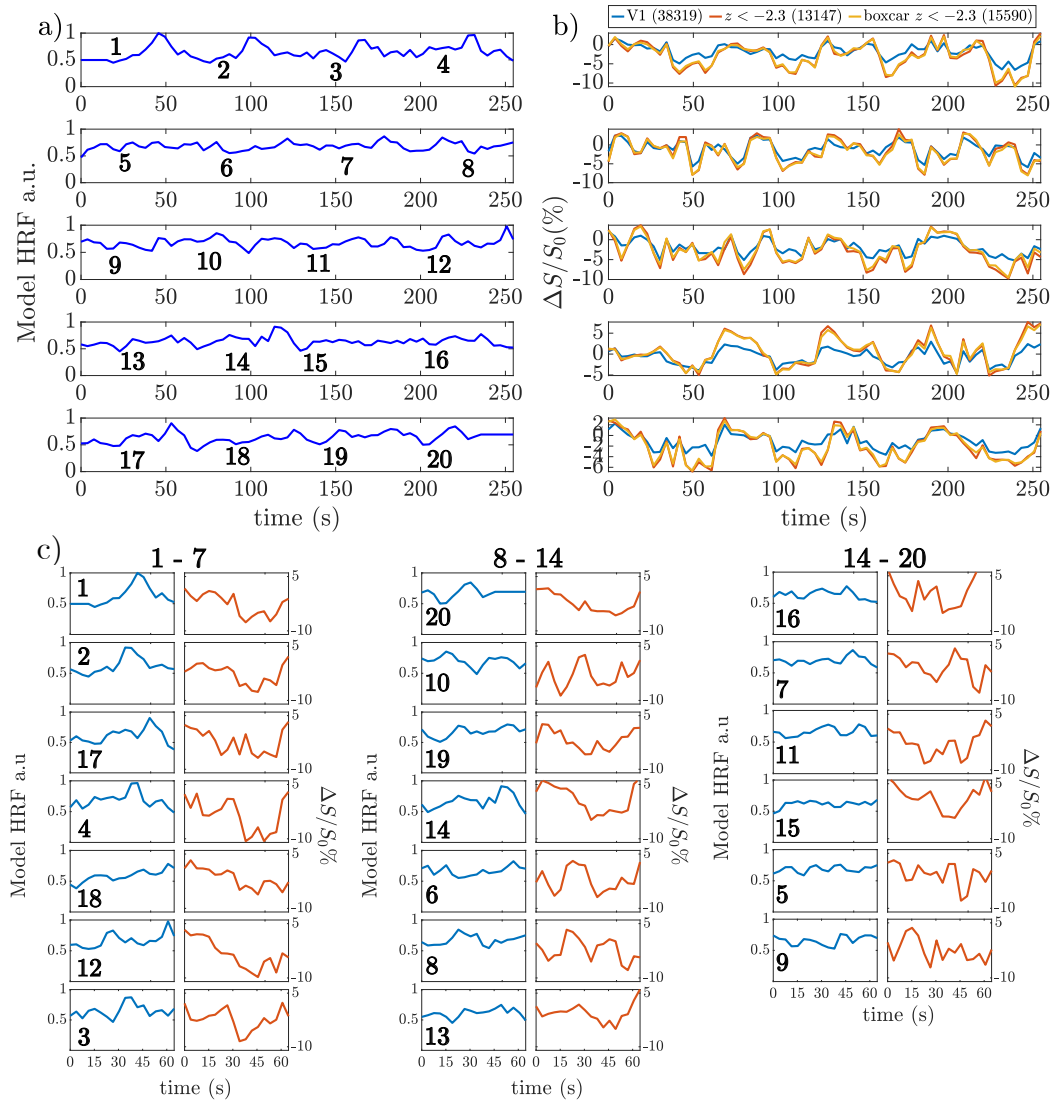


Figure C.4: Comparison of a) the EEG alpha power informed regressors and b) the fMRI timecourse from all voxels in V1 (blue), significant negatively correlated voxels ($z < -2.3$) when using the EEG regressors (orange) and significant negatively correlated voxels ($z < -2.3$) when using the boxcar regressors (yellow). In brackets are the number of voxels that are contributing to each mean timecourse plotted. c) Shows the regressors from a) (blue) split into single eyes open/closed periods ($\sim 65s$) and ranked from largest response to smallest response. The corresponding fMRI period is shown next to it in orange. The numbers in bold correspond to the response numbers in a). Shown for Subject 2.

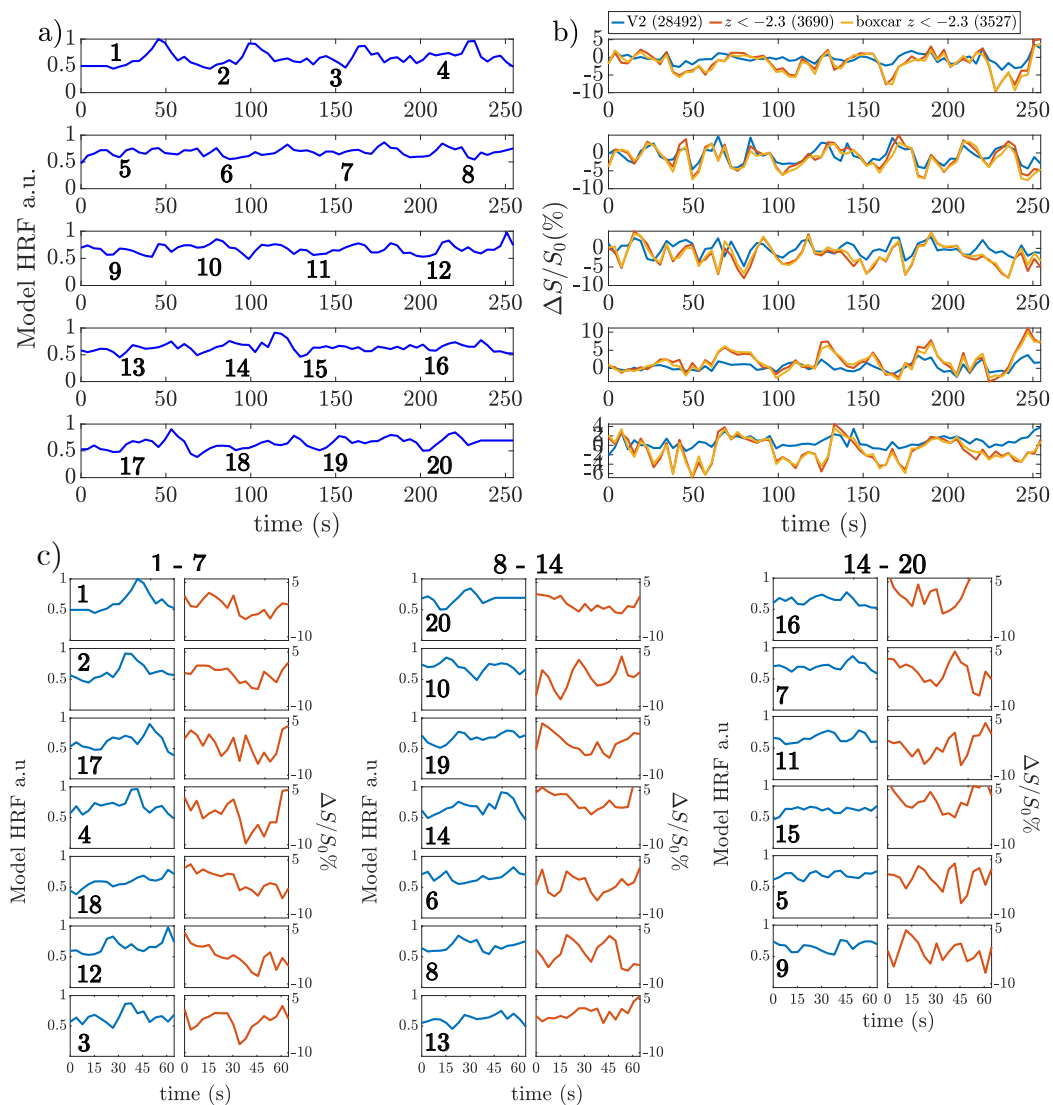


Figure C.5: Comparison of a) the EEG alpha power informed regressors and b) the fMRI timecourse from all voxels in V2 (blue), significant negatively correlated voxels ($z < -2.3$) when using the EEG regressors (orange) and significant negatively correlated voxels ($z < -2.3$) when using the boxcar regressors (yellow). In brackets are the number of voxels that are contributing to each mean timecourse plotted. c) Shows the regressors from a) (blue) split into single eyes open/closed periods ($\sim 65s$) and ranked from largest response to smallest response. The corresponding fMRI period is shown next to it in orange. The numbers in bold correspond to the response numbers in a). Shown for Subject 2.

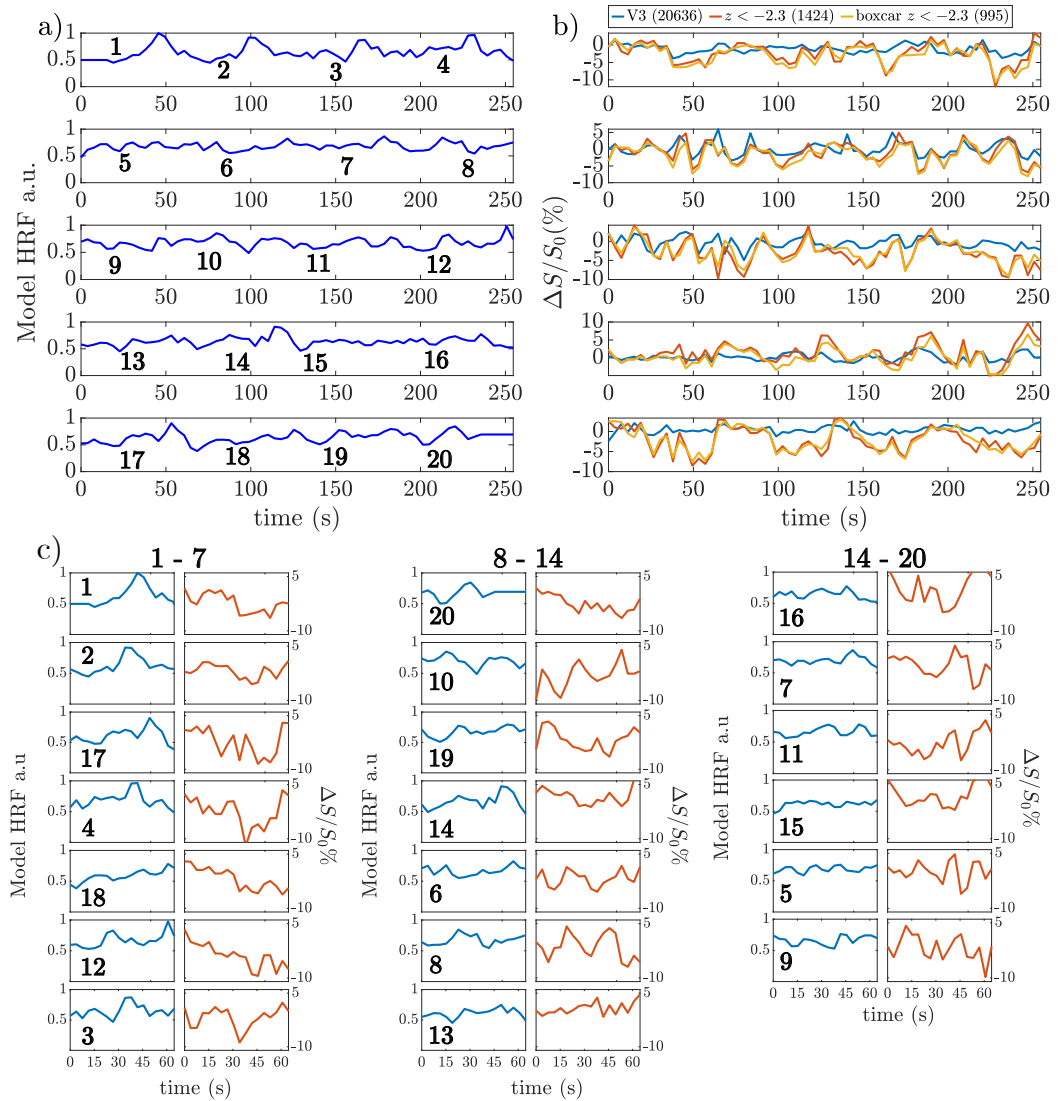


Figure C.6: Comparison of a) the EEG alpha power informed regressors and b) the fMRI timecourse from all voxels in V3 (blue), significant negatively correlated voxels ($z < -2.3$) when using the EEG regressors (orange) and significant negatively correlated voxels ($z < -2.3$) when using the boxcar regressors (yellow). In brackets are the number of voxels that are contributing to each mean timecourse plotted. c) Shows the regressors from a) (blue) split into single eyes open/closed periods ($\sim 65s$) and ranked from largest response to smallest response. The corresponding fMRI period is shown next to it in orange. The numbers in bold correspond to the response numbers in a). Shown for Subject 2.

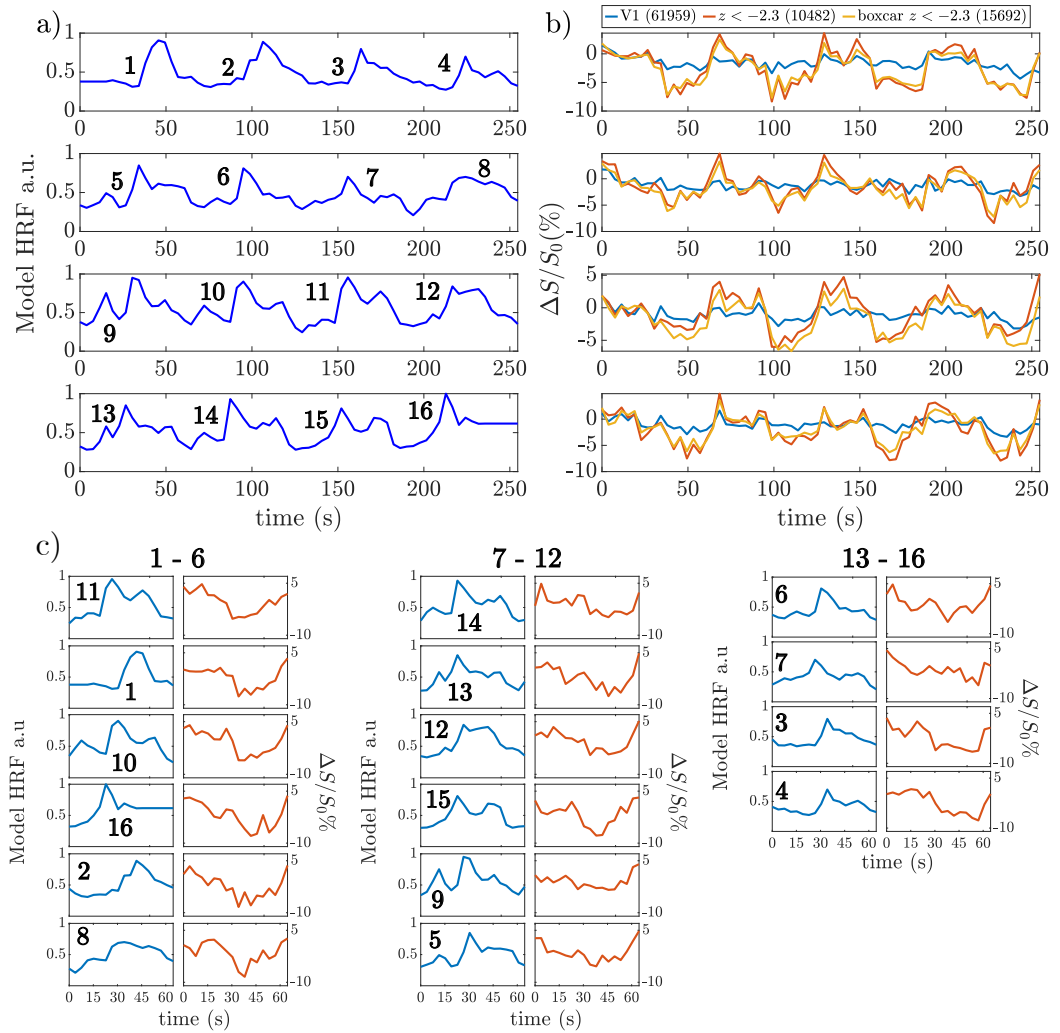


Figure C.7: Comparison of a) the EEG alpha power informed regressors and b) the fMRI timecourse from all voxels in V1 (blue), significant negatively correlated voxels ($z < -2.3$) when using the EEG regressors (orange) and significant negatively correlated voxels ($z < -2.3$) when using the boxcar regressors (yellow). In brackets are the number of voxels that are contributing to each mean timecourse plotted. c) Shows the regressors from a) (blue) split into single eyes open/closed periods (~ 65 s) and ranked from largest response to smallest response. The corresponding fMRI period is shown next to it in orange. The numbers in bold correspond to the response numbers in a). Shown for Subject 3.

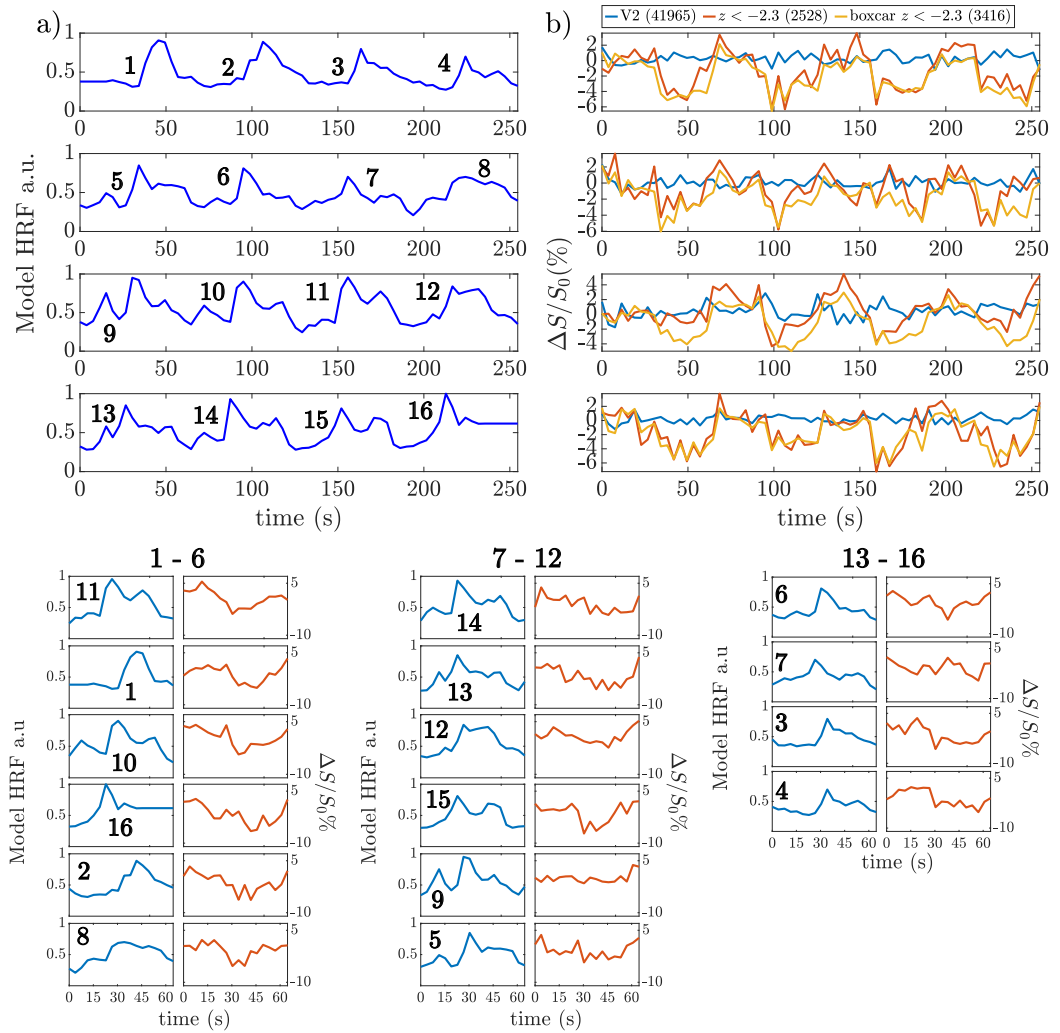


Figure C.8: Comparison of a) the EEG alpha power informed regressors and b) the fMRI timecourse from all voxels in V2 (blue), significant negatively correlated voxels ($z < -2.3$) when using the EEG regressors (orange) and significant negatively correlated voxels ($z < -2.3$) when using the boxcar regressors (yellow). In brackets are the number of voxels that are contributing to each mean timecourse plotted. c) Shows the regressors from a) (blue) split into single eyes open/closed periods (~ 65 s) and ranked from largest response to smallest response. The corresponding fMRI period is shown next to it in orange. The numbers in bold correspond to the response numbers in a). Shown for Subject 3.

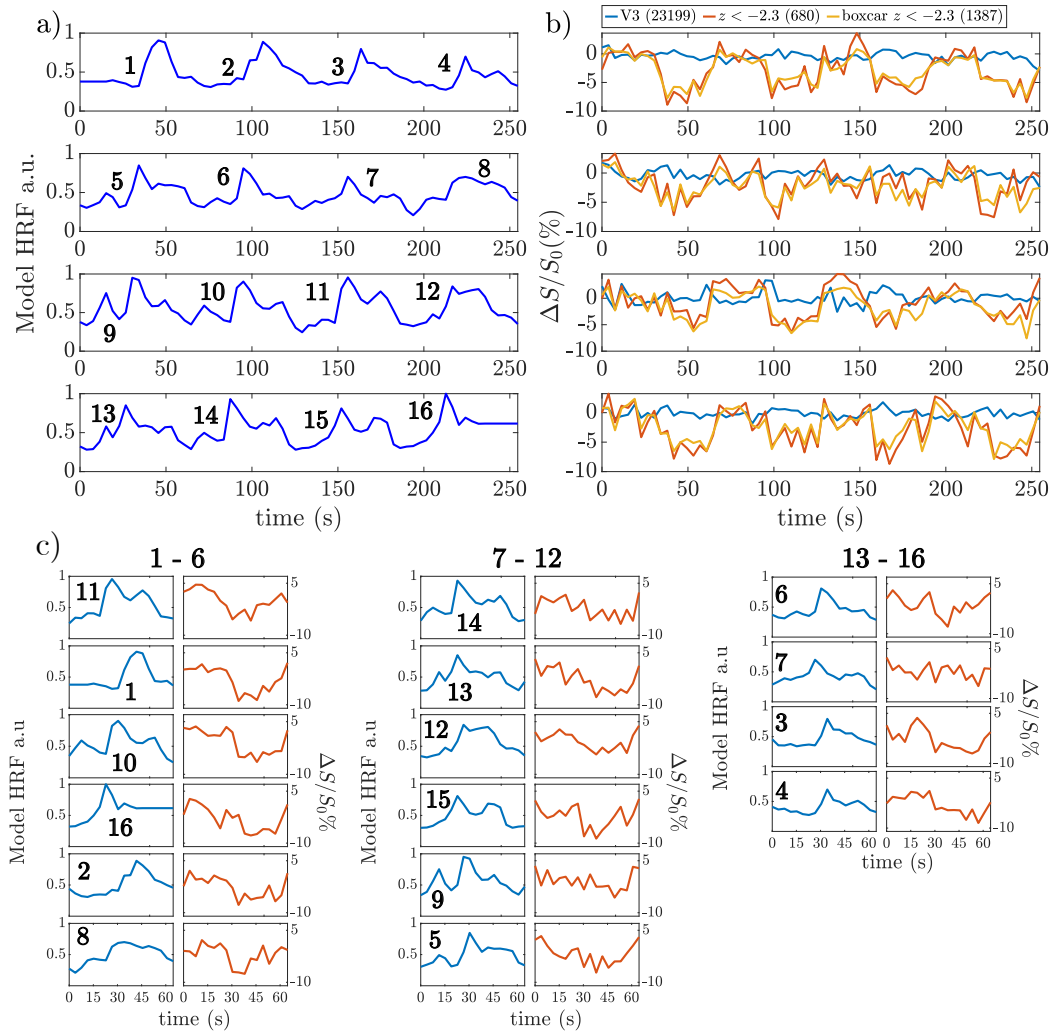


Figure C.9: Comparison of a) the EEG alpha power informed regressors and b) the fMRI timecourse from all voxels in V3 (blue), significant negatively correlated voxels ($z < -2.3$) when using the EEG regressors (orange) and significant negatively correlated voxels ($z < -2.3$) when using the boxcar regressors (yellow). In brackets are the number of voxels that are contributing to each mean timecourse plotted. c) Shows the regressors from a) (blue) split into single eyes open/closed periods (~ 65 s) and ranked from largest response to smallest response. The corresponding fMRI period is shown next to it in orange. The numbers in bold correspond to the response numbers in a). Shown for Subject 3.

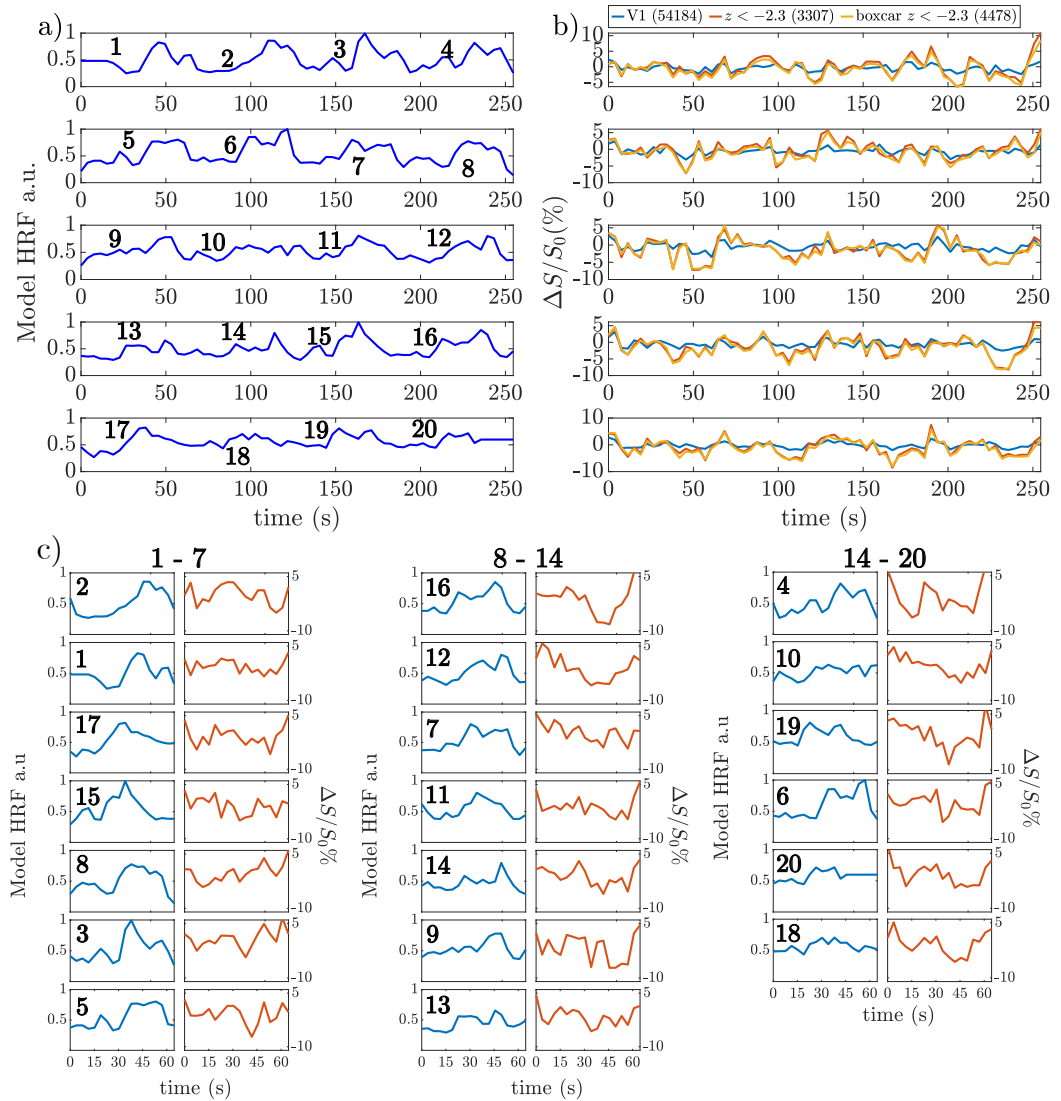


Figure C.10: Comparison of a) the EEG alpha power informed regressors and b) the fMRI timecourse from all voxels in V1 (blue), significant negatively correlated voxels ($z < -2.3$) when using the EEG regressors (orange) and significant negatively correlated voxels ($z < -2.3$) when using the boxcar regressors (yellow). In brackets are the number of voxels that are contributing to each mean timecourse plotted. c) Shows the regressors from a) (blue) split into single eyes open/closed periods ($\sim 65s$) and ranked from largest response to smallest response. The corresponding fMRI period is shown next to it in orange. The numbers in bold correspond to the response numbers in a). Shown for Subject 4.

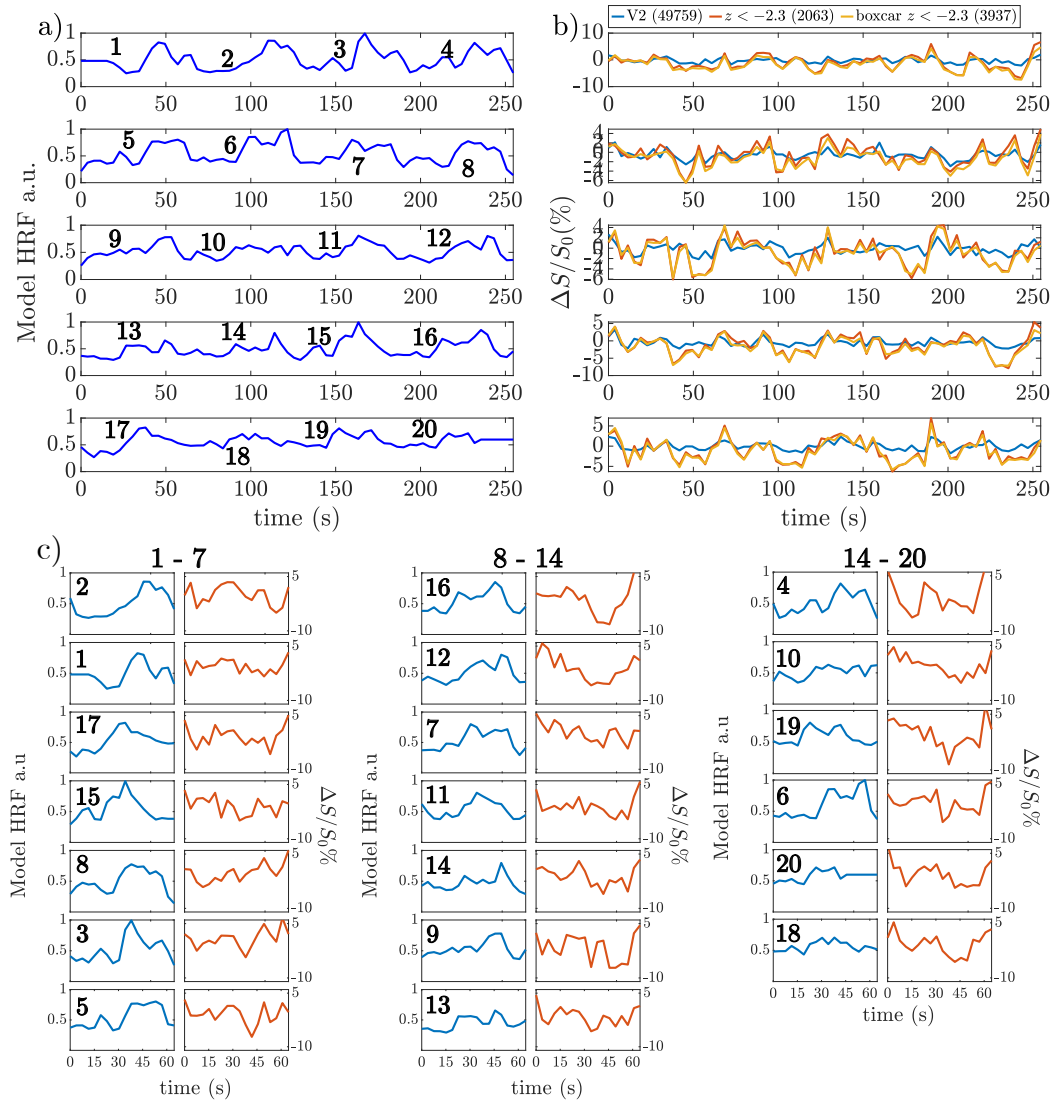


Figure C.11: Comparison of a) the EEG alpha power informed regressors and b) the fMRI timecourse from all voxels in V2 (blue), significant negatively correlated voxels ($z < -2.3$) when using the EEG regressors (orange) and significant negatively correlated voxels ($z < -2.3$) when using the boxcar regressors (yellow). In brackets are the number of voxels that are contributing to each mean timecourse plotted. c) Shows the regressors from a) (blue) split into single eyes open/closed periods ($\sim 65s$) and ranked from largest response to smallest response. The corresponding fMRI period is shown next to it in orange. The numbers in bold correspond to the response numbers in a). Shown for Subject 4.

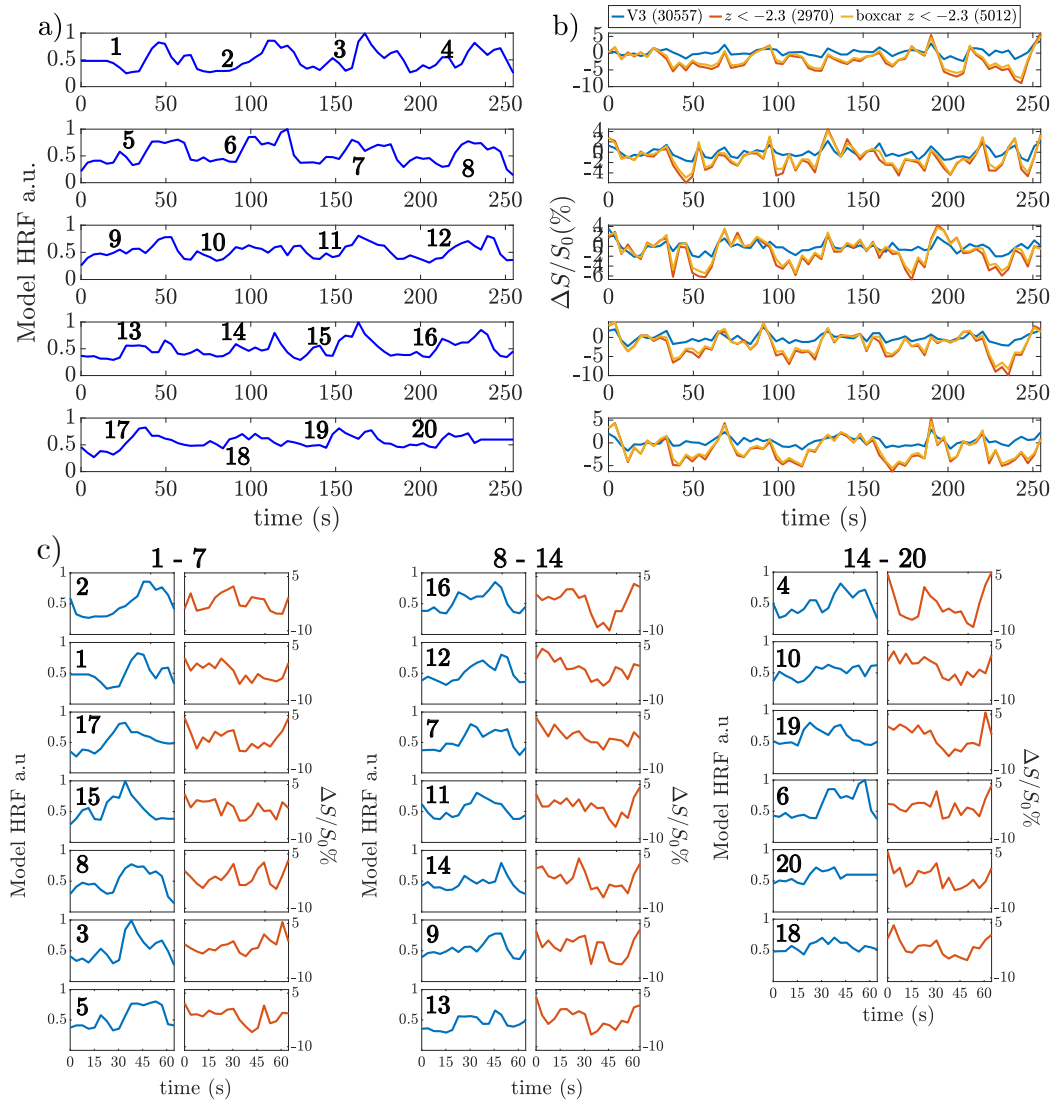


Figure C.12: Comparison of a) the EEG alpha power informed regressors and b) the fMRI timecourse from all voxels in V3 (blue), significant negatively correlated voxels ($z < -2.3$) when using the EEG regressors (orange) and significant negatively correlated voxels ($z < -2.3$) when using the boxcar regressors (yellow). In brackets are the number of voxels that are contributing to each mean timecourse plotted. c) Shows the regressors from a) (blue) split into single eyes open/closed periods ($\sim 65s$) and ranked from largest response to smallest response. The corresponding fMRI period is shown next to it in orange. The numbers in bold correspond to the response numbers in a). Shown for Subject 4.

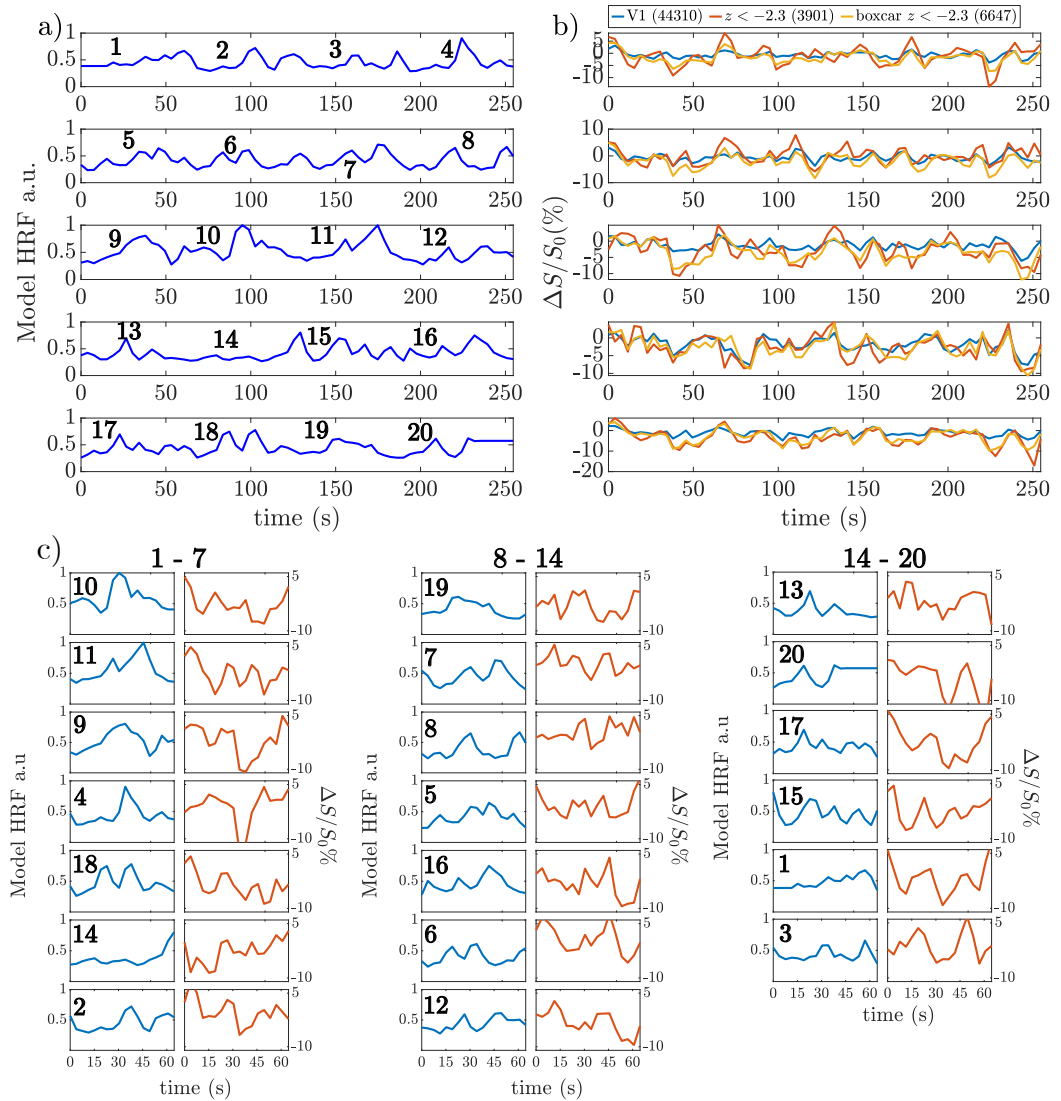


Figure C.13: Comparison of a) the EEG alpha power informed regressors and b) the fMRI timecourse from all voxels in V1 (blue), significant negatively correlated voxels ($z < -2.3$) when using the EEG regressors (orange) and significant negatively correlated voxels ($z < -2.3$) when using the boxcar regressors (yellow). In brackets are the number of voxels that are contributing to each mean timecourse plotted. c) Shows the regressors from a) (blue) split into single eyes open/closed periods ($\sim 65s$) and ranked from largest response to smallest response. The corresponding fMRI period is shown next to it in orange. The numbers in bold correspond to the response numbers in a). Shown for Subject 5.

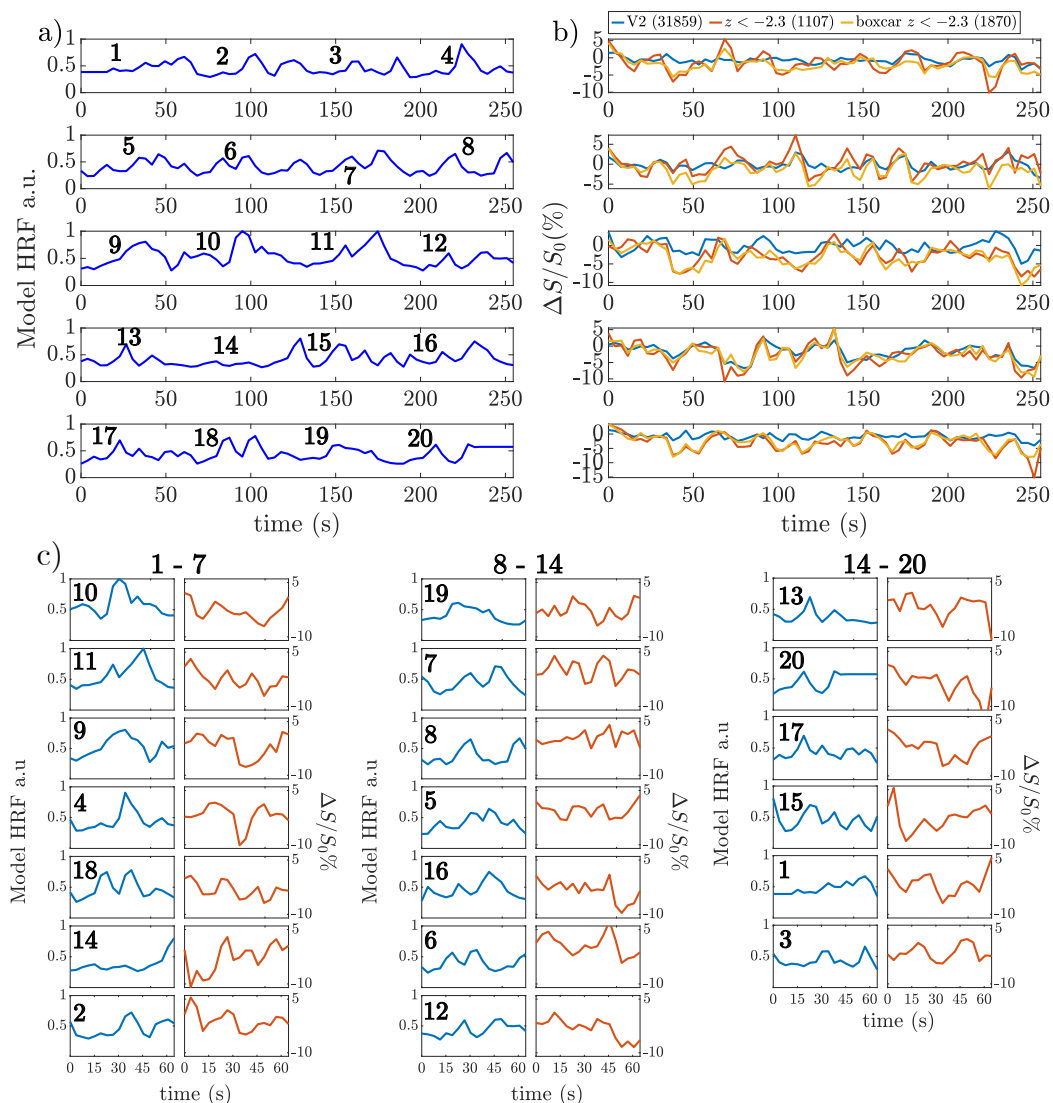


Figure C.14: Comparison of a) the EEG alpha power informed regressors and b) the fMRI timecourse from all voxels in V2 (blue), significant negatively correlated voxels ($z < -2.3$) when using the EEG regressors (orange) and significant negatively correlated voxels ($z < -2.3$) when using the boxcar regressors (yellow). In brackets are the number of voxels that are contributing to each mean timecourse plotted. c) Shows the regressors from a) (blue) split into single eyes open/closed periods (~65s) and ranked from largest response to smallest response. The corresponding fMRI period is shown next to it in orange. The numbers in bold correspond to the response numbers in a). Shown for Subject 5.

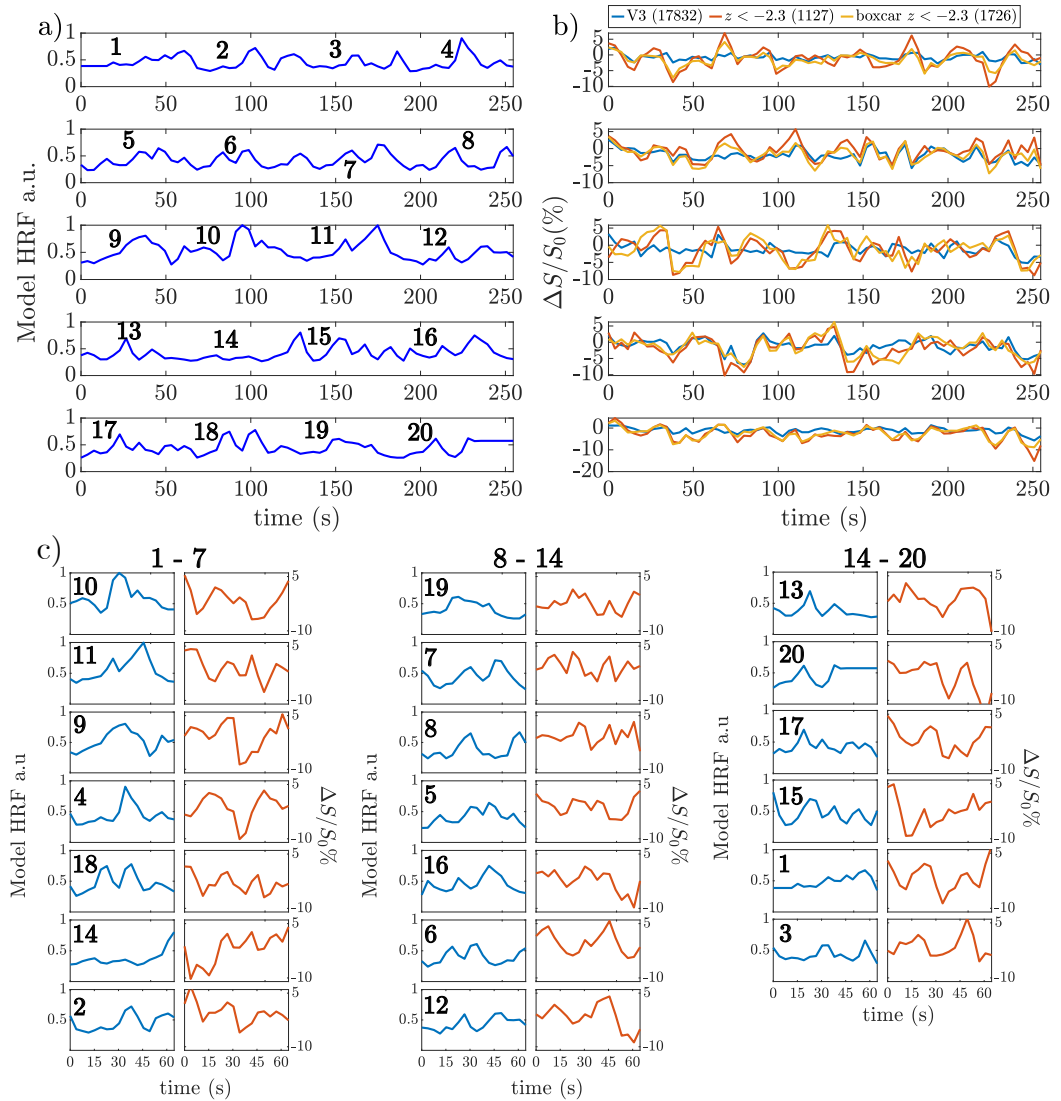


Figure C.15: Comparison of a) the EEG alpha power informed regressors and b) the fMRI timecourse from all voxels in V3 (blue), significant negatively correlated voxels ($z < -2.3$) when using the EEG regressors (orange) and significant negatively correlated voxels ($z < -2.3$) when using the boxcar regressors (yellow). In brackets are the number of voxels that are contributing to each mean timecourse plotted. c) Shows the regressors from a) (blue) split into single eyes open/closed periods ($\sim 65s$) and ranked from largest response to smallest response. The corresponding fMRI period is shown next to it in orange. The numbers in bold correspond to the response numbers in a). Shown for Subject 5.

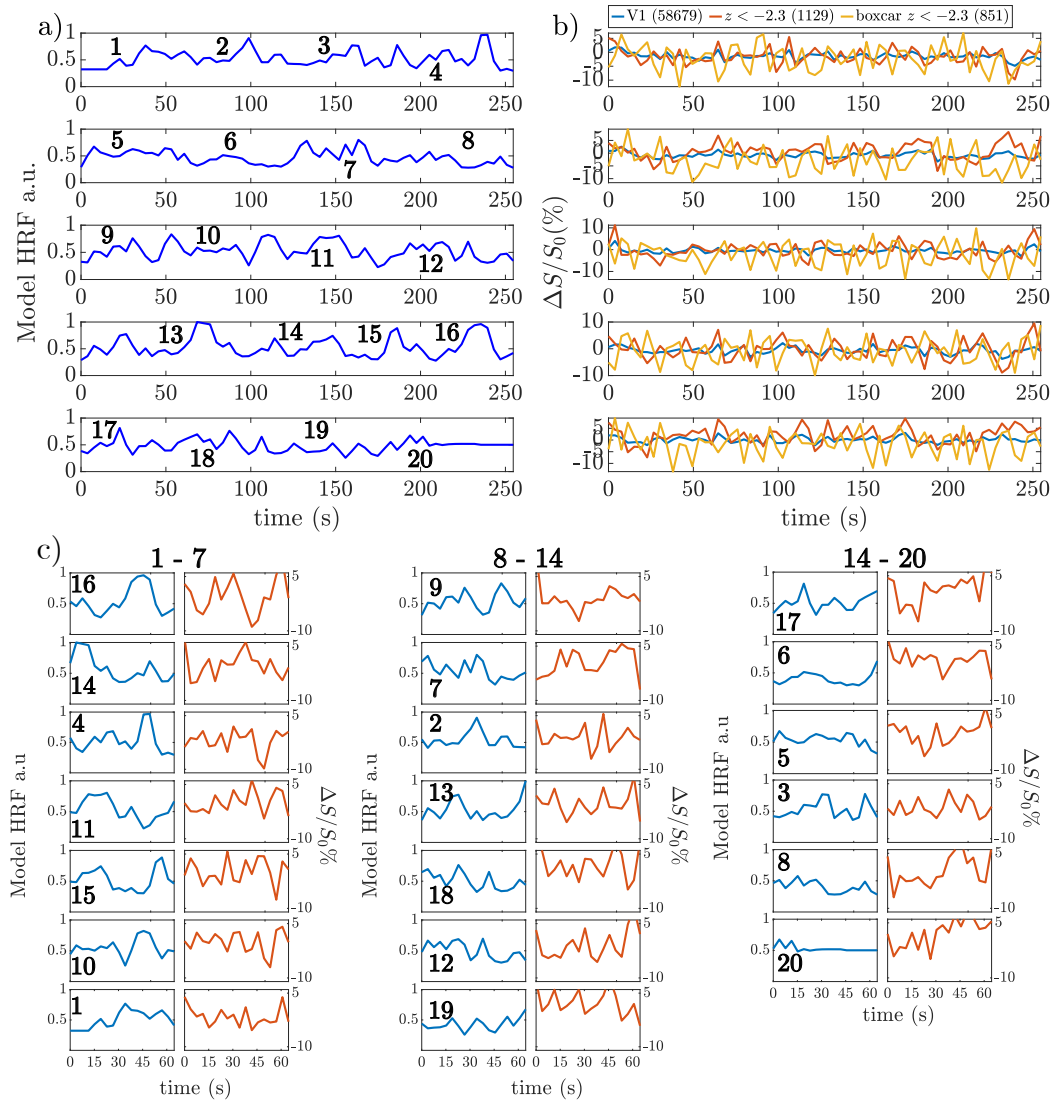


Figure C.16: Comparison of a) the EEG alpha power informed regressors and b) the fMRI timecourse from all voxels in V1 (blue), significant negatively correlated voxels ($z < -2.3$) when using the EEG regressors (orange) and significant negatively correlated voxels ($z < -2.3$) when using the boxcar regressors (yellow). In brackets are the number of voxels that are contributing to each mean timecourse plotted. c) Shows the regressors from a) (blue) split into single eyes open/closed periods ($\sim 65s$) and ranked from largest response to smallest response. The corresponding fMRI period is shown next to it in orange. The numbers in bold correspond to the response numbers in a). Shown for Subject 6.

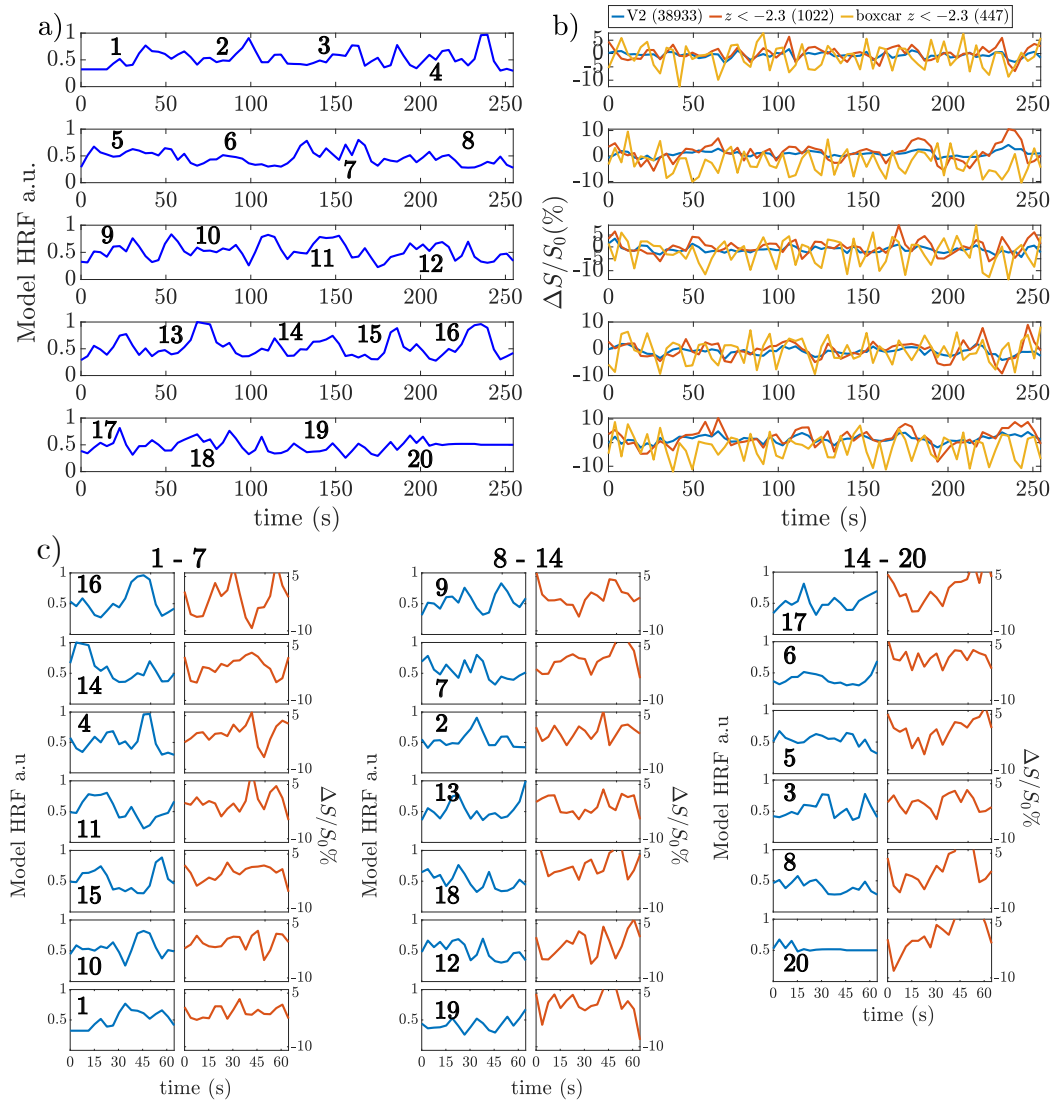


Figure C.17: Comparison of a) the EEG alpha power informed regressors and b) the fMRI timecourse from all voxels in V2 (blue), significant negatively correlated voxels ($z < -2.3$) when using the EEG regressors (orange) and significant negatively correlated voxels ($z < -2.3$) when using the boxcar regressors (yellow). In brackets are the number of voxels that are contributing to each mean timecourse plotted. c) Shows the regressors from a) (blue) split into single eyes open/closed periods ($\sim 65s$) and ranked from largest response to smallest response. The corresponding fMRI period is shown next to it in orange. The numbers in bold correspond to the response numbers in a). Shown for Subject 6.

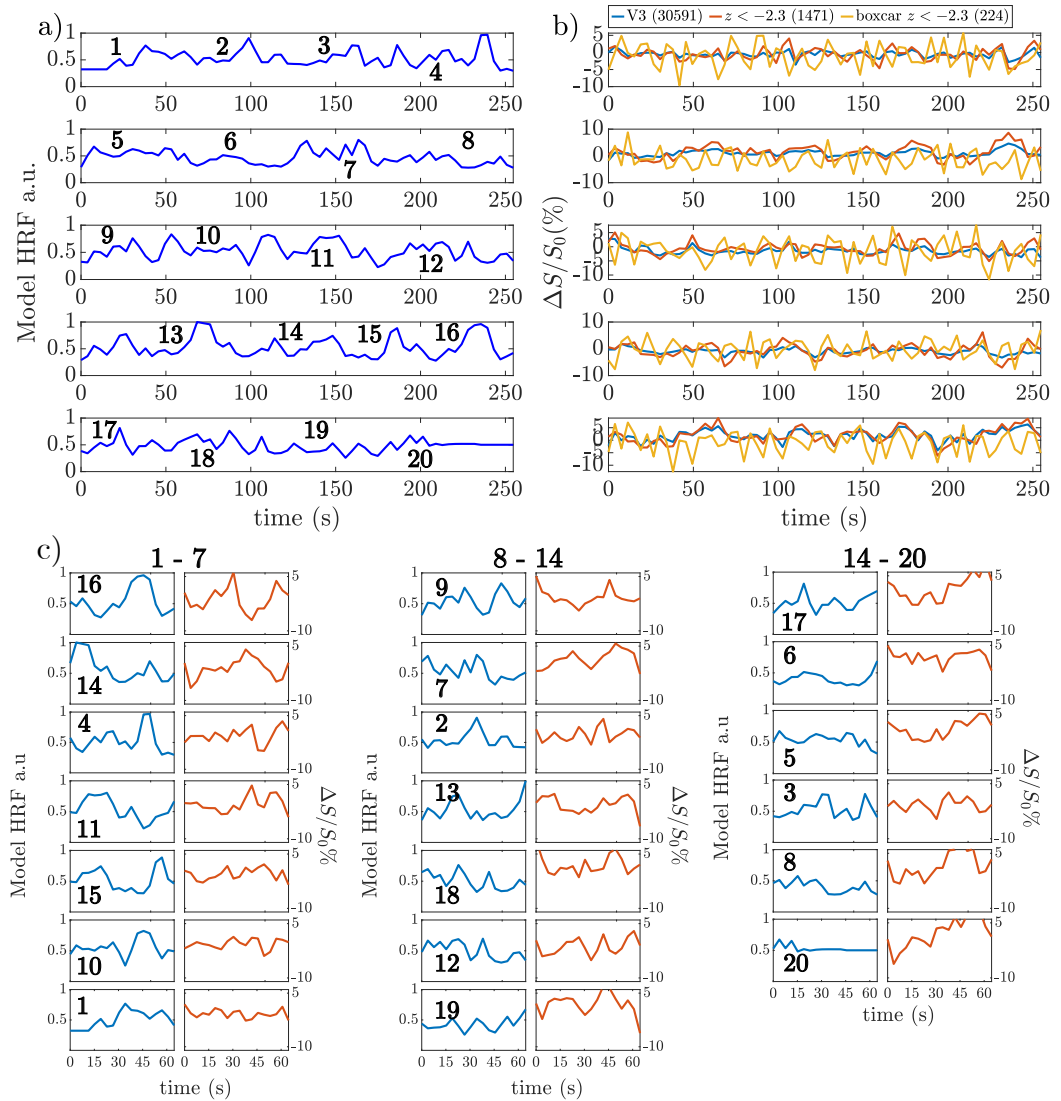


Figure C.18: Comparison of a) the EEG alpha power informed regressors and b) the fMRI timecourse from all voxels in V3 (blue), significant negatively correlated voxels ($z < -2.3$) when using the EEG regressors (orange) and significant negatively correlated voxels ($z < -2.3$) when using the boxcar regressors (yellow). In brackets are the number of voxels that are contributing to each mean timecourse plotted. c) Shows the regressors from a) (blue) split into single eyes open/closed periods ($\sim 65s$) and ranked from largest response to smallest response. The corresponding fMRI period is shown next to it in orange. The numbers in bold correspond to the response numbers in a). Shown for Subject 6.

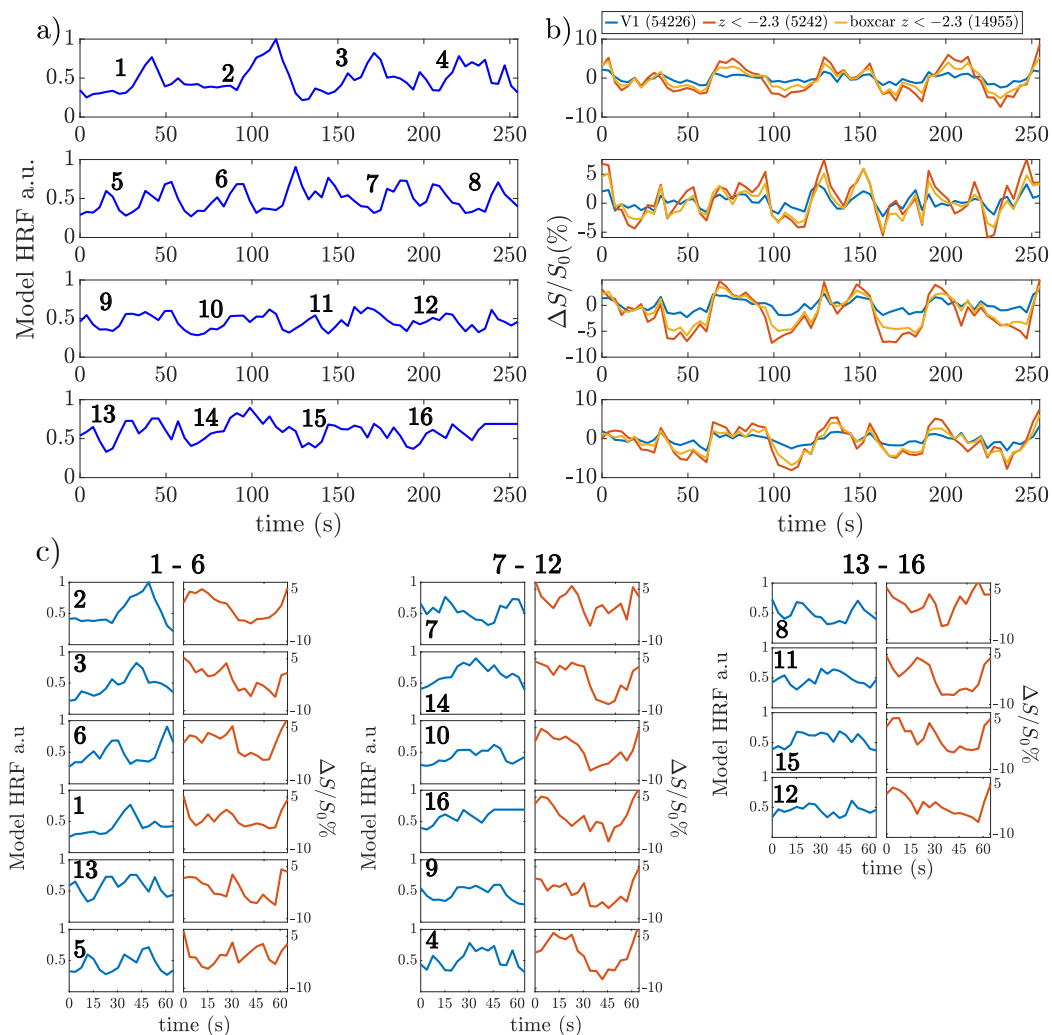


Figure C.19: Comparison of a) the EEG alpha power informed regressors and b) the fMRI timecourse from all voxels in V1 (blue), significant negatively correlated voxels ($z < -2.3$) when using the EEG regressors (orange) and significant negatively correlated voxels ($z < -2.3$) when using the boxcar regressors (yellow). In brackets are the number of voxels that are contributing to each mean timecourse plotted. c) Shows the regressors from a) (blue) split into single eyes open/closed periods ($\sim 65s$) and ranked from largest response to smallest response. The corresponding fMRI period is shown next to it in orange. The numbers in bold correspond to the response numbers in a). Shown for Subject 7.

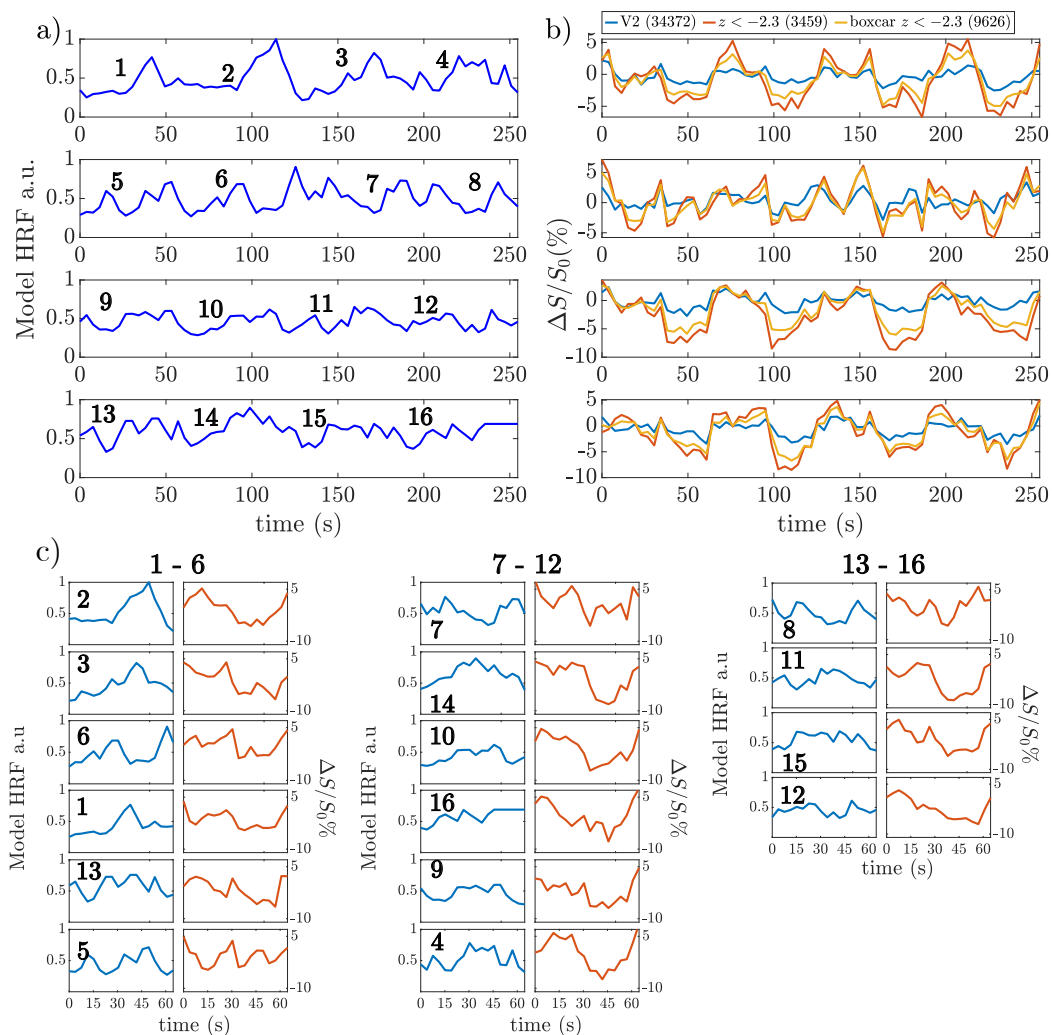


Figure C.20: Comparison of a) the EEG alpha power informed regressors and b) the fMRI timecourse from all voxels in V2 (blue), significant negatively correlated voxels ($z < -2.3$) when using the EEG regressors (orange) and significant negatively correlated voxels ($z < -2.3$) when using the boxcar regressors (yellow). In brackets are the number of voxels that are contributing to each mean timecourse plotted. c) Shows the regressors from a) (blue) split into single eyes open/closed periods ($\sim 65s$) and ranked from largest response to smallest response. The corresponding fMRI period is shown next to it in orange. The numbers in bold correspond to the response numbers in a). Shown for Subject 3.

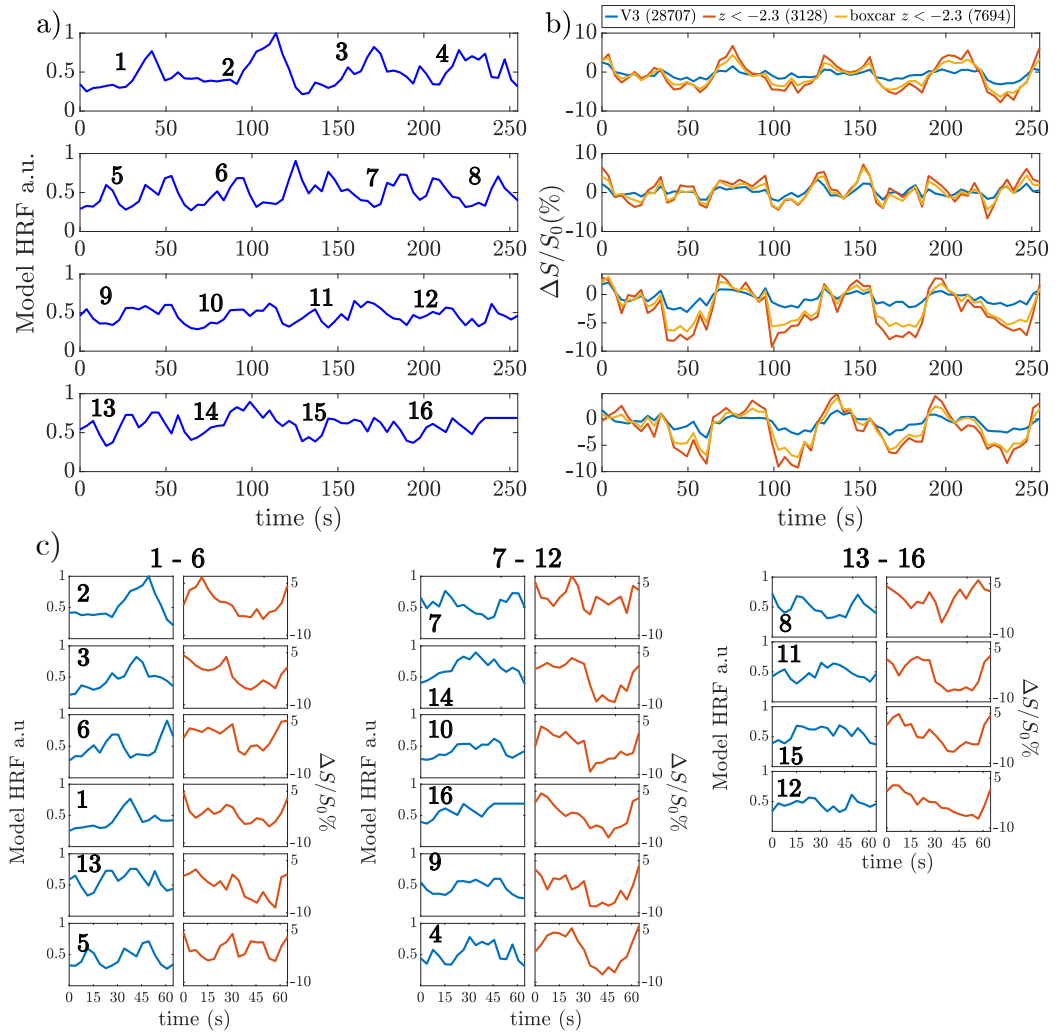


Figure C.21: Comparison of a) the EEG alpha power informed regressors and b) the fMRI timecourse from all voxels in V3 (blue), significant negatively correlated voxels ($z < -2.3$) when using the EEG regressors (orange) and significant negatively correlated voxels ($z < -2.3$) when using the boxcar regressors (yellow). In brackets are the number of voxels that are contributing to each mean timecourse plotted. c) Shows the regressors from a) (blue) split into single eyes open/closed periods ($\sim 65s$) and ranked from largest response to smallest response. The corresponding fMRI period is shown next to it in orange. The numbers in bold correspond to the response numbers in a). Shown for Subject 7.

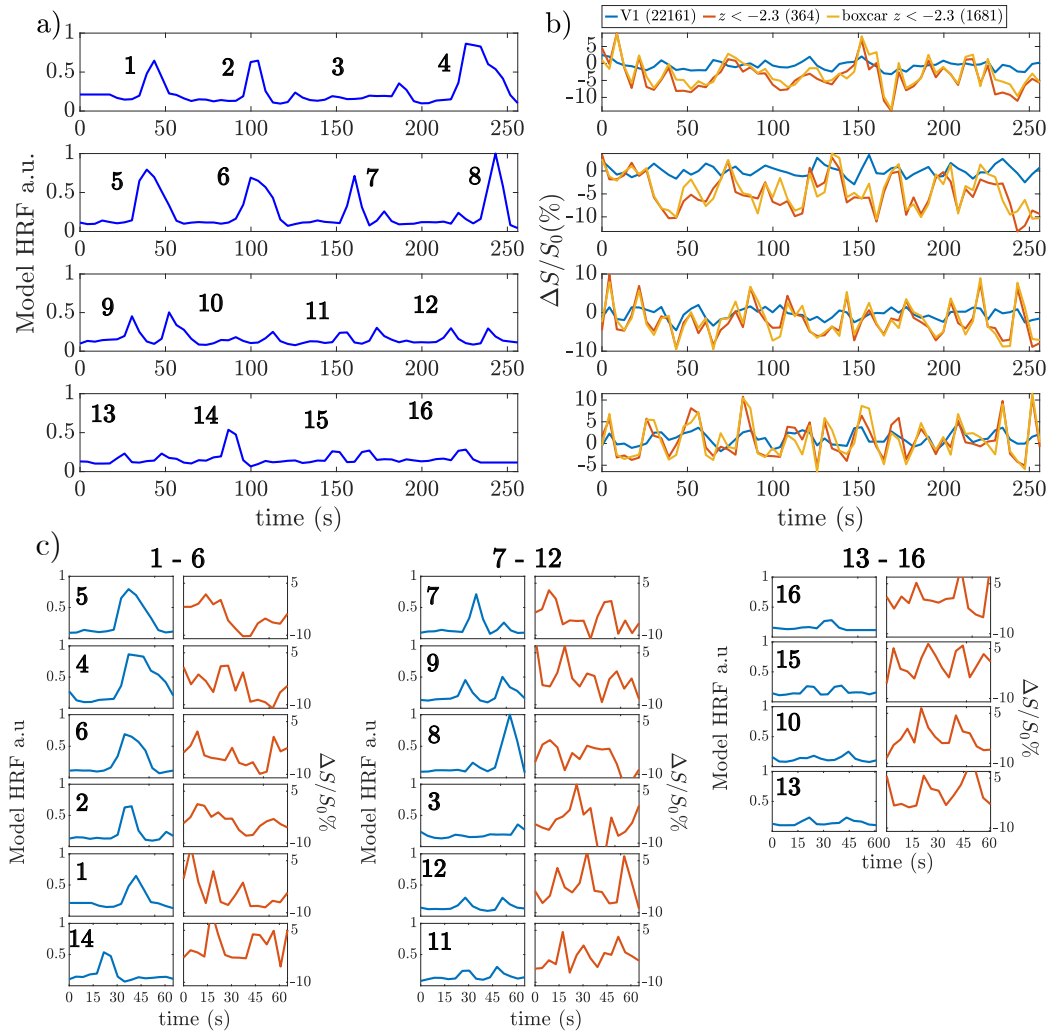


Figure C.22: Comparison of a) the EEG alpha power informed regressors and b) the fMRI timecourse from all voxels in V1 (blue), significant negatively correlated voxels ($z < -2.3$) when using the EEG regressors (orange) and significant negatively correlated voxels ($z < -2.3$) when using the boxcar regressors (yellow). In brackets are the number of voxels that are contributing to each mean timecourse plotted. c) Shows the regressors from a) (blue) split into single eyes open/closed periods ($\sim 65s$) and ranked from largest response to smallest response. The corresponding fMRI period is shown next to it in orange. The numbers in bold correspond to the response numbers in a). Shown for Subject 8.

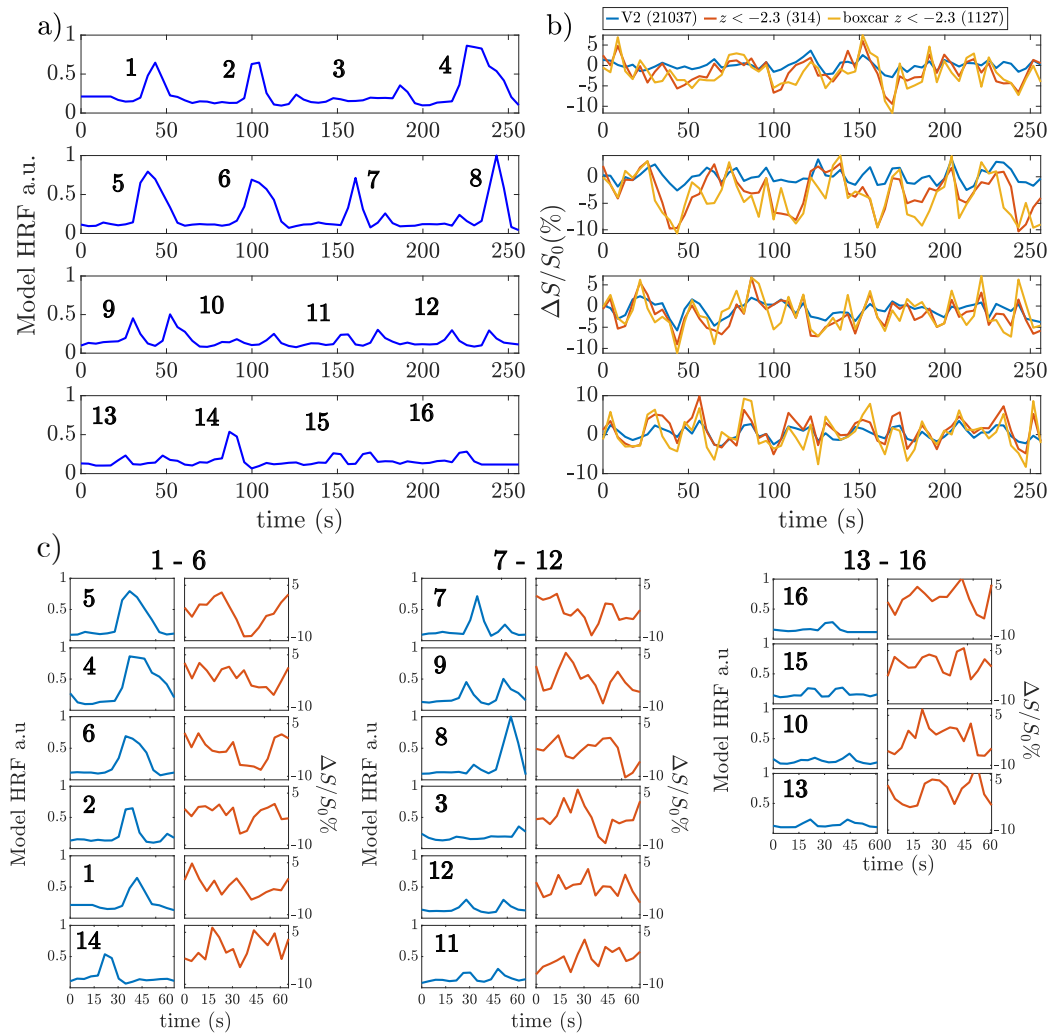


Figure C.23: Comparison of a) the EEG alpha power informed regressors and b) the fMRI timecourse from all voxels in V2 (blue), significant negatively correlated voxels ($z < -2.3$) when using the EEG regressors (orange) and significant negatively correlated voxels ($z < -2.3$) when using the boxcar regressors (yellow). In brackets are the number of voxels that are contributing to each mean timecourse plotted. c) Shows the regressors from a) (blue) split into single eyes open/closed periods ($\sim 65s$) and ranked from largest response to smallest response. The corresponding fMRI period is shown next to it in orange. The numbers in bold correspond to the response numbers in a). Shown for Subject 8.

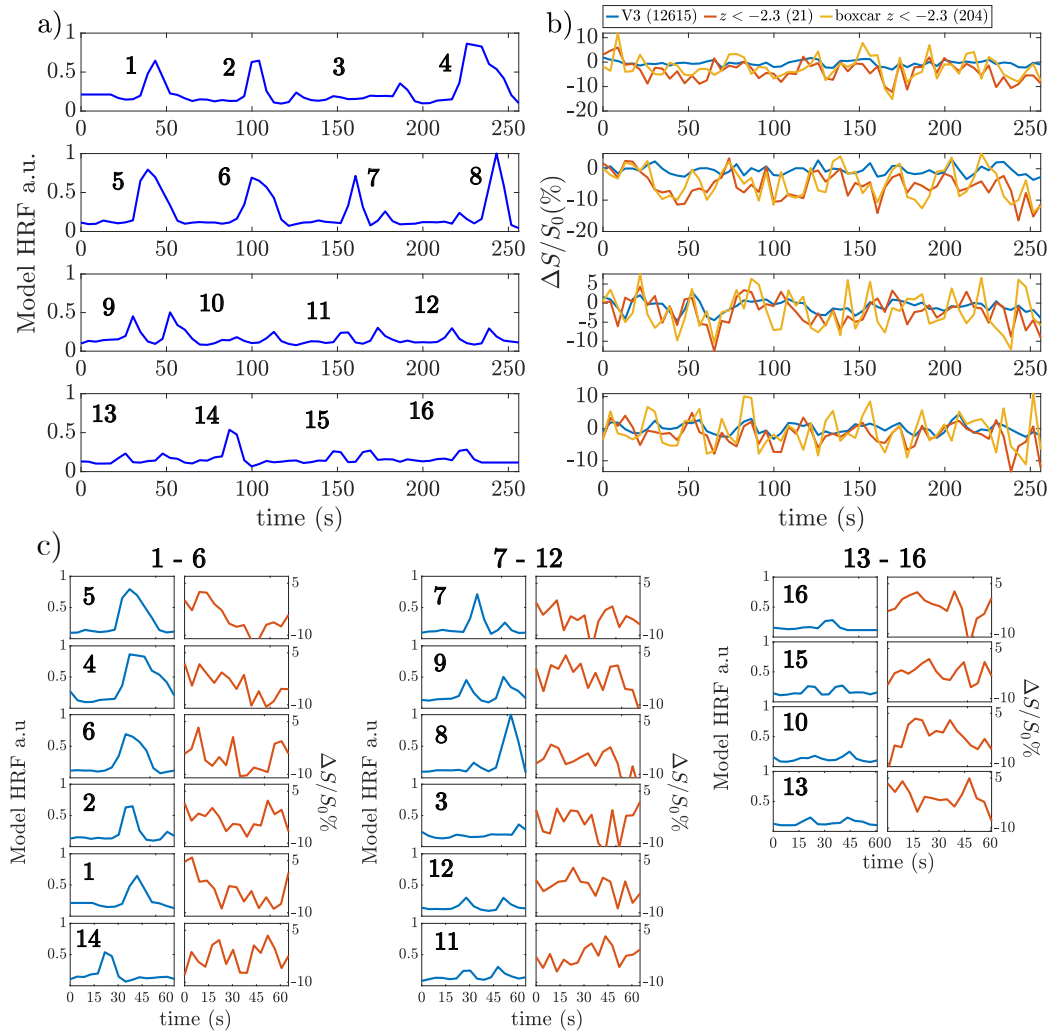


Figure C.24: Comparison of a) the EEG alpha power informed regressors and b) the fMRI timecourse from all voxels in V3 (blue), significant negatively correlated voxels ($z < -2.3$) when using the EEG regressors (orange) and significant negatively correlated voxels ($z < -2.3$) when using the boxcar regressors (yellow). In brackets are the number of voxels that are contributing to each mean timecourse plotted. c) Shows the regressors from a) (blue) split into single eyes open/closed periods ($\sim 65s$) and ranked from largest response to smallest response. The corresponding fMRI period is shown next to it in orange. The numbers in bold correspond to the response numbers in a). Shown for Subject 8.

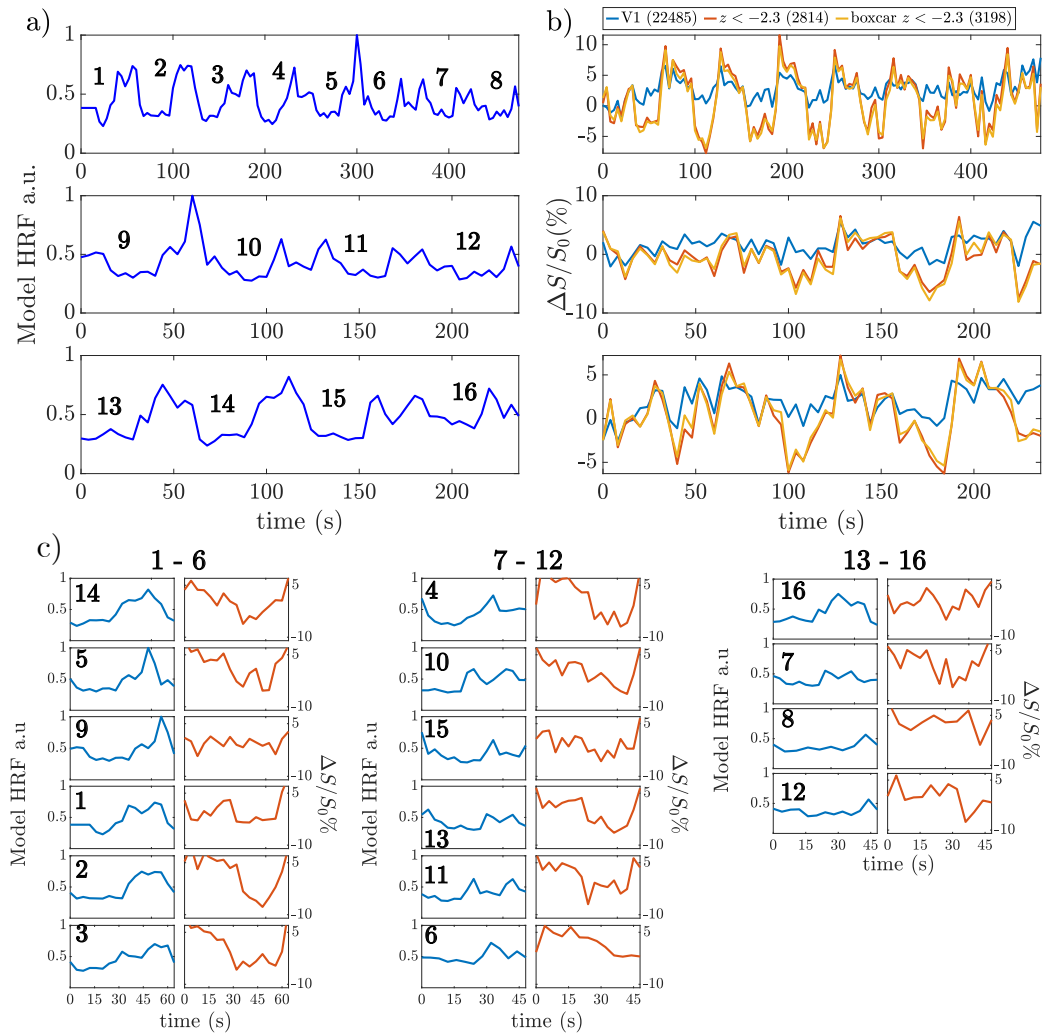


Figure C.25: Comparison of a) the EEG alpha power informed regressors and b) the fMRI timecourse from all voxels in V1 (blue), significant negatively correlated voxels ($z < -2.3$) when using the EEG regressors (orange) and significant negatively correlated voxels ($z < -2.3$) when using the boxcar regressors (yellow). In brackets are the number of voxels that are contributing to each mean timecourse plotted. c) Shows the regressors from a) (blue) split into single eyes open/closed periods ($\sim 65s$) and ranked from largest response to smallest response. The corresponding fMRI period is shown next to it in orange. The numbers in bold correspond to the response numbers in a). Shown for Subject 9.

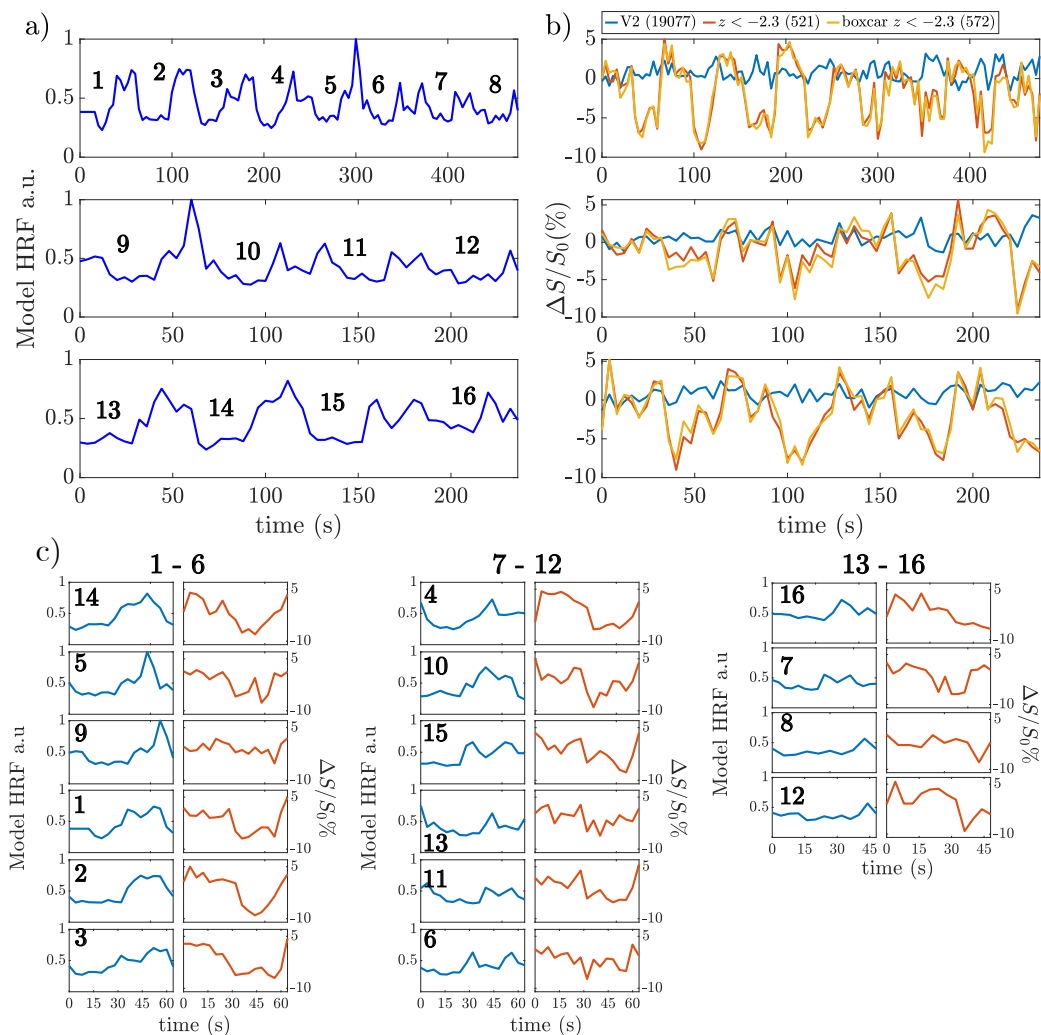


Figure C.26: Comparison of a) the EEG alpha power informed regressors and b) the fMRI timecourse from all voxels in V2 (blue), significant negatively correlated voxels ($z < -2.3$) when using the EEG regressors (orange) and significant negatively correlated voxels ($z < -2.3$) when using the boxcar regressors (yellow). In brackets are the number of voxels that are contributing to each mean timecourse plotted. c) Shows the regressors from a) (blue) split into single eyes open/closed periods (~ 65 s) and ranked from largest response to smallest response. The corresponding fMRI period is shown next to it in orange. The numbers in bold correspond to the response numbers in a). Shown for Subject 9.

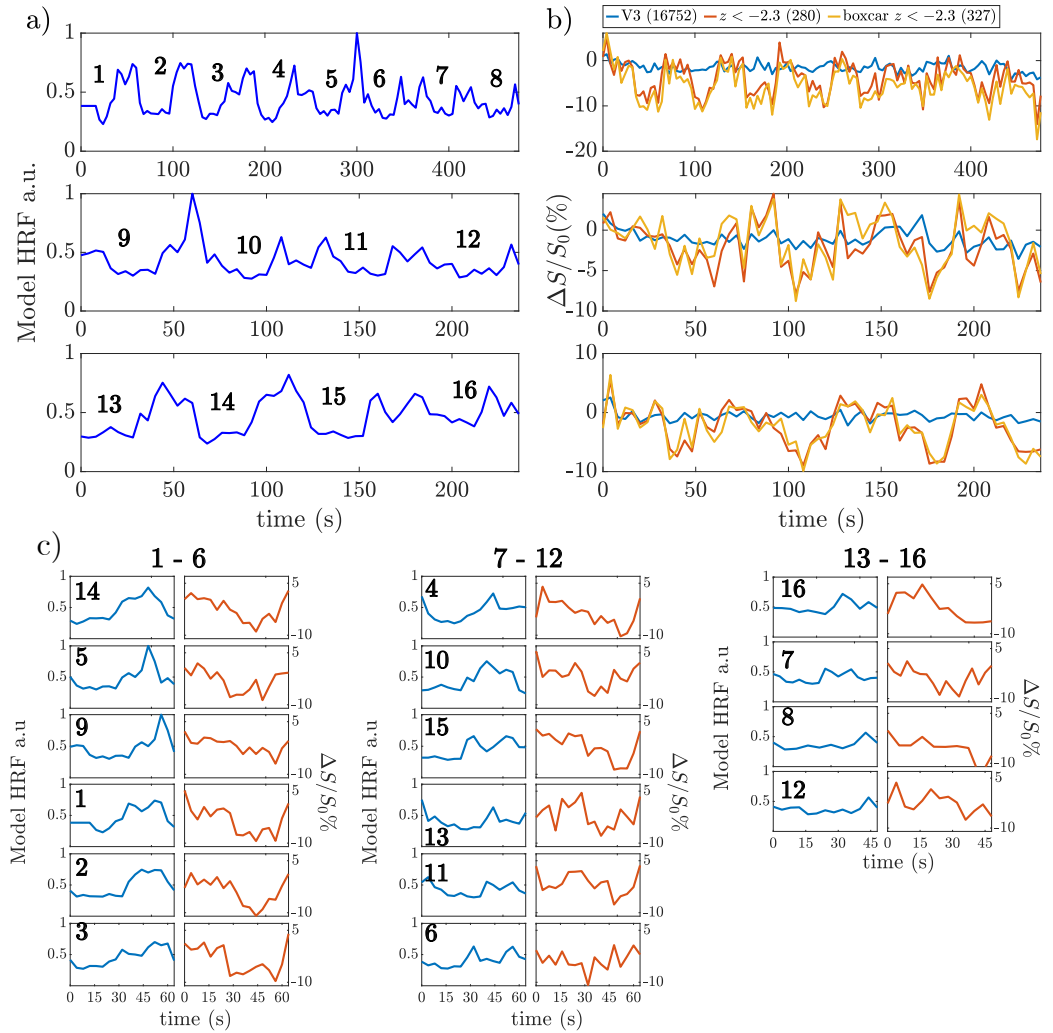


Figure C.27: Comparison of a) the EEG alpha power informed regressors and b) the fMRI timecourse from all voxels in V3 (blue), significant negatively correlated voxels ($z < -2.3$) when using the EEG regressors (orange) and significant negatively correlated voxels ($z < -2.3$) when using the boxcar regressors (yellow). In brackets are the number of voxels that are contributing to each mean timecourse plotted. c) Shows the regressors from a) (blue) split into single eyes open/closed periods ($\sim 65s$) and ranked from largest response to smallest response. The corresponding fMRI period is shown next to it in orange. The numbers in bold correspond to the response numbers in a). Shown for Subject 9.

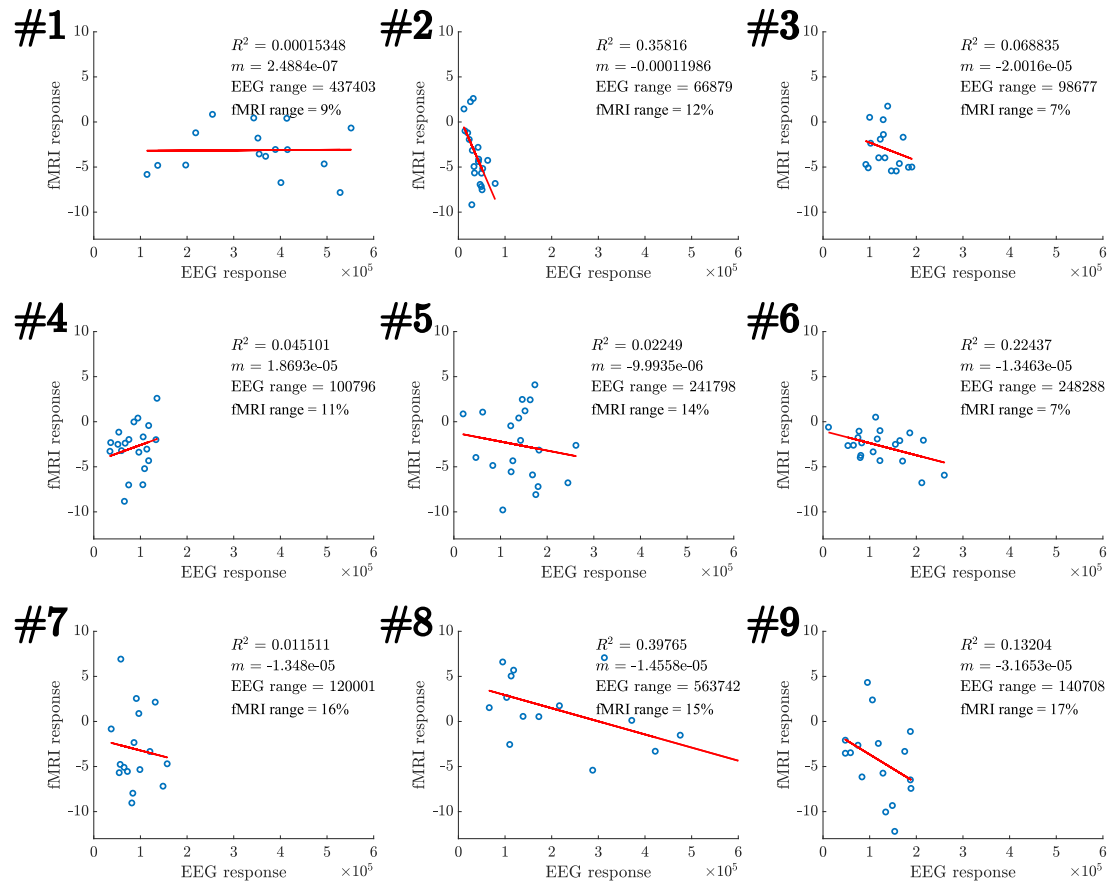


Figure C.28: The mean fMRI response from significant voxels ($z < -2.3$) within V1 for each trial plotted against the EEG alpha power regressor amplitude during the corresponding time period. The subject number is indicated in the top left of each plot.